Queen Mary University of London

SCHOOL OF ENGINEERING AND MATERIALS SCIENCE

Aerofoil broadband and tonal noise modelling using Fast-Random-Particle-Mesh method and Large Eddy Simulation

by

Stanislav Proskurov

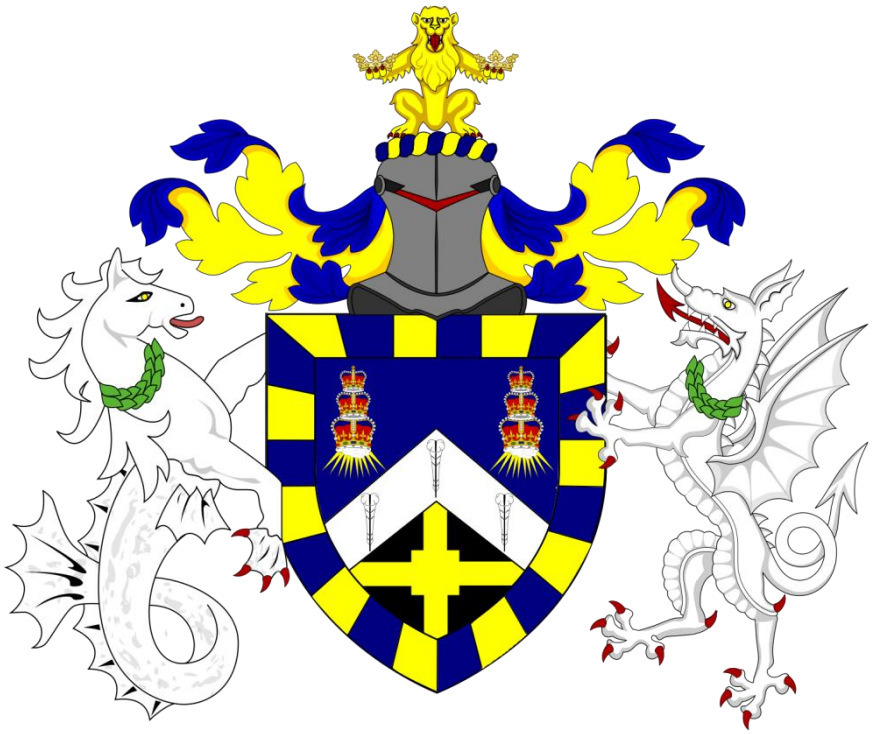

Thesis for the degree of Doctor of Philosophy

November 2017

This page is intentionally left blank

Queen Mary University of London

ABSTRACT

SCHOOL OF ENGINEERING AND MATERIALS SCIENCE

Doctor of Philosophy

Aerofoil broadband and tonal noise modelling using Fast-Random-Particle-Mesh method and Large Eddy Simulation

by Stanislav Proskurov

The aim of this work is to critically examine state-of-the art numerical methods used in computational aero-acoustics with the goal to further develop methods of choice that satisfy the industry requirements for aero-acoustic design, that is being fast, physical and potentially applicable to a variety of airframe noise problems. At the core of this thesis, two different modelling techniques are applied to benchmark aerofoil noise problems. One is based on a modern Fast Random Particle Mesh (FRPM) method with the mean flow and turbulence statistics supplied from the Reynolds-Averaged Navier-Stokes (RANS) simulation. The second technique is a Large Eddy Simulation (LES) method utilising the new in-house fast-turn-around GPU CABARET code.

The novelty of the work presented herein consists in the development of new modifications to the stochastic FRPM method featuring both tonal and broadband noise sources. The technique relies on the combination of incorporated vortex-shedding resolved flow available from Unsteady Reynolds-Averaged Navier-Stokes (URANS) simulation with the fine-scale turbulence FRPM solution generated via stochastic velocity fluctuations in the context of vortex sound theory. In contrast to the existing literature, proposed methodology encompasses a unified treatment for broadband and tonal acoustic noise sources at the source level, thus, accounting for linear source interference as well as possible non-linear source interaction effects. Results of the method's application for two aerofoil benchmark cases, with sharp and blunt trailing edges are presented. In each case, the importance of individual linear and non-linear noise sources was investigated. Several new key features related to the unsteady implementation of the method were tested and brought into the equation.

The source terms responsible for noise generation in accordance with the vortex sound theory are computed to assess the validity range of a digital filter calibration parameter used in the FRPM method for synthetic turbulence generation as compared to the same source reconstructed from the first principle LES solution. Such comparison at the source level has been achieved for the first time in the modelling literature, which allows for the physical interpretation of results obtained by the FRPM method. Finally, solutions of the FRPM method with the calibration parameter tailored in accordance with the LES are used for far-field noise predictions which are compared with experimental measurements.

This page is intentionally left blank

STATEMENT OF ORIGINALITY

I, Stanislav Proskurov, confirm that the research included within this thesis is my own work or that where it has been carried out in collaboration with, or supported by others, that this is duly acknowledged below and my contribution indicated. Previously published material is also acknowledged below.

I attest that I have exercised reasonable care to ensure that the work is original, and does not to the best of my knowledge break any UK law, infringe any third party's copyright or other Intellectual Property Right, or contain any confidential material.

I accept that Queen Mary University of London has the right to use plagiarism detection software to check the electronic version of the thesis.

I confirm that this thesis has not been previously submitted for the award of a degree by this or any other university.

The copyright of this thesis rests with the author and no quotation from it or information derived from it may be published without the prior written consent of the author.

Signature:..... S. Proskurov

Date: 01/11/2017

Details of collaboration and publications:

Proskurov, S., Karabasov S. A. and Semiletov, V. A., "The exploration of numerical methods and noise modelling techniques applied to the trailing edge noise case with evaluation of their suitability for aero-acoustic design", *CEAA International Workshop,* 24-27 September 2014, Svetlogorsk, Russia.

Proskurov, S., Markesteijn, A. P. and Karabasov S. A., "Investigation into the sources of trailing edge noise using the Acoustic Perturbation Equations, LES and RANS-based FRPM technique", *23rd AIAA/CEAS Aeroacoustics Conference*, 5-9 June 2017, Denver, Colorado, USA.

Proskurov, S., Darbyshire, O. R. and Karabasov S. A., "Aerofoil broadband and tonal noise modelling using stochastic sound sources and incorporated large scale fluctuations", *Journal of Sound and Vibration,* vol. 411, pp. 60-74, 2017.

Contents

List of Figures

List of Tables

Nomenclature

Abbreviations

AIAA	American Institute of Aeronautics and Astronautics
AoA	Angle of attack
APE	Acoustic Perturbation Equation
BANC	Benchmark problems for Airframe Noise Computations
BPM	Brooks-Pope-Marcolini (empirical model)
CAA	Computational Aero-Acoustics
CABARET	Compact Accurately Boundary Adjusting high-REsolution Technique
CASE	Cooperative Awards in Science and Technology
CEAA	Computational Experiment in Aero-Acoustics
CFD	Computational Fluid Dynamics
CFL	Courant-Friedrichs-Lewy
DES	Detached Eddy Simulation
DDES	Delayed Detached Eddy Simulation
DG	Discontinuous Galerkin
DNS	Direct Numerical Simulation
DRP	Dispersion Relation Preserving
ENO	Essentially Non-Oscillatory
FCT	Flux Correction Transport
FD	Finite Difference
FDS	Flux Difference Splitting
FE	Finite Element
FRPM	Fast Random Particle Mesh
FV	Finite Volume
FW-H	Ffowcs Williams and Hawkings
GPU	Graphic Processing Unit (graphics card)
LE	Leading Edge
LEE	Linearised Euler Equation
LES	Large Eddy Simulation
LS	Laminar Separation
MILES	Monotonically Integrated LES
PWL	Sound Power Level
QF	Quadrature-Free
RANS	Reynolds-Averaged Navier-Stokes
RPM	Random Particle Method
RSM	Reynolds Stress Model
SA	Spalart-Allmaras (model)
SIL	Sound Intensity Level
SNGR	Stochastic Noise Generation

SPL	Sound Pressure Level
SST	Shear Stress Transport
TE	Trailing Edge
TKE	Turbulent Kinetic Energy
TS	Turbulent Separation
TU	Time Units
TVB	Total Variation Bounding
TVD	Total Variation Diminishing
URANS	Unsteady-RANS
WENO	Weighted-ENO

Greek letters

Where more than one definition provided refer to context

α	Angle / constant coefficient
β	Angle / constant coefficient / volume fraction / blending factor
γ	Heat capacity ratio / phase error
δ	Dirac function
δ_{ij}	Kronecker delta
ε	Turbulence dissipation rate
ε_{ij}	Dissipation tensor
ε_{ijk}	Alternating symbol
ζ_{re}	Reflection coefficient
ζ_{tr}	Transmission coefficient
η	Panikovski's constant / local coordinate frame
θ	Azimuthal angle
κ	Acoustic wavenumber (ω/c)
λ	Wavelength
μ	Dynamic viscosity
ν	Kinematic viscosity
ν_T	Turbulent eddy viscosity (model)
ξ	Langevin force
ξ_c	Cut-off length scale
π	Ratio of circle's circumference to its diameter
ρ	Density
σ	Constant coefficient
τ_s	Integral time scale
τ_{ij}	Shear stress
$\boldsymbol{\tau}$	Viscous stress tensor
φ	Solution flux function / potential
ϕ	Phase / basis function in FE
ψ	Stochastic stream function / random phase
ω	Angular frequency / specific dissipation rate (ε/k)

$\boldsymbol{\omega}$	Vorticity vector
$\mathbf{B}$	Element matrix
Δ	Cartesian mesh width / separation distance
Λ	Integral length scale
Π	Acoustic power
Π_{ij}	Velocity-pressure-gradient tensor
Φ_{ij}	Velocity tensor
Φ_{p}	Poisson equation
Ψ	Local domain
Ω	Frequency

Roman letters

a_c	Gaussian cut-off amplitude
c	Speed of sound / aerofoil chord
c_g	Group speed error
c_D	Drag coefficient
c_f	Skin friction coefficient
c_l	Length scale calibration constant
c_L	Lift coefficient
c_P	Pressure coefficient
d	Diameter
e	Specific internal energy
f	Function / frequency
f_T	Tension force
$\boldsymbol{f}$	Force vector
h	Enthalpy / separation distance (as in *CFL*)
k	Turbulent kinetic energy
$l_{D(max)}$	Maximum length scale supported by the FRPM domain
l_m	Mixing length
l_s	Length scale
l_{sgs}	Cut-off length scale of SGS model
m	Mass
p	Pressure
q	Acoustic source
$\boldsymbol{q}$	Heat flux / acoustic source vector
$\boldsymbol{r}$	Radial distance from origin / relative separation
s	Entropy
t	Time
u, v, w	Velocity components
u^a	Acoustic velocity component
u^v	Vortical velocity component

u_f'	Fine scale velocity fluctuation
u_L'	Large scale velocity fluctuation
u_{URANS}	Unsteady-RANS flow solution
x, y, z	Cartesian coordinates
A	Amplitude
A_α	Gaussian function composed of α azimuthal angles
B	Total enthalpy
C_s	Smagorinsky constant
C_μ	Model constant
D	Amplitude of a dipole
E	Total energy / energy spectrum
$\boldsymbol{F}_j$	Flux vectors
G	Gaussian filter kernel
I	Sound intensity
J_i	Bessel function of i^{th} order
L	Characteristic length
L_i	Source term in FW-H integral equation
$\boldsymbol{L}$	Lamb vector in vortex sound theory
M	Mach number
$\boldsymbol{M}$	Mass matrix
$\boldsymbol{P}$	Fluid stress tensor
Q	Volume rate of change
Q_{Kir}	Kirchhoff source terms
S	Control surface / surface area
T	Temperature
$\boldsymbol{T}_{ij}$	Lighthill's stress tensor
U	Mean velocity
V_p	FRPM particle volume
V_s^n	FRPM source region volume
V_0	Volume region
W	Stochastic source function
Z	Impedance

Symbols

$\not{f}$	Impulse excitation function
$\hat{n}$	Unit normal
Δt	Time step
$\mathbb{G}$	Green's function
$H(f)$	Heaviside function
$\mathcal{H}_1^{(2)}$	Hankel function of the 2nd kind
$\boldsymbol{\mathcal{J}}$	Jacobian matrix

N_λ	Points per wavelength
$\mathcal{P}_{ij}$	Production tensor
$\mathcal{R}_{ij}$	Correlation tensor / Pressure rate of strain tensor
$\mathcal{R}_{\mathcal{U}_i}$	Autocovariance of a white noise field
$\mathcal{R}_{wf}$	Correlation of a white noise field
$\mathbb{S}$	Amplitude of a quadrupole
$\boldsymbol{\mathcal{Q}}$	Acoustic source vector
$\mathcal{T}$	Tension
$\mathcal{U}_i$	White noise field
x^+, y^+, z^+	Near-wall mesh resolution parameter in the reference direction

Notation, subscripts and superscripts

$\mathcal{L}$	Wave operator
$\langle . \rangle$	Ensemble average
$\overline{(.)}$	Time average
$\lvert . \rvert$	Modulus
$(.)_0$	Mean quantity
$\mathrm{Re}(.)$	Real part
$\mathrm{Im}(.)$	Imaginary part
∞	Free-stream variable
$*$	Convolution operator / complex conjugate (if superscript)
∇	Gradient operator
$\nabla \times$	Curl operator
$'$	Fluctuating component
$(\ldots)' = (\ldots) - \langle(\ldots)\rangle$	
avg	Average
max	Maximum
min	Minimum
ref	Reference quantity
RMS	Root-mean-square
$\hat{.}$	Fourier transform

Acknowledgements

I wish to express my sincere gratitude to Dr. Sergey A. Karabasov for his supervision and guidance as well as encouragement throughout the course of this research. Also, my special thanks go to Dr. Mark Allan for his expert advice, assistance with computer programming at early stages of the project and invaluable discussions. I would like to thank Dr. Oliver R. Darbyshire for his support with BAE Altus solver and advice on implementation of various concepts. My thanks go to all fellow colleagues at BAE Systems Ltd. with whom I worked alongside during my time in Bristol.

I am grateful to Dr. Vasily A. Semiletov for his assistance and introduction into the CABARET code and also thanks go to my colleague Dr. Anton P. Markesteijn, as without his brilliant ideas and abilities to work magic with GPU computing it would not be possible to solve some challenging problems presented in this thesis.

This work has been supported by BAE Systems Ltd. and Engineering and Physical Sciences Research Council (EPSRC). Computations were performed on the Queen Mary cluster 'Apocrita' and GPU-Prime Ltd. GPU cards where the support of NVIDIA Corporation with the donation of the Tesla K40 GPU card partly used for this research is gratefully acknowledged. I also wish to express my gratitude to members of staff at School of Engineering and Materials Science (SEMS) for their help and support that has led to completion of this project.

During the course of this research I have met many wonderful people across the globe, who are part of aero-acoustics community: Dr. Alexei M. Sipatov, Dr. Georgy A. Faranosov, Dr. Tatiana K. Kozubskaya, Dr. Stanislav L. Denisov, Dr. Mikhail Y. Zaitsev, Dr. Nikolai N. Ostrikov, Dr. Viktor F. Kopiev, Dr. Vladimir A. Titarev, Prof. Vasily M. Goloviznin, Prof. Sergey N. Gurbatov, Prof. Oleg V. Rudenko, Dr. Ulf Michel, Dr. Philip J. Morris and others who I wish to thank for interesting discussions and getting me involved in the subject of aero-acoustics.

I thank my parents, Igor and Natalja for their support and all family members for genuinely caring about the progress of my project.

This page is intentionally left blank

Chapter 1

Introduction

Aero-acoustics is a research area that explores the physics of noise generated by aerodynamic flows. [1] For many industrial applications that involve turbulent flows, such as turbo-machinery, jets, airframe, various ducts to name the few, there is a problem due to noise generated by these flows which could be very obstructive to human hearing. The human hearing system can sense various sounds within the defined hearing band. Sound is the sensation detected by the ear where noise is regarded as an unwanted sound which may not cause annoyance only but in some cases can lead to a permanent hearing loss. On many occasions noise is very difficult to attenuate at a receiver location which in turn presents the aero-acoustics community with a challenge to develop efficient noise reduction mechanisms. Aero-acoustics has become an important part of aeronautical sciences since the mid-20th century, when as a consequence of rapidly growing aviation the problem of noise pollution became very notable. In the dawn of the jet aircraft age Mawardi and Dyer (1952) [2] published measurements on turbo-jet engine noise and it was the same year when Lighthill's pioneering theory emerged, showing how the turbulence in free space radiated sound waves in proportion to the eighth power of velocity. In the Bakerian lecture held in 1961, Lighthill demonstrated the relevance of his theory to practical engines. [3] The method employing acoustic analogy, initially proposed by Lighthill, gained popularity and was further developed in the works of Lilley [4], Ffowcs Williams [5], Ribner [6], Mani [7], Dowling [8], Goldstein [9] and others. Following the footsteps of classical works we shall review the hierarchy of equations of fluid mechanics and the acoustic analogy formulation in the following chapters but first, the importance of noise in engineering is discussed.

To this day, the aero-acoustics research remains mostly driven by the aerospace industry, mainly because of the size of airframe and engine components, e.g. wing flaps, slats, pylon, nozzle exhaust and others which bear a significant noise impact. As a result, demanding noise regulations constantly push boundaries, so much so that noise reduction has become a very important objective in aircraft design. Since 1950s most efforts in reducing aircraft noise have been devoted to the jet engine noise which used to dominate at take-off and fly-over conditions. Another important noise component associated with a turbo-jet engine is the fan noise and solutions for its reduction via geometry optimisation followed at the time when the fan noise potentially has become of comparable magnitude to the jet noise. With constant improvements to jet engines since 1980s effective noise reductions have been mainly achieved by increasing the bypass ratio of the jet for best aerodynamic efficiency until the jet installation had become a problem. As the pure jet and fan noise have become of a lesser problem, airframe noise as well as new types of noise sources such as the jet installation noise due to jet flow interaction with an airframe are now becoming of a major importance. For landing conditions, airframe noise has always been dominant due to the deployment of

high lift devices such as flaps and slats, which together with a wing leading and trailing edge form a multi-body aerofoil shape, as well as the contribution of a landing gear to overall noise levels. Hence, understanding and predicting the airframe noise is currently at the root of solving the aircraft noise problem. (See Figure 1 for main sources of noise generally attributed to commercial airplanes).

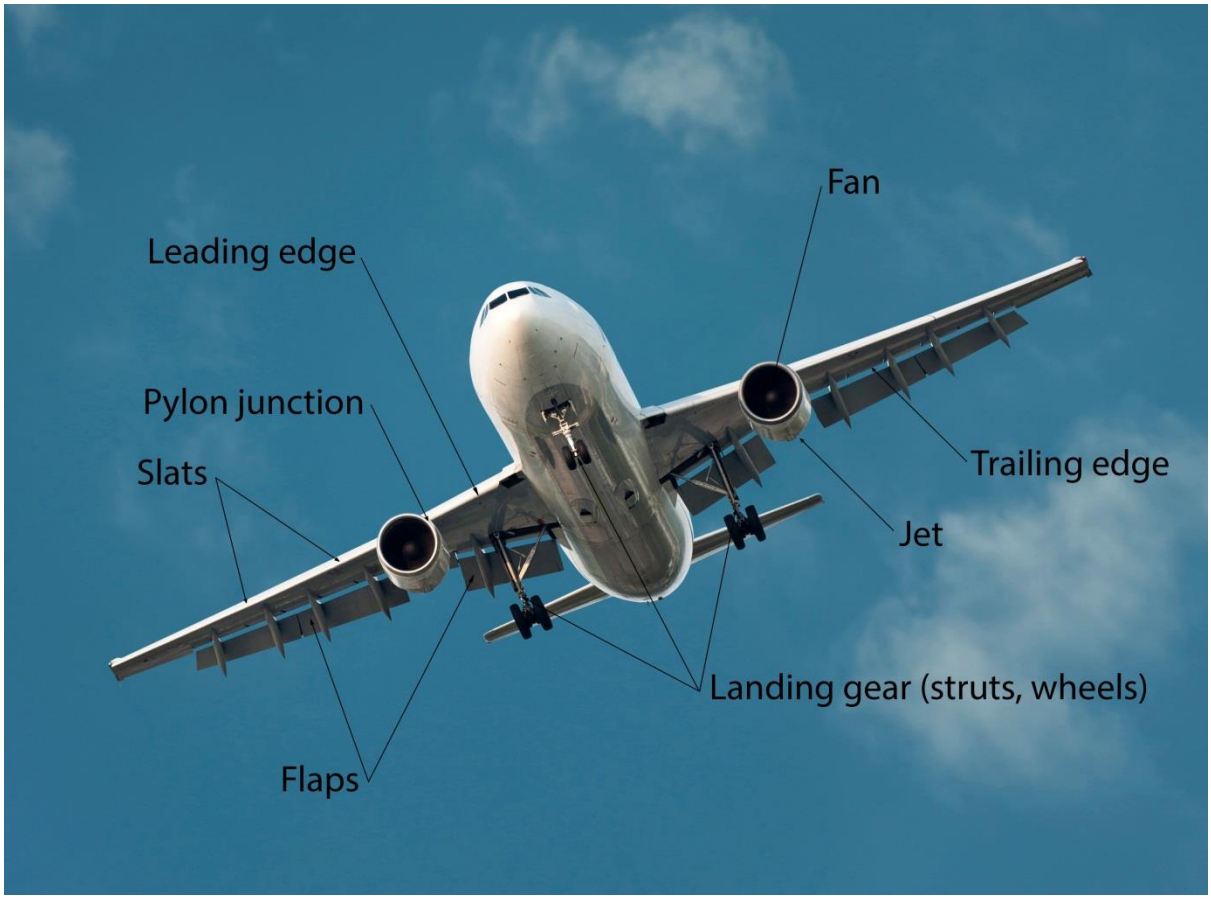

Figure 1 – Main sources of noise of a large commercial airplane depicted while landing.

Beyond aeronautics, the applications of aero-acoustics range from environmental and energy to automotive sectors where in the former case noise reduction is now also an important part of wind turbine design. [10] Being closely related to aero-acoustics, hydro-acoustics also finds important applications such as investigating noise in pipe flow problems. (See acoustic broadband benchmark cases in pipe bends and T-junctions, e.g. [11]). Where automotive industry is concerned, aerodynamic noise often becomes an issue when travelling at motorway speeds. Vehicle components such as wing mirrors, roof racks, railings, antennas, down-force devices such as a rear mounted spoiler and a convertible roof edges may all contribute to the generation of obtrusive sound. For example, open windows or a sunroof can give rise to broadband and tonal noise [12] at high speeds when aerodynamic noise dominates over other sources of noise, such as noise radiated from tires, engine or exhaust. Interior noise caused by heating ventilation and air-conditioning systems also attracts attention. (See HVAC duct benchmark case [13]). Often, long distance motorcycle riders wear ear protection as prolonged exposure to aerodynamic noise becomes a serious issue [14], which to some extent can be reduced by passive noise reduction devices such as a modern helmet. [15] Also, the

top end touring motorcycles with optimised air flow can be distinctly quieter at high speeds. There are many other examples of noise problems in engineering, which inevitably influence a modern life, making aero-acoustics such a great field for research.

It is worth mentioning that not all frequencies having the same sound pressure magnitude are anticipated by the ear in the same way. There is a sensitivity factor that is involved in hearing with a maximum of around 3∼4 kHz and for that reason a special weighting at different frequencies exist, such as dBA weighting. In the A-weighted system the noise is attenuated at low frequencies in contrast with the un-weighted measurements assuming that a low frequency contribution may be less important compared to the high-frequency sound that is very intrusive. Loudness is another measure to be considered. In the next section we shall proceed with the discussion on how to define and measure noise in mathematical terms.

1.1 Physics of sound and noise measurements: basic definitions

The lowest frequency that a human can hear is about 20 Hz and the highest frequency is about 20 kHz. This is a broad audio-frequency range where 50 Hz may represent a low rumble and 20 kHz is a very high whistle. In general, pure tones consist of one frequency only, for example, playing scales on a trumpet note by note or using a tuning fork "kammerton" which vibrates to give a note of specific pitch (commonly "*La*", A = 440 Hz). However, most sounds in our daily life are made up of a mixture of frequencies and it is convenient to represent sound as a spectrum. One important measure commonly used in acoustics is the octave. If two frequencies, f_1 and f_2 describe the octave then f_2 must be twice the f_1. For example, the middle C or "*Do*" has the frequency of about 260 Hz and one octave above the note "*Do*" (C_5) has the frequency of approximately 520 Hz and should be exactly twice the frequency of the middle C, $f_2 = 2f_1$. The centre frequency $f_0 = \sqrt{2}f_1$; is the geometric mean. For environmental and noise control applications, pressure measurements are often recorded for a narrow frequency band and as a method of filtering, usually, the 1/3 octave band is used, which is simply $f_2 = 2^{1/3}f_1$. In general, the nth octave band may be defined as $f_2 = 2^{1/n}f_1$. The octave frequencies are made up of lower band limits, centre frequencies, and upper band limits. For 1/3 octave band, $f_0 = (f_1 f_2)^{1/2} = \left(2^{\frac{1}{3}} f_1^2\right)^{1/2} = 2^{1/6}f_1$.

In addition to the difference in frequencies power and energy are also major descriptors of wave propagation. The power level of the audible sound measured in Watts (W) has a wide variation, where a wind noise on a quiet day at the countryside ($\sim 10^{-10}$ W) and the loud sound of jet airplane at take-off ($\sim 10^{5}$ W) may express such contrast. Wide variation makes it convenient to represent the magnitude and frequency of sound on a logarithmic scale. The sound power level, PWL, is measured in decibels (dB), such that $\mathrm{PWL} = 10\log_{10}(\mathrm{Power}/10^{-12}\ \mathrm{W})$; and the sound pressure level, $\mathrm{SPL} = 20\log_{10}(p_{avg}/p_{ref})$; is expressed in terms

of the root mean square acoustic pressure fluctuations p', where $p_{avg} = \sqrt{(1/T)\int_0^T p'^2 dt}$ and where p_{ref} is the reference pressure, usually taken as 20 μPa in air that corresponds to the threshold of hearing at 1 kHz for a typical human ear. (See Table 1)

The sound intensity level is defined as $\mathrm{SIL} = 10\log_{10}(I/10^{-12}\ \mathrm{W/m^2})$; where intensity, I, is related to sound power and, hence, to the reference pressure via the relationship $I = p'^2/\rho_0 c_0$; In air, $\rho_0 c_0 \sim 400\ \mathrm{kg/m^2 s}$ which is called the characteristic impedance of a fluid. Some examples of sound sources and their corresponding SPL, average pressure and intensity are presented in Table 1.

Noise sources examples with distance	**SPL (dB)**	p_{avg} **(Pa)**	I **(W/m²)**
Jet aircraft, 50 m	140	200	100
Pneumatic drill, 1 m (threshold of pain)	130	63.3	10
Loud locomotive horn, 3 m	120	20	1
Rock concert, 1 m from the speaker	110	6.3	0.1
Inside machine shop	100	2	0.01
Underground train	90	0.63	0.001
Busy road, 10 m	80	0.2	10^{-4}
Vacuum cleaner, 2 m	70	0.063	10^{-5}
Conversation, 1 m	60	0.02	10^{-6}
Office	50	0.0063	10^{-7}
Light rainfall	40	0.002	10^{-8}
Quiet library	30	6.3×10^{-4}	10^{-9}
Audio recording studio	20	2×10^{-4}	10^{-10}
Rustling leaf	10	6.3×10^{-5}	10^{-11}
Threshold of hearing	0	2×10^{-5}	10^{-12}

Table 1 – Table of SPL, corresponding pressure and sound intensity for various noise sources

Sound intensity which is defined as $\boldsymbol{I} = p'\boldsymbol{u}'$ is a vector quantity and in physical terms it expresses how much power is transported in which direction. In this relationship, the intensity is a product of two physical quantities the sound pressure p' and particle velocity $\boldsymbol{u}'$ where phase difference between the two is significant as it determines how well the (pressure) force can generate the velocity (response). Therefore, sound intensity is classified into active and reactive intensity where the former is in phase and the latter has 90° ($\pi/2$) phase difference. [16]

Sound intensity and energy are closely related. First, assume that the dissipated energy in a fluid is negligible in comparison to both potential and kinetic energy which make up the total energy, $e_t = e_p + e_k$. Then the energy per unit volume has to be balanced by the net power flow through the surfaces that enclose the volume of interest. By definition, acoustic intensity is the acoustic power per unit area, which in this case leads to the following conservation equation:

$$\frac{e_t}{\partial t} + \nabla \cdot \boldsymbol{I} = 0 \tag{1}$$

For a spherical wave propagating in free space, the intensity in the radial direction obeys an inverse-square law, meaning that the intensity is decreasing when following the wave front away from the source. For a propagating spherical wave the energy dissipation would be difficult to observe since the total energy would be spread over the rapidly increasing wave front's surface area. Hence, sound waves can propagate much further when the energy is concentrated in one dimension, such as for example in a narrow duct. However, the sound wave would not propagate infinitely even in such favourable one-dimensional environment because energy dissipation is an underlying process in acoustics. As prescribed by the governing equations of fluid dynamics, viscosity acts as a dissipation mechanism of acoustic waves. In a flow where fluid compressibility is fundamental, such as in shock waves, the dilatational viscosity dominates sound attenuation and the absorption of sound energy depends on the frequency, which defines the rate of molecular relaxation. [17] In general, noise attenuation increases with increasing frequency, explaining why predominantly low frequencies are heard of a distant flying airplane. When sound propagates through a viscous medium its energy inevitably dissipates into heat. In addition to pure dissipation effects, the presence of a non-uniformity of media which leads to acoustic wave scattering and reflection can be also regarded as a sound attenuation mechanism.

In acoustics, fundamental physical quantities such as pressure and velocity are important variables that formulate acoustic intensity, acoustic impedance which will be discussed in details in Chapter 2 and so on. In order to get in better grips with acoustics one also has to consider the scales involved in hearing. Acoustic waves displace fluid particles with a fluctuation velocity u', given by:

$$u' = p'/\rho_0 c_0 \tag{2}$$

where from Table 1 for SPL 140 dB, $|u'| \cong 0.5\ \mathrm{m/s}$ and for the harmonic wave at 1 kHz, the acoustic displacement of a fluid particle would be $\Delta = |u'|/\omega \cong 8 \times 10^{-5}$ m. Moreover, dividing Eq. (2) by c_0 and utilising the thermodynamic relationship $p' = c_0^2 \rho'$, the Mach number u'/c_0 can be regarded as the measure of the relative density variation, ρ'/ρ_0. The acoustic Strouhal number can be estimated via the displacement, $St_a = \Delta/L$ where L is the characteristic length. It should be noted that Δ increases with decreasing frequency. As can be seen, the displacement of 8×10^{-5} m is very small in comparison to the wavelength, $\lambda = c_0/f$ which for 1 kHz is $\sim$0.34 m and for the highest audible frequency (20 kHz) $\sim$0.017 m. On such small acoustic scale the displacement still represents the macroscopic average effect that consists of a significant number of molecular collisions as integrated by an ear.

1.2 Computational aero-acoustics

Computational Aero-Acoustics, namely (CAA), is a research area dedicated to obtaining the noise prediction via computational modelling. Once a computational method is successfully validated on a benchmark problem it can be used for obtaining acoustic predictions for a similar class of problems and thus, making engineering design process more efficient. The search for modern computational methods and techniques is aimed at selecting the best compromise between the computational cost and fidelity of the method which can minimise the number of required experiments during a design phase. Only over the last decade computers have become powerful enough to perform high-fidelity simulations for problems relevant for industrial applications. Nevertheless, aero-acoustic modelling remains a challenging task even for problems where aerodynamic modelling has an established approach which had been demonstrated to give reliable flow predictions. The difficulty comes from the wide diversity of the flow scales typical for aero-acoustic problems, usually leading to a necessity of application of different modelling techniques for solving one problem and their further adaptation to specifics of a considered case. For example, problems of sound generation and sound propagation are usually considered separately. For instance, as proposed in [18], the sound generation can be evaluated using the non-linear Navier-Stokes equations in the near-field of the effective sound source, while acoustic propagation to the far-field is performed using the Ffowcs-Williams and Hawkings [19] (FW-H) method. The latter method is based on solving the problem of linear wave propagation to the far-field analytically, with the Green's function method, following the approach of Lighthill. In the FW-H approach acoustic sources are collected on a control surface which can be permeable or impermeable depending on the surface location and definition of noise sources. Sources can be found away from boundaries in the case of jet-mixing or next to a solid wall in airframe noise cases. The details of the FW-H method as well as Lighthill's analogy are considered in Section 2.2.

An alternative approach to using the classical acoustic analogy of Lighthill where a propagation problem can be obtained analytically is solving a form of Linearised Euler Equations (LEE) [9] in the time domain numerically, e.g. using the Finite-Element (FE), Finite-Volume (FV) or Finite-Difference (FD) methods on a mesh incorporating both, noise sources and an observer. The advantage of solving the wave propagation equations for the entire far-field mainly lies in the possibility of eliminating assumptions such as using a constant mean flow when solving the problem via an analytical approach. Also, solving the wave propagation is particularly promising when working with complicated geometries, and thus, accounting for possible wave reflections and refractions that may influence the entire acoustic field. In addition, the input acoustic source terms are taken from a volume, meaning their spatial distribution and magnitude would be more accurately represented when coupled to a sound generation method in comparison to using integration surface approaches, such as the FW-H method mentioned previously. Unfortunately, performing the wave propagation in three dimensions in space and taking into account the required time sampling of a solution to resolve low frequencies comes at a substantial computational cost. Usually, a simulation time step becomes the limiting factor for time accurate simulations as fine mesh resolutions are

required in the source zone as well as next to solid boundaries. For example, at the observer location multiple passes of waves having wavelengths comparable to the size of geometry under consideration are normally required for obtaining the desired frequency resolution of the acoustic signal, inevitably increasing the turnaround time. Still, solving a linear sound propagation problem is considerably less expensive compared to the solution of a fully non-linear problem (e.g. Large Eddy Simulation) because of a coarser grid required to resolve the relevant acoustic scales. Such an approach becomes particularly attractive when the effect of a non-linear flow is modelled with a stochastic method for acoustic source generation. For example, the application of LEE for the stochastic method can be traced back to one of early works of Bailly and Juvé [20]. High order methods [21] are particularly suitable for solving linear propagation problems because of their accuracy on coarse grids which makes them attractive for CAA applications. [22] Furthermore, several techniques have been developed to further improve the speed and accuracy of acoustic solvers such as the Quadrature-Free formulation applied to Discontinuous Galerkin (FE-DG) method. [23]

In the current work the FE-DG is used for solving the Acoustic Perturbation Equations (APE) [22] for the sound propagation, which essentially is an entropy- and vorticity-less version of Linearised Euler Equations. Alongside the APE, the FW-H integral method is also applied to a benchmark case. The availability of several wave propagation methods which are applied to the same benchmark is highly beneficial for assessment of the advantages and disadvantages of the methods of choice. Overall, the wave propagation methods employed in this work are well documented in the literature and widely employed in CAA.

Irrespective of the wave propagation modelling approach, the quality of the acoustic simulation resides on the accuracy of calculated acoustic sources. For this purpose, high fidelity methods such as the Large Eddy Simulation (LES) are most advantageous as all parts of the acoustic source could be obtained by directly solving the governing Navier-Stokes equations. A well-known challenge in solving unsteady fluid dynamic equations such as the Navier-Stokes equations on a discrete finite-difference or finite-volume grid used in the LES approach is associated with high dissipation and dispersion errors. [24] [25] In order to improve dispersion and dissipation properties of the method, advanced solvers usually offer a high-order approximation of variables in space and time. For a numerical solution, fluid dynamics equations that describe convection could be written either in the conservative or in the non-conservative form. For solving fluid dynamics equations in space and time using the conservative approach the flow domain is divided into discrete control volumes. Then, the governing equations are integrated on the individual control volumes to construct algebraic equations for the discrete variables (the unknowns). However, as discretisation leads to approximation errors, only in very special cases the discretised equations lead to the exact solution of the governing equations. In other cases, numerical dissipation or dispersion errors emerge. Numerical oscillations occur in the solution due to the accumulation of dispersion errors. These errors are unavoidable when solving non-linear problems on a fixed grid. In the CFD literature, there have been many techniques developed to suppress these oscillations by adding some artificial viscosity. For example, one of the classical methods of smearing the unwanted oscillations which occur when computing shock problems is the von Neumann-

Richtmyer artificial viscosity. [26] This artificial viscosity is introduced into the governing equations similar to a physical viscosity but is activated with a switch for compression waves only. This method can produce good shock-capturing results but remains very empirical in nature. [27] An alternative to using the classic artificial viscosity method for alleviating the effect of dispersion errors and, thus, preserving shocks/discontinuities was proposed in the work of Boris and Book [28] who developed the Flux-Correction Transport (FCT) approach for advection problems. The idea of FCT was to correct the conservation fluxes so that the solution positivity is enforced as well the conservation property remains preserved. In essence, FCT introduces a non-linear artificial viscosity into the governing equation to preserve the oscillation-free solution. The original FCT approach was largely empirical and applied to one-dimensional problems only. For example, it was not clear how to generalise it to systems of nonlinear conservation laws such as gas dynamics. Then Harten (see [29] [30]) came up with a unified approach for developing high-resolution non-oscillatory schemes for general nonlinear hyperbolic conservation laws. Harten's idea was to develop methods which satisfy the solution Total Variation Diminishing (TVD) property as well as the entropy inequality to make sure that unphysical solutions like expansion shocks do not occur. [31]

Dispersion properties of finite-difference schemes can be optimised by a careful choice of the scheme's stencil. For example, the Dispersion-Relation-Preserving (DRP) scheme [32] employs the fine-tuned coefficients for minimising the numerical dispersion error for linear wave propagation, which is found to work well for smooth solutions. On the other hand the second or third order TVD schemes are particularly good when dealing with shock waves but are too dissipative for linear advection problems. For the Total Variation Bounding (TVB) schemes which are a class of TVD and use high order approximation (5 and above) the dissipation problem could be almost eliminated by using an extended stencil and requiring that the solution variance is limited only globally, thus, preventing its growth in time. The idea of TVB schemes is constructing the hierarchy of the least oscillatory stencils designed for approximating high order derivatives. Then, the best non-oscillatory stencil is used at each time step such as realised in ENO/WENO [33] [34]. Note that TVB uses a more relaxed condition compared to TVD, permitting some small oscillations for the price of having superb low-dissipation properties.

A special attention is attributed to the CABARET numerical scheme utilised in this work for solving fluid dynamics equations. CABARET stands for Compact Accurately Boundary Adjusting high-Resolution Technique [35] that is the extension of Upwind Leapfrog methods [36] [37] [38] [39] to non-oscillatory conservative schemes on staggered grids with preserving low dissipative and low dispersive properties. In comparison to many CFD methods, the CABARET employs a very compact stencil which for linear advection takes only one computational cell in space and time. A relatively simple implementation along with a low dissipation and dispersion is particularly advantageous when the CABARET scheme is used in the framework of Monotonically Integrated LES (MILES) e.g., [40] which is a version of Implicit LES techniques. For the implicit sub-grid scale model within the MILES method, the CABARET uses a low-dissipative conservative non-linear flux correction method directly based on the maximum principle. In accordance with [41], the application of

MILES for low-speed high-Reynolds number flows considered in this work is particularly challenging because of the inherent numerical dissipation typical of many MILES methods.

Up to date, CABARET scheme has been found efficient for a number of unsteady fluid dynamics problems including linear advection in stochastic velocity field [42], non-linear aero-acoustic problems [43] [44], T-junction pipe flows in nuclear engineering [45] and for high-speed turbulent jet flow modelling [46]. More recently, the CABARET flow solver has been extended to asynchronous time-stepping [47], GPU computing, and fully unstructured meshes [48] [49] [50]. The latest GPU version of the CABARET solver will be used in the current work for LES aerofoil flow simulations.

Over the last decade synthetic turbulence methods used for acoustic source generation gained recognition in industry. Contrary to LES methods that typically require a substantial computational effort when applied to an industrial problem, the ability to conduct noise simulations using the stochastic method which does not require obtaining a first principle solution for the entire field like the LES proved attractive. The idea of stochastic turbulence methods is based around introducing stochastic Lagrangian particles whose trajectories and ensemble averaged statistics is found from a precursor Reynolds-Averaged Navier-Stokes (RANS) calculation. Interestingly, the idea of drifting Lagrangian particles in cells used for hydrodynamic calculations originated with the appearance of first computers. [51] Early steps in development of the stochastic method for turbulence generation could be traced back to the work by Careta *et al.* (1993). [52] Around the millennium mark, Ewert *et al.* [53] developed a synthetic turbulence method for CAA applications which is based on white noise filtering approach. [54] It was called the Random Particle Mesh (RPM) method. Later, for broadband noise predictions, a more efficient Fast Random Particle Mesh (FRPM) method was developed [55] [56] [57] which can predict sound generated by turbulent flows over a wide range of Reynolds numbers. The synthetic turbulence fluctuations obtained by specially weighting the stochastic Lagrangian particles are then, typically, substituted into the right-hand-side sources of some acoustic formulation, the same way as the LES fluctuations would be, to propagate the acoustic solution to the far-field.

Importantly, unlike the LES-based noise prediction schemes, which automatically account for all types of noise sources in the flow solution, the original FRPM model can only simulate broadband fluctuations which are generated by the stochastic particles moving with the time-averaged RANS flow field. Therefore, being based on the time averaged flow, the original FRPM model cannot include any unsteady flow features such as vortex shedding or pairing which would produce tones in the noise spectra. In Section 3.3 it is shown how under the scale separation assumption between the high-frequency turbulence fluctuations and the low frequency tones typical of the Unsteady-RANS (URANS) solution methods, the vortex shedding effects should also be possible to incorporate in the corresponding acoustic prediction scheme.

1.3 Representative airframe noise benchmark cases

Because of the diversity of airframe noise problems there is no unique solution procedure applicable to all CAA problems. In attempt to devote efforts of researchers across the field, CAA problems are allocated into different categories. For the purpose of combining the joint effort in development of the state of the art methodologies and benchmarking in aero-acoustics, the workshop on Benchmark problems for Airframe Noise Computations (BANC) [58] was initiated by the American Institute of Aeronautics and Astronautics (AIAA).

Aerofoil trailing edge noise remains one of the prioritised cases in the BANC workshop and it was explored in this work for several reasons. First of all, the consideration of a classical yet representative benchmark case allows isolating and analysing specific features of the noise mechanism. Secondly, the problem is not contaminated by other hydrodynamic effects, which are case and testing facility specific. For the geometry such as a NACA 0012 aerofoil the aerodynamic and aero-acoustic validation data is available from multiple sources. Hence, the use of this benchmark case is convenient for development and validation of new computational models such as considered in this thesis.

Another benchmark considered is the rod-aerofoil configuration. [59] Simulating the flow over a bluff body is always challenging, especially without having a fixed separation point as in the case of a circular cylinder. It is considered to be a very challenging case for the CABARET as a pure LES method where a valuable experience is gained by understanding its limitations. As a consequence, the modelling strategy is developed for simulating the flow around an aerofoil.

This section follows with a literature review on the trailing edge noise (Section 1.3.1) giving an introduction to the first two aerofoil benchmark cases explored in this work with both sharp and blunt trailing edges. Section 1.3.2 presents the second benchmark case, exploring the flow over a circular cylinder that is part of the rod-aerofoil problem.

1.3.1 Aerofoil trailing edge noise

Aerofoil noise, or the noise generated by scattering in a hydrodynamic field in the turbulent boundary layer close to the wing trailing edge, has been a subject of investigation since 1970s. [60] [61] In recent years, this classical problem has kept attracting attention [62] [63] [64] [65] and despite the availability of several experimental databases [66] [67] [68], an understanding of trailing edge noise mechanisms leading to robust scaling laws is still lacking.

Numerical modelling of aerofoil noise based on unsteady computational fluid dynamics approaches such as LES or Direct Numerical Simulation (DNS) came into practice in 2000 [69] [70]. Since then, there have been approaches at various levels of validity and complexity used for modelling the unresolved near-wall turbulence or directly resolving this for low Reynolds number flows [43] [71] [72] [73] [74]. For acoustic modelling of the trailing edge

noise, there has also been a range of formulations of various complexity used starting from Ffowcs Williams-Hawkings (1969) [19] and Amiet's theory (1976) [75] to solving the Acoustic Perturbation Equations (APE) [22] and performing direct noise computations. [76] [77]

A serious limitation of using LES for trailing edge noise modelling is their restriction to relatively low Reynolds numbers due to prohibitively high computational cost of resolving the boundary layer turbulence. This limitation has resulted in a very little use of LES in support of existing experimental aerofoil noise campaigns or industrial design processes where the computational cost is further increased due to the geometrical complexity. Therefore, attention turned to methods with a fast turnaround time, such as RANS simulations that evolved through 1990s and by the end of the decade were extensively used to obtain a time-averaged flow prediction for a wide variety of industrial problems with varying degrees of success. Despite its drawbacks in transition modelling and inability to accurately model the separation, RANS methods can provide a quick prediction for high Reynolds number flows typical to many industrial problems and therefore, these tools remain commonly used to the present day. Compared to LES the validity of acoustic prediction schemes based on RANS strongly depends on the model calibration. This also applies to hybrid RANS/LES methods [78] where a calibrated transition from one scheme to another needs to be performed.

In the context of trailing edge noise modelling, URANS simulations have been used to predict the tonal noise generated by a bluff body vortex generator attached to an aerofoil boundary close to the trailing edge [79]. Pure tonal noise prediction schemes based on URANS were applied for multi-blade configurations in turbo-machinery, for example, in application to fan noise [80] and turbine noise [81] modelling with a reasonable computational efficiency. However, the ability of such schemes to provide reliable tonal noise predictions through estimating the isolated vortex shedding characteristics is rather questionable.

Following the work of Ewert *et al.* [62], the exploration of numerical methods begins by setting a benchmark for comparison using a quick trailing edge broadband noise prediction technique which is implemented in a framework of Altus acoustic solver [11] that is a proprietary code of BAE Systems. The solver applies the FRPM method on a Cartesian grid with the flow field interpolated from the RANS calculation to generate the sound sources. The sources are then interpolated onto an unstructured grid of general complexity around a scattering body to solve a set of Acoustic Perturbation Equations (APE-4 formulation) [22] using a high-order Quadrature-Free Discontinuous Galerkin (QF-DG) method and the explicit ADER scheme for time integration [82]. This solver is further developed to be used in the current work for broadband and tonal noise predictions.

1.3.2 Flow past a circular cylinder

The flow past a cylinder is calculated at the Reynolds number 48,000 which can be identified as the beginning of the upper subcrtical regime with quick transition to turbulence in the free shear layers. The flow separation remains laminar up to the Reynolds number ~ 140,000. Thus, it is sometimes referred as the Laminar Separation (LS) case as explored in [83]. However, at the investigated regime the Reynolds number is sufficiently high to cause a sudden burst of turbulence in the near wake close to the surface of the cylinder where after a short transition the wake becomes highly three-dimensional. The cylindrical rod sheds vortices as a von Kármán street corresponding to the Strouhal number of just below 0.2 for the entire flow regime. [84] The existence of such recirculating pattern is responsible for the generated tonal noise that could be heard as a distinct hiss, scientifically referred to as the aeolian tone. It should be mentioned that the flow at this Re range is not only of interest for CFD / CAA communities but is often encountered in mechanical, chemical and nuclear engineering.

The test case being explored is mildly compressible with the mean flow Mach number equal 0.2. The experiment with these flow conditions was performed by Jacob *et al.* [59] for a rod-aerofoil set up where acoustic results were also measured for the rod alone. Importantly, in the experimental work velocity and turbulence intensity profiles were recorded at different near-field check zones around the cylinder that serve as a valuable comparison. The rod-aerofoil test case which is thought to be relevant to noise mechanisms found in turbomachinery applications comprises of a cylindrical rod followed by a wing section of the NACA 0012 profile where the disturbed flow impacts the leading edge of the aerofoil. The latter not only results in a highly turbulent wake around the aerofoil surface but also affects the development of the boundary layers, their ability to separate or withstand adverse pressure gradients at the rear part of the aerofoil, and the wake shedding behind the trailing edge. The effect of the turbulent wake as well as its interaction with the aerofoil boundary layers results in broadband noise generation.

From the modelling view point, the flow over a bluff body is always a challenging problem. One attribute of this flow regime around a circular cylinder is that the separation point is not fixed in space. Moreover, one should expect a wide azimuthal variation of the separation point depending on phase. Therefore, the near-wall treatment is far from trivial and this flow regime is thought to be more challenging for high fidelity computational modelling than the flow at higher Re number having a turbulent separation (TS case) which is quite unusual. Regarding the numerical methods, first of all, because of the relatively high Reynolds number DNS is prohibitively expensive. On the other hand, because of the large area of separated flow and the nature of the flow regime with an immediate transition to turbulence close to the surface of the cylinder, URANS methods are also hardly suitable for this problem. First of all, due to a relatively large time scales employed in URANS methods crucial details on fine scale turbulence are missing which are responsible for the flow separation. Secondly, span-wise correlations cannot be reproduced in a URANS simulation where a rolling vortex sheet is obtained instead. In general, methods based on RANS have a tendency to over-predict the

shedding frequency. [85] One of the main characteristics of this flow case is attributed to large span-wise correlations that extend over several cylinder diameters in the span-wise direction as reported in the experiment. [59] In order to correctly capture the flow physics of the cylinder case under consideration, the span-wise correlations must not be neglected, particularly as the broadband noise will be largely affected and of course, the tonal noise would be prescribed by the shedding frequency that is highly dependent on the near-wall modelling. At present, the main bottleneck in applying the stochastic FRPM method to the cylinder benchmark is the missing information about the span-wise correlations, which cannot be obtained from the URANS solutions employed in this thesis.

Hybrid RANS-LES techniques such Detached Eddy Simulation (DES) methods, which combine RANS in the boundary layer zone with LES in the wake region, potentially offer a stable control on the boundary layer modelling with explicitly resolving large-scale eddies. Potential problems of hybrid RANS-LES methods include the treatment of boundary layer regions where flow separation and transition occurs, and the model behaviour strongly depends on the turbulence model used as well as on the numerical switch from RANS to LES. To some extent, these problems have been addressed in most advanced hybrid models of this type, e.g., [78]. Examples of solutions using the Delayed-Detached Eddy Simulation (DDES) methods applied to this benchmark problem include the following: [86] [87] [88]. However, these methods are not employed in this work since the prime target is to investigate into acoustic sources that are generated in the turbulent boundary layer close to the wall. Hence, a high portion of vortex sound sources falls within a 'grey area' of DES methods, making investigation into acoustic sources based on a hybrid RANS/LES technique less valid. Therefore, there is a need to search for a suitable Large Eddy Simulation (LES) method which could be applied for simulating the flow and acoustics of this benchmark case.

In the literature, high-fidelity LES modelling has been applied to simulate the flow in the entire computational domain that includes the near-wall region and the wake. [89] [90] Near-wall modelling remains by far the most challenging part, especially for such complicated flow case with a floating separation point. A sub-grid scale model seems to play a significant role when modelling the near-wall eddies and this part remains a grey area in existing practice. The flow past a circular cylinder considered in this work has a sufficiently high Re number at which DNS resolutions may not be easily achievable, making it also very challenging for pure LES methods like the MILES CABARET.

1.4 Aims and contributions of this thesis

This project has been initiated by BAE Systems through the Cooperative Awards in Science & Technology (CASE) with Engineering and Physical Sciences Research Council (EPSRC). The aim of the project is to examine the existing stochastic FRPM method in terms of assumptions involved when comparing to a first principle LES solution and extend its applicability range by developing a unified approach that also incorporates tonal noise effects. All method developments discussed in the present thesis have been implemented in

the engineering code Altus that is used by BAE Systems Ltd. for the complete aero-acoustics problem solution cycle.

The MILES CABARET method has been chosen for providing first principle solutions which should provide an insight into vortex sound sources and, hence, help in the development of the FRPM method. Also, the applicability of MILES CABARET to the benchmark aerofoil and cylinder cases has been investigated. This can be considered as an additional contribution of this thesis since the CABARET method is constantly improving and finding new applications in CAA [49], with the snappy mesh and asynchronous time stepping being implemented recently. [50]

Outline of the main results of the thesis:

I. For a low Mach number ideal flow, where the exact analytical solution is available the CABARET solver has been applied to show the absence of excessive numerical entropy generation when compared to the standard second order finite-volume method used in the conventional CFD (Fluent) solver. The absence of excessive numerical entropy generation means the method is low dissipative, hence, suitable for acoustics sensitive simulations. This is a major requirement on accuracy as discussed by Hirsch [24] (*see Chapter 11 in the textbook*) which can indicate whether an acceptable mesh refinement level has been achieved and whether the numerical dissipation of the applied method is sufficiently low, making it suitable for high-fidelity simulations.

II. Several boundary layer tripping techniques have been investigated for LES in application to aerofoil flow problems and the corresponding solutions of the MILES CABARET have been analysed and compared with the existing RANS and experimental data; a fair agreement is reported.

III. The FRPM method has been used to reconstruct the effective aerofoil trailing edge noise sources with the help of RANS mean quantities in accordance with the vortex sound theory. [57] [91] The sources have been compared with the same extracted from LES for obtaining the calibration parameter used for the FRPM acoustic source scaling.

IV. For aerofoil trailing edge noise investigations, vortex sound components contributing most to the overall sound pressure level are evaluated and compared to results previously reported in the literature; consistency in findings is reported.

V. A new scale decomposition method is developed to extend the original FRPM method to modelling of broadband and tonal noise sources in the same simulation framework. Results are validated in comparison to the experiment of Brooks & Hodgson [92] where a NACA 0012 aerofoil with a blunt trailing edge is used.

The original contributions of this thesis are explained below:

- Solving the flow past a circular cylinder with Laminar Separated (LS) shear layers at Reynolds number 50,000 using MILES CABARET has been attempted for the first time. The LS case is believed to be the most numerically challenging flow regime of a flow past a cylinder problem. Initially, the dissipation and dispersion properties were examined for the inviscid case, thus, providing guidance on computational grids. Consequently, the benchmark cylinder flow case allowed assessing limitations of the MILES method when predicting the flow separation.

- Several boundary layer tripping techniques have been implemented in LES CABARET code and discussed in details in this work. These include a steady suction & blowing flow tripping in a form of a step and sine functions, correlated and uncorrelated stochastic tripping spatially represented by a Gaussian, and a physical rectangular tripping device. While various boundary layer tripping techniques proved to be insufficient for reproducing the correct physics on a LS cylinder case, their implementation in the framework of MILES CABARET led to accurate resolution of a tripped aerofoil benchmark case at high Re number.

- Several concepts and assumptions used in FRPM method were implemented and tested in the Altus code. Specifically, trailing edge noise predictions were obtained for all linear and non-linear source terms according to the vortex source model, presenting the acoustic spectra for individual source terms as well as their combination.

- Investigation into the sources of trailing edge noise at the source level has permitted the comparison of effective noise sources between the two methods, namely the FRPM and MILES CABARET considered in this work. Instead of using the standard calibration based on the far-field sound, the scaling parameter of the FRPM method was obtained by matching the vortex sources solution with that from LES. A multi-stage comparison between two simulations and the experiment has been used. Firstly, the near-field flow solution of RANS on which FRPM relies and the LES solution have been validated with the help of the benchmark experiment. Secondly, the root-mean-square (*rms*) of turbulent quantities and vortex source terms have been evaluated and compared between the two methods. Finally, performing the correlation analysis at the trailing edge location provided valuable insight into the accuracy of source modelling.

- A new acoustic model based on the flow decomposition has been developed for consistent modelling of the flow scales responsible for broadband and tonal noise generation at the source level in the FRPM method and implementing the new algorithm in the Altus code. The new approach automatically accounts for

all tonal and broadband noise sources present in the zone of interest, only requiring a single simulation run. Stochastic methods are usually criticised for their inability to predict noise from coherent structures, such as vortex shedding and also being unsuitable for flows with highly pronounced three-dimensional features, such as flows over bluff bodies where information on flow correlations would be absent. The current work is the first step in the direction of unification of such classic stochastic turbulence methods for broadband noise prediction which do not contain any information about the flow coherent structures and the methods such as URANS that can predict some of the coherent dynamic features in 2D, i.e. those associated with the vortex shedding, thus, generating tonal noise. Previously, CAA problems containing tones had to be solved by a combination of separate methods which involved additional assumptions about how the resulting noise signal is formed at the far-field observer location as well as required solving the far-field propagation problem at least twice compared to the new unified approach.

- Broadband and tonal noise predictions are performed for a NACA 0012 aerofoil with a blunt trailing edge [92] using the FRPM method. Since for this benchmark the thickness of the blunt trailing edge is still only a small fraction of the chord length and the flow over a surface remains attached broadband noise prediction should still be valid. In Section 1.3.2 it has been discussed that URANS methods tend to over-predict the shedding frequency which can deviate from the target experiment by 10 ~ 15 %. Therefore, in an attempt to correctly model important features of the process of the flow separation near the blunt trailing edge in the framework of URANS modelling the trailing edge thickness has been slightly reduced to capture the target shedding frequency. Hence, the same tonal information is fed to the acoustic propagation model. Acoustic results presented in this thesis include both unaltered and calibrated URANS flow solutions supplied to the new acoustic model which is based on the small scales (broadband) large scales (tonal) decomposition. The calibrated mean flow solution leads to improved far-field acoustic predictions when compared to the experiment.

1.5 Outline of contents

This thesis is organised as follows.

- Chapter 2 provides the reader with the background on computational methods for turbulence and acoustic modelling considered in this work. The hierarchy of equations of fluid mechanics is reviewed, starting from the Navier-Stokes governing equations following with the Euler equations and with the classical acoustic analogy. Popular methods used for obtaining the acoustic signal at the far-field are reviewed. A review of numerical methods for unsteady fluid dynamics equations including the theoretical

background on the CABARET numerical scheme is provided. In the context of turbulence modelling approaches, the background on the RANS methods is discussed demonstrating their limitations. Finally, the LES methods used for turbulence modelling are considered, which includes the discussion on application of the MILES CABARET method to high Reynolds number flows.

- In Chapter 3, after a brief introduction into synthetic turbulence methods, the work follows with a description of the FRPM method as implemented in Altus code, also, introducing the new technique for tonal noise modelling. The concepts from this chapter are used for obtaining reliable acoustic predictions for the aerofoil benchmark case explored in one of the early works entitled: "The exploration of numerical methods and noise modelling techniques applied to the trailing edge noise case with evaluation of their suitability for aero-acoustic design" presented at CEAA International Workshop, 24-27 September 2014, Svetlogorsk, Russia.

- In Chapter 4 the selected benchmark problems are considered. First, the CABARET solution for the Euler and Navier-Stokes equations are obtained. Some variations of the obtained solution from the benchmark experiment are discussed along with the accuracy of modelling the flow separation and transition to turbulence. Secondly, the MILES CABARET is applied to an aerofoil flow problem at a high Reynolds number where it is demonstrated how two different tripping techniques can be used for obtaining aerodynamic solution which closely resembles the solution of the tripped aerofoil experiment. In addition, the FRPM solution which is based on the averaged statistics from the RANS/URANS model is applied for the flow and noise sources predictions of a sharp and blunt trailing edges. In this chapter we show how by modifying the geometry of the trailing edge tip one can obtain the correct shedding frequency for the blunt aerofoil benchmark in the framework of URANS modelling and its influence on far-field acoustic predictions. Some important findings presented in this chapter are published in the Journal of Sound and Vibration (JSV) entitled "Aerofoil broadband and tonal noise modelling using stochastic sound sources and incorporated large scale fluctuations". [93]

- In Chapter 5 the trailing edge noise sources which are described by the vortex source model are compared between the LES and RANS-based FRPM methods. The analysis is used to validate the acoustic model and to better understand the empirical calibration involved in the FRPM source modelling. Far-field acoustic predictions are compared using different vortex source term description in the framework of the FRPM model and compared to findings of other researchers for similar airframe noise cases. Also, the importance of individual noise components is discussed according with the far-field spectra predictions for the tonal and broadband noise obtained using the new formulation in the FRPM method. Some key findings included in this chapter were presented in [94] at the 23rd AIAA/CEAS Aero-acoustics conference.

- Finally, Chapter 6 discusses the main conclusions and future areas of research. In addition, the overview of the Altus code algorithm is provided in the appendix which can serve as a useful roadmap between different parts of the solver.

Chapter 2

Theory

2.1 Governing equations of fluid mechanics: Navier-Stokes

In continuum fluid mechanics gases and liquids are considered as macroscopic averages. A "fluid particle" can be defined as a small "control volume" which is assumed large enough compared to molecular scales and contain its average but small compared to length scales of the flow problem. The fluxes acting on the virtual "control volume" are conserved by assumption. The conservation law is the fundamental concept behind the laws of fluid mechanics. The laws describing the evolution of fluid flows are totally defined by the conservation of mass, momentum and energy, which are augmented by closing relations such as the equation of state, viscous stress/strain relation, and the closure model in case of equations written in ensemble averaged quantities for turbulence modelling.

The conservation of mass or continuity equation derived through the idea of the variation of quantity in the "control volume" per unit time in differential form reads:

$$\frac{\partial \rho}{\partial t} + \nabla \cdot (\rho \boldsymbol{U}) = 0 \tag{2.1}$$

The momentum equation is based on Newton's second law that relates the acceleration of fluid (advection part) to surface forces and body forces experienced by the fluid:

$$\frac{\partial}{\partial t}(\rho \boldsymbol{U}) + \nabla \cdot (\boldsymbol{P} + \rho \boldsymbol{U}\boldsymbol{U}) = \boldsymbol{f} + m\boldsymbol{U} \tag{2.2}$$

In the above expression, $\boldsymbol{f}$ is the external force and $m\boldsymbol{U}$ is the added momentum. The fluid stress tensor (denoted by $\boldsymbol{P}$) is related to the pressure p and the viscous stress tensor, $\boldsymbol{\tau}$ via the relationship:

$$\boldsymbol{P} = p\boldsymbol{I} - \boldsymbol{\tau} \tag{2.3}$$

In Eq. (2.3) $\boldsymbol{I} = (\delta_{ij})$ is the unit tensor, δ_{ij} – Kronecker[1] delta. The relationship between $\boldsymbol{\tau}$ and the deformation rate of a fluid element $\nabla \boldsymbol{U} + (\nabla \boldsymbol{U})^T$ could be assumed linear for a Newtonian fluid. Further, applying Stokes' hypothesis of local thermodynamic equilibrium yields:

$$\boldsymbol{\tau} = \mu(\nabla \boldsymbol{U} + (\nabla \boldsymbol{U})^T) - \frac{2}{3}\mu(\nabla \cdot \boldsymbol{U})\boldsymbol{I} \tag{2.4}$$

[1] $\delta_{ij} = 1$ if $i = j$, $\delta_{ij} = 0$ if $i \neq j$

Eq. (2.4) is called the constitutive equation where μ is the dynamic viscosity determined experimentally. By substituting (2.4) into the momentum equation (2.2), exploiting the solenoidal condition ($\nabla \cdot \boldsymbol{U} = 0$) from (2.1) we obtain the Navier-Stokes equations:

$$\frac{D\boldsymbol{U}}{Dt} = -\frac{1}{\rho}\nabla p + \nu \nabla^2 \boldsymbol{U} \tag{2.5}$$

$D\boldsymbol{U}/Dt = \partial \boldsymbol{U}/\partial t + \boldsymbol{U} \cdot \nabla \boldsymbol{U}$ is known as the total derivative and $\nu = \mu/\rho$ is the kinematic viscosity.

The energy conservation law reads:

$$\frac{\partial}{\partial t}\rho\left(e + \frac{1}{2}U^2\right) + \nabla \cdot \left(\rho \boldsymbol{U}\left(e + \frac{1}{2}U^2\right)\right) = -\nabla \cdot \boldsymbol{q} - \nabla \cdot (\rho \boldsymbol{U}) + \nabla \cdot (\boldsymbol{\tau} \cdot \boldsymbol{U}) + \boldsymbol{f} \cdot \boldsymbol{U} \tag{2.6}$$

where e is the specific internal energy and $\boldsymbol{q}$ is the heat flux due to conduction. A further discussion on derivation of the above equations and explanation of physical meaning with appropriate assumptions could be found, for example, in [17] [24] [95].

By neglecting viscosity and heat transfer that are not very important for acoustic wave propagation, the Navier-Stokes Eq. (2.5) reduces to the Euler equation:

$$\frac{D\boldsymbol{U}}{Dt} = -\frac{1}{\rho}\nabla p \tag{2.7}$$

An additional relationship between density and velocity is derived from the continuity equation, $\partial \rho/\partial t + \nabla \cdot (\rho \boldsymbol{U}) = 0$; Also, pressure is a function of density and temperature, $p = p(\rho, T)$ which follows from thermodynamic relations and the energy equation, $\partial E/\partial t + \nabla \cdot (\boldsymbol{U}(E + p)) = 0$; with the internal energy $e = e(p, \rho)$ completes the set of gas dynamics equations.

The above gas dynamics equations are non-linear and are difficult to solve analytically in a general case. However, in many cases of interest in aero-acoustics, perturbations can be assumed small. Hence, the linearised Euler equations can be considered for acoustic propagation which can become more amendable for analytical or semi-analytical solutions.

2.2 Linearised Euler, Lighthill's analogy and Acoustic Perturbation Equations (APE)

In Section 2.1 the relationship between pressure and velocity described by Euler's equation was derived from the Navier-Stokes equations for the condition of adiabatic flow and zero viscosity. Euler's equation (2.7) can be linearised, making it easier to solve with the following assumptions:

The pressure p is decomposed into a mean static pressure p_0 and a small pressure fluctuation expressed as p', such as $p = p_0 + p'$. Similarly, using the decomposition for the density, $\rho = \rho_0 + \rho'$ and the velocity, $u = u_0 + u'$ and then inserting decomposed variables into Eq.

(2.7), ignoring all non-linear terms as part of the linearisation procedure, and subtracting from the Euler equation for the mean flow quantities, yields:

$$-\nabla p' = \rho_0 \frac{\partial \boldsymbol{u}'}{\partial t} \tag{2.8}$$

The above equation is the simplest form of the linearised Euler equation where $\boldsymbol{u}' = (u', v', w')$. Eq. (2.8) states that the resulting acceleration $\partial \boldsymbol{u}'/\partial t$ is caused by the acoustic pressure gradient. For example, if two identical microphones are placed a small distance (dx) apart the acoustic velocity can be determined according to Eq. (2.8),

$$\boldsymbol{u}'(x,t) = \int_T \frac{p_2' - p_1'}{x_1 - x_2} \frac{1}{\rho_0} dt \tag{2.9}$$

Also, in Section 2.1 it was stated that three equations are required in order to completely characterise the relations so two more equations are needed. From continuity we get:

$$\frac{\partial \rho'}{\partial t} = -\rho_0 \nabla \boldsymbol{u}' \tag{2.10}$$

Therefore, the final equation must characterise how the acoustic pressure is related to the fluctuating density. As the local pressure fluctuation inevitably causes a local change in density ρ' and entropy s'. Thus, the relationship can be described as follows:

$$p' = \left(\frac{\partial p}{\partial \rho}\right)_s \rho' + \left(\frac{\partial p}{\partial s}\right)_\rho s' \tag{2.11}$$

For an isentropic assumption, as typically used in acoustics, the second term in Eq. (2.11) can be neglected which leads to a constitutive relation:

$$\frac{p'}{\rho'} = c^2 \tag{2.12}$$

In Eq. (2.12) c is the speed of sound. Note that the relationship in Eq. (2.12) can be derived using the equation of state of an ideal gas. If ρ_0 and u' are eliminated from Eq. (2.8) using the continuity equation and the constitutive relation one can obtain:

$$\nabla^2 p' = \frac{1}{c^2} \frac{\partial^2 p'}{\partial t^2} \tag{2.13}$$

which is a three-dimensional form of a linearised wave equation. The next point to consider is what makes the solution unique: the boundary and initial conditions. Indeed, the above relations satisfy solutions to wave propagation in time and space but without regard to acoustic sources, that is, excitations. Eq. (2.13) is therefore, a homogeneous governing equation. The inhomogeneous source terms may include arbitrary mass, momentum and entropy/enthalpy sources that can give rise to acoustic waves but in this work only the first two are considered which excite waves via changing pressure or a sudden volumetric change. In Section 2.4.3 the derivation details of the vortex sound sources will be discussed. First, Eq. (2.10) has to be modified to include the additional rate of mass change per unit volume term:

$$\frac{\partial \rho'}{\partial t} = -\rho_0 \nabla \boldsymbol{u}' + \rho_0 q(x,t) \tag{2.14}$$

Then, following the same procedure as was employed for obtaining Eq. (2.13) but with the new Eq. (2.14) instead of Eq. (2.10) gives:

$$\nabla^2 p' - \frac{1}{c^2}\frac{\partial^2 p'}{\partial t^2} = -\rho_0 \frac{\partial q}{\partial t} \tag{2.15}$$

The source term on the right hand side is the mass source term. We then consider the harmonic solution, $p(x,t) = P(x)e^{-i\omega t}$ and the right-hand side term can be expressed as[2] $f(x) = F(x)e^{-i\omega t}$ with a point source at $x = x_0$ such as:

$$\nabla^2 P + \kappa^2 P = -f(x_0)\delta(x - x_0) \tag{2.16}$$

where $\delta(x - x_0)$ is a Dirac delta function; $\kappa = \omega/c_0$. Eq. (2.16) is known as the inhomogeneous Helmholtz equation. Similarly, assuming the source occupies the finite volume region since $f(r)$ has finite support and r_0 being the source spatial coordinate, we arrive at the formulation for inhomogeneous three-dimensional wave equation, where the solution to $P(r)$ is the convolution with the Green's function:

$$P(r) = (G * f)(r) = \int_{\mathbb{R}^n} f(r_0)G(r - r_0)dr_0 \tag{2.17}$$

In general, source terms in inhomogeneous wave equation may contain quite complicated acoustic definitions that are derived from fluid mechanical processes. It has been shown above that the inhomogeneous wave equation can be derived for the limited source region in a confined volume. Then, a uniform stagnant fluid with sound speed c_0, density ρ_0 and pressure p_0 is assumed at the listeners' location. By taking the time derivative of mass conservation, Eq. (2.1), one finds:

$$\frac{\partial^2 \rho}{\partial t^2} + \frac{\partial^2}{\partial t \partial x_i}(\rho u_i) = \frac{\partial^2 \beta \rho}{\partial t^2} \tag{2.18}$$

where $\frac{\partial^2 \beta \rho}{\partial t^2} = \frac{\partial m}{\partial t}$; β is the volume fraction, and $\rho = \rho_0 + \rho'$ is the density used for expressing the rate of change of injected mass, m. Subsequently, taking the divergence of momentum of Eq. (2.2):

$$\frac{\partial^2}{\partial t \partial x_i}(\rho u_i) + \frac{\partial^2}{\partial x_i \partial x_j}\left(P_{ij} + \rho u_i u_j\right) = \frac{\partial f_i}{\partial x_i} \tag{2.19}$$

The following relationship may be established from Eq. (2.18) and Eq. (2.19):

$$\frac{\partial^2 \rho}{\partial t^2} = \frac{\partial^2}{\partial x_i \partial x_j}\left(P_{ij} + \rho u_i u_j\right) + \frac{\partial^2 \beta \rho}{\partial t^2} - \frac{\partial f_i}{\partial x_i} \tag{2.20}$$

Assume that the fluctuating density ρ' is used as an acoustic variable instead of pressure and in Eq. (2.20) the term $c_0^2(\partial^2 \rho'/\partial x_i^2)$, where c_0 is the sound speed at the listeners' location,

[2] where $i = \sqrt{-1}$ is the unit imaginary number

can be subtracted from both sides to reform Eq. (2.20) into a wave equation similar to Eq. (2.13):

$$\frac{\partial^2 \rho\prime}{\partial t^2} - c_0^2 \left(\frac{\partial^2 \rho'}{\partial x_i^2}\right) = \frac{\partial^2 \boldsymbol{T}_{ij}}{\partial x_i \partial x_j} + \frac{\partial^2 \beta\rho}{\partial t^2} - \frac{\partial f_i}{\partial x_i} \tag{2.21}$$

Eq. (2.21) above is the famous Lighthill equation.

where $\boldsymbol{T}_{ij} = \rho u_i u_j - \tau_{ij} + (p' - c_0^2 \rho')\delta_{ij}$ is Lighthill's stress tensor.

Term by term it follows as:

1) The non-linear convective force is described by the Reynolds stress tensor, $\rho u_i u_j$.
2) The term τ_{ij} is the shear stress.
3) The term $p' - c_0^2 \rho'$ accounts for the deviation from an isentropic relationship or a deviation from a uniform velocity, c_0.

Lighthill's equation is regarded as a fundamental analogy in acoustics theory. However, Eq. (2.21) is in fact not any easier to solve than the original equations of motion as it was derived using the mass conservation and the three components of momentum equation that all became part of the single equation. Therefore, some simplifying assumptions have to be introduced to get closer to the solution. In the original work of Lighthill it was recognised that information on the acoustic field can be obtained ignoring the effect of an acoustic variable inside the Lighthill stress term $\boldsymbol{T}_{ij}$ using the integral formulation, thus, replacing the non-linear equation with a non-homogeneous linear wave equation that can be solved analytically. [1] It proved an efficient approach that cuts down by an order of magnitude in comparison to solving the Navier-Stokes equations.

By using the thermodynamic relation, the mass source term $p' - c_0^2 \rho'$ can be written out as derived in [61]:

$$\frac{D}{Dt}\left(\frac{p\prime}{c_0^2} - \rho'\right) = \left(\frac{c^2}{c_0^2} - 1\right)\frac{D\rho\prime}{Dt} - \frac{\rho^2}{c_0^2}\left(\frac{DT}{D\rho}\right)_s \frac{Ds\prime}{Dt} \tag{2.22}$$

From the above, the expression which can be analysed is derived using the mass conservation law and 'excess' density, $\rho_e = \rho' - p'/c_0^2$:

$$-\frac{\partial^2 \rho_e}{\partial t^2} = \frac{\partial}{\partial t}\left[\left(\frac{c^2}{c_0^2} - 1 + \frac{\rho_e}{\rho}\right)\frac{D\rho'}{Dt} + \frac{\rho^2}{c_0^2}\left(\frac{DT}{D\rho}\right)_s \frac{Ds'}{Dt} + \nabla \cdot (\rho_e u_i)\right] \tag{2.23}$$

In Eq. (2.23) the first term in the brackets vanishes for sound propagation in free space $(c^2/c_0^2 - 1 + \rho_e/\rho) = 0$; the second term, $(\rho^2/c_0^2)(DT/D\rho)_s(Ds'/Dt)$ which is derived from a fundamental law of thermodynamics gives rise to sound sources as a result of non-isentropic processes, such as combustion and the final, third term, $\nabla \cdot (\rho_e u_i)$ excites sound waves by spatial density variations.

While Lighthill's analogy can provide an order of magnitude estimate of sound produced by various processes, the formulation may not be robust enough for arbitrary complex flows

because of the assumptions made. More advanced versions of the acoustic analogy include those of Lilley [4] and Goldstein [9] where increasingly more realistic wave propagation models are considered. Still, solving the Linearised Euler Equations for arbitrary mean flows can be rather computationally challenging because of the convective instabilities which can experience an unbounded growth for linear problems compared to the non-linear equations. Acoustic Perturbation Equations (APE) [22] use another formulation which maintains the main features of the full acoustic propagation process while is simpler for implementation than LEE. The idea behind APE is to explicitly separate the potential (acoustic) fluctuations from the vorticity and entropy effects. This separation is not possible for LEE because of the mode coupling in case of a non-uniform mean flow. Hence, several assumptions are required for obtaining the APE model. The APE system has been derived for acoustic perturbation quantities p' and u' where the governing equation for enthalpy, h, served as an underlying formulation from which pressure was deducted using the thermodynamic relationship $h' = p'/\rho_0 + T_0 s'$. Then, with the help of the mass conservation and Navier-Stokes equations the governing equation for the perturbation velocity was derived, initially containing the enthalpy, h, and velocities, $\boldsymbol{u}$, as variables. The APE system reads:

$$\frac{\partial p'}{\partial t} + c_0^2 \nabla \cdot \left(\rho \boldsymbol{u}^a + u_0 \frac{p'}{c_0^2} \right) = c_0^2 q_c \tag{2.24}$$

$$\frac{\partial \boldsymbol{u}^a}{\partial t} + \nabla \cdot (\boldsymbol{u}_0 \cdot \boldsymbol{u}^a) + \nabla \cdot \left(\frac{p'}{\rho_0} \right) = \boldsymbol{q}_m \tag{2.25}$$

with sources:

$$q_c = -\nabla \rho \cdot \boldsymbol{u}^v + \frac{\rho_0}{c_p} \frac{Ds'}{Dt} \tag{2.26}$$

$$q_m = \nabla \Phi_\mathrm{p} + \nabla q_{\omega_0} + T' \nabla s_0 - s' \nabla T_0 \tag{2.27}$$

In Eq. (2.25) $\boldsymbol{u}_0$ and $\boldsymbol{u}^a$ denote mean and acoustic velocities respectively while $\boldsymbol{u}^v$, found in the in the first term of Eq. (2.26) and inside the Poisson equation $\nabla \Phi_\mathrm{p}$, represents solenoidal vortical perturbations. The velocity decomposition follows the convention, $\boldsymbol{u} = \boldsymbol{u}_0 + \boldsymbol{u}' = \boldsymbol{u}_0 + \boldsymbol{u}^a + \boldsymbol{u}^v$. The term ∇q_{ω_0} contains the mean vorticity, $\boldsymbol{\omega}_0 \times \boldsymbol{u}^a$ terms and the rest of Eq. (2.27) contains entropy fluctuations.

$$\nabla \Phi_\mathrm{p} = -\nabla \cdot \left[\frac{\partial \boldsymbol{u}^v}{\partial t} + (\boldsymbol{u_0} \cdot \nabla) \boldsymbol{u}^v + (\boldsymbol{u}^v \cdot \nabla) \boldsymbol{u_0} + \left((\boldsymbol{u}^v \cdot \nabla) \boldsymbol{u}^v \right)' - \left(\frac{\nabla \cdot \underline{\tau}}{\rho} \right)' \right] \tag{2.28}$$

Eq. (2.28) is the Poisson equation enclosed in Eq. (2.27) where all $\boldsymbol{u}^a$ containing terms have been neglected. Terms with a prime refer to the quantity in parenthesis with a subtracted mean. Also, in Eq. (2.28) $\underline{\tau}$ denotes the stress tensor.

The system describes wave propagation in a non-uniform mean flow field $\boldsymbol{u}_0$. It can be reminded that the non-linear terms as well as vortical and entropy disturbances were entirely excluded from the propagation side and as a result non-linear convection effects as well as sound generation effects due to non-linear interaction are not considered in the APE system. Naturally, an unsteady simulation is required for obtaining the right-hand side source terms.

Therefore, the sources described by Eq. (2.26-2.27) have to be shaped into a form that can be conveniently computed with a compressible flow simulation without having to solve the Poisson equation. On the other hand, the propagation can be performed based on time-averaged flow information which can be obtained, for example, using efficient RANS methods.

For a low Mach number flow, mostly encountered in airframe noise problems at atmospheric condition, entropy fluctuations found in $\{T'\nabla s_0 - s'\nabla T_0\}$ and in monopole heat sources $\rho_0/c_p \cdot Ds'/Dt$ can be assumed negligible. This leaves three terms containing vortical modes where the first term in Eq. (2.27), which is described by the Poisson equation $\nabla\Phi_\mathrm{p}$, is most relevant to airframe noise. [22] Also, this term could be directly obtained from an LES solution via a perturbation pressure, $\nabla\Phi_\mathrm{p} \approx \nabla p'/\rho$. Details of the formulation of vortex sound sources used to drive the APE system are discussed in Section 2.4.3.

The stability of the APE system having properties outlined above was examined through eigenmode analysis by Ewert and Schröder [22] making this acoustic approach attractive for the propagation of acoustic waves in arbitrary time-averaged mean flow fields. Interestingly, the stability could be assessed qualitatively using a similarity with the equivalent wave operator exercised in Möhring's acoustic analogy for a moving acoustic medium. [96] [97] The perturbation velocity $\boldsymbol{u}'$ can be split into an irrotational acoustic velocity $\boldsymbol{u}^a$ expressed through a potential $\nabla\varphi'$ and $\boldsymbol{u}^v$ that contains all vortical modes. Note, $\nabla\varphi' = \nabla(\varphi - \varphi_0)$; Furthermore, imposing the condition where the unsteady pressure is expressed in terms of the unsteady potential, $p' = -\rho_0(D\varphi/Dt)$; where $D/Dt = \partial/\partial t + \boldsymbol{u}_0 \cdot \nabla$ is a substantial derivative. Then, re-writing the propagation part of Eq. (2.24) without entropy sources in terms of the potential gives:

$$\nabla \cdot \left(\rho_0 \nabla\varphi - \frac{\rho_0}{c_0^2}\frac{D\varphi}{Dt}\boldsymbol{u}_0\right) - \frac{\partial}{\partial t}\left(\frac{\rho_0}{c_0^2}\frac{D\varphi}{Dt}\right) = -\nabla \cdot (\rho_0 \boldsymbol{u}^v) \tag{2.29}$$

Applying the same for Eq. (2.25) and assuming the mean flow relation $\nabla \cdot (\rho_0 \boldsymbol{u}_0) = 0$; for simplicity:

$$\mathcal{L}'\varphi = \left[\frac{D}{Dt}\left(\frac{1}{c_0^2}\frac{D}{Dt}\right) - \frac{1}{\rho_0}\nabla \cdot (\rho_0 \nabla)\right]\varphi = \frac{1}{\rho_0}\nabla \cdot (\rho_0 \boldsymbol{u}^v) \tag{2.30}$$

and the vortical perturbations of the system:

$$\frac{\partial \boldsymbol{u}^v}{\partial t} + \nabla \cdot (\boldsymbol{u}_0 \cdot \boldsymbol{u}^v) = 0 \tag{2.31}$$

The inhomogeneous wave operator $\mathcal{L}'$ for the potential φ on the left-hand side of Eq. (2.30) describes the behaviour of the acoustic mode while Eq. (2.31) depicts the vortical mode, where the condition $D\omega'/Dt = 0$ holds, thus, preventing the growth of instabilities. Moreover, Eq. (2.30) is equivalent to the linearised wave operator in Möhring's acoustic analogy found in [97], which reads:

$$\mathcal{L}'B = \frac{D}{Dt}\left(\frac{1}{c_0^2}\frac{DB}{Dt}\right) - \frac{1}{\rho_0}\nabla \cdot (\rho_0 \nabla B) = \frac{-q_{tot}}{\rho_0} \tag{2.32}$$

In Eq. (2.32) $B = h + 0.5(\boldsymbol{u} \cdot \boldsymbol{u})^2$; is the total enthalpy and q_{tot} contains vortical and entropy sound sources. Möhring showed that applying the energy theorem to the solution of an initial value problem with vanishing right-hand side q_{tot} at a sufficiently large distance maintains the constant total energy of the sound field. Hence, instabilities cannot occur as none of the contributions to the left-hand side can grow exponentially in time. If $\mathcal{L}'$ is proven to be stable then the APE equivalent system Eq. (2.30) is also stable. The APE system allows for density gradients in an arbitrary mean flow and therefore, in acoustic calculations a no-slip boundary condition can be applied to solid bodies, thus, endowing the physical aspect of wave propagation with APEs.

2.3 Analytical and semi-analytical methods for solving the acoustic equations

2.3.1 Basics of wave propagation: solution as an analogy with elementary vibrations

The wave equation can be defined from first principles by considering a space-time vibration. Mathematically, vibrations can be described by two representative characteristics, namely, time period, T, and amplitude, A. Initially, let $y(t)$ be a function of time only that describes a simple sinusoidal vibration, $y(t) = A \sin\left(2\pi \frac{1}{T} t\right)$ where $1/T$ is the frequency of oscillations in Hz. Then, a slightly more complicated mode of vibration may be described by the summation of simple vibrations.

$$y(t) = \sum_{n=1}^{\infty} A_n \sin(2\pi f_n t + \phi_n) \tag{2.33}$$

The cosine function is a possibility as well and the phase difference, ϕ_n is introduced as vibrations may not start all at the same time. In general:

$$y(t) = \sum_{n=1}^{\infty} A_n \sin(2\pi f_n t + \phi_n) + \sum_{n=1}^{\infty} B_n \cos(2\pi f_n t + \phi_n) \tag{2.34}$$

The simplest mode of vibration which is the first harmonic is illustrated in Figure 2 with a string attached at both ends. All points on the string vibrate with the same frequency yet their spatial distribution is unique.

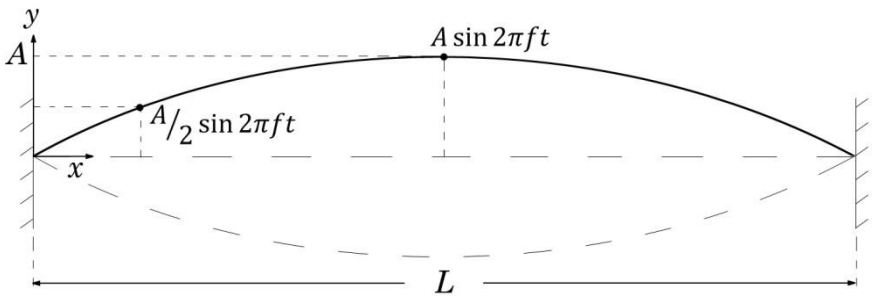

Figure 2 – Illustration of the first harmonic with a vibrating string

Eq. (2.34) can be extended to include the spatial part which satisfies the condition of a wave problem. The general equation for this type of vibration can be expressed as:

$$y(x,t) = \sum_{n=1}^{\infty} A_n \sin(2\pi f_n t + \phi_n) \sin\left(\frac{n\pi}{L}x\right) \tag{2.35}$$

In the above equation index *n* represents the mode of vibration and A_n is the contribution of this mode to the displacement $y(x,t)$. Recalling the identity, $\sin\alpha \sin\beta = \frac{1}{2}\{\cos(\alpha-\beta) - \cos(\alpha+\beta)\}$, Eq. (2.35) can be manipulated into the form that provides an insight into a physical meaning:

$$y(x,t) = \sum_{n=1}^{\infty} \frac{1}{2} A_n \left\{\cos\frac{n\pi}{L}\left(x - \frac{2L}{nT_n}t - \frac{\phi_n}{(n\pi/L)}\right) - \cos\frac{n\pi}{L}\left(x + \frac{2L}{nT_n}t + \frac{\phi_n}{(n\pi/L)}\right)\right\} \tag{2.36}$$

This equation states that each mode propagates with a velocity $2L/nT_n$ in opposite directions. A general form which is not simply a cosine wave is:

$$y(x,t) = g(x-ct) + h(x+ct) \tag{2.37}$$

The shape of the propagating wave is defined by functions g and h. For example, if $y(x,t) = g(x-ct) = Asin(\kappa x - \kappa ct)$ is assumed a sinusoidal shape wave, the statement $\kappa = \omega/c$ must hold where κ is a wave number, $\kappa = 2\pi/\lambda$ and $\lambda = c/f$ is known as the dispersion relation. By differentiating Eq. (2.37) w.r.t. x and t twice one would obtain a general form of a one-dimensional linear wave equation:

$$\nabla^2 y = \frac{1}{c^2}\frac{\partial^2 y}{\partial t^2} \tag{2.38}$$

The above equation is hyperbolic and links the variation in space with the variation in time and can be solved for any problem with the application of appropriate boundary conditions.

2.3.2 Solution method via Green's function and impedance

For a harmonic wave considered in 2.3.1, let $\not{f}(x,t)$ be the impulse excitation function at $x = x_0$, then the response of the string using the general Eq. (2.38) would be:

$$\nabla^2 y - \frac{1}{c^2}\frac{\partial^2 y}{\partial t^2} = \not{f}(x,t) \tag{2.39}$$

More precisely, the response $\not{f}(x,t)$ can be written in terms of the Green's function:

$$y(x,t) = \mathbb{G}(x|x_0)e^{-i\omega t} \tag{2.40}$$

where the excitation on the string is represented as the summation of delta functions having a certain magnitude and Eq. (2.39) can be approximated as:

$$\nabla^2 \mathbb{G}(x|x_0) - \frac{1}{c^2}\frac{\partial^2 \mathbb{G}(x|x_0)}{\partial t^2} = \delta(x - x_0)$$

$$\nabla^2\mathbb{G} - \kappa^2\mathbb{G} = -\frac{1}{f_T}\delta(x - x_0) \tag{2.41}$$

In the above equation f_T represents a tension force and the solution can be assumed:

$$\mathbb{G}(x|x_0) = Ae^{-i\kappa|x-x_0|} \tag{2.42}$$

If Eq. (2.41) is integrated at the vicinity of $x = x_0$,

$$\int_{x=x_0^-}^{x=x_0^+}(\nabla^2\mathbb{G} - \kappa^2\mathbb{G})dx = -\frac{1}{f_T} \tag{2.43}$$

$$\frac{\partial\mathbb{G}}{\partial x}\Big]_{x=x_0^+} - \frac{\partial\mathbb{G}}{\partial x}\Big]_{x=x_0^-} = -\frac{1}{f_T} \tag{2.44}$$

Inserting Eq. (2.42) into Eq. (2.44) gives:

$$A = -\frac{1}{2i\kappa f_T}; \quad \mathbb{G}(x|x_0) = -\frac{1}{2i\kappa f_T}e^{-i\kappa|x-x_0|} \tag{2.45}$$

This is the Green's function for an infinite string because the boundary conditions were not considered so far. Assume, the string is attached at both ends as in Figure 2 then $\mathbb{G}(x|x_0) = 0$ at $x = 0\,, L$. There are two possible waveforms that may satisfy Eq. (2.45): a *sine* and *cosine* functions. However, the cosine function does not satisfy the boundary conditions and hence,

$$\mathbb{G}(x|x_0) = \begin{cases} A\sin\kappa(L - x_0)\sin\kappa x, & x < x_0 \\ A\sin\kappa(L - x)\sin\kappa x_0, & x > x_0 \end{cases} \tag{2.46}$$

Substituting Eq. (2.46) into Eq. (2.41) and integrating:

$$A = \frac{1}{f_T\kappa\sin\kappa L} \tag{2.47}$$

Eqns. (2.46-2.47) show the Green's function solution that predicts the response at any position along the string as a result of an impulse excitation applied at $x = x_0$.

Acoustic impedance is used to analyse instant, reflected and transmitted waves. In [98], an impedance based approach is regarded as a fundamental concept in acoustics. In CAA applications the knowledge of impedance is essential when developing physical boundary conditions. The simplest possible way of demonstrating a solution to a simple problem via an impedance approach is to imagine two media with different properties where the wave is propagating from one to another as shown in Figure 3.

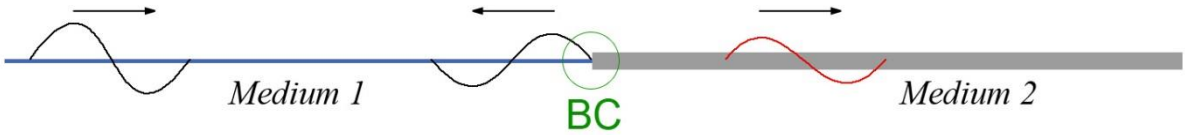

Figure 3 – Wave propagation between different media in a 1D case, illustrated with two attached strings.

According to Eq. (2.37), the instant and reflected waves in medium 1 may be described as $g(x - c_1 t) + h(x + c_1 t)$, and the wave transmitted to medium 2 is $d(x - c_2 t)$. The velocity, c_1 and c_2 would depend on the properties of medium 1 and medium 2 respectively. It is possible to solve three equations by analysing the boundary condition. At the interface of two strings the displacement must be identical and the velocity should be so too. For a one-dimensional case, such as wave propagation in a string, it can be assumed that the displacement in *y* direction is much larger than the displacement in *x* direction. This makes the description of impedance clearer, yet similar velocity and force conditions can be applied to *x* direction, if necessary. Characteristic impedance is defined as the ratio of force over velocity, $Z = f/u$ where the force in y-direction can be expressed via tension $\mathcal{T}$ multiplied by the gradient:

$$Z = \frac{\pm \mathcal{T} \frac{\partial y}{\partial x}}{\frac{\partial y}{\partial t}} = \frac{f_T}{c_n} \tag{2.47}$$

In Eq. (2.47) f_T is a tension force and c_n is the velocity in *y*-direction according with the above mentioned assumption. Hence, the reflection coefficient at the interface is $\zeta_{re} = h/g = (z_1 - z_2)/(z_1 + z_2)$; and the transmission coefficient at the interface is $\zeta_{tr} = g/d = 2z_1/(z_1 + z_2)$. A physical meaning of impedance is the force applied per unit velocity. If impedance is very large, for example, $z \to \infty$ an infinite amount of force would be required to move the point. Assuming $z_1 \ll z_2$ in the above example, $\zeta_{re} \sim -1$ and $\zeta_{tr} \sim 0$ and the wave would be reflected back, almost entirely. On the other hand, if $z_1 \gg z_2$, $\zeta_{re} \sim 1$ and $\zeta_{tr} \sim 2$ meaning the amplitude of the transmitted wave would be increased approximately by a factor of 2. However, the energy transmitted in the case of $z_1 \gg z_2$ would not increase by a factor of 2 as it is impossible to get the power gain through wave transmission to another medium. One has to derive the power transmission coefficient and as a matter of fact in this case where $z_1 \gg z_2$ there would be almost none. In this simple example it has been demonstrated that the impedance mismatch causes reflection and transmission of waves.

2.3.3 Elementary sources: monopole, dipole and quadrupole

2.3.3.1 Monopole source

In previous chapters we considered the inhomogeneous wave equation with the source terms isolated on the right-hand side. In theory, the right-hand side point source is only non-zero at the origin and elsewhere the homogeneous equation may be used. To grasp the physical meaning of the pressure wave behaviour in space and time the periodic pressure variation shall be considered as a simple solution to the homogeneous wave equation. By starting with a simplest case of a one-dimensional wave, which can also be described by Eq. (2.13), the pressure at position x and time t, denoted $p(x, t)$, may be written as:

$$p(x, t) = P(x)e^{-i\omega t} = Ae^{-i(\omega t - \kappa x)} \tag{2.48}$$

For convenience, expressing Eq. (2.13) in spherical coordinates and choosing distance from the origin, $\boldsymbol{r}$ vector, in the direction of wave propagation and assuming pressure only depends on the distance from the origin, r, as for the plane wave, also, ignoring any angular dependence which is a possibility when using spherical coordinates, the wave equation becomes:

$$\frac{\partial^2}{\partial r^2}(rp) = \frac{1}{c^2}\frac{\partial^2}{\partial t^2}(rp) \tag{2.49}$$

and the simplest solution by analogy with Eq. (2.48):

$$p(r,t) = \frac{A}{\boldsymbol{r}} e^{-i(\omega t - \boldsymbol{\kappa r})} \tag{2.50}$$

where A is a complex amplitude. The periodic pressure variation in Eq. (2.50), in fact, provides the definition of a monopole source. In Eq. (2.50) pressure is inversely proportional to the distance r and when $r = 0$; that is at the origin, pressure has a singularity (as it tends to infinity). Furthermore, by using Euler's relationship the velocity corresponding to the behaviour in Eq. (2.50) can be examined. Expressing the Euler equation (2.8) for u_r which is the velocity in the radial direction, in spherical coordinates reads:

$$\frac{\partial u_r}{\partial t} = -\frac{1}{\rho_0}\frac{\partial p}{\partial r} \tag{2.51}$$

meaning that,

$$u_r = \frac{A}{\boldsymbol{r}} \cdot \frac{1}{\rho_0 c}\left(1 + \frac{i}{\kappa r}\right) e^{-i(\omega t - \boldsymbol{\kappa r})} \tag{2.52}$$

At this stage, it is convenient to express the impedance using Eq. (2.50) and Eq. (2.52) and manipulating into a form as shown in [98], given below:

$$z_r = \frac{p}{u_r} = \rho_0 c \left[\frac{(\kappa r)^2}{1+(\kappa r)^2} - i\frac{(\kappa r)}{1+(\kappa r)^2}\right] \tag{2.53}$$

In the above equation, the impedance is expressed in terms of the dimensionless distance κr, having real and imaginary parts. The behaviour of the monopole source is best illustrated on the impedance plot shown in Figure 4 below.

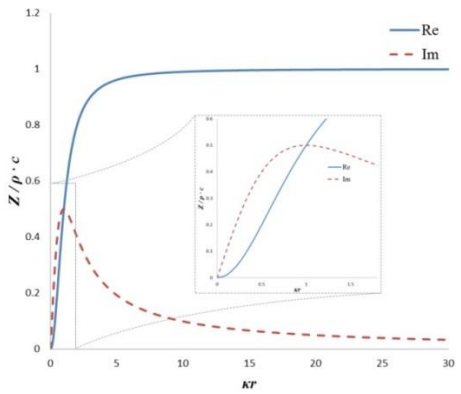

Figure 4 – Impedance function for a monopole radiation.

When $\kappa r \gg 1$ and the distance from the origin is large in comparison to the wavelength in κ, the impedance $z_r/\rho_0 c$ levels out and approaches the plane wave impedance that is equal to the characteristic impedance of a medium. In this 'far-field' region the one-dimensional wave propagation could be thought of as a wave propagating along the string and linear propagation laws apply. On the other hand, when $\kappa r \ll 1$, the pressure and velocity is 90° out of phase. In this region, fluid particles are accelerated by the changing pressure and the imaginary component, clearly, is not negligible. This can be referred to as the 'near-field' region. Moreover, as this simple solution satisfies the wave equation, one can assume that superposition of simple solutions will also satisfy the governing wave equation, allowing for more complicated waves to be constructed by using the monopole source concept. For example, two monopoles located next to each other with the opposite phase form a dipole. Following the same principle and grouping 4 monopoles with alternating opposite phases results in a quadrupole. A complicated wave pattern may be formed by observing multiple monopoles in action in a shallow water ripple tank.

In a three dimensional space, a monopole source could be described by a repeatedly expanding and contracting sphere. The sound pressure at the source could be represented in exactly the same way as Eq. (2.50) suggests:

$$p(r) = \frac{A}{\boldsymbol{r}} e^{i(\boldsymbol{\kappa r})} \tag{2.54}$$

Here, the complex amplitude A must represent a 'driving force' of a fluid mass per unit time and angle. The equation for the amplitude reads:

$$A = \frac{1}{4\pi}\rho_0(-j\omega Q) \tag{2.55}$$

where Q is the volume rate of change of a monopole source. Dimensional analysis suggests that units of Q are [L^3/T]. Again, from Euler's equation, the velocity in the direction of $\boldsymbol{r}$ is:

$$u_r = \frac{1}{i\kappa\rho_0 c}\frac{\partial p}{\partial r} = \frac{A\, e^{i(\kappa r)}}{\boldsymbol{r}\,\rho_0 c}\left(1 + \frac{i}{\kappa r}\right) \tag{2.56}$$

Hence, the impedance could be obtained:

In the near-field: $$z_r = \frac{p(r)}{u_r(r)} \approx -i\rho_0 c(\kappa r) \tag{2.57}$$

In the far-field: $$z_r = \frac{p(r)}{u_r(r)} \approx \rho_0 c \tag{2.58}$$

The average intensity in the direction of r could be obtained by multiplying $p(r)$ and $u_r(r)$ in Eq. (2.54) and Eq. (2.56). Both of the above mentioned equations have a complex phase and as for plane waves the phase of sound pressure is identical to that of particle velocity and only the active intensity (the real part) exists and the reactive intensity (the imaginary part) becomes zero. In general, the complex intensity reads:

$$I(r) = I_{avg}(r) + iI(r) = \frac{1}{2} PU\, e^{-i(\phi_p - \phi_u)} \tag{2.59}$$

With the following definitions $p(r,t) = P\cos(\omega t + \phi_p)$; and $u(r,t) = U\cos(\omega t + \phi_u)$; for pressure and velocity, where ϕ_p and ϕ_u is the phase of the sound pressure and particle velocity respectively. The magnitude of complex intensity is $|I(r)| = 1/2\,(PU)$; and the average intensity by definition is:

$$I_{avg}(r) = \frac{1}{2}PU\cos(\phi_p - \phi_u) \equiv \frac{1}{2}\mathrm{Re}\{p(r)u_r(r)^*\} \tag{2.60}$$

In Eq. (2.60), * implies a complex conjugate. Comparing the definition to Eq. (2.54) and Eq. (2.56), the average intensity can be written as:

$$I_{avg}(r) = \frac{1}{2}\cdot\frac{1}{\rho_0 c}\frac{|A|^2}{r^2} \tag{2.61}$$

When reviewing Figure 4 with the definition of intensity in mind, in the far-field region where there is no phase difference between the sound pressure and particle velocity, the intensity is inversely proportional to the square of the distance but independent of κr. On the other hand, by thinking of the reactive intensity derived from the imaginary part of Eq. (2.56), and where pressure and velocity would have 90° phase difference, it is inversely proportional to the square of the distance and also inversely proportional to κr. Therefore, the reactive intensity decreases rapidly when moving away from the origin and in the vicinity of the origin, as highlighted in Figure 4, it dominates the acoustic behaviour and waves do not propagate well.

The average acoustic power can be obtained by integrating the intensity Eq. (2.61) over an area with a radius r. Due to the spherical symmetry, the integration of intensity of a monopole source corresponds to its multiplication with a surface ($S = 4\pi r^2$).

$$\Pi_{avg} = \int_0^{\pi}\int_0^{2\pi} I_{avg}(r)\, r^2 \sin\theta\, d\varphi d\theta = \frac{2\pi\,|A|^2}{\rho_0 c} \tag{2.62}$$

2.3.3.2 Dipole source

In a situation when two monopole sources are placed in a close proximity to each other with a 180° phase difference, as each of them is effectively a point source the collective effect forms a dipole. The sound pressure of a dipole can be expressed mathematically as:

$$p(r,\theta,\varphi) = \lim_{\Delta\to 0} A\left(\frac{e^{i(\kappa r_1)}}{r_1} - \frac{e^{i(\kappa r_2)}}{r_2}\right) \tag{2.63}$$

where Δ is the separation distance between two monopole sources. In following derivations, the separation and the position of sources has to be handled with care, as the sound field may change with respect to these characteristics. The generalised form of the sound pressure exerted by a dipole source is given below. (See Appendix A for derivation)

$$p(r,\theta,\varphi) = -i\kappa D\frac{e^{i(\kappa r)}}{r}\frac{z}{r}\left(1 + \frac{i}{\kappa r}\right) = -i\kappa D\frac{e^{i(\kappa r)}}{r}\cos\theta\left(1 + \frac{i}{\kappa r}\right) \tag{2.64}$$

In this equation $D = A\Delta$; and it is assumed that the two sources are located on the z axis. From Euler's equation, the velocity in the direction of r could be written as:

$$u_r(r,\theta,\varphi) = -i\frac{\kappa D}{\rho_0 c}\frac{e^{i(\kappa r)}}{r}\cos\theta\left(1 + 2i\left(\frac{1}{\kappa r}\right) - 2\left(\frac{1}{\kappa r}\right)^2\right) \tag{2.65}$$

Hence, the impedance could be obtained:

$$z_r(r,\theta,\varphi) = \rho_0 c\frac{1+i\left(\frac{1}{\kappa r}\right)}{1+2i\left(\frac{1}{\kappa r}\right)-2\left(\frac{1}{\kappa r}\right)^2} \tag{2.66}$$

The average intensity then obtained similarly to Eq. (2.61),

$$I_{avg}(r,\theta,\varphi) = \frac{\kappa^2|D|^2}{2\rho_0 c}\frac{1}{r^2}\cos^2\theta \tag{2.69}$$

and sound power is just an area integral,

$$\Pi_{avg} = \frac{2\pi\,\kappa^2|D|^2}{3\rho_0 c} \tag{2.70}$$

2.3.3.3 Quadrupole source

A quadrupole source can be formed by two closely located dipole sources with the opposite phase or four closely placed monopoles. Following the Section 2.3.3.2 the sound pressure of a quadrupole can be expressed mathematically as:

$$p(r,\theta,\varphi) = \lim_{\Delta\to 0}(-i\kappa D)\left[\frac{e^{i(\kappa r_1)}}{r_1}\cos\varphi_1\left\{1 + i\left(\frac{1}{\kappa r_1}\right)\right\} - \frac{e^{i(\kappa r_2)}}{r_2}\cos\varphi_2\left\{1 + i\left(\frac{1}{\kappa r_2}\right)\right\}\right] \tag{2.71}$$

The generalised form of Eq. (2.71) for the sound pressure exerted by a quadrupole source is given below. (See Appendix A for derivation)

$$p(r,\theta,\varphi) = -\kappa^2\mathbb{S}\frac{e^{i(\kappa r)}}{r}\sin 2\theta\cos\varphi\left(1 + 3i\left(\frac{1}{\kappa r}\right) - 3\left(\frac{1}{\kappa r}\right)^2\right) \tag{2.72}$$

where $\mathbb{S}$ is the quadrupole amplitude. As before, proceeding with the corresponding velocity equation and impedance:

$$u_r(r,\theta,\varphi) = -\frac{\kappa^2\mathbb{S}}{\rho_0 c}\frac{e^{i(\kappa r)}}{r}\sin 2\theta\cos\varphi\left(1 + 4i\left(\frac{1}{\kappa r}\right) - 9\left(\frac{1}{\kappa r}\right)^2 - 9i\left(\frac{1}{\kappa r}\right)^3\right) \tag{2.73}$$

$$z_r(r,\theta,\varphi) = \rho_0 c\frac{1+3i\left(\frac{1}{\kappa r}\right)-3\left(\frac{1}{\kappa r}\right)^2}{1+4i\left(\frac{1}{\kappa r}\right)-9\left(\frac{1}{\kappa r}\right)^2-9i\left(\frac{1}{\kappa r}\right)^3} \tag{2.74}$$

Intensity in the r direction is:

$$I_{avg}(r,\theta,\varphi) = \frac{\kappa^4|\mathbb{S}|^2}{2\rho_0 c}\frac{1}{r^2}\sin^2 2\theta\cos^2\varphi \tag{2.75}$$

And power in the r direction is:

$$\Pi_{avg} = \frac{\kappa^4 |\mathbb{S}|^2}{15\rho_0 c} \tag{2.76}$$

It can be observed that that for all source types, monopole, dipole and quadrupole considered, when $\kappa r \gg 1$ that is the far-field condition, the impedance in the r direction, $z_r(r, \theta, \varphi) \approx \rho_0 c$ is identical to the impedance of a plane wave. Distinctively, the radiated power in the r direction is independent of the wavenumber κ for the monopole source, while for the dipole and quadrupole it is proportional to κ^2 and κ^4 respectively.

2.4 Popular far-field noise prediction methods based on a combination of the theory and numerical simulations

In this section the review on far-field noise prediction methods is presented, ranging from more simple / less general to more complex / more general in terms of the acoustic modelling. The section begins with an introduction into Kirchhoff's integral method which is fundamental to Ffowcs Williams-Hawkings acoustic surface integration technique, which remains one of the popular methods of choice in aero-acoustic community to this day. In this work FW-H is the method of choice for obtaining far-field acoustic predictions with noise sources derived from LES. Finally, a vortex sound method based on solving Acoustic Perturbation Equations is reviewed. Note that APEs represent the second sound propagation technique which is employed in the current work in conjunction with the FRPM method. For airframe noise applications, the vortex sound model is believed to describe the underlying physics behind sound generation processes. In Section 2.4.3, important noise source components are identified and discussed as well as some popular assumptions applied when using these techniques.

2.4.1 Kirchhoff's integral method

Among various acoustic analogies proposed over the years, Kirchhoff's integral method [99] [100] [101] remains one of the simplest techniques for determining far-field acoustics. Usually, an observer is located at a relatively large distance from an acoustic source and a problem can be split into a near-field region, where sources are computed or determined experimentally and a far-field zone. In practice, a control surface *S* that provides coupling between wave propagation and right-hand side sources is introduced to separate the two zones. In order to determine the solution at the observer's location, the homogeneous wave equation is solved using the free-space Green's function approach with an input source term specified from the inside of the control surface. The volume $V(t)$ may be enclosed by the control surface $S(t)$, which is defined by a smooth function $f(x,t) = 0$ if $x \in S(t)$. Otherwise, the domain is divided as discussed:

$$\tilde{f}(x,t) = \begin{cases} f(x,t) < 0 & if \quad x \in V(t) \\ f(x,t) > 0 & outside \quad V(t) \end{cases} \tag{2.77}$$

Assuming the medium moves with a constant velocity $\boldsymbol{U}_\infty$, the homogeneous wave equation for any acoustic variable, for example, $p'(x,t)$ could be defined for the outer and inner regions in accordance with Eq. (2.77) as follows:

$$\frac{1}{c_0^2}\frac{\partial^2}{\partial t^2}\tilde{p}(x,t) - \nabla^2\tilde{p}(x,t) = 0 \tag{2.78}$$

In Eq. (2.78) $\tilde{p}(x,t) = p'(x,t)H(f)$ where $H(f)$ is the Heaviside function specified as zero inside $V(t)$ and 1 in the outer wave propagation region. In accordance to Farassat & Myers [102], the discontinuity across the control surface at $f(x,t) = 0$, $\Delta\tilde{p} = \tilde{p}\big(f(0^+)\big) - \tilde{p}\big(f(0^-)\big)$ is treated with a Dirac delta function and the generalised derivative becomes:

$$\frac{\bar{\partial}\tilde{p}}{\partial x_i} = \frac{\partial\tilde{p}}{\partial x_i} + \Delta\tilde{p}\frac{\partial f}{\partial x_i}\delta(f) = \frac{\partial\tilde{p}}{\partial x_i} + p\hat{n}_i\delta(f) \tag{2.79}$$

where $\hat{n}_i$ is the surface unit normal and $p = \tilde{p}\big(f(0^+)\big)$. A bar over a derivative operator is used to denote a generalised differentiation. By differentiating again for obtaining $\nabla^2\tilde{p}(x,t)$ term in Eq. (2.78) we get the following expression:

$$\bar{\nabla}^2\tilde{p} = \nabla^2\tilde{p} + \frac{\partial}{\partial x_i}[p\hat{n}_i\delta(f)] + p_n\delta(f) \tag{2.80}$$

where $p_n = \hat{n}\cdot\nabla p$. Following the same procedure for the time derivative yields:

$$\frac{\bar{\partial}\tilde{p}}{\partial t} = \frac{\partial\tilde{p}}{\partial t} + p\frac{\partial f}{\partial t}\delta(f) \tag{2.81}$$

In Eq. (2.81) above, the time derivative of the function f includes the mean flow convection, such as, $\partial f/\partial t = -\hat{n}\cdot\boldsymbol{u} + \hat{n}\cdot\boldsymbol{U}_\infty$; where $\hat{n}\cdot\boldsymbol{u} = \boldsymbol{u}_n$ and $\hat{n}\cdot\boldsymbol{U}_\infty = \boldsymbol{U}_{\infty n}$ then,

$$\frac{\bar{\partial}^2\tilde{p}}{\partial t^2} = \frac{\partial^2\tilde{p}}{\partial t^2} - \frac{\partial}{\partial t}[p(\boldsymbol{u}_n - \boldsymbol{U}_{\infty n})\delta(f)] - \frac{\partial p}{\partial t}(\boldsymbol{u}_n - \boldsymbol{U}_{\infty n})\delta(f) \tag{2.82}$$

By using Eq. (2.80) and Eq. (2.82) to form the relationship:

$$\frac{1}{c_0^2}\frac{\bar{\partial}^2\tilde{p}}{\partial t^2} - \bar{\nabla}^2\tilde{p} = \frac{1}{c_0^2}\frac{\partial^2\tilde{p}}{\partial t^2} - \frac{1}{c_0}\frac{\partial}{\partial t}[p(M_n - M_{\infty n})\delta(f)] - \nabla^2\tilde{p} - p_n\delta(f) - \frac{M_n - M_{\infty n}}{c_0}\frac{\partial p}{\partial t}\delta(f) - \frac{\partial}{\partial x_i}[p\hat{n}_i\delta(f)]; \tag{2.83}$$

where $M_n = \boldsymbol{u}_n/c_0$; is the local Mach number normal to the surface and $M_{\infty n} = \boldsymbol{U}_{\infty n}/c_0$; is the normal Mach number of the moving frame. Substituting Eq. (2.78) into Eq. (2.83) gives the Kirchhoff's formula in the moving medium:

$$\frac{1}{c_0^2}\frac{\bar{\partial}^2\tilde{p}}{\partial t^2} - \bar{\nabla}^2\tilde{p} = -\left[p_n + \frac{M_n - M_{\infty n}}{c_0}\left(\frac{\partial p}{\partial t} + \boldsymbol{U}_\infty\cdot\nabla p\right)\right]\delta(f) - \frac{1}{c_0}\frac{\partial}{\partial t}[p(M_n - M_{\infty n})\delta(f)] - \frac{\partial}{\partial x_i}[p\hat{n}_i + p(M_n - M_{\infty n})M_\infty\delta(f)] \tag{2.84}$$

Without convection, the wave equation Eq. (2.84) simply reads:

$$\frac{1}{c_0^2}\frac{\overline{\partial}^2\tilde{p}}{\partial t^2} - \overline{\nabla}^2\tilde{p} = -\left[p_n + \frac{M_n}{c_0}\frac{\partial p}{\partial t}\right]\delta(f) - \frac{1}{c_0}\frac{\partial}{\partial t}[pM_n\delta(f)] - \frac{\partial}{\partial x_i}[p\hat{n}_i\delta(f)] \qquad (2.85)$$

The above equations, Eq. (2.84) or Eq. (2.85) can be solved using the Green's function approach for a wave equation. All three terms in above equations (2.84-2.85) are of monopole and dipole type with delta function acting at the control surface. Hence, an acoustic solution can be obtained by simply solving three surface integrals, derived from spatio-temporal integration.

The main advantage of Kirchhoff's formulation is in the relatively simple definition where variables have to be integrated over a surface for estimation of acoustics in the far-field. Additionally, the specific formulation of acoustic sources as well as the unsteadiness inside $V(t)$ is immaterial in the above definition and averaged acoustic quantities are used as the only input information. The simplicity of this formulation can also be a disadvantage where, for example, one of the method's notable shortcomings arises by neglecting inhomogeneity of the flow field as well as other sound sources present inside $V(t)$, as there is no direct link between turbulent quantities.

2.4.2 Ffowcs Williams-Hawkings method

Another integral method commonly adopted in CAA application and employed in this work is known as Ffowcs-Williams Hawkings (FW-H) acoustic analogy [19], which is based on Lighthill's equation introduced in Section 2.2 previously. In practice, FW-H is considered the superior method over Kirchhoff's formulation due to a more flexible definition of the control surface and especially because Lighthill's analogy is derived from equations of motion. As a matter of fact, the definition in Eq. (2.84) and Eq. (2.85) is consistent with the FW-H analogy when the input data are compatible with the linearised wave equation, i.e. when the control surface is located in a linear propagation zone.

The FW-H equation reads:

$$\left(\frac{1}{c_0^2}\frac{\partial^2}{\partial t^2} - \nabla^2\right)\widetilde{p'}(x,t) = \frac{\partial^2 \boldsymbol{T}_{ij}}{\partial x_i \partial x_j} - \nabla[L_i\delta(f)] + \frac{\partial}{\partial t}[Q_n\delta(f)] \qquad (2.86)$$

where $\widetilde{\boldsymbol{T}}_{ij} = \left(\rho u_i u_j - \tau_{ij} + (p' - c_0^2\rho')\delta_{ij}\right)H(f)$ is the Lighthill tensor with perturbations $p' = p - p_0$ and $\rho' = \rho - \rho_0$. An additional multiplier $H(f)$ is the Heaviside function specified as zero inside $V(t)$ and 1 in the outer wave propagation region.

$L_i = \rho u_i[u_n - (v_n - U_{\infty n})] + p_{ij}\hat{n}_j$; and $Q_n = \rho[u_n - (v_n - U_{\infty n})] + \rho_0(v_n - U_{\infty n})$;

At this time it is convenient to show the relationship between Eq. (2.86) and Eq. (2.84), discussed previously. Let, Q_{Kir} denote the right-hand side sources in Kirchhoff's formula Eq. (2.84) such that:

$Q_{Kir} = -\left[p_n + \frac{M_n - M_{\infty n}}{c_0}\left(\frac{\partial p}{\partial t} + \boldsymbol{U}_\infty \cdot \nabla p\right)\right]\delta(f) - \frac{1}{c_0}\frac{\partial}{\partial t}[p(M_n - M_{\infty n})\delta(f)] - \frac{\partial}{\partial x_i}[p\hat{n}_i + p(M_n - M_{\infty n})M_\infty \delta(f)]$;

Then, by adding Q_{Kir} and subtracting source terms, Eq. (2.86) can be re-written as:

$$\left(\frac{1}{c_0^2}\frac{\partial^2}{\partial t^2} - \nabla^2\right)\widetilde{p'}(\boldsymbol{x}, t) = Q_{Kir} + \frac{\partial^2 \boldsymbol{T}_{ij}}{\partial x_i \partial x_j}H(f) + \left[\frac{\partial p'}{\partial n} + \frac{M_n - M_{\infty n}}{c_0}\left(\frac{\partial p'}{\partial t} + \boldsymbol{U}_\infty \cdot \nabla p\right)\right]\delta(f) + \frac{\partial}{\partial t}\left[(p' - c_0^2\rho')\frac{M_n - M_{\infty n}}{c_0}\delta(f)\right] - \nabla\{\rho u_i[u_n - (v_n - U_{\infty n})]\delta(f)\} + \frac{\partial}{\partial t}[\rho u_n \delta(f)]; \quad (2.87)$$

By using the continuity and momentum equations, along with the relationship $\partial/\partial t\,[\hat{n}_i\delta(f)] = -\partial/\partial x_i\,[v_n\delta(f)]$; [100] one can re-write Eq. (2.87) as following:

$$\left(\frac{1}{c_0^2}\frac{\partial^2}{\partial t^2} - \nabla^2\right)\widetilde{p'}(\boldsymbol{x}, t) = Q_{Kir} + \frac{\partial^2 \boldsymbol{T}_{ij}}{\partial x_i \partial x_j}H(f) + \frac{\partial}{\partial t}[p' - c_0^2\rho']\frac{M_n - M_{\infty n}}{c_0}\delta(f) + \frac{\partial}{\partial t}\left[(p' - c_0^2\rho')\frac{M_n - M_{\infty n}}{c_0}\delta(f)\right] - \frac{\partial}{\partial x_j}\left[\rho u_i u_j\right]\hat{n}_i\delta(f) - \frac{\partial}{\partial x_i}[\rho u_i u_n \delta(f)] \quad (2.88)$$

Finally, for the linear flow region, $p' = \rho' c_0^2$, Eq.(2.88) becomes:

$$\left(\frac{1}{c_0^2}\frac{\partial^2}{\partial t^2} - \nabla^2\right)\widetilde{p'}(\boldsymbol{x}, t) = Q_{Kir} + \frac{\partial^2(\rho u_i u_j)}{\partial x_i \partial x_j}H(f) \quad (2.89)$$

The only remaining term is the second order perturbation velocities that are negligible in the derivation of the wave equation. Hence, the FW-H formulation could be assumed equivalent to Kirchhoff's formula if the control surface is placed in the linear flow region.

Consider the right-hand side source terms in the FW-H equation, Eq. (2.86), which consists of a quadrupole term, $\frac{\partial^2 \boldsymbol{T}_{ij}}{\partial x_i \partial x_j}$ along with the dipole and monopole terms, $\nabla[L_i\delta(f)]$ and $\frac{\partial}{\partial t}[Q_n\delta(f)]$, where for the last two terms surface integrals could be obtained. If the integration surface could be matched to an aerofoil profile these source terms gain a physical meaning which is related to aerodynamic characteristics. In essence, the dipole term, $\nabla[L_i\delta(f)]$ is proportional to the normal pressure force of a solid body. On the other hand, the monopole term, $\frac{\partial}{\partial t}[Q_n\delta(f)]$ in a close proximity to the aerofoil's surface describes the divergence of velocity $(\rho_0 v_n)$, practically signifying on the compressibility effects next to a solid surface. To conclude, for a so called impenetrable formulation when the control surface

S is described by the outline of an aerofoil's profile, the dipole source term is defined by a lift force while the monopole is proportional to the compressibility effects, which strengthen with increasing Mach number and profile thickness. In the propagation region, the quadrupole term is described by the Lighthill stress tensor $\boldsymbol{T}_{ij}$ as shown in Section 2.2. This term consists of three components, where the sources of noise may originate due to non-linear convection, viscous effects described via shear stresses and anisotropic flow behaviour. The correct representation of the quadrupole term is very challenging from the modelling viewpoint but thankfully, for most low Mach number CAA problems its contribution to overall noise generally is negligible, as will be demonstrated when investigating into the sources of the trailing edge noise in later chapters. Therefore, it is beneficial to ignore the quadrupole term from the FW-H analogy.

As mentioned previously, the FW-H differential equation can be solved via Green's function approach, $G(\boldsymbol{x},t,\boldsymbol{y},\tau)=\delta(g)/4\pi r$ where $\tau \le t$ and $g=\tau-t+r/c_0$. The distance between the source and the observer, $r=|x(t)-y(\tau)|$; by neglecting the quadrupole term, a far-field pressure signal at the observer's location can be determined through integration:

$$p'(x,t)=-\nabla\int_{-\infty}^{t}\int_{-\infty}^{+\infty}\frac{L_i\delta(f)\delta(g)}{4\pi r}d^3yd\tau+\frac{\partial}{\partial t}\int_{-\infty}^{t}\int_{-\infty}^{+\infty}\frac{Q_n\delta(f)\delta(g)}{4\pi r}d^3yd\tau \qquad (2.90)$$

In Eq. (2.90), $p'(x,t)$ represents $p'(x,t)/c_0^2$; where by assumption the flow is linear and isentropic at the observer's location. By following the definition for $f(x,t)=0$; at S in the local reference frame, called the η frame, which is specified with respect to the control surface, the variable y could be transformed to the variable η and the surface integral is then evaluated. Additionally, accounting for a temporal delay before the signal reaches the observer, $\tau^*=t-|x(t)-y(\tau^*)|/c$; and after several transformations [103] [104] one could obtain:

$$\begin{aligned}4\pi p'(x,t,M_\infty)=\ &\int_S\left[\frac{\rho_0\left\{\left(\frac{\partial}{\partial\tau}u_i\right)\hat{n}_i+u_i\frac{\partial}{\partial\tau}\hat{n}_i\right\}}{r|1-M_{\infty r}|^2}\right]_{\tau^*}dS+\int_S\left[\frac{\rho_0u_i\hat{n}_iK}{r^2|1-M_{\infty r}|^3}\right]_{\tau^*}dS+\\ &\frac{1}{c}\int_S\left[\frac{\left(\frac{\partial}{\partial\tau}L_i\right)(r_i/r)}{r|1-M_{\infty r}|^2}\right]_{\tau^*}dS+\int_S\left[\frac{L_i(r_i/r)-L_iM_{\infty i}}{r^2|1-M_{\infty r}|^2}\right]_{\tau^*}dS+\frac{1}{c}\int_S\left[\frac{L_i(r_i/r)K}{r^2|1-M_{\infty r}|^3}\right]_{\tau^*}dS\end{aligned} \qquad (2.91)$$

where $K=\left(\frac{\partial}{\partial\tau}M_{\infty i}\right)r_i+c(M_{\infty r}-M_\infty)$; Here, $M_{\infty i}$ is the projection of Mach number onto η_i and $M_{\infty r}$ is the Mach number relative to the moving reference frame. Furthermore, $|1-M_{\infty r}|^{-1}$ denotes a Doppler's shift in a moving source reference frame. Clearly, this approach may lose precision when approaching sonic speeds and more complicated integration procedures should be adopted. [104] However, when dealing with low Mach number aerofoil flows, the above formulation can be used. In the current work Eq. (2.91) is used in conjunction with the LES CABARET method where at a specified time interval near-wall pressure fluctuations are linearly interpolated onto the control surface, which is wrapped about the quasi-2D slice of an aerofoil. Then, surface integrals are evaluated numerically using the trapezium rule.

2.4.3 Vortex sound method and its implementation based on solving Acoustic Perturbation Equations (APE)

In contrast to integral methods reviewed so far where acoustic sources have to be specifically derived using the definition of a control surface, the vortex sound method uses a less general formulation. In essence, vortex sound theory translates the particular vortical description derived from a turbulent flow into sound sources, meaning that the spatial location of such sources would be completely prescribed by physics of the turbulent flow. Also, vortex sound sources could be specified in a 3D space which makes inclusion of a quadrupole term possible. This can be regarded as an advantage, yet the sound mechanism formulated by the turbulent flow is quite complicated as seen from Lighthill's equation, Eq. (2.21), which source terms do not have a simple physical meaning except for the simplest case of sound generation in uniform stationary media. As observed by Powell (1964) [91], the sound generation in subsonic flows with constant entropy assumption is associated to the vortex dynamics, $\boldsymbol{\omega} = \nabla \times \boldsymbol{u}$. Other notable research work focusing on elaboration of vortex sound theory includes works of Möhring [105], Schram and Hirschberg [106], Howe [107], Ewert and Schröder [22]. In the literature on acoustic modelling, typically, the effective sound sources are evaluated with the help of additional simplifying assumptions. In the current work, the sound sources which correspond to the vortex sound model are analysed in details for the aerofoil trailing edge problem using the LES solution. Specifically, vortex sound sources are based on the Lamb vector, (generally defined as $\boldsymbol{\omega} \times \boldsymbol{u}$) which describes the right-hand side source term. This can be implied considering the APEs discussed in Section 2.2. The governing equations for the APE system can be derived from continuity and momentum equations [22]:

$$\frac{\partial \rho'}{\partial t} + \nabla \cdot (\bar{\rho}\boldsymbol{u}' + \rho'\overline{\boldsymbol{u}} + \rho'\boldsymbol{u}' - \overline{\rho'\boldsymbol{u}'}) = 0 \tag{2.92}$$

$$\frac{\partial \boldsymbol{u}'}{\partial t} + (\overline{\boldsymbol{u}} \cdot \nabla)\boldsymbol{u}' + (\boldsymbol{u}' \cdot \nabla)\overline{\boldsymbol{u}} + \nabla\left(\frac{p'}{\bar{\rho}}\right) = \boldsymbol{f} \tag{2.93}$$

where $\boldsymbol{f}$ consists of the non-linear part, $\boldsymbol{f}_{nl} = -\left((u' \cdot \nabla)u' - \frac{\nabla \cdot \underline{\tau}}{\rho}\right)'$ and entropy terms, $\boldsymbol{f}_s = T'\nabla\bar{s} - s'\nabla\bar{T}$. The density and pressure fluctuations are related thermodynamically, $p' - \bar{c}^2\rho' = \left(\gamma\bar{p}/c_p\right)s'$. For obtaining the specific form of Eq. (2.93), the enthalpy and entropy gradients are substituted for the pressure gradient using $\nabla p/\rho = \nabla h - T\nabla s$ relation and the equations for perturbation quantities follow by subtracting the time-averaged momentum equation. Then, the only enthalpy term, $\nabla h'$, which remains in the momentum equation is eliminated utilising the relationship $h' = p'/\rho_0 + T_0 s'$ as it was already mentioned in Section 2.2. Finally, using the identity Eq. (2.94) in application to Eq. (2.93) the APE system could be manipulated into the form given by Eq. (2.24-2.25) in Section 2.2 but the definition of the right-hand side source terms will differ from Eq. (2.26-2.27) in the new formulation called the APE-4 system. (See below)

$$(\overline{\boldsymbol{u}} \cdot \nabla)\boldsymbol{u}' + (\boldsymbol{u}' \cdot \nabla)\overline{\boldsymbol{u}} \equiv \nabla(\overline{\boldsymbol{u}} \cdot \boldsymbol{u}') + \boldsymbol{\omega}' \times \overline{\boldsymbol{u}} + \overline{\boldsymbol{\omega}} \times \boldsymbol{u}' \tag{2.94}$$

In Section 2.2 the general formulation for APE system was presented. However, using the derivation method as outlined above, Ewert and Schröder [22] formulated the right-hand side source terms without the Poisson equation, calling the modified version the APE-4 system, where the source terms q_c and q_m in Eq. (2.26-2.27) read instead:

$$q_c = -\nabla \cdot (\boldsymbol{u}'\rho')' + \frac{\bar{\rho}}{c_p}\frac{\bar{D}s'}{Dt} \tag{2.95}$$

$$q_m = -(\boldsymbol{\omega} \times \boldsymbol{u})' + T'\nabla\bar{s} - s'\nabla\bar{T} - \left(\nabla\frac{(\boldsymbol{u}')^2}{2}\right)' + \left(\frac{\nabla\cdot\bar{\bar{\tau}}}{\rho}\right)' \tag{2.96}$$

In this form it is much easier to provide the source input, where non-linear and entropy terms can be ignored due to being of minor importance in vortex sound problems and the remaining dominant source term is simply the Lamb vector. Therefore, the governing APE equations can be re-written as following:

$$\frac{\partial p'}{\partial t} + \nabla \cdot (\bar{c}^2\bar{\rho}\boldsymbol{u}' + p'\bar{\boldsymbol{u}}) = 0 \tag{2.97}$$

$$\frac{\partial \boldsymbol{u}'}{\partial t} + \nabla \cdot (\bar{\boldsymbol{u}} \cdot \boldsymbol{u}') + \nabla\left(\frac{p'}{\bar{\rho}}\right) = \boldsymbol{Q} \tag{2.98}$$

where $\boldsymbol{Q}$ is the effective acoustic source vector. In practice, time averaged quantities, namely pressure, density and velocity fields could be obtained from a separate calculation such as a RANS simulation and mapped to an acoustic grid, where the wave propagation takes place. Subsequently, the acoustic source vector $\boldsymbol{Q}$ is calculated and provided to the system of equations, Eq. (2.97-2.98), at every time step of the simulation. The acoustic sources are defined following the vortex sound theory model from [57] specifying the Lamb vector which is established as the dominant source, expressed through the following three terms:

$$\boldsymbol{Q} = -(\boldsymbol{\omega} \times \boldsymbol{u})' = \underset{\textit{Term I}}{-\{\boldsymbol{\omega}_0 \times \boldsymbol{u}'\}} \underset{\textit{Term II}}{-\{\boldsymbol{\omega}' \times \boldsymbol{u}_0\}} \underset{\textit{Term III}}{-\{\boldsymbol{\omega}' \times \boldsymbol{u}'\}} \tag{2.99}$$

In Eq. (2.99), $\boldsymbol{\omega}_0$ and $\boldsymbol{\omega}'$ represent the mean flow vorticity vector and its fluctuation, respectively. The vorticity fields can be defined from the mean flow and fluctuating velocity component through the standard relationships, e.g. $\boldsymbol{\omega}' = \nabla \times \boldsymbol{u}'$. The first two terms in Eq. (2.99) represent linear sources with respect to velocity and vorticity fluctuations, later referred to $\boldsymbol{\omega}_0 \times \boldsymbol{u}'$ part as term I and to $\boldsymbol{\omega}' \times \boldsymbol{u}_0$ part as term II, and the third one is quadratic in terms of the fluctuations. The third non-linear part $\boldsymbol{\omega}' \times \boldsymbol{u}'$ of the vortex source in Eq. (2.99) is thought to be smaller than the first two terms for low Mach number aerofoil flows at moderate angles of attack and by assumption is neglected. As discussed in [57] it is often the second, linear vorticity fluctuation term, $\boldsymbol{\omega}' \times \boldsymbol{u}_0$ included while the rest of the sources are ignored. In the present work, all three source terms of Eq. (2.99) will be retained to verify their relative importance for the test cases considered.

In accordance with the original FRPM model, where various source descriptions could be implemented [57], the underlying part of the fluctuating solution field in Eq. (2.99) is obtained from synthetic turbulence generated using the method discussed in Chapter 3.

2.5 Numerical methods for CAA

This section presents a review on numerical methods for solving fluid dynamics and acoustics equations. The scope of this work includes solving APEs with the Finite Element (FE) method using Galerkin elements discussed in Section 2.5.1, finite difference / volume methods are employed for implementing the CABARET scheme in the framework of MILES presented in Section 2.5.2. Since the scope covers a variety of numerical methods the key conceptual properties shall be briefly reviewed first. According to the basic terminology, finite difference methods evolve in time the point-values of the solution whereas finite volume numerical methods evolve in time the cell averages of the solution. On the other hand, in finite element Discontinuous Galerkin (DG) methods an exact solution is approximated through polynomials which are specified as an expansion (or sometimes referred to as a projection) with respect to the bases functions. In other words, DG methods evolve in time the degrees of freedom of the solution, i.e. the time evolution of expansion coefficients with respect to the bases functions is determined for the entire polynomial. Various time marching methods applied in DG deserve particular attention, including a single time-step evolution ADER scheme [82] used in this work which is high-order accurate in both space and time. In addition, this work employs commercial software as a credible tool for RANS simulations. All in all this section is designed to provide the reader with the knowledge of a link between theoretical concepts reviewed earlier and their numerical realisation for CAA applications.

2.5.1 Finite Element Discontinuous Galerkin method

CAA methods used for solving the wave propagation in space and time must exceed the accuracy of conventional second order CFD methods, primarily because of geometrical complexity or issues associated with the solution efficiency. These qualities are particularly desirable in presence of some non-linearity which occurs, for example, in the presence of shock waves. Furthermore, for aero-acoustic applications where fine details of the solution are important using high-order methods can be advantageous due to the ability of using fewer elements in the far-field and also, using automated p-refinement for the smallest frequency of interest is beneficial not only for calculation efficiency but also, from mesh-generation viewpoint. Major development of a DG method was undertaken in the works by Cockburn, Shu *et al.* [108] [109] [110] In this work FE-DG method [21] is used in the framework of Altus solver for acoustic wave propagation in the time domain. First, consider the FE formulation for PDEs written in the conservative form:

$$\frac{\partial \boldsymbol{U}}{\partial t} + \nabla \cdot \boldsymbol{F}(\boldsymbol{U}) = 0 \qquad x \in \Omega \subset \mathbb{R}^d \tag{2.100}$$

In the above equation, $\boldsymbol{U}$ is the vector of conserved quantities, while $\boldsymbol{F}(\boldsymbol{U})$ is a non-linear flux tensor that depends on the state $\boldsymbol{U}$. For example, the net flux through an element (which represents a control volume) will cause a change in a conserved quantity. For hyperbolic PDEs the flux matrix must have real roots and the system such as given by Eq. (2.100) in the conservative form can be solved through conservative numerical schemes. [111] If the non-conservative form is used instead the solution follows a different approach as for the so-called path-conservative numerical schemes which are based on the theory proposed by Dal Maso *et al.* [112] but such schemes are not considered in this work.

The weak form solution of the PDEs (specified in the conservative form) is the integral over the global domain $\Omega \in (-\infty, +\infty)$ multiplied by any continuously differentiable test function, ϕ of compact support[3] and integrated in time, $t \in [0, \infty)$.

$$\int_0^\infty \int_{-\infty}^\infty \left(\phi \frac{\partial \boldsymbol{U}}{\partial t} + \phi \nabla \boldsymbol{F}\right) d\Omega dt = 0 \tag{2.101}$$

Integration by parts and using the property of the compact support where the test function vanishes in the limit of spatial and temporal infinity leads to the following weak formulation:

$$\int_0^\infty \int_{-\infty}^\infty \left(\boldsymbol{U} \frac{\partial \phi}{\partial t} + \boldsymbol{F} \nabla \phi\right) d\Omega dt = -\int_{-\infty}^\infty \phi(\Omega, 0) \boldsymbol{U}(\Omega, 0) d\Omega \tag{2.102}$$

The Discontinuous Galerkin method is based on a weak formulation Eq. (2.102) where a function $\boldsymbol{U}$ is called a weak solution of the conservative equation for all functions ϕ.

2.5.1.1 Discontinuous Galerkin discretisation

In DG the global computational domain Ω is split into N elements where the local solution is defined for each individual element l_i.

$$\Omega = \bigcup_{i=1}^{N} l_i \tag{2.103}$$

In Eq. (2.103) the index i ranges from 1 to the total number of elements N and similar to a FE approach the global solution is the sum of the piecewise polynomials. However, in DG the continuity of polynomial functions is not enforced between elements and thus, it usually requires the solution of a Riemann problem for determining the flux between elements. Following the weak solution procedure, applying the divergence theorem and integration by parts with integration being performed over an individual element l_i, the DG formulation reads:

$$\int_{l_i} \frac{\partial \boldsymbol{U}}{\partial t} \phi d\boldsymbol{x} + \int_{\partial l_i} [\boldsymbol{F}(\boldsymbol{U}) \cdot \boldsymbol{n}] \phi \, dS - \int_{l_i} \boldsymbol{F}(\boldsymbol{U}) \nabla \phi \, d\boldsymbol{x} = 0 \tag{2.104}$$

In the above equation, the second term is a surface integral whose solution can be best explained using a one-dimensional example where it would simply read:

$$\int_{\partial l_i} [\boldsymbol{F}(\boldsymbol{U}) \cdot \boldsymbol{n}] \phi \, dS = [\boldsymbol{F}(\boldsymbol{U}) \phi] \Big|_{x_L}^{x_R} \tag{2.105}$$

[3] The function will vanish approaching limits of the domain, $\phi(\boldsymbol{x}, t = \infty) = 0 = \phi(+\infty, t) = \phi(-\infty, t)$;

In Eq. (2.105) x_L and x_R are left and right states with respect to the one-dimensional element l_i. Since the end points of neighbouring elements are coincident, for example, the local solution at x_L for the element l_i would also correspond to the solution at x_R for the element l_{i-1} and therefore, the solution at this point is *multiply* defined. By conservation, the flux between elements must be equal:

$$-\boldsymbol{F}_{l_i-1}\{\boldsymbol{U}(x_R)\} = \boldsymbol{F}_{l_i}\{\boldsymbol{U}(x_L)\} \tag{2.106}$$

At this point we may refer to a FV approach where some flux function, $\widetilde{\boldsymbol{F}}(\boldsymbol{U})$, which is an approximation to the flux, permits communication between elements and thus, allowing to recover the global solution. The choice of the flux function is problem specific and providing that characteristics of the flux is known the numerical flux function could be crafted into the solution to reflect the physicality of the system. There are a variety of Riemann solvers available for determining the approximation to a numerical flux on the element's surface such as Lax-Friedrichs [113], Roe [114], Engquist-Osher, Harten-Lax-van Leer (HLL) etc. Also, the Godunov's flux method [115] attempts to analytically solve a Riemann problem, describing several flux cases for advection, shock and expansion wave treatment. The Godunov scheme is a simple treatment which for linear advection equation is identical to the standard upwind scheme that is known to yield a physical solution.

There are two volume integrals $|l_i| = \int_{l_i} d\boldsymbol{x}$ in Eq. (2.104) requiring the solution approximation within the element l_i to compute the integral of the solution based on a discrete formulation. Assume, that the solution approximation $\widetilde{\boldsymbol{U}}(x)$ belongs to a finite vector space $\widetilde{\boldsymbol{U}} \in V_h$ and is represented within each cell by piecewise polynomials of the order M, such that:

$$\widetilde{\boldsymbol{U}}_h(\boldsymbol{x}, t^n) = \sum_{k=0}^{M} \widetilde{\boldsymbol{U}}_k^n \, \psi_k(\boldsymbol{x}) \qquad\qquad x \in l_i \tag{2.107}$$

where $\psi_k(\boldsymbol{x})$ is a spatial basis vector function, $\widetilde{\boldsymbol{U}}_h$ is referred to as the discrete representation of the solution and the coefficients $\widetilde{\boldsymbol{U}}_k^n$ are the degrees of freedom. For simplicity at first it can be assumed that the vector space V_h contains polynomials of order $M = 1$ and from the definition Eq. (2.107) there must be two basis functions. One can think of these as two linear ramp functions (see Figure 5) specified for a given one-dimensional element l_i such that the sum of two bases at any point inside the element is equal to 1, following the partition of unity concept.

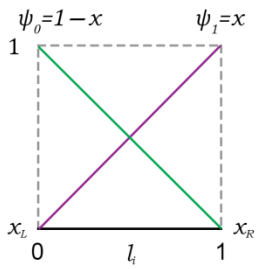

Figure 5 – Sketch showing two ramp functions for a linear element l_i within the approximation space V_h defined from 0 at x_L to 1 at x_R.

In FE-DG the space for the weighting functions is chosen such that it corresponds to the approximation space $\phi \in V_h$, meaning that in the above example for $M = 1$ weighting functions would be ramp functions too, $\phi_0(\boldsymbol{x}) = \psi_0(\boldsymbol{x})$ and $\phi_1(\boldsymbol{x}) = \psi_1(\boldsymbol{x})$. In order to solve for approximation to Eq. (2.104) the weak form solution must be satisfied for each weighting function as will be shown in Section 2.5.1.2 when assembling a semi-discrete system.

In practice, using the first order polynomials at most is not very efficient and ultimately, with DG methods, most benefits come when exploiting high-order properties (where M is typically $4 \sim 7$). [116] From Godunov's order theorem [115] it follows that the linearity of the numerical scheme has to be sacrificed in favour of non-oscillatory properties for high-order schemes. Therefore, all DG schemes which are of the high-order of approximation are non-linear. In principle, any polynomial function can be chosen to represent the approximation but in practice some choices of polynomial bases are better than others and several fundamental classes exist, namely modal (or hierarchical) and nodal. [117] The hierarchical bases consist of a set of $M + 1$ polynomials with degree ranging from zero (a constant) to a maximum degree M where Legendre polynomials may represent such a set. (See Figure 6*a*) On the other hand, the nodal bases all consist of polynomials of degree M with a total number of functions also being $M + 1$. [118] In the nodal approach the "nodal coordinates" are computed in the reference space forming $M + 1$ Lagrange interpolation polynomials that pass through $M + 1$ Gauss-Legendre quadrature nodes. Importantly, nodal bases functions are constructed to satisfy the "Kronecker delta" condition, i.e. the first polynomial function may have an approximation value at the first node while being zero at all other control nodes within the reference space. In contrast, other polynomial functions would coincide at zero at the first node and then one of the functions will appear to have some value in the second node and so on. (See Figure 6*b*) The shape of bases is determined by the degree M.

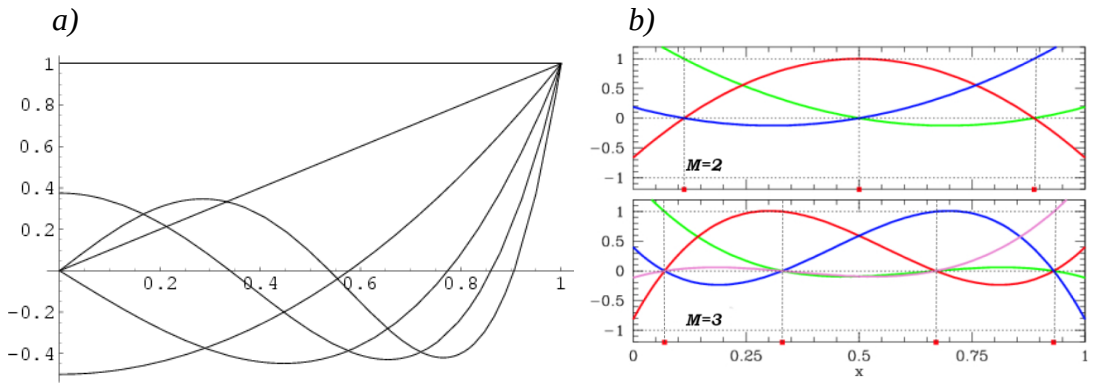

Figure 6 – Legendre polynomials (modal / hierarchical) (*a*) and Lagrange $M = 2$ quadratic and $M = 3$ cubic polynomials (nodal) (*b*)

In computational practice the Lagrange interpolation polynomials are evaluated via the solution of linear systems with coefficients arranged in a matrix form.

2.5.1.2 Towards assembling of a semi-discrete system

The governing DG equation (Eq. (2.104)) can be re-written using the discrete representation of solution and flux vectors discussed above and the property of Eq. (2.105) where a one-dimensional system can be assembled as following:

$$\underbrace{\int_{l_i} \frac{\partial \widetilde{\boldsymbol{U}}_h(x,t^n)}{\partial t} \phi_k(x) dx}_{\textit{Mass matrix}} + \underbrace{\left[\widetilde{\boldsymbol{F}}(\widetilde{\boldsymbol{U}}(x,t^n))\phi_k(x)\right]\Big|_{x_L}^{x_R}}_{\textit{Numerical flux}} - \underbrace{\int_{l_i} \widetilde{\boldsymbol{F}}(\widetilde{\boldsymbol{U}}_h(x,t^n))\nabla\phi_k(x) dx}_{\textit{Stiffness matrix}} = 0 \quad (2.108)$$

where $x \in l_i$, the solution approximation $\widetilde{\boldsymbol{U}}_h(x,t^n)$ is given by Eq. (2.107) and the weighting functions $\phi_k(x)$ can be assumed to be the ramp functions for $M = 1$, which is the appropriate choice for conceptual derivation. First, substituting the solution approximation Eq. (2.107) into the Mass matrix gives:

$$\int_{l_i} \frac{\partial \widetilde{\boldsymbol{U}}_h(x,t^n)}{\partial t} \phi_k(x) dx = \sum_{k=0}^{M} \frac{\partial}{\partial t} \widetilde{\boldsymbol{U}}_k^n \int_{l_i} \psi_k(x)\phi_k(x)\, dx \quad (2.109)$$

Note that in the above expression the coefficients $\widetilde{\boldsymbol{U}}_k^n$ are functions of time only and the integral over the element l_i could be readily pre-computed containing bases and weights which are both spatial functions. If the vector space is chosen as prescribed in Figure 5 the bases $\psi_0 = 1 - x$; and $\psi_1 = x$; when substituted in Eq. (2.109) with integration limits from 0 to 1 result in the following mass matrix:

$$\int_{l_i} \psi_k(x)\phi_k(x)\Big|_0^1 \Rightarrow \begin{bmatrix} \psi_0\phi_0 & \psi_1\phi_0 \\ \psi_0\phi_1 & \psi_1\phi_1 \end{bmatrix}\Big|_0^1 = \begin{bmatrix} 1/3 & 1/6 \\ 1/6 & 1/3 \end{bmatrix} = \mathbb{M}_k \quad (2.110)$$

The solution of the *Numerical flux* term which provides coupling between elements could be difficult to obtain due to the flux being multiply defined at the element's boundary leading to a Riemann problem. If the wave is propagating from left to right in a one-dimensional incompressible case with a constant velocity c, one can simply choose the 'upwind' flux as an approximation to $\widetilde{\boldsymbol{F}}$, such that:

$$\widetilde{\boldsymbol{F}}\left(\widetilde{\boldsymbol{U}}^+, \widetilde{\boldsymbol{U}}^-\right) = c\widetilde{\boldsymbol{U}}^- \quad \text{if} \quad c > 0; \quad (2.111)$$

where the conserved quantity $c\widetilde{\boldsymbol{U}}^-$ moves to the right and for the element l_i it would represent the flux at the boundary x_L being equated to the incoming (or 'upwind') flux. In the DG formulation there is no enforced continuity for the fluxes at the interface, i.e. $\widetilde{\boldsymbol{F}}_{l_i}(x_L) \neq \widetilde{\boldsymbol{F}}_{l_{i-1}}(x_R)$ by default. In this case, using the upwind flux in Eq. (2.108) results in the following approximation:

$$\left[\widetilde{\boldsymbol{F}}(\widetilde{\boldsymbol{U}}(x,t^n))\phi_k(x)\right]\Big|_{x_L}^{x_R} = c\widetilde{\boldsymbol{U}}_{l_i}(x_R)\phi_k(x_R) - c\widetilde{\boldsymbol{U}}_{l_{i-1}}(x_R)\phi_k(x_L) \quad (2.112)$$

Note the $\widetilde{\boldsymbol{U}}_{l_{i-1}}(x_R)$ term in the above equation coming from the right state of the l_{i-1} cell. Moreover, from Figure 5 it is possible to deduct that $\phi_0(x_R) = 0$ and similarly, $\phi_1(x_L) = 0$, resulting in the following flux matrix:

$$\widetilde{\boldsymbol{F}} = \begin{bmatrix} c\widetilde{\boldsymbol{U}}_{l_{i-1}}(x_R) \\ c\widetilde{\boldsymbol{U}}_{l_i}(x_R) \end{bmatrix} = c \begin{bmatrix} \widetilde{\boldsymbol{U}}_{l_{i-1}}(x_R) \\ \widetilde{\boldsymbol{U}}_{l_i}(x_R) \end{bmatrix} \tag{2.113}$$

The stiffness matrix in Eq. (2.108) also contains a numerical flux yet there is no Riemann solver involved since the approximation is well defined everywhere within the element. Similarly to the Mass matrix the final term can be pre-computed by substituting the approximate solution and bases which were already evaluated in Section 2.5.1.1 into the stiffness term.

$$\int_{l_i} \widetilde{\boldsymbol{F}}(\widetilde{\boldsymbol{U}}_h(x,t^n))\nabla\,\phi_k(x)dx = \sum_{k=0}^{M} c\widetilde{\boldsymbol{U}}_k^n \int_{l_i} \psi_k(x)\nabla\phi_k(x)\,dx \tag{2.114}$$

Assembling the stiffness matrix for the specified vector space gives:

$$\int_{l_i} \psi_k(x)\nabla\phi_k(x)\,\Big|_0^1 \Rightarrow \begin{bmatrix} \psi_0\nabla\phi_0 & \psi_1\nabla\phi_0 \\ \psi_0\nabla\phi_1 & \psi_1\nabla\phi_1 \end{bmatrix}\Big|_0^1 = \begin{bmatrix} -1/2 & -1/2 \\ 1/2 & 1/2 \end{bmatrix} = \mathbb{K} \tag{2.115}$$

Using Eq. (2.110), Eq. (2.113) and Eq. (2.115) it is now possible to assemble a semi-discrete system which in the matrix form reads:

$$\mathbb{M}_k\widetilde{\boldsymbol{U}}_k' + \widetilde{\boldsymbol{F}} - c\mathbb{K}\widetilde{\boldsymbol{U}}_k = 0 \tag{2.116}$$

where prime denotes a time derivative. For each time step there would be a number of coefficients starting from $\widetilde{\boldsymbol{U}}_k^0$ initial conditions. For example, if the solution to a sinusoidal function has to be advanced in time using the DG method, for the initial conditions all coefficients will be spatially pre-defined with a reference to sinusoidal function. Then the time rate of change $\widetilde{\boldsymbol{U}}_k'$ of the solution has to be evaluated numerically. In the introduction to Section 2.5 it was mentioned that the DG method advances the degrees of freedom (or coefficients) in time and after assembling a semi-discrete system Eq. (2.116) the basic DG mechanism could be summarised as follows:

$$\widetilde{\boldsymbol{U}}_k' = \left[c\mathbb{K}\widetilde{\boldsymbol{U}}_k - \widetilde{\boldsymbol{F}}\right]\mathbb{M}^{-1} \tag{2.117}$$

The solution to Eq. (2.117) requires the Mass matrix to be inverted which could be easily obtained using hand calculations for something as simple as a 2x2 symmetric matrix Eq. (2.110) which is obtained for the first order polynomials. However, using higher degree of approximation yields a higher number of operations. The R.H.S. of Eq. (2.117) could be entirely pre-computed using the initial conditions for $\widetilde{\boldsymbol{U}}_k$ coefficients and in the final step the semi-discrete system needs to be discretised in time which is the subject of the next section.

2.5.1.3 Time marching methods

The solution $\widetilde{\boldsymbol{U}}^n$ is known at a time level t_n and a prediction has to be made for evaluating the solution at t_{n+1}. In the simplest case the time rate of change $\widetilde{\boldsymbol{U}}'$ can be directly used to make such a prediction which results in a 'forward Euler' explicit scheme:

$$\widetilde{\boldsymbol{U}}_k^{n+1} = \widetilde{\boldsymbol{U}}_k^n + \widetilde{\boldsymbol{U}}'^{(n)}\Delta t \tag{2.118}$$

where Δt is the time step. Eq. (2.118) can be used together with a semi-discrete system Eq. (2.117) for implementing a one-dimensional incompressible DG solver. Also, non-linear DG schemes are known to be L_2 stable which proof can be found in the literature [113], thus, positively influencing the robustness of a DG method. However, the L_2 stability does not guarantee the absence of oscillations and neither the absence of excessive numerical dissipation originating due to a flux jump. For a more advanced implementation of a high-order DG solver better temporal accuracy than the 'forward Euler' is required and in that instance a multi-stage time-marching scheme is commonly adopted for solving coupled differential equations such as Runge-Kutta (RKDG) schemes. [119] Since DG is a variable order method the selection of the most suitable time marching scheme in terms of accuracy and computational performance will depend on implementation specifics. Consider cubic polynomials $M = 3$ representation of $\boldsymbol{U}(\xi, t)$ where ξ is the coordinate of the local domain. Then using the modal bases to represent the discretisation one may get the following expression:

$$\boldsymbol{U}(\xi, t) = \widetilde{\boldsymbol{U}}_0(t)\phi_0(\xi) + \widetilde{\boldsymbol{U}}_1(t)\phi_1(\xi) + \widetilde{\boldsymbol{U}}_2(t)\phi_2(\xi) + \widetilde{\boldsymbol{U}}_3(t)\phi_3(\xi) \qquad (2.119)$$

When the approximation of the solution Eq. (2.119) is substituted into the governing DG equation (Eq. (2.108)) it results in a system of 4 coupled ordinary differential equations for each of the degrees of freedom (in a modal approach) which have to be solved simultaneously since each degree of freedom is implied in the computation of the non-linear flux term. In RKDG discretisation the first term in Eq. (2.119), namely $\widetilde{\boldsymbol{U}}_0(t)\phi_0(\xi)$, is evolved in time using a "finite-volume" procedure, since the expansion of a constant is simply a cell average, giving the scheme an "upwind" property. The fluxes at the interface $\widetilde{\boldsymbol{F}}(0)$ and $\widetilde{\boldsymbol{F}}(1)$ can be obtained by solving a Riemann problem which are subsequently weighted by the bases in three other equations. Hence, the higher order equations could be thought of as performing the error correction.

In CAA an explicit RKDG time discretisation method is commonly used so its various formulations are not discussed in this work. However, one thing to note would be that with RKDG there is a decrease in efficiency when the formal order of accuracy is higher than four, leading to an effect which is known as the "Butcher's barrier" after John C. Butcher [120] where the number of intermediate stages becomes too large in comparison to any benefits gained by the increased order of accuracy.

In order to improve the time integration techniques the ADER (Arbitrary DERivative) approach has been proposed by Toro *et al.* [121] Over the last decade numerical schemes based on ADER have become attractive due to being significantly more efficient in comparison to Runge-Kutta for very high order (5-7) DG schemes [122] and also, ADER is almost a factor of two faster for non-stiff problems[4]. [123] Such computational efficiency achieved by the ADER approach is mainly due to its single time-step evolution for a DG scheme which still remains high-order accurate both in space and time. The complexity of

[4] Stiffness is the phenomenon attributed to the system of differential equations which may include terms describing physical processes which occur on different time scales and thus, restricting the time integration to excessively small steps over an interval where the analytical solution is expected to exhibit smoothness.

this approach lies in the treatment of the generalised Riemann problem. Hence, there is a difference between the original concept of Toro *et al.* [121] and its modified version (Titarev and Toro [82]) which uses the *local time-space DG predictor*. Since the ADER concept and a DG method as a whole very much rely on the accurate flux reconstruction we shall begin by looking into a high order generalised Riemann problem and exploring some computationally feasible options. By definition of a generalised Riemann problem, initial data between interfaces of adjacent cells are no longer piecewise constant but piecewise polynomial. (See Figure 7)

$$\boldsymbol{U}(x,0)=\begin{cases}\boldsymbol{U}(x_L)=\boldsymbol{q}_L(x) & \text{if} \quad x<0\\ \boldsymbol{U}(x_R)=\boldsymbol{q}_R(x) & \text{if} \quad x>0\end{cases}; \tag{2.120}$$

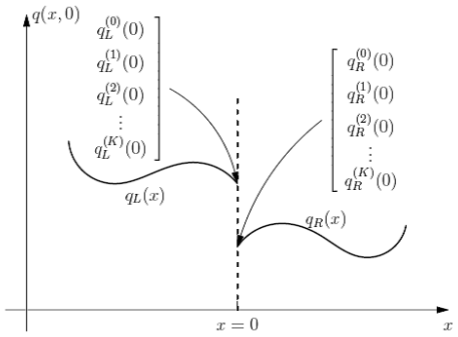

Figure 7 – Schematic initial conditions for a generalised Riemann problem for a component $q(x,t)$. The data are smooth functions away from the interface located at $x=0$.

The standard procedure for solving such Riemann problem is to apply the Taylor expansion in time at the interface so that the leading term can be solved using the standard Riemann problem approach and higher-order derivatives using the Cauchy-Kovalewski procedure. In short, the approximate solution $\boldsymbol{U}(x_0,\tau)$ can be evaluated as follows, first beginning with the Taylor expansion.

$$\boldsymbol{U}(x_0,\tau)=\boldsymbol{U}(x_0,0^+)+\sum_{k=1}^{M}\frac{\tau^k}{k!}\partial_t^{(k)}\boldsymbol{U}(x_0,0^+) \tag{2.121}$$

where $\partial_t^{(k)}\boldsymbol{U}(x,t)=\frac{\partial^k}{\partial t^k}\boldsymbol{U}(x,t)$; and $0^+\equiv\lim_{\tau\to 0^+}\tau$. In Eq. (2.121) the leading term represents the solution to a linear Riemann problem with constant left and right states and higher-order terms are represented with a set of space-time derivatives:

$$\partial_t\boldsymbol{U}=-\left(\frac{\partial\boldsymbol{F}}{\partial\boldsymbol{U}}\right)\partial_x\boldsymbol{U} \tag{2.122}$$

$$\partial_{tx}\boldsymbol{U}=-\left(\frac{\partial^2\boldsymbol{F}}{\partial\boldsymbol{U}^2}\right)(\partial_x\boldsymbol{U})^2-\left(\frac{\partial\boldsymbol{F}}{\partial\boldsymbol{U}}\right)\partial_{xx}\boldsymbol{U} \tag{2.123}$$

$$\partial_t^2\boldsymbol{U}=-\left(\frac{\partial^2\boldsymbol{F}}{\partial\boldsymbol{U}^2}\right)\partial_x\boldsymbol{U}\partial_t\boldsymbol{U}-\left(\frac{\partial\boldsymbol{F}}{\partial\boldsymbol{U}}\right)\partial_{xt}\boldsymbol{U} \tag{2.124}$$

There are more equations with progressive order. Time derivatives may be represented by Eq. (2.122) and the spatial derivatives then have to be obtained via solving a sequence of M linear Riemann problems for the equations:

$$\partial_t\left[\partial_x^{(k)}\boldsymbol{U}(x_0,0)\right]+\widetilde{\boldsymbol{A}}\partial_x\left[\partial_x^{(k)}\boldsymbol{U}(x_0,0)\right]=0 \tag{2.125}$$

where $\widetilde{\boldsymbol{A}}=\boldsymbol{A}[\boldsymbol{U}(x_0,0)]$; is the constant matrix computed in the leading state and $k=1\dots M$, where M is the degree of the polynomial as stated previously. For a linear system where the coefficients of the matrix $\widetilde{\boldsymbol{A}}$ are constants for all analytic derivatives the matrix can be evaluated only once. As a result of the above procedure, the solution approximation can be established for a generalised Riemann problem, which is represented by a temporal evolution of $\boldsymbol{U}$ Eq. (2.121) at the interface.

The philosophy of ADER is to use the above result in a single time step evolution scheme so that the DG discretisation is integrated in time directly. [124]

$$\left(\int_{T_i}\psi_l\psi_k\,dx\right)\left(\widetilde{\boldsymbol{U}}_l^{n+1}-\widetilde{\boldsymbol{U}}_l^{n}\right)+\int_{t_n}^{t_{n+1}}\int_{\partial l_i}\psi_k\,\boldsymbol{F}\left(\boldsymbol{U}_h\right)\cdot\boldsymbol{n}\,dSdt-\int_{t_n}^{t_{n+1}}\int_{l_i}\nabla\psi_k\,\boldsymbol{F}\left(\boldsymbol{U}_h\right)dxdt=0 \tag{2.126}$$

In Eq. (2.126) the main ingredients of the governing equation, namely the Mass and Stiffness matrices and the fluxes in the form of a surface integral are retained but with the incorporated time integration. This procedure may get very complicated depending on the system of PDEs. Aero-acoustic problems typically involve the source terms and the system of equations drawn in place of Eq. (2.122-2.124) becomes virtually impossible to solve beyond a simple analytic problem. Thus, for a realistic case to be solved numerically an alternative to the Cauchy-Kovalewski procedure and the Taylor expansion in time is required which involves performing an operation locally for each cell, taking the DG polynomial $\boldsymbol{U}_h$ as input and the output becomes its evolution in time. This operation involves the local "predictor" which determines the evolved solution approximation within each cell.

In Section 2.5.1.1 it was necessary to perform the spatial expansion of the solution with the polynomial bases following the standard Galerkin procedure and now using the ADER approach we shall include the temporal expansion at once.

$$\boldsymbol{U}_h(x,y,z,t^n)\rightarrow\boldsymbol{q}_h(\boldsymbol{\xi},\tau)=\phi_{\boldsymbol{p}}(\boldsymbol{\xi},\tau)\widetilde{\boldsymbol{q}}_{\boldsymbol{p}} \tag{2.127}$$

In the above equation, $\boldsymbol{U}_h$ is the conserved quantity, $\boldsymbol{q}_h$ is its evolution in time known as the sought polynomial and the terms $\widetilde{\boldsymbol{q}}_{\boldsymbol{p}}$ are the space-time degrees of freedom (the unknowns), where the bases are given by a product.

$$\phi_{\boldsymbol{p}}(\boldsymbol{\xi},\tau)=\psi_p(\xi)\psi_q(\eta)\psi_r(\zeta)\psi_s(\tau) \tag{2.128}$$

The local predictor step is best illustrated starting with a PDE which includes the source term $\boldsymbol{S}$ as often will be the case in acoustics in the reference coordinates.

$$\frac{\partial\boldsymbol{U}}{\partial\tau}+\nabla\cdot\boldsymbol{F}^*(\boldsymbol{U})=\boldsymbol{S}^* \tag{2.129}$$

where the "star" flux and source terms include the transformation Jacobian from physical into the reference domain. As a next step Eq. (2.129) is multiplied by the space-time test functions $\boldsymbol{\phi_p}$ and integrated both in time and in space over the control volume. Since spatio-temporal integration remains local to each cell there is no Riemann solver involved at this stage, which absence simplifies this procedure significantly.

$$\int\int\int\int \boldsymbol{\phi_p}\left(\frac{\partial \boldsymbol{U}}{\partial \tau}+\frac{\partial \boldsymbol{F}^*}{\partial \boldsymbol{\xi}}-\boldsymbol{S}^*\right)\partial\xi\partial\eta\partial\zeta\partial\tau=0 \tag{2.130}$$

When performing the integration by parts the fluxes and the sources can be expanded over the same bases as in Eq. (2.127). It is worth mentioning that by using the nodal shape functions there is an apparent advantage as it allows expressing the physical fluxes at the nodes through the degrees of freedom $\widetilde{\boldsymbol{q}}_{\boldsymbol{p}}$, such as $\widetilde{\boldsymbol{F}}_{\boldsymbol{p}}^{*}=\boldsymbol{F}^{*}\left(\widetilde{\boldsymbol{q}}_{\boldsymbol{p}}\right)$ and similarly for the sources $\widetilde{\boldsymbol{S}}_{\boldsymbol{p}}^{*}=\boldsymbol{S}^{*}\left(\widetilde{\boldsymbol{q}}_{\boldsymbol{p}}\right)$. Then, the system of matrices is pre-computed at the initial conditions for the unknown coefficients $\widetilde{\boldsymbol{q}}_{\boldsymbol{p}}$. The system of equation has to be solved iteratively up to a desired tolerance which results in the approximate solution to Eq. (2.127). Now that the space-time predictor $\boldsymbol{q}_h(\boldsymbol{\xi},\tau)$ is known for each cell it can be used in the governing equation:

$$\left(\int_{l_i}\psi_l\psi_k\,dx\right)\left(\widetilde{\boldsymbol{U}}_l^{n+1}-\widetilde{\boldsymbol{U}}_l^{n}\right)+\int_{t_n}^{t_{n+1}}\int_{\partial l_i}\psi_k\,\widetilde{\boldsymbol{F}}_{\mathrm{RP}}\left(\boldsymbol{q}_h^{-},\boldsymbol{q}_h^{+}\right)\cdot\boldsymbol{n}\,dSdt-\int_{t_n}^{t_{n+1}}\int_{l_i}\nabla\psi_k\,\boldsymbol{F}\left(\boldsymbol{q}_h\right)dxdt=0 \tag{2.131}$$

where $\boldsymbol{q}_h^{-}$ and $\boldsymbol{q}_h^{+}$ are the left and right states of the Riemann problem $\widetilde{\boldsymbol{F}}_{\mathrm{RP}}$ respectively, which evaluation completes the coupling between elements, allowing to recover the global solution. In ADER terminology this final step is referred to as the corrector step. [125]

2.5.1.4 DG methods for aero-acoustics

This subsection provides a brief review of the DG method which closely resembles the solution to the Acoustic Perturbation Equations (APE) in the Altus code used in this work with the source term $\boldsymbol{S}$ appearing on the right-hand side. The equations are solved in a general conservation form:

$$\frac{\partial \boldsymbol{U}(\boldsymbol{x},t)}{\partial t}+\frac{\partial F_j}{\partial x_j}=\boldsymbol{S}(\boldsymbol{x},t) \tag{2.132}$$

where $\boldsymbol{U}$ and F_j are the corresponding solution and flux vectors, j=1,2,3, and Einstein summation over the repeated index is implied. For numerical computation with the DG scheme [21] [23], the flow solution, the flux vectors and the sources are expanded in terms of the finite-element basis functions $\psi_k(x_i)$, as discussed previously, e.g.:

$$\begin{aligned}\boldsymbol{U}(\boldsymbol{x},t)&=\sum_{k=0}^{M}\psi_k(\boldsymbol{\xi})\,\widetilde{\boldsymbol{U}}_k^{M}(\tau)=\psi_k(\boldsymbol{\xi})\widetilde{\boldsymbol{U}}_k^{M}(\tau)\qquad \boldsymbol{x}\to\boldsymbol{\xi}\in k_i\\ F_j(\boldsymbol{x},t)&=\sum_{k=0}^{M}\psi_k(\boldsymbol{\xi})\,\widetilde{F}_{j_k}(\tau)=\psi_k(\boldsymbol{\xi})\widetilde{F}_{j_k}^{M}(\tau)\\ \boldsymbol{S}(\boldsymbol{x},t)&=\sum_{k=0}^{M}\psi_k(\boldsymbol{\xi})\,\widetilde{\boldsymbol{S}}_k(\tau)=\psi_k(\boldsymbol{\xi})\widetilde{\boldsymbol{S}}_k^{M}(\tau)\end{aligned} \tag{2.133}$$

Following the standard weak solution procedure, the governing equations are multiplied by the test function ϕ_i, which are up to the 6th order of approximation in this work, integrated over the volume, applying integration by parts.

$$\int_V \phi_i \frac{\partial \boldsymbol{U}(x,t)}{\partial t} dV + \left\{ \int_V \frac{\partial \phi_i F_j}{\partial x_j} dV - \int_V F_j \frac{\partial \phi_i}{\partial x_j} dV \right\} = \int_V \phi_i \, \boldsymbol{S}(\boldsymbol{x}, t) dV \tag{2.134}$$

Furthermore, applying the divergence theorem to the first term in brackets and using Eq. (2.133) leads to a system of ordinary differential equations for unknown time amplitudes $\widetilde{\boldsymbol{U}}_k$

$$\mathbb{M}_k \frac{\partial \widetilde{\boldsymbol{U}}_k}{\partial t} + \int_\Gamma \phi_i \psi_k \widetilde{F}_{j_k} n_i dS - \int_V F_{j_k} \frac{\partial \phi_i}{\partial x_j} \psi_k dV = \int_V \phi_i \psi_k \widetilde{\boldsymbol{S}}_k dV \tag{2.135}$$

where the mass matrix is:

$$\mathbb{M}_k = \int_V \phi_i \psi_k \, dV \tag{2.136}$$

In the second term of Eq. (2.135), n_i is an outward pointing surface element normal and $\widetilde{F}_{j_k} n_i$ is an approximation to a Riemann flux which solution depends on the element under consideration and on the neighbouring element. This term is referred to as the boundary integral and the only term involving the Riemann problem which provides a crucial solution coupling between elements as discussed in the previous section.

Due to linearity of the fluxes F_j with respect to the acoustic variable, the corresponding Jacobian matrix can be pre-computed using the Quadrature-Free method. [23] [124] In this formulation there is a fundamental restriction on the type of elements that are permitted, ensuring that in the reference coordinate system, the Jacobian matrix is not a function of space, $|\mathcal{J}| \neq |\mathcal{J}|(\xi, \eta, \zeta)$. The solution volume V is defined in terms of the local domain, which is partitioned into non-overlapping elements. Then, the Quadrature-Free concept is best illustrated on the flow quantity for which the solution has to be obtained. Consider the acoustic density variation in space and time, $\rho(\boldsymbol{x}, t) = \psi_j(\boldsymbol{\xi}) \rho_j(\tau)$ where a Jacobian is used for the transformation between the physical space and the reference domain.

$$\int_V \phi_i \psi_k \rho_k dV = \int_\xi \phi_i(\boldsymbol{\xi}) \psi_k(\boldsymbol{\xi}) d\xi |\mathcal{J}_n| \rho_k(\tau) \tag{2.137}$$

Essentially, the integration determined numerically via the integration over volume and then over all elements n is performed only once and stored, while the remaining part $|\mathcal{J}_n| \rho_k(\tau)$ is computed. The Jacobian $|\mathcal{J}_n|$ is different for every element yet in this case it appears outside the integral due to the property $|\mathcal{J}| \neq |\mathcal{J}|(\xi, \eta, \zeta)$ which leads to improved calculation efficiency. For better clarity it is possible to simplify the formulation further by using Eq. (2.136) knowing that for a given type of elements the mass matrix $\mathbb{M}_k$ would be the same, (i.e. one mass matrix is applicable to all prisms, another is applicable to all squares and so on). If we assume that in a particular calculation all elements are of the same type the temporal term can be re-written as $|\mathcal{J}_n| \mathbb{M}_k \widetilde{\boldsymbol{U}}_t$ where $\widetilde{\boldsymbol{U}}_t = \frac{\partial}{\partial t} \left[\widetilde{\boldsymbol{U}}_k \right]$.

Volume integral

The volume integral in the governing equation, Eq. (2.135), can be re-written as a matrix times a vector quantity and the system in a short representation without element and order notation reads:

$$\mathcal{J}\mathbb{M}\widetilde{\boldsymbol{U}}_t + \int_\Gamma \boldsymbol{\Phi}\mathcal{J}\boldsymbol{\mathcal{J}}^{-1}\tilde{F}^n dS - \mathbf{B}\cdot\boldsymbol{F} = \mathcal{J}\mathbb{M}\widetilde{\boldsymbol{S}} \tag{2.138}$$

where $\mathbf{B} = \left[\boldsymbol{b_{i,k}}\right]$ and $\boldsymbol{b_{i,k}} = \int_\Gamma(\nabla\phi_i)\psi_k d\Gamma$; $\boldsymbol{F} = \left[\tilde{F}_j\right]$ and $\tilde{F}_j = \mathcal{J}\boldsymbol{\mathcal{J}^{-1}}F_j$; $\boldsymbol{\Phi} = [\phi_i\psi_k]$. Note the vector matrices **B** and $\mathbb{M}$ which are constant for all elements can be pre-computed at the pre-processing stage and stored. The volume integral can be evaluated for each cell without solving a Riemann problem since there are no discontinuities present within the cell and the only remaining term which solution is required for determining the time evolution of $\widetilde{\boldsymbol{U}}_t$ in Eq. (2.138) is the boundary integral $\int_\Gamma \boldsymbol{\Phi}\mathcal{J}\boldsymbol{\mathcal{J}}^{-1}\tilde{F}^n dS$.

Boundary integral

For evaluation of the boundary integral all elements within the domain of interest are partitioned into segments where every segment is associated with the side of an element. Then, according to Eq. (2.138) the boundary integral can be represented as a multiplication of the flux vector with the corresponding matrix. The difficulty comes from $\tilde{F}^n$ being the function of the solution in elements adjacent to the boundary segment as discussed previously and each segment has its own local coordinate system. For that reason, firstly, the bases functions contained in $\boldsymbol{\Phi}$ must be translated into the coordinate system that is common to both elements which in practice is performed using an auxiliary matrix which is exactly specified for each edge and remains constant. Secondly, the approximate Riemann flux is computed in the edge coordinates and finally, the computed flux is projected onto the space using the expansion with a set of basis functions. The solution to a Riemann problem could be as simple as using the upwind flux as demonstrated in Section 2.5.1.2 for a simple scalar DG solver or it may involve quite complicated procedures containing a full set of wave speed estimates where an improved accuracy in flux reconstruction is necessary. In this work a high order DG method is employed for aero-acoustic wave propagation where a Roe solver [114] is used for evaluating the standard Riemann problem at the element's interfaces and thus, approximating $\mathcal{J}\boldsymbol{\mathcal{J}^{-1}}\tilde{F}^n dS$ term.

The FE-DG method is used in conjunction with the FRPM method described in details in Chapter 3 which provides the definition for the source vector $\boldsymbol{S}$. Altogether, these calculations are implemented in the framework of the Altus solver. Appendix B provides the outline of the CAA procedure starting from the calculation of the source terms and feeding them into APEs which are then evaluated on a mesh with the aid of FE-DG method using the ADER time marching scheme.

2.5.2 CABARET scheme for convection dominated flow modelling

This section presents the concept of the finite-difference / finite-volume CABARET scheme which has been primarily developed for solving convection dominated flow problems. The scope of applicability of the scheme includes simulating vortex and turbulent flow at high Re number which is of interest in this work. From all numerical schemes commonly adopted in CAA, the CABARET scheme's advantages include ease of implementation and improved solution accuracy in comparison to the conventional second order schemes. [126]

Following the motivation in searching of high-fidelity CFD/CAA methods as outlined in Chapter 1, the CABARET scheme with improved dissipation and dispersion properties deserves attention.

A one-dimensional linear advection equation is written down to illustrate the CABARET method's concept:

$$\frac{\partial u}{\partial t} + \frac{\partial F(u)}{\partial x} = 0 \tag{2.139}$$

$F(u) = c \cdot u;\ c = \text{const.} > 0$. A non-uniform finite difference grid is considered where $t_{n+1} - t_n = \tau_{n+1/2}$ and $x_{i+1} - x_i = h_{i+1/2}$ temporal and spatial discretisation respectively. It is assumed that all variables are known at the nth time level. Marching a half time step using the forward-time central-space approximation then yields:

$$\frac{U_{i+1/2}^{n+1/2} - U_{i+1/2}^{n}}{1/2\,\tau_{n+1/2}} + \frac{F(u_{i+1}^{n}) - F(u_i^{n})}{h_{i+1/2}} = 0 \tag{2.140}$$

Eq. (2.140) is constructed over a rectangular space-time stencil with central points both on the edges and in the middle of the stencil, allowing marching in half steps. (See Figure 8) The variables u_i^n are attributed to mesh nodes, while $U_{i+1/2}^{n+1/2}$ are calculated on the intermediate time level $t_{n+1/2}$ first, then, an upwind extrapolation to a new time level takes place, $\tilde{u}_{i+1}^{n+1} = 2 \cdot U_{i+1/2}^{n+1/2} - u_i^n$, where $u_{i+1}^{n+1} = \min\max(\tilde{u}_{i+1}^{n+1})$ Finally, Eq. (2.140) is followed by another half step using the backward-time central-space approximation:

$$\frac{U_{i+1/2}^{n+1} - U_{i+1/2}^{n+1/2}}{1/2\,\tau_{n+1/2}} + \frac{F(u_{i+1}^{n+1}) - F(u_i^{n+1})}{h_{i+1/2}} = 0 \tag{2.141}$$

The equations (2.140-2.141) are written in the form of predictor-corrector, making the CABARET scheme an explicit single-temporal-stage method which can be shown second order accurate even on non-uniform grids due to its compact one cell computational stencil. For Eq. (2.139) the scheme is conservative over a single cell control volume and stable under the Courant condition $0 \le c \cdot \tau/h \le 1$, and the scheme is exact when the Courant number is equal to 0, 0.5 and 1.

The CABARET stencil shown in Figure 8 has some similarities with the upwind Leapfrog (UL) scheme first proposed by Iserles [36]. For one dimensional linear advection equation

both schemes are the same and have good dispersion properties and zero numerical dissipation. However, the compact stencil of CABARET allows its effective extension to multiple dimensions in space and for non-linear flows.

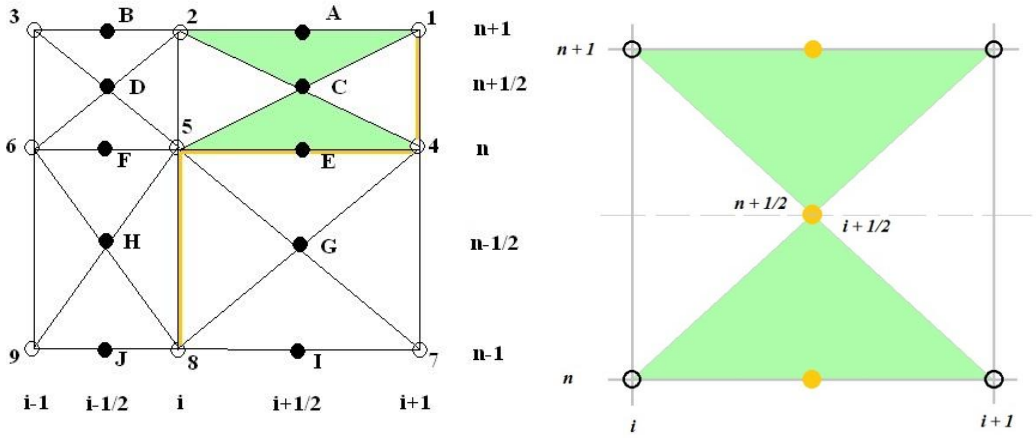

Figure 8 – CABARET spatio-temporal single cell compact numerical stencil in 1D

If the CABARET scheme is to be applied for solving non-linear flows, such as in the framework of the MILES method, similar to other CFD methods, its resolution will be limited by the grid. Hence, the unresolved small scales need to be removed from the solution without spurious backscatter from small to large scales and keep the simulation stable. For example, the simplest practical solution consists of introducing a small amount of artificial viscosity such that the CABARET scheme represented by Eq. (2.140-2.141) is modified to include a constant Panikovski's dissipater [126] without extending the scheme's stencil:

$$u_{i+1}^{n+1} = \frac{2 \cdot U_{i+1/2}^{n+1/2} - (1-\eta) u_i^n}{1+\eta} \tag{2.142}$$

When $\eta = 0$ the scheme is non-dissipative and when $\eta = 1$, it exhibits the properties of the first order upwind monotonic Godunov (simple upwind scheme) [115] in which case $u_{i+1}^{n+1} = U_{i+1/2}^{n+1/2}$; $u_{i+1}^{n} = U_{i+1/2}^{n-1/2}$. In the work of Goloviznin and Samarskii [126] it was demonstrated that generally, η can be greater than 1 and the scheme's stability would not be affected. However, in practical applications η is can be set ~ 0.1 leading to a very mild smoothing in the vicinity of unresolved solution gradients and the scheme can still maintain good stability. A more advanced method used in this work employs the non-linear flux limiters for overcoming spurious oscillations making the method robust enough for practical applications and maintaining the second order of accuracy in space and time. The non-linear correction procedure is based on the maximum principle [33] [127], according to which the variable u_{i+1}^{n+1} must not exceed the maximum or fall behind the minimum where the following applies:

$$\max(U)_{i+1/2}^{n} = \max_{x \in [x_{i+1},\, x_i]} \{u(x, t^n)\} \approx \max(u_i^n, U_{i+1/2}^n, u_{i+1}^n)$$

$$\min(U)_{i+1/2}^{n} = \min_{x \in [x_{i+1},\, x_i]} \{u(x, t^n)\} \approx \min(u_i^n, U_{i+1/2}^n, u_{i+1}^n) \tag{2.143}$$

For an extrapolated variable on a new time level the non-linear correction reads:

$$u_{i+1}^{n+1} = \begin{cases} u_{i+1}^{n+1} & if \quad \left[\max(U)_{i+1/2}^{n} \geq u_{i+1}^{n+1} \geq \min(U)_{i+1/2}^{n}\right]; \\ \min(U)_{i+1/2}^{n} & if \quad u_{i+1}^{n+1} < \min(U)_{i+1/2}^{n}; \\ \max(U)_{i+1/2}^{n} & if \quad u_{i+1}^{n+1} > \max(U)_{i+1/2}^{n}. \end{cases} \tag{2.144}$$

The dissipation and dispersion properties were analysed closely in [36] [126], applying the CABARET scheme without the non-linear flux correction. In this analysis a travelling wave solution, $u_m^n \sim \exp[i\omega \cdot \tau \cdot n - i\kappa \cdot h \cdot m]$ is substituted into the scheme. The characteristic equation is then derived that establishes a link between the frequency, ω and the wavenumber, κ and the roots of the characteristic equation are the function of the Courant number ($CFL = |c|\tau/h$) and the dimensionless wavenumber:

$$q_{1,2} = f_{1,2}(CFL, \kappa h) \tag{2.145}$$

where

$$f_{1,2}(CFL, \kappa \cdot h) = \frac{(1-2\cdot CFL)\cdot(1-e^{i\kappa h})}{2} \pm \frac{1}{2} \cdot \sqrt{(1-2\cdot CFL)^2 \cdot (1-e^{i\kappa h})^2 + 4 \cdot e^{i\kappa h}} \tag{2.146}$$

As shown in [126] the modulus of the root, $\left|q_{1,2}\right| \equiv 1$ for $0 < CFL \leq 1$. Thus, wave amplitudes stay the same when marching to a new time layer, meaning that the scheme is non-dissipative and stable for $CFL \leq 1$. Hence, the dispersion is the only source of error. Assume that we need to find a solution to Cauchy's one dimensional problem with periodic initial conditions:

$$u_m^n = \sum_{\kappa=0}^{\kappa=N-1} [\alpha(\kappa h) \cdot q_1^n + \beta(\kappa h) \cdot q_2^n] \cdot e^{-i\kappa h} \tag{2.147}$$

The coefficients $\alpha(\kappa h)$ and $\beta(\kappa h)$ are determined by initial conditions at the first grid point and $q_{1,2}^n$ are the roots that determine the solution as it progresses in time. The solution can be evaluated in such a way that only one of the two roots in Eq. (2.147) is necessary to determine the evolution in time while the other one would only affect the stability. [126] Hence, one with better dispersion properties should be used which can be determined by investigating the values of the roots. By knowing that $q_{1,2} = \exp(i\omega_{1,2} \cdot \tau)$, the phase velocities $\gamma_{1,2}$ given in Eq. (2.148) below could be determined.

$$\omega_1 \cdot \tau = arctan[\mathrm{Im}(q_1)/\mathrm{Re}(q_1)]; \quad \omega_2 \cdot \tau = arctan[\mathrm{Im}(q_2)/\mathrm{Re}(q_2)];$$

$$\gamma_1(CFL, kh) = \frac{\omega_1}{\kappa \cdot c} = \frac{1}{CFL \cdot \kappa h} \cdot arctan[\mathrm{Im}(q_1)/\mathrm{Re}(q_1)]$$

$$\gamma_2(CFL, kh) = \frac{\omega_2}{\kappa \cdot c} = \frac{1}{CFL \cdot \kappa h} \cdot arctan[\mathrm{Im}(q_2)/\mathrm{Re}(q_2)] \tag{2.148}$$

The scheme is free from phase error when $\gamma_1$and γ_2 are equal to 1. Therefore, the dispersion error would be characterised as $\gamma_1(CFL, \kappa h) - 1 \neq 0$ and $\gamma_2(CFL, \kappa h) - 1 \neq 0$. It has to be said that, usually, most first order upwind schemes are resilient to dispersion for a linear advection problem when the Courant number is equal 1, while for smaller *CFL* numbers the

first order upwind scheme is quite dissipative. On the contrary, the CABARET scheme is exact for both ($CFL = 1$) and at mid-range ($CFL = 0.5$) where the scheme has good stability. Dispersion properties improve when approaching the ($CFL = 0.5$) condition from either side, where for $\gamma_1(1, \kappa h) = \gamma_1(0.5, \kappa h) = 1$ the scheme is completely dispersion free. Figure 9(a) shows the dispersion error comparison of the CABARET scheme at different Courant numbers against other conventional finite difference schemes where E2, E4 and E6 denote standard central differences of second, fourth and sixth order respectively at the Courant number which allows for most accurate time marching. DRP is the fourth order scheme of Tam & Webb (1993) [32] and LUI stands for the optimised sixth order compact scheme of Lui & Lele [128]. Throughout the entire range of $\mathrm{N}_\lambda = 2\pi/(\kappa \cdot h)$ which denotes a number of points per wavelength (P.P.W.), the error in CABARET approaches the accuracy of conventional sixth order schemes for the Courant number of 0.51. Moreover, away from the optimal condition, for example, when ($CFL = 0.1$) the phase error in CABARET is still comparable to the fourth order scheme. Figure 9(b) shows the group speed error comparison, $c_g = \frac{\tau}{c}\frac{\partial(\omega(\kappa \cdot h))}{\partial(\kappa \cdot h)}$, which is an approximation error instigated by the propagation speed of wave packets. Any deviation of c_g from 1 corresponds to an error in physical wave propagation. Importantly, for the CABARET scheme, the numerical group speed, c_g, always remains positive, while c_g dips to negative values for other schemes at low resolution N_λ, meaning that CABARET would remain free of artificial reflections / wave cut-offs on a coarse grid in comparison to other central difference schemes which will suffer beyond some threshold frequency.

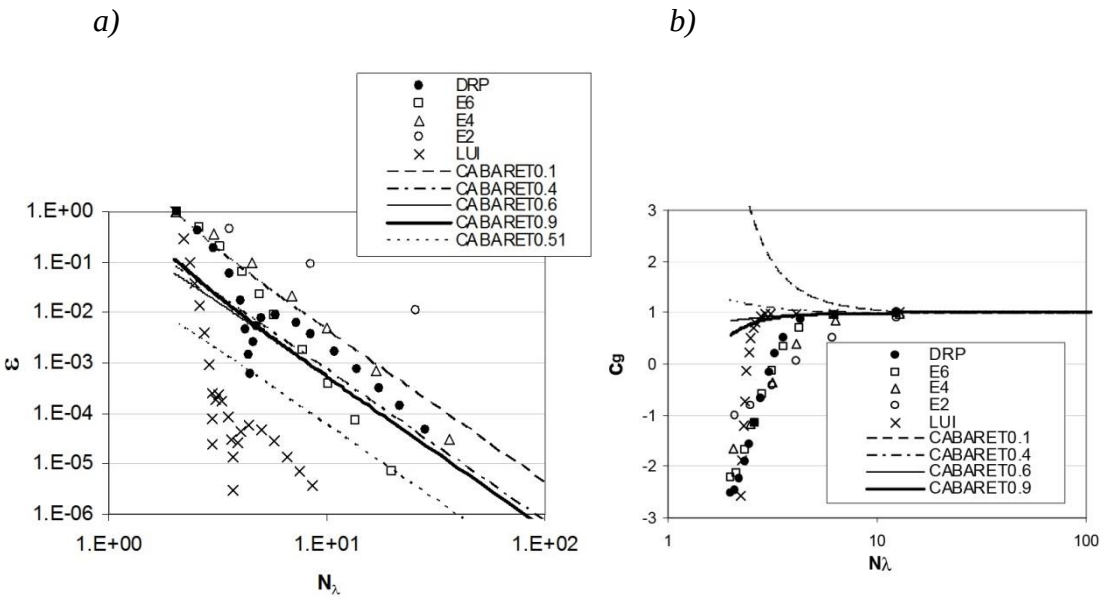

Figure 9 – Comparison of linear dispersion errors of several finite-difference schemes, namely E2, E4, E6, 4th order DRP and 6th order LUI in comparison to the CABARET scheme at different CFL condition in terms of grid points per wavelength N_λ (P.P.W.) (a), numerical group speed error comparison (b), published in [129].

2.5.2.1 CABARET scheme for one-dimensional gas dynamic equations in Euler coordinates

In this section the CABARET extension for solving the system of hyperbolic equations describing the conservation of mass, momentum and energy is reviewed. [130] In the Euler coordinates these equations read:

$$\frac{\partial \rho}{\partial t}+\frac{\partial \rho u}{\partial x}=F_{\rho}, \qquad \frac{\partial \rho u}{\partial t}+\frac{\partial (\rho u^2+p)}{\partial x}=F_{\rho u}, \qquad \frac{\partial \rho E}{\partial t}+\frac{\partial (\rho E u+p u)}{\partial x}=F_{E},$$

$$E=\varepsilon+u^2/2, \qquad p=P(\rho,\varepsilon) \tag{2.149}$$

where $F_{\rho}=F_{\rho}(\rho,\varepsilon,u,x,t)$, $F_{\rho u}=F_{\rho u}(\rho,\varepsilon,u,x,t)$ and $F_{E}=F_{E}(\rho,\varepsilon,u,x,t)$ are the source functions and all other quantities have their usual meaning. The equation of state can be specified as the following:

$$\frac{\partial P}{\partial \varepsilon}\cdot\frac{P}{\rho^2}+\frac{\partial P}{\partial \rho}=c^2\geq\mu_0>0 \tag{2.150}$$

In the above equation c is the speed of sound. The hyperbolic system can be written in the characteristic form.

$$\left\{\Omega\cdot\frac{\partial \boldsymbol{\varphi}}{\partial t}\right\}+\Lambda\cdot\left\{\Omega\cdot\frac{\partial \boldsymbol{\varphi}}{\partial x}\right\}=\Omega\cdot\boldsymbol{f}, \qquad \boldsymbol{\varphi}^T=(\rho,u,p) \tag{2.151}$$

$$\Omega=\begin{bmatrix}0 & 1 & (\rho c)^{-1}\\ 0 & 1 & -(\rho c)^{-1}\\ -c^2 & 0 & 1\end{bmatrix} \text{ and } \Lambda=\begin{bmatrix}\lambda_1 & 0 & 0\\ 0 & \lambda_2 & 0\\ 0 & 0 & \lambda_3\end{bmatrix}=\begin{bmatrix}u+c & 0 & 0\\ 0 & u-c & 0\\ 0 & 0 & u\end{bmatrix} \tag{2.152}$$

$\boldsymbol{f}^T=(f_1,f_2,f_3)$ where $f_1=F_{\rho}$, $f_2=(F_{\rho u}-u\cdot F_{\rho})/\rho$,

and $f_3=\frac{\partial P}{\partial \varepsilon}\cdot\frac{1}{\rho}\cdot\left[F_E+(u^2-E)\cdot F_{\rho}-u\cdot F_{\rho u}\right]+\frac{\partial P}{\partial \rho}\cdot F_{\rho}$.

In the work by Goloviznin [130] the CABARET scheme is described as the balance-characteristic method, combining the properties of the characteristic and conservative approaches in a numerical scheme which involves the so-called conservative and flux variables. The conservative variables, namely $U_{i+1/2}$, $\Theta_{i+1/2}$, $P_{i+1/2}$, $\mathcal{E}_{i+1/2}$ and $E_{i+1/2}$ denoting velocity, density, pressure, internal energy and the total energy in that order are attributed to cell centres with the index $i+1/2$ while the flux variables u_i, ρ_i and p_i are defined at the mesh nodes.

Assuming that the conservative and flux variables are known at the time level t^n, the system of equations can be written in the conservative form using the finite difference discretisation with the second order of approximation. Then, the new conservative variables will have to be evaluated at the time level t^{n+1} but first, Eq. (2.149) are approximated for the time level $t^{n+1/2}=t^n+0.5\cdot\tau^{n+1/2}$.

$$\frac{\Theta_{i+1/2}^{n+1/2}-\Theta_{i+1/2}^{n}}{\tau^{n+1/2}/2}+\frac{(\rho u)_{i+1}^{n}-(\rho u)_{i}^{n}}{h_{i+1/2}}=(F_{\rho})_{i+1/2}^{n},$$

$$\frac{(\Theta\cdot U)_{i+1/2}^{n+1/2}-(\Theta\cdot U)_{i+1/2}^{n}}{\tau^{n+1/2}/2}+\frac{(\rho u^2+p)_{i+1}^{n}-(\rho u^2+p)_{i}^{n}}{h_{i+1/2}}=(F_{\rho u})_{i+1/2}^{n},$$

$$\frac{(\Theta\cdot E)_{i+1/2}^{n+1/2}-(\Theta\cdot E)_{i+1/2}^{n}}{\tau^{n+1/2}/2}+\frac{(\rho\cdot e\cdot u+pu)_{i+1}^{n}-(\rho\cdot e\cdot u+pu)_{i}^{n}}{h_{i+1/2}}=(F_{E})_{i+1/2}^{n}, \tag{2.153}$$

where $E_{i+1/2}^{n+1/2}=\mathcal{E}_{i+1/2}^{n+1/2}+0.5\cdot U_{i+1/2}^{n+1/2}\cdot U_{i+1/2}^{n+1/2}$, and $e_i^n=\varepsilon_i^n+0.5\cdot u_i^n\cdot u_i^n$

The characteristic system Eq. (2.151) is approximated in a similar way:

$$\left\{\Omega_{i+1/2}^{n+1/2}\cdot\frac{\partial\boldsymbol{\varphi}}{\partial t}\right\}+\Lambda_{i+1/2}^{n+1/2}\cdot\left\{\Omega_{i+1/2}^{n+1/2}\cdot\frac{\partial\boldsymbol{\varphi}}{\partial x}\right\}=\Omega_{i+1/2}^{n+1/2}\cdot\boldsymbol{f}_{i+1/2}^{n+1/2} \tag{2.154}$$

and similarly filling the matrices Eq. (2.152),

$$\Omega_{i+1/2}^{n+1/2}=\begin{bmatrix}0 & 1 & \left(\Theta_{i+1/2}^{n+1/2}\cdot C_{i+1/2}^{n+1/2}\right)^{-1}\\ 0 & 1 & -\left(\Theta_{i+1/2}^{n+1/2}\cdot C_{i+1/2}^{n+1/2}\right)^{-1}\\ -\left(C_{i+1/2}^{n+1/2}\right)^{2} & 0 & 1\end{bmatrix} \tag{2.155}$$

$$\Lambda_{i+1/2}^{n+1/2}=\begin{bmatrix}(\lambda_1)_{i+1/2}^{n+1/2} & 0 & 0\\ 0 & (\lambda_2)_{i+1/2}^{n+1/2} & 0\\ 0 & 0 & (\lambda_3)_{i+1/2}^{n+1/2}\end{bmatrix}=\begin{bmatrix}(U+C)_{i+1/2}^{n+1/2} & 0 & 0\\ 0 & (U-C)_{i+1/2}^{n+1/2} & 0\\ 0 & 0 & (U)_{i+1/2}^{n+1/2}\end{bmatrix}$$

$$C_{i+1/2}^{n+1/2}=\sqrt{\left(\frac{\partial P}{\partial\varepsilon}\right)_{i+1/2}^{n+1/2}\cdot\frac{P_{i+1/2}^{n+1/2}}{\left(\Theta_{i+1/2}^{n+1/2}\right)^2}+\left(\frac{\partial P}{\partial\rho}\right)_{i+1/2}^{n+1/2}}$$

Eq. (2.154) can be re-written as:

$$\frac{\partial I_k}{\partial t}+(\lambda_k)_{i+1/2}^{n+1/2}\cdot\frac{\partial I_k}{\partial x}=(\mathcal{g}_k)_{i+1/2}^{n+1/2} \tag{2.156}$$

with the following notation:

$$\boldsymbol{I}=\Omega_{i+1/2}^{n+1/2}\cdot\boldsymbol{\varphi},\quad \boldsymbol{\mathcal{g}}_{i+1/2}^{n+1/2}=\Omega_{i+1/2}^{n+1/2}\cdot\boldsymbol{f}_{i+1/2}^{n+1/2},\quad G_{i+1/2}^{n+1/2}=\left(\Theta_{i+1/2}^{n+1/2}\cdot C_{i+1/2}^{n+1/2}\right)^{-1},\quad \boldsymbol{I}^T=(r,q,s)$$

$$\begin{aligned}r&=u(x,t)+G_{i+1/2}^{n+1/2}\cdot p(x,t),\\ q&=u(x,t)-G_{i+1/2}^{n+1/2}\cdot p(x,t),\\ s&=p(x,t)-\left(C_{i+1/2}^{n+1/2}\right)^2\cdot\rho(x,t)\end{aligned} \tag{2.157}$$

The quantities (r,q,s) are the Riemann invariants which are to be calculated at the time level $t^{n+1/2}$ using the mid-point "conservative" variables and the flux information from the time level t^n. As discussed in [129] and [130] the balance-characteristic procedure is based on Eq. (2.153), numerically implemented as a system Eq. (2.154) which describes a "predictor" step.

The "corrector" step follows requiring the invariants to satisfy conditions which are outlined below, at the same time linearly extrapolating the values to a new time level t^{n+1} where the invariants will be compared against the min/max values as part of the non-linear correction.

$$(I_k)_{i+1}^{n+1} = 2 \cdot (I_k)_{i+1/2}^{n+1/2} - (I_k)_i^n, \qquad (I_k)_i^{n+1} = 2 \cdot (I_k)_{i+1/2}^{n+1/2} - (I_k)_{i+1}^n \tag{2.158}$$

$$\begin{aligned} \min(I_k)_D &= \min\left[(I_k)_i^n, (I_k)_{i+1/2}^{n+1/2}, (I_k)_{i+1}^n\right] + \tau^{n+1/2} \cdot (\mathcal{g}_k)_{i+1/2}^{n+1/2} \\ \max(I_k)_D &= \max\left[(I_k)_i^n, (I_k)_{i+1/2}^{n+1/2}, (I_k)_{i+1}^n\right] + \tau^{n+1/2} \cdot (\mathcal{g}_k)_{i+1/2}^{n+1/2} \end{aligned} \tag{2.159}$$

where D is the stencil $(x,t) \in \left[x_{i+1/2}, x_i\right] \times [t^{n+1}, t^n]$. Hence, the correction procedure can be defined as:

$$[(\tilde{I}_k)_{i+1}^{n+1}]_{i+1/2} = \begin{cases} (I_k)_{i+1}^{n+1} & if \quad [\max(I_k)_D \geq (I_k)_{i+1}^{n+1} \geq \min(I_k)_D]; \\ \min(I_k)_D & if \quad (I_k)_{i+1}^{n+1} < \min(I_k)_D; \\ \max(I_k)_D & if \quad (I_k)_{i+1}^{n+1} > \max(I_k)_D. \end{cases} \tag{2.160}$$

Same conditions for the correction as in Eq. (2.160) apply to $[(\tilde{I}_k)_i^{n+1}]_{i+1/2}$. Therefore, at every node with the index $(i, n+1)$ there would be six solutions to the invariants (r, q, s), namely $(\tilde{r}_i^{n+1})_{i-1/2}$, $(\tilde{r}_i^{n+1})_{i+1/2}$, $(\tilde{q}_i^{n+1})_{i-1/2}$, $(\tilde{q}_i^{n+1})_{i+1/2}$, $(\tilde{s}_i^{n+1})_{i-1/2}$ and $(\tilde{s}_i^{n+1})_{i+1/2}$. Since the scheme is directional, the flux variables at the new time level $n+1$ are determined via characteristic equations where the choice of invariants will depend on the direction from which information arrives at the node $(i, n+1)$. (See [39] [130]) In short, the sought values of $\tilde{u}_i^{n+1}$ and $\tilde{c}_i^{n+1}$ are approximated using the following equations:

$$\tilde{u}_i^{n+1} = U_{i+1/2}^{n+1/2} + U_{i-1/2}^{n+1/2} - u_i^n, \qquad \tilde{c}_i^{n+1} = C_{i+1/2}^{n+1/2} + C_{i-1/2}^{n+1/2} - c_i^n \tag{2.161}$$

And the characteristic velocities are defined at the new time level:

$$\left(\tilde{\lambda}_1\right)_i^{n+1} = \tilde{u}_i^{n+1} + \tilde{c}_i^{n+1}, \qquad \left(\tilde{\lambda}_2\right)_i^{n+1} = \tilde{u}_i^{n+1} - \tilde{c}_i^{n+1}, \qquad \left(\tilde{\lambda}_3\right)_i^{n+1} = \tilde{u}_i^{n+1} \tag{2.162}$$

Then the above characteristic velocities are compared to zero, drawing the system of equations for evaluating the flux variables p_i^{n+1}, ρ_i^{n+1} and u_i^{n+1} using the corresponding invariants. This stage completes the calculation of the flux variables at the new time level $n+1$. More details on various modifications of the algorithm, boundary conditions, extenson to 2D / 3D flows as well as its application to practical problems and comparison with other numerical schemes could be found in works of Goloviznin [39] [130], Karabasov *et al.* [35] [44] [129], Faranosov *et al.* [46] and Markesteijn *et al.* [48] [49] [50].

Summary of main properties

- The CABARET scheme uses a single cell stencil over which the fluxes p_i^{n+1}, ρ_i^{n+1} and u_i^{n+1} are computed for maximum compactness.
- The scheme is second order accurate in space and time even on non-uniform computational grids.

- The scheme is stable for $0 < CFL \leq 1$ and exact for the Courant number of 0, 0.5 and 1.
- Non-dissipative. Therefore, potentially free from amplitude errors.
- Improved dispersion properties in comparison to the conventional finite-difference schemes as demonstrated in Figure 9 which for example, makes the application of CABARET attractive in the framework of Monotonically Integrated Large-Eddy Simulation (MILES). This will be discussed further down.
- Nonlinear flux correction can be applied directly based on the maximum principle without the introduction of any additional tuning parameters to better control dissipation and dispersion properties.

2.6 Turbulence modelling approaches

2.6.1 Reynolds-Averaged Navier-Stokes: the basic concept

In numerical modelling, RANS involves the solution of the Reynolds-averaged equations to determine the mean flow field. The concept of RANS is illustrated by solving the transport equation as it is fundamental for low Mach / incompressible flows. The governing Navier-Stokes equations are re-arranged by inserting a sum of mean and fluctuating parts, $\boldsymbol{U} = \bar{\boldsymbol{u}} + \boldsymbol{u}'$, $p = \bar{p} + p'$ into the momentum equation. It is easy to verify that the continuity equation applies to the averaged flow as well as to fluctuations.

$$\frac{\partial \bar{u}_i}{\partial t} + \bar{u}_j \frac{\partial \bar{u}_i}{\partial x_j} + \frac{1}{\rho} \nabla \bar{p} = \nu \frac{\partial^2 \bar{u}_i}{\partial x_j^2} - \frac{\partial \overline{u'_i u'_j}}{\partial x_j} \tag{2.163}$$

Eq. (2.163) is a time averaged transport equation for velocity components. Time averaging of the non-linear convective term resulted in appearance of the "Reynolds stress" term $\partial \overline{u'_i u'_j} / \partial x_j$ that embodies the average dissipative effect of the fluctuation turbulence. Due to the closure problem, RANS equations have to be solved with "Reynolds stress" term being represented by some empirical model.

In this work RANS models are used to supply the mean flow information into a fast turnaround FRPM acoustic code discussed in Chapter 3 where the two-equation model is required for obtaining the turbulence length scales which are then manipulated into the length scales of the acoustic solution following the definition of source terms.

Usually, RANS models do not require an in-house code to be written specifically for solving Reynolds averaged equations because these are too generic and do not involve complicated procedures in problem solving due to time-averaged characteristics. In this case, commercial software can be more robust and offer various options for pre- and post-processing, as well as capabilities to fine tune model constants used within a solver, making equations fully customisable in application for a wide range of problems. In terms of the modelling options, the mixing length model could be thought of as the simplest turbulence model in terms of RANS which can produce incorrect results for all but the simplest flows. Alternatively,

instead of using a local equilibrium assumption, a transport equation can be solved for the turbulent kinematic viscosity, ν_T. A most widely used one equation turbulence model is Spalart-Allmaras (SA) [131] which is numerically well conditioned and the closure is achieved using empirical constants. Other one equation models, originated approximately at the same period include Baldwin-Barth (1992) [132] and Menter (1994) [133] but are seldom used.

In an attempt to improve RANS modelling, a two-equation model class was proposed, [134] solving transport equations for the turbulent kinetic energy and the dissipation rate, k and ε. Unlike with the one-equation model, closure is achieved using the definition for a turbulence length scale, $l = k^{\frac{3}{2}}/\varepsilon$ as well as utilising the relationship, $\nu_T \propto k^2/\varepsilon$ that endowed the model with a generally correct behaviour for ν_T. As a consequence, two-equation models can be deemed "complete" and hence, have the broadest range of applicability. In CAA applications, when RANS models are used, in addition to supplying mean flow information, the features of the two-equation model allow augmenting the two turbulent quantities to obtain the unknowns, for example, using the property of the length scale. Therefore, this class of RANS models is preferred in this work and deserves particular attention.

Historically, many two-equation turbulence models have been proposed. The choice of k is fairly convenient when transport equations are derived from the Navier-Stokes following a similar procedure as shown in Eq. (2.118), where $k = 1/2\langle \overline{\boldsymbol{u}} \cdot \overline{\boldsymbol{u}} \rangle$. However, the equation for ε is purely empirical, presenting a diverse choice for the second quantity. The second most popular model is $k-\omega$, [135] where ω is the specific dissipation rate $\omega = \varepsilon/k$. Essentially, the description of k and ν_T is identical to the $k-\varepsilon$ model with subtle differences between ε and ω equations, more precisely the difference lies in the diffusion term. As a result, the $k-\omega$ model became superior in viscous near-wall region treatment and improved stream-wise pressure gradient prediction for turbulent flows, as described in details by Wilcox (1993) [135]. Furthermore, Menter [133] has attempted to derive a turbulence model that combines the best properties of both, $k-\varepsilon$ and $k-\omega$ models with the introduction of a blending function that switches between zero close to the wall, behaving like ω equation and unity away from wall making it a standard ε equation. Such treatment is called $k-\omega$ *SST* which stands for the 'shear stress transport'. Importantly, with all RANS models there is no increase in computational effort with increasing Re number.

In this work the code for solving RANS and URANS equations is implemented in ANSYS CFX which is the preferred solver from which data is input into the acoustic code Altus discussed in Chapter 3. The CFX solver is selected mainly for the reason of having powerful post-processing and data export capabilities. For simulations implemented in this project a non-linear recipe for a blending factor based on the boundedness principle proposed by Barth and Jespersen [136] is used making the advection scheme second order accurate in space. The algorithm used can be shown Total Variation Diminishing (TVD) when applied to a one-dimensional flow problem. Other solvers, namely ANSYS Fluent and OpenFOAM are also employed for comparison between RANS simulations, solving the flow past a NACA 0012 aerofoil. See Appendix C for results and discussion.

2.6.2 Time accurate turbulence simulation techniques

In general, all RANS models have significant shortcomings – there is not a single satisfactory model with a versatile validity, particularly there is none for separated flows. Also, solving an acoustics problem requires the knowledge of perturbation quantities that cannot be obtained directly from RANS and even in most advanced RANS-based acoustic solvers some empirical scaling is required. Moreover, with RANS-based CAA methods it is impossible to get reliable acoustic predictions where correlations are fundamental to flow behaviour. For example, considering the flow over a bluff body such as a circular cylinder, where the accuracy of broadband noise prediction would be largely influenced by span-wise correlations and tonal noise by the shedding frequency – neither can be predicted by RANS/URANS methods. Therefore, clearly, there is a need for developing high-fidelity methods that will ultimately yield the physically accurate and reliable solution.

From the Kolmogorov analysis it is evident that for sufficiently high Reynolds number flows typical in engineering applications the grid resolution and the associated time-step Δt requirements in explicit models are truly demanding. For resolving the smallest scales down to the Kolmogorov scale the minimum number of mesh points required would approximately scale with $\mathrm{Re}^{9/4}$. By definition, the smallest length scale known as the Kolmogorov scale is $(\nu^3/\varepsilon)^{1/4}$ and expressing the dissipation rate using dimensional analysis, $\varepsilon \sim U^3/L$ where L is the reference length scale, the ratio of a typical length L to the smallest eddy size can be defined as $(UL/\nu)^{3/4} = \mathrm{Re}^{3/4}$. Hence, in three dimensions the minimum number of points required to represent a fluctuation is of order $\mathrm{Re}^{9/4}$. The Direct Numerical Simulation (DNS) methods are designed to explicitly resolve all turbulent scales present in the simulation, thus, offering the most accurate solution with only discretisation errors being the source of discrepancy between the simulated and real flow. With an exception of work specifically dedicated to advanced research (e.g. performing DNS as a validation of turbulence modelling approaches at sufficiently low Re number), DNS simulations are not feasible for practical cases performed on a reasonable timescale even using the most advanced computational facilities as for today. In a high-fidelity turbulent flow simulation the most computational effort is dedicated to resolving the smallest scales. Therefore, if those scales could be partly modelled or even neglected without any significant loss of information in key areas, simulation efficiency can be increased substantially. Also, from the fluid dynamics theory it is understood that large scales carry most energy, typically up to 80%. For example, in aerodynamic modelling of airframe components the smallest scales are usually found in the near-wall region. Hence, a much simplified treatment for achieving a high-fidelity simulation would be to model the boundary layer using a RANS approach and simulate the turbulent mixing of large eddies away from the wall through a hybrid Detached Eddy Simulation (DES) method. [137] Such treatment can be very efficient and powerful, primarily, because it is much cheaper than DNS and also, the advantages and disadvantages of RANS modelling are explored reasonably well as RANS is now regarded the industry's workhorse. The increased computational cost of DES in comparison with RANS is associated with extension of the former to three dimensions and using a fine grid resolution in a wake zone. Main

complexity of the DES method is in the switch between RANS and LES and feedback from large to small scales.

Large Eddy Simulation (LES) is an alternative class of methods which is based on scale separation and filtering procedure where instead of resolving the smallest scales as in DNS some statistical model can be used for representation of the fine scales. Such model may be referred to as a 'sub-filter scale' model. In practice, the finest affordable near-wall grid resolution is commonly adopted with a first mesh point being within a viscous sub-layer and because computational grid often limits the scales that could be resolved, the cut-off beyond which filtering removes length and time scales is termed as 'sub-grid scale' (SGS) model. In general, the filtering procedure can be explicit where a convolution filter is applied to a DNS solution or implicit where it is attempted to remove unresolved scales from the solution and filtering is imposed by a computational mesh resolution. Since LES schemes operate in the time domain contrary to the frequency domain, filtering also takes place in the time domain which takes a form of artificial viscosity. It is also possible to use a combination of explicit SGS and implicit for excluding the overlap between the numerical error and effects of SGS.

In the previous section on RANS methods the assumption was to take the time-average of $u(x,t)$ over a statistically invariant time period as prescribed by Eq. (2.164) below.

$$\overline{\boldsymbol{u}}(x,t) = \frac{1}{T}\int_0^T \boldsymbol{u}(x,t)\, dt \tag{2.164}$$

In LES a low-pass filter is applied to $u(x,t)$, which is designed to remove length and time scales below the cut-off scale.

$$\overline{\boldsymbol{u}}(x,t) = \int_{-\infty}^{T}\int_{-\infty}^{+\infty} G(\bar{\Delta},\bar{\theta},|x-x'|,t-t')u(x',t')dx'dt' \; = G(\bar{\Delta},\bar{\theta}) * \boldsymbol{u}(x,t) \tag{2.165}$$

where $G(\bar{\Delta},\bar{\theta},|x-x'|,t-t')$ is the filter kernel. The parameters $\bar{\Delta}$ and $\bar{\theta}$ are the cut-off length and the cut-off time, respectively. Moreover, by taking advantage of $\bar{\Delta}$ parameter, the isotropic filter width could be specified. Most authors consider spatial filtering only, $G(\bar{\Delta},|x-x'|)$. Examples of usual spatial convolution filters in physical space as well as in spectral space are presented in Table 2.

Examples of filters	$G(\bar{\Delta},\|x-x'\|)$	$G(\kappa)$
Box / top hat	$\begin{cases} \frac{1}{\bar{\Delta}} \text{ if } \|x-x'\| \le \bar{\Delta}/2 \\ 0 \text{ otherwise} \end{cases}$	$\sin(\kappa\bar{\Delta}/2) \,/\, (\kappa\bar{\Delta}/2)$
Gaussian	$\sqrt{\frac{6}{\pi\bar{\Delta}^2}}\exp\left(\frac{-6\|x-x'\|^2}{\bar{\Delta}^2}\right)$	$\exp\left(\frac{-\kappa^2\,\bar{\Delta}^2}{24}\right)$
Sharp cut-off	$\frac{\sin(\kappa_c\|x-x'\|)}{\kappa_c\|x-x'\|}$	$\begin{cases} 1 \text{ if } \kappa \le \kappa_c \\ 0 \text{ otherwise} \end{cases}$

Table 2 – Examples of commonly used spatial convolution filters in LES, $\kappa_c = \pi/\bar{\Delta}$.

Applying the convolution filter to the non-linear conservation law yields [18]:

$$\frac{\partial \bar{u}_i}{\partial t} + \nabla \cdot \overline{F(u_\iota, u_j)} = 0 \tag{2.166}$$

where F is the non-linear flux function with a quadratic behaviour in terms of u. In Eq. (2.166) bar denotes filtered quantities. Leonard (1974) [138] proposed the following decomposition of the non-linear convection term consisting of $\boldsymbol{u} = \bar{\boldsymbol{u}} + \boldsymbol{u}'$where $\bar{\boldsymbol{u}}$ is the filtered quantity.

$$\overline{u_\iota u_j} = \overline{(\bar{u}_\iota + u_\iota') * (\bar{u}_j + u_j')} = \overline{\bar{u}_\iota \bar{u}_j} + \overline{\bar{u}_\iota u_j'} + \overline{\bar{u}_j u_\iota'} + \overline{u_\iota' u_j'} \tag{2.167}$$

There are 4 RHS terms in Eq. (2.167) with the first term being resolved, the following two are the cross terms and the last one is the Reynolds stress. The resolved term is further decomposed through the expression of the Leonard's stress.

$$\overline{\bar{u}_\iota \bar{u}_j} = \bar{u}_i \bar{u}_j + \{\tau_{ij}^L\} \tag{2.168}$$

where the resolved part contains the Leonard's stress tensor τ_{ij}^L, defined as $\{\overline{\bar{u}_\iota \bar{u}_j} - \bar{u}_i \bar{u}_j\}$, representing fluctuations of the interaction between resolved scales. The cross terms in Eq. (2.167) form the cross-stress tensor which accounts for direct interaction between resolved and unresolved scales. Note, the cross-stress tensor and the Leonard's stress tensor are zero for RANS, meaning that the Reynolds stress term is the only remaining part as one would expect. For LES, Eq. (2.166) can be re-written by substituting the Leonard's decomposition into the non-linear flux term and keeping the resolved part on the LHS.

$$\frac{\partial \bar{u}_i}{\partial t} + \nabla \cdot \overline{F(\bar{u}_\iota, \bar{u}_j)} = -\nabla \cdot \left(\overline{F(\bar{u}_\iota, u_j')} + \overline{F(u_\iota', \bar{u}_j)} + \overline{F(u_\iota', u_j')} \right) \tag{2.169}$$

Since it is difficult to solve for fine scales and the purpose of LES is to apply some sort of filtering to the sub-grid scale terms, the unresolved stresses are grouped on the RHS of Eq. (2.169) and expressed as a residual stress which is then modelled by SGS. Typically, there is little energy contained in these small scales if the cut-off is set sufficiently far down the energy cascade. Hence, the SGS model may only represent a small amount of TKE. For that reason, in some cases the SGS model does not need to be very accurate to produce physical and reliable results as, for example, in the case of free jets where the smallest scales do not have large influence on the bulk flow. On the other hand, small scales are crucial for predicting separation where selection of a particular SGS model may play a significant role.

2.6.2.1 MILES concept as a special class of implicit SGS

As mentioned previously, implicit LES methods use numerical dissipation as a low-pass filter for removing high wavenumbers from the solution. In addition to turbulence modelling, a small amount of dissipation is necessary in all LES algorithms to guarantee stability and in 1992 Boris *et al.* [139] proposed a concept of monotonically integrated LES (MILES) where the role of the near-wall model is replaced by viscosity-like dissipation. In essence, no

additional SGS model is required and LES results could be obtained by solving the Navier-Stokes equations. However, as discussed by Grinstein and Fureby [40] the application of MILES for low-speed high-Reynolds number flows is very challenging due to excessive numerical dissipation. Moreover, in most cases the dissipation does not occur only at the desired location which makes MILES methods based on conventional second order schemes unsuitable for many problems.

For solving the problem of inherent numerical dissipation typical of many MILES methods, the non-dissipative CABARET scheme introduced in Section 2.5.2 is implemented in the framework of MILES and its application to benchmark cases is demonstrated and discussed in Chapter 4. As with any pure LES, such as those that do not employ any boundary layer modelling, the simulation of high Reynolds number flows near the boundary is extremely challenging for the MILES method. Hence, in this work we proceed with the validation of the MILES CABARET solver step by step. First, considering a mildly compressible solution around a cylinder and then the scheme is applied in the context of the Navier-Stokes equations for solving the flow over an aerofoil where we find that there is a need for tripping the boundary layer in a similar way as done in the experiment.

2.6.2.2 Synthetic turbulence methods

In contrast to LES, synthetic turbulence methods discussed in Chapter 3 do not solve the Navier-Stokes equations but re-create turbulent fluctuations through local scaling of mean flow data using appropriate length and time scales. As a result, these methods are considerably less computationally expensive but require calibration and can be quite laborious to implement. Synthetic turbulence methods find their applicability ranging from generating inflow turbulence in the LES or DNS simulations with taking into account more realistic flow physics to re-producing stochastic turbulence fields, leading to acquisition of acoustic sources, as discussed in this work. For this purpose, the capability of the synthetic turbulence method should be validated first by reproducing physically accurate turbulence data. It often means that for obtaining reliable results the method has to be carefully calibrated for a particular class of problems. For example, in this work only the application to aerofoil noise modelling is considered. A review on synthetic turbulence methods and in particular, the Fast-Random-Particle-Mesh (FRPM) method first proposed and implemented by Ewert *et al.* [53-57] can be found in the next chapter.

Chapter 3

Synthetic turbulence

Main aspects of the acoustics background theory and numerical methods used in this work were reviewed in Chapter 2. A numerical approach for source modelling usually consists of a 3D simulation in a reference space where a turbulent flow is resolved using non-linear Navier-Stokes equations down to acoustic scales. However, the computational expense grows rapidly with increasing Reynolds number, making the application of high-fidelity method such as LES unsuitable for obtaining a global solution of problems of interest found in industry. Synthetic turbulence methods have been developed as an alternative to solving the Navier-Stokes equations for source acquisition and quickly gained popularity due to their ability to provide rapid yet accurate broadband noise prediction. There are two distinct groups of commonly applied synthetic turbulence methods. One method is based on Fourier modes reconstruction and the other adheres to white noise filtering. These approaches are based on different underlying principles. Section 3.1 provides a brief historic overview on the development of both stochastic approaches.

In this work, the focus is on the Fast-Random-Particle-Mesh (FRPM) synthetic turbulence method [55] which is based on digital filtering. Special attention is given to the procedure of obtaining the turbulent velocity field from RANS mean flow data. Subsequently, acoustic sources which follow the definition of the vortex sound (see Section 2.4.3) are derived via augmenting turbulent velocities with the local mean flow parameters. The novel approach presented in Section 3.3 discusses a mechanism for tonal noise prediction which is implemented in a framework of the stochastic FRPM method. In this work, the tonal noise mechanism relies on the scale separation assumption where large scale fluctuations are obtained by means of a modified input which can accept URANS data. Previously, it was necessary to search for some alternative techniques when applying any of the existing synthetic turbulence methods to the problem where tones are part of the acoustic solution. Thus, a simple yet effective mechanism implemented in this work now allows for all-in-one broadband and tonal noise prediction.

At first, it is often difficult to establish the connection of processes involved in recovering missing data with the aid of synthetic turbulence. The complexity involved with method's implementation is a compromise for rapid yet physical acoustic source modelling. For this purpose the classic FRPM method developed by Ewert *et al.* [55] [56] is reviewed in Section 3.2 in the context of vortex sound theory. The method is applied for simulating noise sources in the vicinity of an aerofoil's trailing edge in Chapter 4. Appendix B shows the algorithm outline which serves as a link between equations and numerical implementation, allowing to see how FRPM fits into the framework of the 'Altus' CAA code.

3.1 Overview of stochastic methods for synthetic turbulence generation in CAA applications

The aim of synthetic turbulence methods is to reproduce unsteady source information from time-averaged data via realistic representation of integral turbulence length and time scales. One point statistics available from RANS is insufficient for determining the flow correlations. Thus, the integral length scale definition involves a calibration parameter, which selection and range for trailing edge noise cases is discussed in Chapter 5. Methods based on digital filtering reconstruct a fluctuating velocity field which is used to calculate noise sources in the time domain. In FRPM, stochastic velocity fluctuations are reproduced locally on an auxiliary grid. These velocity fluctuations contribute to a sound source vector in accordance with the vortex sound theory. The remaining mean flow information required to assemble a source vector Eq. (2.99) is readily available from a RANS simulation. For accurate derivation of fluctuating components the acoustic model has to include convection. Therefore, several options for representing temporal correlations are discussed in Section 3.2. Specifically for airframe noise, a frozen turbulence concept may represent a simple yet effective solution of temporally evolving stochastic field. The characteristics of the synthetic velocity field can be analysed from contours of the time-averaged turbulent kinetic energy field that has been recovered from the stochastic simulation, whose statistics should match the target TKE input from RANS. Thus, these methods can offer quick noise prediction without the knowledge of the reference turbulence length scales from the corresponding experiment or from a high-fidelity simulation, being solely based on the RANS simulation instead.

Early attempts to obtaining the stochastic velocity fluctuations for acoustic source generation relied on expressing the fluctuating field as a finite sum of Fourier modes with random amplitudes. In other words, the resulting velocity field is periodic, which is made up of weighted sinusoidal functions, containing a discrete number of frequencies. Increasing the number of modes of the solution leads to a well-defined spectral content but at the increased computational cost. In 1970, Kraichnan [140] formulated the stochastic method based on Fourier modes, which was applied to reproduce the diffusion of fluid particles. Kraichnan's formulation can be regarded as a predecessor to the Stochastic Noise Generation and Radiation (SNGR) method. (See Bailly *et al.* [141]) Also, Béchara *et al.* [142] extended the method for CAA applications to simulate jet noise by evaluating the finite sum of sinusoidal functions but with the addition of a random phase. Other subtle differences from the original method include the definition of the scaling amplitude, where instead of being a random variable for each mode it is deterministically prescribed in accordance with the von Kármán energy spectrum, which was selected instead of a simple Gaussian representation. Moreover, the method in [142] has evolved to account for the mean flow convection effects as found in later works of Bailly *et al*. [20] [143]. Notably, the modified equation for a random velocity field features the angular frequency term for each Fourier mode as well as the convection term. Billson *et al*. [144] introduced a modification to SNGR method, where an exponential temporal correlation was added to the stochastic velocity field. As a result, Billson *et al.*'s

[144] method could employ fewer Fourier modes to achieve similar accuracy to that of Bailly *et al.*'s method, since at every time step the velocity field is a weighted sum of previous velocity fields. This came at the expense of additional storage required for time-dependent stochastic velocities in the modified method. In the field of LES simulations, Smirnov *et al.* [145] extended the SNGR method for anisotropic turbulence generation that is advantageous for 3D simulations via a transformation of the velocity correlation tensor. The transformation proposed by Smirnov *et al.* [145] was also adopted in the later work of Billson *et al.* [146]. Other notable publications that contributed to stochastic methods development based on the summation of Fourier modes include but are not limited to [147], [148], [149]. Up to date, SNGR methods remain popular in industry but are not considered any further in this work. Instead, a relatively new approach based on digital filtering in the time domain is applied to aerofoil trailing edge noise benchmark cases. Also, in this work the method is further developed to incorporate the tonal noise mechanism.

Stochastic methods based on digital filtering generate fluctuating velocities through spatial weighting of a convecting white noise field using the appropriate area-weighted filter function which properties are discussed in details in Section 3.2. Integration of the white noise field is performed on the auxiliary grid resulting in a stream function that satisfies conservation laws. The numerical realisation of a convective white-noise field is based on random particles that are advanced in a mean flow through area-weighting from neighbouring mesh points. Unlike with the Fourier modes method, the resulting turbulent signal is not monochromatic but rather presents a broadband spectral content. Also, the CAA approach based on a numerical simulation of a sound propagation allows to obtain the solution for all frequency bands with a single computation. To achieve this, an unsteady source is modelled via the Fast-Random-Particle-Mesh (FRPM) method [56] [57] which realises two-point space-time correlations. FRPM is a natural extension of the Random-Particle-Mesh method presented in earlier works by Ewert *et al.* [54]. Main difference of the former more recent version of the method is performing the acoustic source calculation on a Cartesian auxiliary grid. Thus, the FRPM method is computationally more efficient than the original RPM, easier to modify and introduce additional features, such as computing correlations for data analysis. Over the last decade quick CAA methods gained popularity and wide recognition and their applicability to industrial problems is expanding. Nevertheless, several drawbacks associated with the FRPM method still remain. Due to temporal correlations of the fluctuating velocity field a natural choice is to perform the acoustic wave propagation in the time domain, where a filtered source field is supplied to the right-hand-side of the APE equations at every time step as was described in Sections 2.4.3 of Chapter 2. Numerical computation of acoustic wave propagation for industrial-type problems can be significantly beyond a tolerable expense. Therefore, a simplified 2D propagation model is used to reduce the cost. Normally, a large acoustic domain, which must encompass the source and the observer, in conjunction with high-order propagation methods bears a substantial impact on computational cost, potentially comparable to efforts required for the acoustic sources derivation via LES methods. Thus, the benefits of quickly obtaining the stochastic sources with the FRPM method can be outweighed by a time-consuming propagation method. Typically, only several computational cores are sufficient for performing the FRPM simulation on its own on a scale

usually associated with industrial problems. On the other hand, dozens or even hundreds of cores have to be attributed to CAA propagation to keep up with a realistic time frame for aero-acoustic design. One may argue that because of a superb efficiency of acoustic sources calculation in the framework of the FRPM method and a possibility of anisotropic turbulence generation it can be attractive to couple a 3D problem to some other acoustic analogy, e.g. the FW-H similar to that used with LES methods. Indeed, this approach can be selected in preference to simulating wave propagation. However, all limitations of the FW-H method, such as those associated with the control surface placement, source simplification tailored for a specific formulation and other assumptions may apply. To save on the computational time, a 2.5D cylindrical domain is used as a trade-off in sound propagation modelling. Therefore, the amplitude correction has to be taken into account which adds further complexity to the method and at least one extra empirical scaling. In fact, the correction may account for more than just 3D effects, but also, other effects that can become inseparable in such formulation. In this work a Mach number correction for airframe noise applications proposed in [62] is performed and discussed in Chapter 5. Fundamentally, the validation of obtained noise predictions reverts to the source calculation and scaling at the source level according to the definition used in the FRPM method. For aerofoil trailing edge noise simulations this problem is addressed in Chapter 5, where noise sources are compared between LES and FRPM methods. The near-field comparison with the experiment is presented in Chapter 4. The data is analysed at several trailing edge locations highlighting some modelling problems incurred with the FRPM and MILES methods. This analysis also includes comparison of the near-field contours and velocity correlations, inspiring greater confidence in acoustic source derivation for aerofoil trailing edge noise problem. Furthermore, the far-field acoustic spectra comparison for different source models used in the vortex sound theory is presented in Chapter 5.

Thus far, a computational expense has been a pivotal point when a quick stochastic source generation method is coupled to a costly propagator in the time domain. However, there are more issues associated with general applicability of stochastic sound generation methods to various problems. All synthetic turbulence methods were originally designed to simulate broadband noise only. It has proven to be a significant achievement as in digital filtering methods, such as FRPM, generated fluctuations can reproduce very accurately autocorrelations and statistics which match a RANS simulation. Main advantage of stochastic source generation methods is that they are based on solving a simple convection equation which is much faster than solving Navier-Stokes equations by the scale resolved methods such as LES. However, since the FRPM method is based on the time-averaged turbulent flow from RANS its velocity correlations do not include any large scale unsteadiness of the actual flow. For that reason, there have been previous attempts in the literature to combine the FRPM method with a URANS solution for improved broadband noise predictions. Recently, Wohlbrandt *et al.* [150] extended the FRPM method to periodic turbulent flows for improved fan broadband noise prediction. The work presented in [150] focuses on the influence in far-field noise predictions when introducing unsteady quantities for scaling of a Gaussian filter. On the other hand, the main focus of the approach discussed in this thesis is on the possibility of integrating a tonal noise mechanism, where large scale unsteadiness is utilised to

reformulate the velocity component of acoustic sources obtained at the source level. The application of unsteady FRPM model for a centrifugal fan noise problem can be also found in [151]. However, the underlining acoustic formulation used in that work remains unclear. For example, in [151] the U-FRPM approach uses the technique of simply adding up squares of two far-field pressure amplitudes, one being the broadband signal from FRPM and the other is the tonal signal from a separate steady-state model, for obtaining the final power spectral density amplitude at the far-field observer location. Thus, first of all, this approach requires two acoustic calculations of the sound propagation to the far-field for a single flow case that may be expensive. Moreover, such simplified treatment does not only ignore any possible nonlinear source interaction but also neglects any acoustic interference of the different source components that are assumed to be uncorrelated at the far-field despite sound propagation effects, which assumption needs to be verified.

3.2 Fast-Random-Particle-Mesh method

3.2.1 Theoretical background

FRPM method is a stochastic method for synthetic turbulence generation designed to locally reproduce the two point space time correlation $\mathcal{R}(\boldsymbol{x},\boldsymbol{r},\tau)=\overline{\psi(\boldsymbol{x},t)\psi(\boldsymbol{x}+\boldsymbol{r},t+\tau)}$ of a stochastic variable $\psi(\boldsymbol{x},t)$. The method specifically focuses on acoustic source generation where the broadband noise sources Eq. (2.99) are evaluated via differentiation of the fluctuating stream function $\boldsymbol{u}'=\nabla\times\boldsymbol{\psi}$, which combines source convection with a temporal cross-correlation model. Due to a combination of temporal and spatial properties the method is known to realise a 4-D synthetic turbulence model. [57]

Firstly, we shall review the theoretical background of the fluctuating stream function $\psi(\boldsymbol{x},t)$ in the context of a white noise field and the resulting cross-correlation model. Secondly, the particle representation used for discretising analytical equations is briefly discussed to give the idea on numerical implementation of the FRPM method.

The fluctuating stream function of a continuous convolution is expressed analytically via filtering integral which for n dimensional space reads:

$$\psi(\boldsymbol{x},t)=\int_{V_s^n}\hat{A}^n(\boldsymbol{x}')G(|\boldsymbol{x}-\boldsymbol{x}'|,l_s(\boldsymbol{x}'))\mathcal{U}(\boldsymbol{x}',t)d\boldsymbol{x}' \tag{3.1}$$

In Eq. (3.1) $\hat{A}$ is the amplitude of the filter that is the function of the local kinetic energy and position, n indicates the dimension of the problem, and V_s is the considered source region in which unsteady sources are generated. G is the filter kernel that is a function of a separation distance $|\boldsymbol{x}-\boldsymbol{x}'|$ and also, a function of the position-dependent integral length scale l_s. The filter kernel is normalised to unity $\overline{\psi(\boldsymbol{x},t)\psi(\boldsymbol{x},t)}=1$ for $\hat{A}=1$. All quantities of Eq. (3.1) are attributes of spatial filtering apart from a spatiotemporal white noise field $\mathcal{U}$ which properties are described in details in [57] [62]. In short, the random field has a zero mean and when $\mathcal{U}$ is convected frozen its covariance $\overline{\mathcal{U}(\boldsymbol{x},t)\mathcal{U}(\boldsymbol{x}+\boldsymbol{r},t)}$ has a result of a delta function.

The frozen turbulence concept means that convection effects only are accounted for in a model, leading to a temporal correlation of a white noise field being expressed as $\overline{\mathcal{U}(\boldsymbol{x},t)\,\mathcal{U}(\boldsymbol{x},t+\tau)} \rightarrow \delta(\boldsymbol{r}-\boldsymbol{u_c}\tau)$ where τ is the relative separation time. Temporal properties are discussed in further details at the end of the section. Overall, the unique spatiotemporal white noise field properties are briefly summarised below:

$$\overline{\mathcal{U}(\boldsymbol{x},t)} = 0 \tag{3.2}$$

$$\overline{\mathcal{U}(\boldsymbol{x},t)\mathcal{U}(\boldsymbol{x}+\boldsymbol{r},t)} = \lim_{T\rightarrow\infty}\frac{1}{2T}\int_{-T}^{T}\mathcal{U}(\boldsymbol{x},t)\mathcal{U}(\boldsymbol{x}+\boldsymbol{r},t)dt = \delta(\boldsymbol{r}) \tag{3.3}$$

$$\frac{D}{Dt}\mathcal{U} = 0 \tag{3.4}$$

Eq. (3.4) introduces convection into the model where $D/Dt = \partial/\partial t + \boldsymbol{u_c}\nabla$ is a material derivative. In context of a frozen turbulence a white noise field passively convects with a mean flow $\boldsymbol{u_c}$ and remains locally static. [55] In Eq. (3.3) $\delta(\boldsymbol{r})$ is a multi-dimensional delta function, e. g. in 2D $\delta(\boldsymbol{r}) = \delta(r_1)\delta(r_2)$. The correlation of the white noise field, $\mathcal{R}_{wf}(\boldsymbol{r}) = \overline{\psi(\boldsymbol{x},t)\psi(\boldsymbol{x}+\boldsymbol{r},t)}$, can be obtained by using the form of Eq. (3.1) together with the property of Eq. (3.3).

$$\mathcal{R}_{wf}(\boldsymbol{r}) = \frac{1}{2T}\int_{-T}^{T}\int_{-\infty}^{\infty}\mathcal{U}(\boldsymbol{x}',t)G(|\boldsymbol{x}-\boldsymbol{x}'|)d\boldsymbol{x}'\int_{-\infty}^{\infty}\mathcal{U}(\boldsymbol{x}'',t)G(|\boldsymbol{x}+\boldsymbol{r}-\boldsymbol{x}''|)d\boldsymbol{x}''dt =$$

$$= \frac{1}{2T}\int_{-\infty}^{\infty}\int_{-\infty}^{\infty}G(|\boldsymbol{x}-\boldsymbol{x}'|)G(|\boldsymbol{x}+\boldsymbol{r}-\boldsymbol{x}''|)\int_{-T}^{T}\mathcal{U}(\boldsymbol{x}',t)\mathcal{U}(\boldsymbol{x}'',t)dt\,d\boldsymbol{x}'d\boldsymbol{x}'' \tag{3.5}$$

where the covariance of the white noise field can be simply represented by $\delta(\boldsymbol{x}'-\boldsymbol{x}'')$ which leads to the core property of the method where the correlation of the white noise field, $\mathcal{R}_{wf}(\boldsymbol{r})$, is represented by the convolution of the filter kernel with itself as shown in Eq. (3.6) below. Let $\boldsymbol{\xi} = \boldsymbol{x}' - \boldsymbol{x}$ to be the relative separation distance between points $\boldsymbol{x}$ and $\boldsymbol{x}'$, $d\boldsymbol{x}' = d\boldsymbol{\xi}$, also assuming $G(\boldsymbol{r})$ is an even function, where $G(\boldsymbol{r}) = G(-\boldsymbol{r})$ then the above integral in Eq. (3.5) becomes,

$$\mathcal{R}_{wf}(\boldsymbol{r}) = \int_{-\infty}^{\infty}G(-\boldsymbol{\xi})G(|\boldsymbol{r}-\boldsymbol{\xi}|)d\boldsymbol{\xi} = \boldsymbol{G}*\boldsymbol{G} \tag{3.6}$$

Then, the spatial correlation can be expressed through a Gaussian filter kernel having half the width as:

$$\mathcal{R}(\boldsymbol{r}) = \exp\left[-\frac{\pi|\boldsymbol{r}|^2}{4l_s^2}\right] \tag{3.7}$$

where $|\boldsymbol{r}|$ is the relative separation distance, l_s is the integral length scale derived by scaling the mean turbulent kinetic energy, k, and the dissipation rate, ϵ, from a RANS simulation through the following relationship:

$$l_s = c_l\frac{k^{\frac{3}{2}}}{\epsilon} \tag{3.8}$$

In the above equation c_l is a calibration constant. In accordance with [62] its recommended value for trailing edge noise problems is in the range of 0.5 - 0.75. The turbulent viscosity of the $k-\epsilon$ and the $k-\omega$ models is related so that $\epsilon = C_\mu k\omega$, where $C_\mu = 0.09$ and in case if $k-\omega$ is used the relationship of the integral length scale simply becomes:

$$l_s = \frac{c_l}{C_\mu}\frac{k^{\frac{1}{2}}}{\omega} \tag{3.9}$$

The scaling amplitude, $\hat{A}^n(\boldsymbol{x}')$ in Eq. (3.1) that scales the Gaussian Eq. (3.7) must be chosen such that fluctuating velocities that are derived from the stochastic stream function Eq. (3.1) achieve a local turbulent kinetic energy $k(\boldsymbol{x}') = 1/2\,\langle u^2(\boldsymbol{x}',t) + v^2(\boldsymbol{x}',t)\rangle$, in accordance to [56] [62] for a 2D case the scaling amplitude becomes:

$$\hat{A}^{(2)}(\boldsymbol{x}') = \sqrt{\frac{4}{3\pi}}k^{\frac{1}{2}}(\boldsymbol{x}') \tag{3.10}$$

Thus far the focus has been on spatial properties controlled by the Gaussian filter where the length scale is proportional to the filter width. On the other hand, temporal properties of synthetic turbulence are solely controlled by a white noise field $\mathcal{U}$. The autocovariance of the convective white noise field can be expressed as $\mathcal{R}_\mathcal{U}(\boldsymbol{x},\tau) = \langle \mathcal{U}(\boldsymbol{x},t)\,\mathcal{U}(\boldsymbol{x},t+\tau)\rangle$. In the classic FRPM method turbulence is convected frozen by assumption as defined in Eq. (3.4), meaning that the integral time scale of turbulence would tend to infinity and the time correlation of $\mathcal{U}$ is independent of the temporal separation τ, resulting in the model only accounting for convection effects. In general, the time correlation can be described using a Taylor's hypothesis $\langle \mathcal{U}(\boldsymbol{x},t)\,\mathcal{U}(\boldsymbol{x},t+\tau)\rangle \rightarrow \delta(\boldsymbol{r}-\boldsymbol{u_c}\tau)\mathcal{R}_\mathcal{U}(\tau)$, where $\boldsymbol{u_c}$ is the convection velocity which can be supplied, for example, from a RANS simulation. Following [152], turbulence is a chaotic mixing process and for some jet noise cases (see [144] [153]) a time de-correlation model was proposed, where instead of simulating a convected frozen velocity pattern a turbulent evolution is modelled using Langevin equations, ultimately resulting in $D/Dt\,(\mathcal{U}) \neq 0$ condition. Originally, Langevin stochastic differential equations were derived to represent the Brownian motion. [154] In the field of aero-acoustics a similar model applied for the time evolution of a stochastic field was of a natural choice. For example, as described by Ewert *et al.* [55] in application to the Random-Particle-Mesh (RPM) method. In such modified description, the characteristic time of evolving turbulence gives the temporal scale of relaxation of the velocity fluctuations, potentially resulting in a more physical representation of the synthetic turbulence. As a result, temporal properties of the stochastic field $\mathcal{U}$ are modelled via the equation of the form,

$$\frac{D}{Dt}(\mathcal{U}) = -\propto \mathcal{U} + \beta\xi \tag{3.11}$$

where α and β are the Langevin equation coefficients and ξ is the uncorrelated Langevin force, e.g. $\langle \xi(\boldsymbol{x}',t')\xi(\boldsymbol{x},t)\rangle = \delta(t-t')\delta(\boldsymbol{x}-\boldsymbol{x}')$; The first part $-\propto \mathcal{U}$ is deterministic, which is related to the departure of the solution from initial conditions and normally, represented by an exponential decay. The second part, $\beta\xi$ is stochastic which accounts for the

inertial diffusion process with β influencing the strength of the Langevin force term, which has a vanishing average $\langle \xi(t) \rangle = 0$.

There are several issues associated with solving Eq. (3.11). As pointed out in [155] the diffusion process may not be continuous and cannot be represented as a conventional function of time. Thus, being analogous to a Wiener process, Eq. (3.11) should be regarded as a stochastic differential equation, meaning that when coupled to partial differential equations, such as Eq. (2.98) it can be problematic to perform time differentiation. Secondly, the $\propto$ coefficient has to be expressed in terms of a physical temporal correlation which is not trivial.

For simplicity, consider $\mathcal{U}(t)$ as a function of time only and where a total derivative is taken along the stream function moving with the mean flow, which would be an appropriate assumption in a Lagrangian frame of reference such as used in the RPM method and the total derivative simply reduces to $\partial/\partial t \{\mathcal{U}(t)\}$. Then, the exact solution of Eq. (3.11) follows: [154]

$$\mathcal{U}(t) = \mathcal{U}_0 e^{-\alpha t} + \beta e^{-\alpha t} \int_0^t e^{-\alpha t'} \, \xi(t') dt' \tag{3.12}$$

where $\mathcal{U}(0) = \mathcal{U}_0$ at the initial time. Then, using the properties of ξ in Eq. (3.12), the variance of a random process is expressed as [155]:

$$\langle \mathcal{U}(t)^2 \rangle = \left(\langle \mathcal{U}_0^2 \rangle - \frac{\beta^2}{2\alpha} \right) e^{-2\alpha t} + \frac{\beta^2}{2\alpha} \tag{3.13}$$

In order to ensure $\langle \mathcal{U}(t)^2 \rangle$ remains constant in time, the condition $\beta = \sqrt{2\alpha \langle \mathcal{U}_0^2 \rangle}$ must be satisfied. Another constraint is related to the time correlation $\mathcal{R}_{\mathcal{U}}(\tau) = \langle \mathcal{U}(t) \, \mathcal{U}(t+\tau) \rangle$ where it is logical to assume that it decays in time as $e^{-\tau/\tau_s}$ and τ_s denotes the integral time scale of the flow. This condition yields $\alpha = 1/\tau_s$ and Eq. (3.11) can be re-written as:

$$\frac{D}{Dt}(\mathcal{U}) = \frac{1}{\tau_s} \mathcal{U} + \sqrt{\frac{2}{\tau_s} \langle \mathcal{U}_0^2 \rangle} \, \xi \tag{3.14}$$

In addition to the above, the correlation of white noise field could be expressed also, as a function of position as considered previously, $\langle \mathcal{U}(\boldsymbol{x}, t) \, \mathcal{U}(\boldsymbol{x}, t+\tau) \rangle \rightarrow \delta(\boldsymbol{r} - \boldsymbol{u_c}\tau) e^{-\tau/\tau_s}$ where $\mathcal{R}_{\mathcal{U}}(\tau) = e^{-\tau/\tau_s}$. It can be verified that for a frozen turbulence $\tau_s \rightarrow \infty$ and the right-hand side of Eq. (3.14) vanishes, and only the convection effects are left in place. In essence, the flow convection can be included in the correlation of the white noise field as shown below.

$$\mathcal{R}_{wf}(\boldsymbol{r}, \tau) = \exp\left[-\frac{\pi |\boldsymbol{r} - \boldsymbol{u}_c \tau|^2}{4 l_s^2} \right] \tag{3.15}$$

The time scale of turbulence, τ_s, is a function of the turbulence dissipation rate, ϵ, and a weak function of the Reynolds number. The definition of τ_s relies entirely on the empirical scaling procedure [95] and its validity remains rather questionable. For example, as suggested in [155] $\tau_s \sim 2k/C_0\epsilon$ where $C_0 = 2.1$ is an empirical constant. Moreover, due to lack of

smoothness, modelling the time-dependence of vortex sound sources with a standard Langevin model may give rise to spurious oscillations and therefore, realisation of a modified treatment could be preferred, such as using the second order Langevin model instead. Thus, in [156] Eq. (3.14) is modified by introducing a stochastic source W that is a continuous function and also assumed to be correlated with the white noise field $\mathcal{U}$. The second order Langevin model is given by:

$$\begin{cases} \frac{D}{Dt}(\mathcal{U}) = \frac{1}{\tau_s}\mathcal{U} + W \\ \frac{D}{Dt}(W) = -\gamma W + \sqrt{2\gamma\langle W_0^2\rangle}\xi \end{cases} \tag{3.16}$$

Following the derivation in [156], $\gamma = 1/\tau_d - 1/\tau_s$ where τ_d is the characteristic time scale of W, $\tau_d \ll \tau_s$ and is of the order of Kolmogorov time scale. The initial condition, $W_0 = W(0)$; and the Langevin force ξ is still uncorrelated with $\mathcal{U}$ and W. If the frozen turbulence is assumed, both τ_d and τ_s tend to infinity and the right-hand side vanishes, making the formulation consistent with simplified definitions Eq. (3.2-3.4).

Notably, the results presented in [156] in application to fan noise are in very close agreement between considering frozen and evolving turbulence concepts, where in the latter case a calibrated time correlation having a smooth solution was employed that produced a marginal difference if any, judging from far-field SPL spectra comparison. For the benefit of the doubt, it is thought that for airframe noise applications it can be advantageous to use a frozen turbulence assumption, the correlation Eq. (3.15), which would not only eliminate extra complexity brought in with the use of the Langevin equation but importantly, abolish the supplemental empirical scaling τ_s and τ_d, thus, making the model rely on the minimum number of fine-tuning parameters where at this stage only the length scale augmentation in Eq. (3.8) through empirical scaling applies.

The unsteady perturbation quantities $\boldsymbol{u}'$ and $\boldsymbol{\omega}'$ necessary for a source description Eq. (2.99) can be derived from the fluctuating stream function Eq. (3.1):

$$\boldsymbol{u}' = \nabla \times \boldsymbol{\psi} \tag{3.17}$$

Considering a source calculation on a 2D plane,

$$u' = \frac{\partial \psi_3}{\partial y}, \qquad v' = -\frac{\partial \psi_3}{\partial x} \tag{3.18}$$

and the *z*-component of the fluctuating vorticity, ω_3', is the vorticity in *x*-*y* plane, is evaluated via second order differentiation, which for a 2D source representation reads:

$$\omega_3' = -\frac{\partial^2 \psi_3}{\partial x^2} - \frac{\partial^2 \psi_3}{\partial y^2} \tag{3.19}$$

3.2.2 Numerical discretisation

In order to obtain the fluctuating stream function component $\psi(\boldsymbol{x}, t)$ in Eq. (3.1) numerically, a random white-noise field $\mathcal{U}$ is represented by Lagrangian particle tracers which carry random numbers.

$$r_i(t) = \int_{\Delta V_i} \mathcal{U}(\boldsymbol{x}', t) d\boldsymbol{x}' \tag{3.20}$$

In Eq. (3.20) r_i is a random component and ΔV_i is the ith control volume of the source domain. Furthermore, the continuous integral Eq. (3.1) is approximated through a finite sum over M non-overlapping control volumes

$$\psi(\boldsymbol{x}, t) = \sum_{i=1}^{M} \hat{A}_i(\boldsymbol{x}) G_i(\boldsymbol{x}) \langle \mathcal{U}_i \rangle \Delta V_i \tag{3.21}$$

where $\langle \mathcal{U}_i \rangle \cong r_i / \Delta V_i$ represents the average of the white noise field over ΔV_i and in the limit of infinitely small subdomains $\Delta V_i \to 0$, the above equation is a consistent approximation to Eq. (3.1).

Collectively, the stochastic particles follow the definition of Eq. (3.2) and are evenly seeded over the mesh in the region not occupied by the geometry. In essence, when the concept of a white noise field is put into a discrete form, the range of a random value becomes associated with a particle volume. [57] Since the number of particles per cell required to realise the concept of a white noise field and dimensions of a Cartesian grid are user-prescribed, the particle volume, V_p, is computed as the volume of the fluid domain divided by the total number of particles. In the following step, random values are generated in the range proportional to $\pm\sqrt{3 \cdot V_p}$. Assuming, the particle volume is constant, the mean square of all random values assigned to particles should equal the particle volume. This represents an ensemble average which value is verified by conducting a simple comparison test. As the simulation progresses, these particles are convected with the local mean flow inside the defined FRPM source region. During run-time, particles that leave the domain due to the mean flow convection are substituted by new particles at the in-flow boundary to preserve the same particle density in the flow domain. At every time step, a set of random values are interpolated onto the neighbouring Cartesian mesh node (as shown in Figure 10). This represents an approximation to the convective white-noise field. Information on the source scaling amplitude, Eq. (3.10), the length scale, Eq. (3.9), which is used in the correlation model Eq. (3.15), as well as the mean flow velocity is stored on the background mesh. At this point one may choose to strictly follow the theoretical model when discretising a stochastic stream function Eq. (3.1) and thus, evaluating $\hat{A}(\boldsymbol{x}')$ and $l_s(\boldsymbol{x}')$ at the $\boldsymbol{x}'$ location for weighting a random field. Alternatively, it is possible to perform filtering using data stored at the nodes, $\hat{A}(\boldsymbol{x})$ and $l_s(\boldsymbol{x})$. In this work the latter option, given by Eq. (3.21), is preferred which is computationally more efficient but the results between two formulations can differ, especially if a fundamental mean quantity used in the cross-correlation, such as the length scale, is not a smooth function in space.

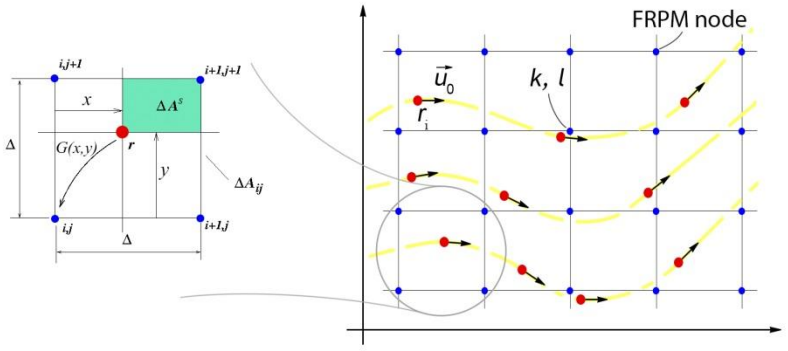

Figure 10 – Random particles on mesh and area-weighting, denoting a bi-linear interpolation from particle to the grid point and vice versa. $G(x,y) = \Delta A^s/\Delta A_{ij}$, where ΔA_{ij} denotes the cell centred area related to lower left point i and $\Delta A^s(x,y)$ is the depicted solid area that is a function of space related to cell's area.

It is worth noting that a Gaussian scaling amplitude given by Eq. (3.9), which 2D and 3D definition is provided, e.g. in [56] is specified for the unity scaling $\overline{\psi(\boldsymbol{x},t)\psi(\boldsymbol{x},t)} = 1$ for $\hat{A} = 1$. As a result of area weighting, shown in Figure 10, an additional mesh related scaling must be enforced. The FRPM method employs an auxiliary Cartesian grid, meaning that scaling can be performed as function of the mesh width Δ. Hence, there are two successive convolutions, first with a $\{1 - |x|/\Delta\}$ function for $|x| < \Delta$ followed by Eq. (3.9) and the result of that is convolved with a Gaussian subsequently giving a filtered field. In summary, the amplitude in Eq. (3.9) needs to be adjusted to account for the first Δ convolution, which for 2D is a factor of $1/\Delta^2$, so that in a simulation the turbulent kinetic energy does not vary with the FRPM grid density.

In this work, the FRPM method is used as an acoustic source generator in the framework of the Altus code and a few words on implementation of specific details deserve attention. Primarily, the maximal integral length scale $l_{D(max)}$ for which a Gaussian can be supported by the FRPM domain[5] is calculated using dimensions of the auxiliary mesh together with a user-specified value for the Gaussian cut-off amplitude, a_c. A small constant value, usually in the range $a_c \sim 0.001 \cdots 0.1$, is used to improve computational efficiency and cut-off the unwanted "tail" of a Gaussian function, which influence is considered negligible. At this point it is convenient to introduce anisotropy that can be used as additional length scale weighting in each direction, if necessary. Using the above measures, the parameter R is then derived as shown in Eq. (3.22), denoting a cut-off radial distance for which Gaussian amplitude is negligible. Subsequently, the parameter $N \sim R/\Delta$ (evaluated as the integer value + 1) is introduced denoting a number of auxiliary cells to consider in each direction for which Gaussian amplitude would not be negligible.

$$R = \sqrt{-\frac{2l_s^2}{\pi} \cdot \log(a_c)} \tag{3.22}$$

[5] During the initialisation of the acoustic solver, $l_{D(max)}$ serves as a guide.

Finally, the distance squared between points of interest, $\boldsymbol{x}$ and $\boldsymbol{x}'$, is evaluated in each direction and used in the numerator of the Gaussian filter, Eq. (3.7). As discussed in [57], using a Gaussian type filter one can take advantage of a Gaussian separation property in discretised equations. Thus, it is possible to compute the Gaussian kernel as a product of kernels in each direction of a problem. By using a pre-computed area-weighting kernel on a background mesh that incorporates the statistics of the local mean flow solution, and applying the additional weighting with the amplitude $\hat{A}(\boldsymbol{x})$ one can obtain the corresponding solenoidal velocity field as a required input for the acoustic sources. Stochastic noise sources are calculated from the fluctuating stream function by following a standard procedure described by Eq. (3.17-3.19) and then the sources are interpolated onto a CAA grid. Figure 11 presents a diagram showing the FRPM method for source generation being part of a hybrid CFD/CAA approach for airframe noise computation.

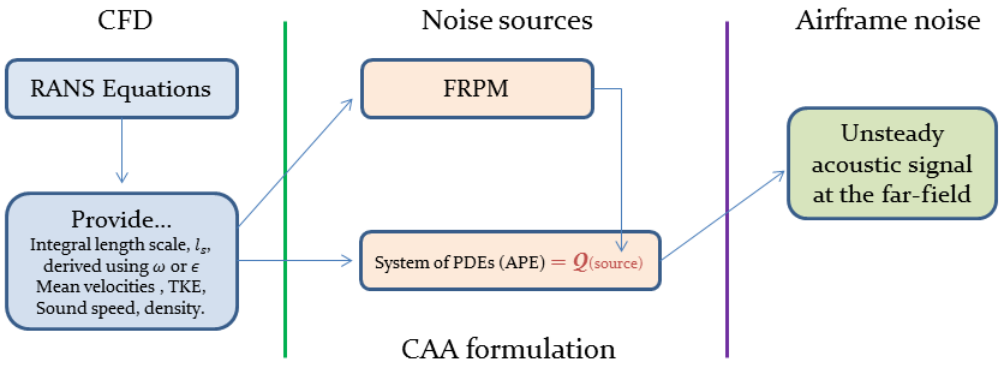

Figure 11 – Diagram of a hybrid CFD/CAA approach where airframe noise sources are obtained via the FRPM method.

3.2.3 Implementation using a Gaussian energy spectrum

In order to verify that the result of Eq. (3.21) after performing a Gaussian convolution yields the correct statistics a simple simulation test case was carried out. A Cartesian grid of arbitrary cell width and spatial dimensions was generated to represent a source domain and the flow parameters were set to constant values. A one point turbulent statistics was collected over a period of time for a chosen variable, u', in Eq. (3.18) which is the fluctuating velocity in x-direction. Figure 12 presents the analytical plot, showing normalised Gaussian correlations where "s" is the correlation size. The time correlations obtained from the FRPM match very closely with the analytical Gaussian profile plotted using Eq. (3.7). A small discrepancy for large s values is associated with fluctuations about zero for the real solution.

Figure 13 shows synthetic turbulent velocity fields obtained via the FRPM method by prescribing constant flow settings for the mean velocity and turbulent kinetic energy, used for convection and the Gaussian amplitude scaling respectively, and a constant length scale.

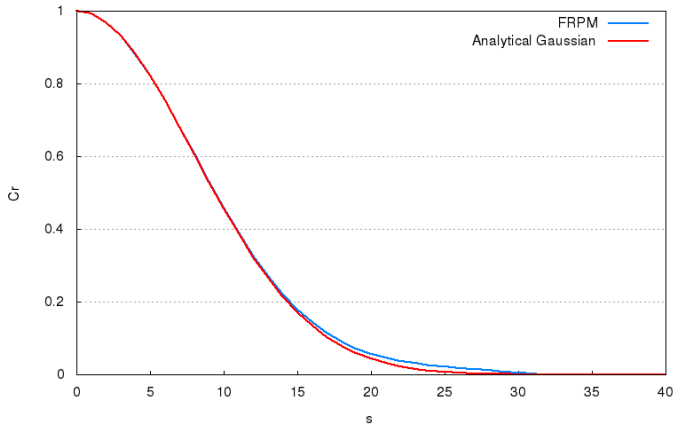

Figure 12 – Comparison of correlations obtained from the FRPM method with a Gaussian function, Eq. (3.7).

Despite that turbulent fields in both Figure 13(*a*) and Figure 13(*b*) are isotropic in nature, a directional pattern can be clearly recognised. This effect is observed since a two-point correlation of the fluctuating velocity field follows a relationship between lateral and longitudinal correlation functions which derivation could be found in Appendix D(II.). Hence, turbulent fluctuations seen in Figure 13 are purely artificial. The test values used for generation of the stochastic velocity fields follow the length scale, $l_s \ll l_{D(max)}$, condition. This condition ensures that turbulent fragments fit inside the domain of interest.

a) *b)*

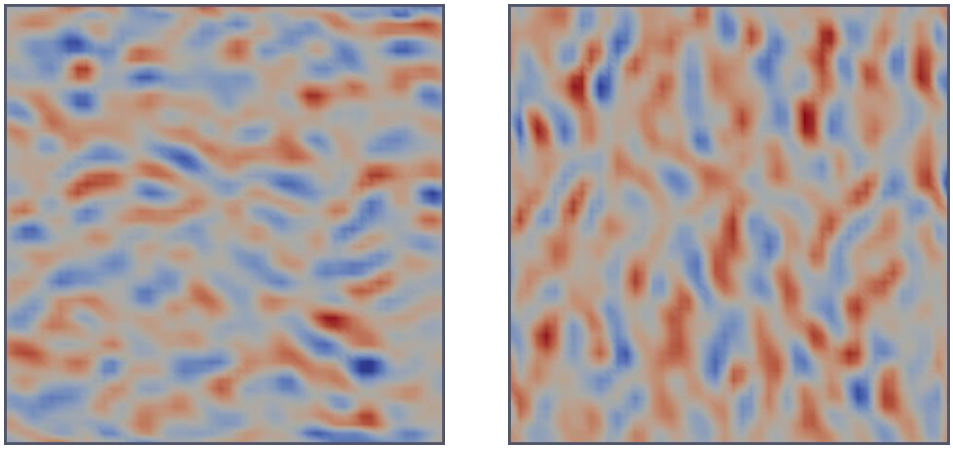

Figure 13 – Instantaneous stochastic velocity fields $\boldsymbol{u}'$ (*a*) and $\boldsymbol{v}'$ (*b*)

Following the result generated in Figure 13, we may try to control the turbulent field generated by FRPM via changing its input parameters. The resulting stochastic amplitudes are a function of kinetic energy as it is used to scale the Gaussian function. Therefore, a realistic estimate of a turbulent kinetic energy (TKE) can be provided. For example, for low Mach number airframe noise problems it is not unusual to find the mean TKE value of 20 m^2/s^2 so it can be picked for this test case. Then, adjusting the cell size according to the smallest length scale of choice should approximately represent the realistic case. The cell

width Δ selection is explained in Chapter 5 for the trailing edge noise benchmark problem. For simplicity, the length scale value is simply reduced in comparison to the one used in Figure 13, which allows keeping the same source domain size. Figure 14 shows the resulting synthetic turbulence fields for the entire FRPM domain which also correspond to the test used to determine autocovariance in Figure 12, which was conducted using constant flow settings as described and without a solid body.

b) *b)*

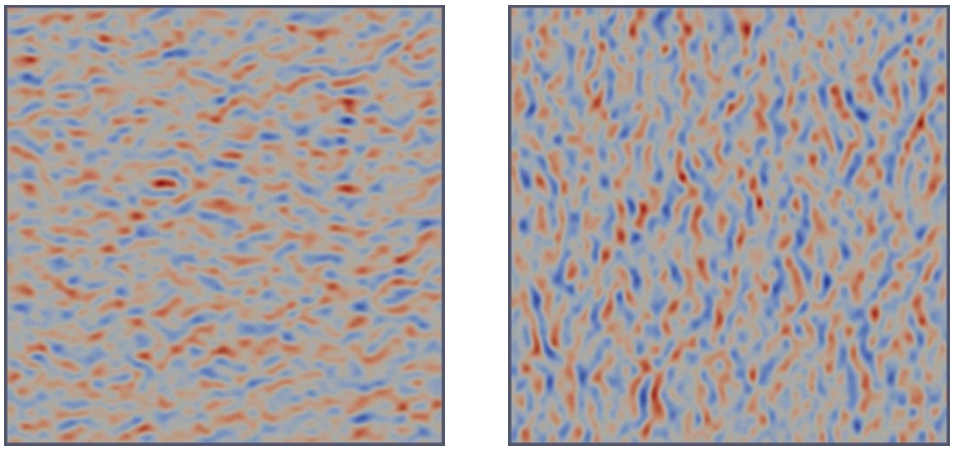

Figure 14 – Instantaneous stochastic velocity fields $\boldsymbol{u}'$ (*a*) and $\boldsymbol{v}'$ (*b*) of typical nature to be found in airframe noise cases

For an airframe noise problem such as in the trailing edge noise case, stochastic velocity fields $\boldsymbol{u}'$ and $\boldsymbol{v}'$ may not necessarily be of the equal magnitude and will depend on scaling using RANS data. In fact, it is often possible to judge if stochastic fluctuations correctly reflect the physics of a particular problem by qualitatively comparing the contour plots that show amplitudes of reproduced fluctuations for different velocity components and corresponding source vector strength. For the test case shown in Figure 14, the amplitude of velocity fields was arbitrarily adjusted only to display stochastic fields of a test case with user specified input. Also, the size of turbulent fragments depends on the characteristic turbulence length scale which in the second test case (Figure 14) was set to a typical value to be found in airframe noise cases.

Similarly, the two point spatio-temporal correlations could be obtained by recording turbulent statistics at a specified separation distance. In Chapter 5 of this work, the two point space time correlations are evaluated for a real problem that is at the aerofoil's trailing edge including the comparison of both, streamwise and normal velocity components with the available experimental validation data.

For qualitative discussions, it may be useful to represent the two point correlation, such as $\mathcal{R}_{wf}(\boldsymbol{r})$ defined in Eq. (3.5), in terms of the wavenumber spectrum. Consider the velocity tensor $\Phi_{ij}(\boldsymbol{\kappa}, t)$ which represents the contribution to the covariance $\overline{\mathcal{U}(\boldsymbol{x}, t)\mathcal{U}(\boldsymbol{x}+\boldsymbol{r}, t)}$ of

different velocity modes with the wavenumber vector $\boldsymbol{\kappa}$. Naturally, $\Phi_{ij}(\boldsymbol{\kappa}, t)$ could be defined as the Fourier transform of the two point correlation.

$$\Phi_{ij}(\boldsymbol{\kappa}, t) = \frac{1}{(2\pi)^n} \iiint_{-\infty}^{\infty} e^{-i\boldsymbol{\kappa}\cdot\boldsymbol{r}}\, \mathcal{R}_{ij}(\boldsymbol{r}, t) d\boldsymbol{r} \tag{3.23}$$

Then, the energy spectrum follows [95]:

$$E(\boldsymbol{\kappa}, t) = \iiint_{-\infty}^{\infty} \frac{1}{2} \Phi_{ii}(\boldsymbol{\kappa}, t) \delta(|\boldsymbol{\kappa}| - \kappa) d\boldsymbol{\kappa} \tag{3.24}$$

Integrating Eq. (3.24) over scalar wavenumbers, κ, and applying Parseval's theorem yields:

$$\int_0^{\infty} E(\kappa, t)\, d\kappa = \frac{1}{2}\mathcal{R}_{ii}(t) = \frac{1}{2}\overline{u_i u_i} \tag{3.25}$$

Eq. (3.25) shows that the energy spectrum in wavenumber space, $E(\kappa, t)$, could be represented via the turbulent kinetic energy contribution from all scales.

The correlation of the velocity field in the FRPM method can be expressed as following:

$$\mathcal{R}_{ij}(r) = \langle u_i'(\boldsymbol{x}, t)\, u_j'(\boldsymbol{x} + \boldsymbol{r}, t) \rangle \tag{3.26}$$

where brackets denote an ensemble average and $r = |\boldsymbol{r}|$. Since the velocities are derived from the stochastic stream function, Eq. (3.1), similarly to Eq. (3.26), it is possible to define a stationary two-point correlation in terms of the stream function, ψ:

$$C(r) = \langle \psi(\boldsymbol{x}, t)\, \psi(\boldsymbol{x} + \boldsymbol{r}, t) \rangle \tag{3.27}$$

As the next step, transforming the correlation Eq. (3.27) into a wavenumber space and following the definition given in Appendix D we arrive at the formulation, Eq. (3.29).

$$C(r) = \frac{1}{(2\pi)^n} \iiint_{-\infty}^{\infty} \hat{C}(\boldsymbol{\kappa}) e^{-i\boldsymbol{\kappa}\cdot\boldsymbol{r}}\, d\boldsymbol{\kappa} \tag{3.28}$$

$$C(r) = \frac{1}{4\pi^2} \int_0^{\infty} \kappa \hat{C}(\boldsymbol{\kappa}) \left[\int_0^{2\pi} \exp\left(i\kappa r \cos(\theta - \alpha)\right) d\theta \right] d\kappa \tag{3.29}$$

where $\boldsymbol{r}$ and $\boldsymbol{\kappa}$ are expressed in polar coordinates. In Eq. (3.29) $\kappa = |\boldsymbol{\kappa}|$, $r = |\boldsymbol{r}|$, and $\alpha, \theta \in [0, 2\pi]$. Moreover, by looking at the integral in Eq. (3.29) above, there is an apparent similarity with the Bessel function of order 0, defined as:

$$J_0(x) = \frac{1}{2\pi} \int_0^{2\pi} \exp(ix \cos\theta)\, d\theta \tag{3.30}$$

If the phase $\alpha = 0$, which is claimed to be a valid assumption for isotropic turbulence, Eq. (3.24) can be expressed in terms of the Bessel function (See Appendix D):

$$C(r) = \frac{1}{2\pi} \int_0^{\infty} \kappa \hat{C}(\boldsymbol{\kappa}) J_0(\kappa r) d\kappa \tag{3.31}$$

The energy spectrum could be related to the correlation tensor $\mathcal{R}_{ij}(\boldsymbol{r})$ and normally, for convenience, the trace of the correlation is considered. Then, by inserting the definition of $\boldsymbol{u}'$ (Eq. (3.17)) into Eq. (3.26) using component indices i, j:

$$\mathcal{R}_{ij}(r) = (-1)^{i+j} \langle \frac{\partial}{\partial x_j} \psi(\boldsymbol{x}) \, \frac{\partial}{\partial x_i} \psi(\boldsymbol{x}+\boldsymbol{r}) \rangle \tag{3.32}$$

Applying properties of partial derivatives in the correlation where the limits of integration depend also on r at infinity it can be assumed $\partial/\partial x_i \, \psi(\boldsymbol{x}+\boldsymbol{r}) \cong \partial/\partial r_i \, \psi(\boldsymbol{x}+\boldsymbol{r})$, yields:

$$\mathcal{R}_{ij}(r) = (-1)^{i+j} \frac{\partial}{\partial r_i} \langle \frac{\partial}{\partial x_j} \psi(\boldsymbol{x}) \, \psi(\boldsymbol{x}+\boldsymbol{r}) \rangle \tag{3.33}$$

For locally homogeneous flows by hypothesis $\partial/\partial x_j \, \langle \psi(\boldsymbol{x}) \, \psi(\boldsymbol{x}+\boldsymbol{r}) \rangle = 0$; and Eq. (3.33) is equivalent to:

$$\mathcal{R}_{ij}(r) = (-1)^{i+j+1} \frac{\partial}{\partial r_i} \langle \psi(\boldsymbol{x}) \frac{\partial}{\partial x_j} \, \psi(\boldsymbol{x}+\boldsymbol{r}) \rangle \tag{3.34}$$

$$\mathcal{R}_{ij}(r) = (-1)^{i+j+1} \frac{\partial^2}{\partial r_i \partial r_j} C(\boldsymbol{r}) \tag{3.35}$$

Performing the second order partial derivative of $C(\boldsymbol{r})$ with respect to r_i and r_j using the chain rule gives:

$$\frac{\partial^2}{\partial r_i \partial r_j} C(\boldsymbol{r}) = \delta_{ij} \frac{1}{r} \frac{d}{dr} C(\boldsymbol{r}) - \frac{r_i r_j}{r^3} \frac{d}{dr} C(\boldsymbol{r}) + \frac{r_i r_j}{r^2} \frac{d^2}{dr^2} C(\boldsymbol{r}) \tag{3.36}$$

After some re-arrangements, half the trace of the correlation $\mathcal{R}_{ij}(r)$ is given by: (Also, see [52] and Appendix D (II.))

$$\mathcal{R}(r) = \frac{1}{2} \left[\mathcal{R}_{ii}(\boldsymbol{r}) + \mathcal{R}_{jj}(\boldsymbol{r}) \right] = -\frac{1}{2} \left[\frac{1}{r} \frac{d}{dr} C(\boldsymbol{r}) + \frac{d^2}{dr^2} C(\boldsymbol{r}) \right] \tag{3.37}$$

The relation between the correlation of velocity field and the correlation of the stream function $C(r)$, Eq. (3.32) can be obtained in a wavenumber space by using the properties of Fourier transform of the Bessel function as in Eq. (3.26):

$$\mathcal{R}(r) = \frac{1}{8\pi} \int_0^\infty \kappa^3 \, \hat{C}(\boldsymbol{\kappa}) \left[\frac{2}{\kappa r} J_1(\kappa r) + J_0(\kappa r) - J_2(\kappa r) \right] d\kappa \tag{3.38}$$

where J_0, J_1 and J_2 are Bessel functions of zero, first and second order respectively with the following relation: $J_1(\kappa r) = kr[J_0(kr) + J_2(\kappa r)]/2$; where '2' is the dimension.

$$\mathcal{R}(r) = \frac{1}{4\pi} \int_0^\infty \kappa^3 \, \hat{C}(\boldsymbol{\kappa}) J_0(kr) d\kappa \tag{3.39}$$

$$\hat{\mathcal{R}}(\boldsymbol{\kappa}) = \frac{1}{2} \kappa^2 \hat{C}(\boldsymbol{\kappa}) \tag{3.40}$$

Eq. (3.40) above is obtained when comparing to Eq. (3.31) which is given for 2D following the formulation in Eq. (3.29). The Fourier transform of half the trace, $1/2\,[\mathcal{R}_{ii}(\boldsymbol{r})]$; is $\hat{\mathcal{R}}(\boldsymbol{r}) = \Phi_{ii}(\boldsymbol{\kappa})/2$; and comparing to Eq. (3.40), the velocity tensor is:

$$\Phi_{ii}(\boldsymbol{\kappa}) = \kappa^2 \hat{C}(\boldsymbol{\kappa}) \tag{3.41}$$

Using the definition for the energy spectrum, Eq. (3.24):

$$E(\kappa) = \oint \frac{1}{2}\,\Phi_{ii}(\boldsymbol{\kappa}) dS(\kappa) \tag{3.42}$$

In general, $\oint dS(\kappa) = 4\pi\kappa^2$ for a sphere in 3D with the radius κ. Here, a 2D definition must be used because the result of Eq. (3.41) is obtained for Eq. (3.40) that uses a 2D formulation. Hence, the closed loop integral is a circle, $2\pi\kappa$. Also, the integral Eq. (3.42) is scaled with $1/4\pi^2$. Then, the energy spectrum defined in term of the velocity spectrum follows:

$$E(\kappa) = \frac{1}{4\pi}\kappa\Phi_{ii}(\boldsymbol{\kappa}) \tag{3.43}$$

As a final step, inserting the definition in Eq. (3.41) into Eq. (3.43) we get the relation between the correlation of the stream function and the energy spectrum:

$$E(\kappa) = \frac{1}{4\pi}\kappa^3 \hat{C}(\boldsymbol{\kappa}) \tag{3.44}$$

By using the properties of a Gaussian filter function, Eq. (3.6) one can re-write Eq. (3.44) in terms of $\hat{G}(\kappa)$ giving the energy spectrum relation:

$$E(\kappa) = \frac{1}{4\pi}\kappa^3 \left|\hat{G}(\kappa)\right|^2 \tag{3.45}$$

When comparing Eq. (3.45) to Kraichnan's definitions of the energy spectrum [140], $E(\kappa) \propto \kappa^3$ for a 2D formulation and $E(\kappa) \propto \kappa^4$ for a 3D case. This is an important result of the analysis where according to Kraichnan the three-dimensional formulation reads:

$$E(\kappa) = \frac{8}{3\pi^3} k l^5 \kappa^4 \exp\left(\frac{-l^2k^2}{\pi}\right) \tag{3.46}$$

and a 2D formulation:

$$E(\kappa) = \frac{2}{\pi^2} k l^4 \kappa^3 \exp\left(\frac{-l^2k^2}{\pi}\right) \tag{3.47}$$

where k is turbulent kinetic energy and l is the integral length scale.

The respective filter in the physical domain, $G(r)$, is obtained by taking the integral of $E(\kappa)$. The definition of Eq. (3.45) makes use of the Gaussian spectrum where terms are re-arranged and compared with a respective 2D formulation, Eq. (3.47). This analysis leads to the definition of the Gaussian filter Eq. (3.7) which when convolved with a white noise field yields meaningful statistics of a fluctuating field.

3.3 Scale decomposition approach for tonal noise mechanism in FRPM

In the previous section, the benefits of the frozen turbulence assumption implied in the FRPM model have been examined when compared to an exponential time de-correlation for the RPM approach in the sense that in the former case an extra empirical scaling procedure is omitted. For the condition in Eq. (3.4), $D/Dt\ (\mathcal{U}) = 0$, the random field is frozen in time and simply convects along the mean flow path. Furthermore, the FRPM model is inherently steady, hence, cannot account for the unsteady effects such as vortex shedding and the resulting acoustic model is not suitable for tonal noise. Wohlbrandt *et al.* [150] have implemented the unsteady model for the sources calculation in FRPM by adjusting Gaussian filter width and amplitude in accordance with URANS as simulation progresses. For turbo-machinery applications a mean flow is expected to vary significantly at the noise sources location as the problem is inherently unsteady. Therefore, in contrast to using a steady RANS input for turbo-machinery applications, the proposed alteration is seen as a natural progression towards accurate broadband noise prediction where accounting for the mean flow unsteadiness potentially yields a more physical realisation of source scaling. Around the same time an unsteady FRPM model was implemented in Altus [93] but with a focus on all-in-one broadband and tonal noise simulations, applying the new mechanism on a NACA 0012 aerofoil with a blunt trailing edge. This work includes a core part of analysis, which consists of the near-field results in Chapters 4 and the corresponding far-field acoustics in Chapter 5. To account for the tonal noise sources with the FRPM model, the present work uses the idea of scale separation and considers of a total velocity fluctuation consisting of the two parts:

$$\boldsymbol{u}' = \boldsymbol{u}'_f + \boldsymbol{u}'_L \tag{3.48}$$

where $\boldsymbol{u}'_f$ is the 'fine-scale' fluctuating velocity component obtained from stochastic particles in accordance with the original FRPM scheme and $\boldsymbol{u}'_L$ is the 'large-scale' fluctuating velocity component. The latter can be obtained from a vortex-shedding resolving unsteady RANS (URANS) solution as a fluctuation of the time mean:

$$\boldsymbol{u}'_L = \boldsymbol{u}_{URANS}(t) - \boldsymbol{u}_0, \tag{3.49}$$

where $\boldsymbol{u}_{URANS}(t)$ is the unsteady URANS flow solution and $\overline{\boldsymbol{u}_{URANS}(t)} = \boldsymbol{u}_0$ is its corresponding time-averaged field.

From the resulting velocity fluctuation field Eq. (3.48), the fluctuating vorticity is obtained via a numerical differentiation as in Eq. (3.19) that by definition will also incorporate the $\boldsymbol{u}'_L$ term. The resulting velocity and vorticity fields are then manipulated into the governing acoustic source equations, Eq. (2.99).

In a classic approach when considering a RANS solution input, problem solving is sub-divided into two parts – source generation performed on the FRPM side and acoustic wave propagation on the CAA side. By using a URANS input instead, the source generation

problem gains an additional temporal dependence associated with 'large-scales', which could be thought of in terms of a CFD time step. At every CFD time step $\boldsymbol{u}_L'$ is evaluated following Eq. (3.48) in accordance with the updated $\boldsymbol{u}_{URANS}(t)$ flow solution. This adds further options in terms of filter scaling. For example, the integral length scale l_s in Eq. (3.9) and the amplitude $\hat{A}$ in Eq. (3.10) could be evaluated from URANS. Essentially, the mean flow used for FRPM source calculation has to be substituted (re-mapped) at every CFD time step, where quantities such as the local turbulent kinetic energy, k, and the specific dissipation, ω, which influence the filter amplitude and width, could be chosen as the time-averaged or instantaneous values from URANS. By assumption, in the vicinity of a blunt trailing edge the fine scale fluctuations, $\boldsymbol{u}_f'$, would be more physically represented in a changing velocity field, i.e. using URANS flow data. However, this assumption has to be verified by conducting simulations with one changing parameter at a time. Since this approach is novel, the influence of time-varying amplitude $\hat{A}$ as well as time-varying filter width on trailing edge noise sources has to be established first. Then, results are compared to a classic FRPM model where filter scaling is based on time-averaged data from RANS. After gaining confidence in modelling, the all-in-one broadband and tonal noise mechanism is tested on the blunt trailing edge aerofoil noise problem. In the final modification presented in this work, besides a vortex-shedding calculation on an auxiliary Cartesian grid, which is sufficient for obtaining large scale fluctuations, unsteady flow data is efficiently used accomplishing new capabilities of a Gaussian filter.

For low Mach number flows of interest in the current work, the acoustic propagation velocity is much larger compared to the hydrodynamic velocity. In application to the FRPM model this means that the acoustic time scale is very small as compared to the time scale required for the stochastic particle to travel any appreciable distance, in particular to traverse between the FRPM Cartesian grid cells. The same applies to the vortex shedding effect which scales with the local mean flow velocity rather than sound speed, allowing the URANS solution to march in time with a very large time step as compared to the acoustic wave propagation solution. To exploit the difference in the time scales, following [11], further computational savings are achieved by keeping the time step of the effective noise source computation an order of magnitude, 10 times larger in this case, in comparison with the acoustic propagation time step and using a linear interpolation to obtain the acoustic source distribution at the intermediate time steps. Following this procedure for 2D aerofoil cases, the acoustic source generation part of the model takes only a fraction of a cost of the entire run time, most of which is spent on computing the acoustic wave propagation. Therefore, the new modification for tonal noise presented in this section has not affected the run-time significantly. For trailing edge noise problems implemented in this work, it was discovered that wall clock times are consistent with FRPM simulation runs performed in [62]. In this work, a 2.5D acoustic grid consisting of 3~4M degrees of freedom and the auxiliary Cartesian grid with approximately $300 \times 85 \times 2$ (x, y, z) points were used. Computational times ranged between 40 and 60 hours per case depending on achieved frequency resolution on a small cluster of 64 computational cores where only 4 cores were attributed to FRPM. It must be noted that for problems presented in Chapter 5, wave propagation is resolved up to an observer meaning

that wall clock time estimates also depend on the distance between the source and the observer. An initial stage of the simulation is called the spin-out time which is defined as the time period required for reaching a statistically stationary acoustic solution. For trailing edge noise problems presented in Chapter 5, the spin-out time takes several through-flow times of acoustic wave propagation across the domain and the pressure data recorded at the observer's location from the beginning of the simulation, while the acoustic wave has not reached the microphone, is simply cut out from the analysis.

Chapter 4

Flow solutions to the benchmark cases

This chapter presents flow solutions to the benchmark cases reviewed in Chapter 1. First, a comparison of the ideal flow past a circular cylinder using CABARET and ANSYS Fluent solvers is presented in section 4.1 following with the discussion of issues faced when solving this challenging case using the MILES method in Section 4.2. Using the experience gained in solving the cylinder problem in the second part of Chapter 4 aerofoil flow simulations are computed with the CABARET MILES method where various boundary layer tripping techniques are used for overcoming the grid resolution limitation with modifications discussed in details. Also, RANS/URANS methods are used for computing the mean flow past aerofoils with both sharp and blunt trailing edges. Numerical simulations are set up in accordance to the flow settings of corresponding experiments where both experimental cases make use of tripping devices located on a leading edge for triggering an early flow separation. In the RANS simulation a fully turbulent boundary layer assumption applies and no transition modelling was attempted so that mean flow results could be more easily reproduced by other researchers. To compensate for modelling inaccuracy, the shedding frequency obtained from the URANS simulation was adjusted by slightly changing the trailing edge thickness. Finally, the reconstruction of the unsteady flow field using the FRPM method which statistics are based on the RANS input is demonstrated for sharp and blunt trailing edge cases. Properties of the FRPM solution are presented and discussed. These include the analysis of an instantaneous signal in the wake zone behind the blunt trailing edge to support the hypothesis of scale separation presented in Section 3.3. Also, for the flow solution validation, velocity correlations are compared with available experimental data for the sharp trailing edge case.

4.1 Ideal flow past a circular cylinder (CABARET vs. standard second order density-based finite-volume scheme from Fluent)

In this Section, the ideal flow test is performed to give an indication of the numerical dissipation within the applied schemes. Initially, the least dissipative scheme available in the commercial solver has to be identified among several options. The two popular Fluent schemes tested include SIMPLE which is pressure-based and Roe Flux-Difference Splitting (Roe-FDS) which is density-based. The flow around the cylinder is mildly compressible with

a Mach number of 0.2. The absence of excessive numerical entropy generation means the method is low dissipative. This is a major requirement on accuracy, especially for acoustic sensitive simulations, as discussed by Hirsch. [24] The pressure coefficient for an ideal flow around a cylinder can be calculated analytically by using the Joukowski transformation in the complex plane, then expressing the velocity components through velocity potential and using Bernoulli's theorem results in the following equation:

$$c_p = \frac{p-p_0}{1/2 \rho u_0^2} = 1 - 4\sin^2\theta \tag{4.1}$$

Test cases are evaluated on a computational mesh, featuring an LES-type near-wall refinement. The mesh has an O-grid topology with a wall resolution $(x^+ = y^+ = z^+) < 5$ and a single mesh layer in the span-wise direction, which is sufficient for the Euler flow test cases. Figure 15 presents the comparison of the surface pressure coefficient between selected Fluent schemes and theoretical distribution, described by Eq. (4.1). From symmetry of the problem and ideal flow conditions only one half has to be considered, either the top or bottom side of a cylinder. The leading edge is referred to as the frontal part of the cylinder facing the flow which is labeled 0° and the trailing edge corresponds to 180° respectively. In Figure 15 the plot depicted by green markers which represent Roe-FDS returns to the value of just below 1 at the trailing edge with sufficiently low dissipation. However, a different result is found for the SIMPLE scheme where the flow has separated at ~150° and the pressure coefficient does not return to the initial value. The separation would be clearly visible from contours of velocity, which has occurred due to the artificial viscosity that gets introduced for stability in the SIMPLE pressure-based scheme implemented in Fluent. This test demonstrates that low numerical dissipation can play a crucial role in capturing the correct flow effects without generating a spurious energy transition from acoustic pressure to vorticity waves.

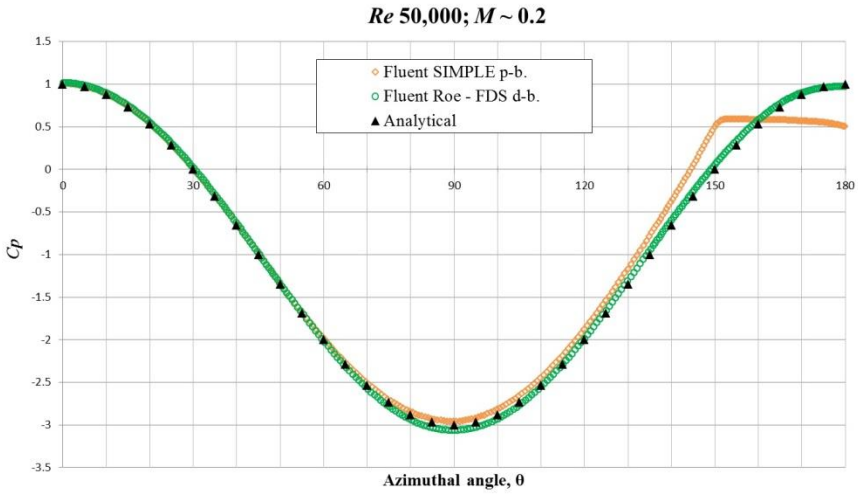

Figure 15 – Plot of the surface pressure coefficient against the azimuthal position shown for top half of the cylinder immersed in the Euler flow; the comparison between selected Fluent models and theory.

Figure 16 shows the velocity trailing edge contours for the Fluent density-based solver Roe-FDS, which has been established to have a superior performance over the SIMPLE scheme, and it is compared to the CABARET scheme. Since both algorithms, Roe and CABARET had not encountered a flow separation the surface pressure comparison alone is insufficient to differentiate between the two. Figure 16 shows contours of velocity for the same number of levels. As part of the initial validation, dissipation levels could be judged qualitatively by examining the trail behind the cylinder where the flow merges. Figure 16 shown the apparent difference between two numerical methods under consideration where the CABARET scheme keeps the symmetry of the velocity profile downstream of the cylinder much better without any notable spurious trailing wake generation in comparison with the Roe scheme solution.

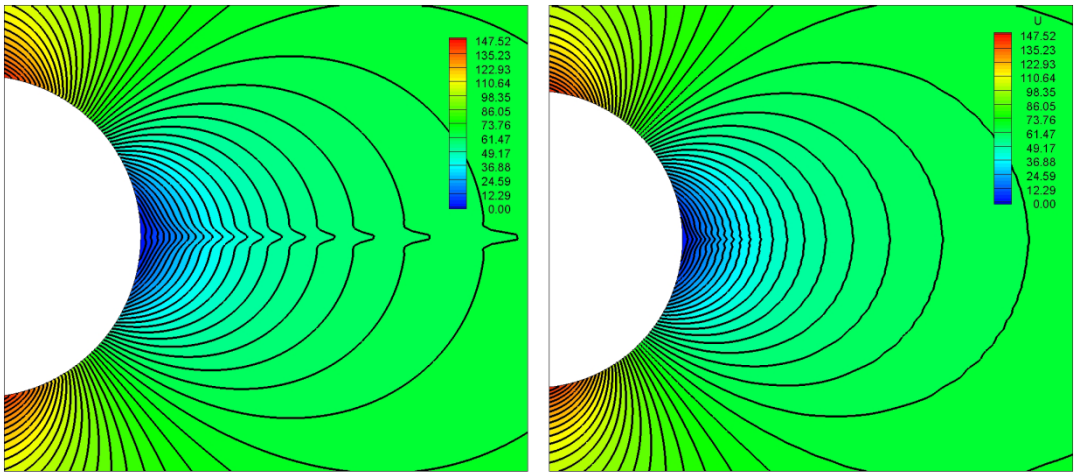

Figure 16 – Contours of *u* velocity for the Euler flow in *x*-*y* plane with the flow direction left to right; Fluent Roe-FDS (*left*), CABARET (*right*)

In addition, it is possible to compare the pressure profiles obtained via numerical modelling with theoretical values derived for the ideal flow. This comparison is essential for both schemes before proceeding with viscous flow or acoustic simulations as it first ensures that idealised numerical solutions agree well with the flow theory. Figure 17 shows the plot of vertical pressure profiles for both numerical schemes in key areas of the field. The pressure profile 'P1' at $x/d = 0.1$ lies within the region of accelerating flow and it also corresponds to the typical experimental measurement location. [59] The midline profile is given for a reference as it starts from the point of a largest pressure drop, which occurs at 90° for the ideal flow. Both solvers are in good agreement with theory for predicting the overall pressure field as found in this test case.

Theoretical results for the pressure distribution around the cylinder, such as plotted in Figure 17 are calculated using the perturbation theory [152] and the potential equation for a mildly compressible flow case (M ~ 0.2) for an ideal gas.

$$\frac{P}{P_\infty} = 1 + \frac{\gamma}{2} M_\infty^2 (1 - \alpha_1) + \frac{\gamma}{2} M_\infty^4 (\alpha_1^2 - \alpha_1 - \alpha_2) \tag{4.2}$$

with the following coefficients:

$$\alpha_1 = 1 + \frac{1}{r^4} - \frac{2}{r^2}\cos 2\theta\,;$$

$$\alpha_2 = \cos\theta\left(1+\frac{1}{r^2}\right)\left[\cos\theta\left(\frac{3}{r^4}-\frac{13}{6r^2}-\frac{5}{6r^6}\right)+\frac{1}{2}\cos 3\theta\left(\frac{1}{r^2}-\frac{1}{r^4}\right)\right]$$

$$+\sin\theta\left(1+\frac{1}{r^2}\right)\left[\cos\theta\left(\frac{13}{6r^2}-\frac{1}{r^4}+\frac{1}{6r^6}\right)+\frac{1}{2}\cos 3\theta\left(\frac{1}{r^4}-\frac{3}{r^2}\right)\right];$$

where r is the distance measured from the centre of the cylinder, θ is the polar angle, taken from the direction of the flow and γ is a constant equal to 1.4.

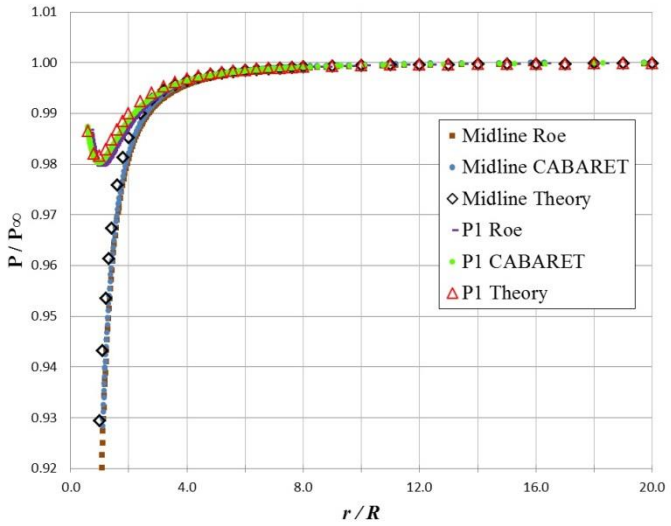

Figure 17 – Vertical pressure profiles comparison of theory and CABARET, 'P1' at $x/d = 0.1$ and 'midline' at $x/d = 0.5$ with the origin at the LE of the cylinder.

4.2 Modelling the flow past a circular cylinder using high-resolution MILES method

Following the encouraging results obtained in the previous section with the Euler CABARET scheme the unsteady flow modelling past the circular cylinder is attempted. A low numerical dissipation in the CABARET scheme is an advantage for modelling the evolution of vortex shedding and for accurately resolving vortical structures at a relatively large distance behind the cylinder, of the order of 10d for the rod-aerofoil benchmark case in diameter units (d). The main difficulty in application of MILES to a circular cylinder case is predicting a floating separation point at the correct location. Mainly fine scales are responsible for the separation mechanism. Hence, it is most challenging to achieve a suitable near-wall grid resolution which is required to resolve these fine scales. At such fine resolutions the computational time step can be a bottleneck. Section 1.3.2 introduced the reference publications from other researchers on this benchmark. For the flow regime considered, currently there is no comparison to a solution which employed implicit LES without the SGS

model. On the other hand, where a SGS model was employed, e.g. in [157], the near-wall resolution of the mesh is estimated to be far too coarse for MILES CABARET. It should be noted that the choice of a SGS model may heavily influence the flow solution past a circular cylinder since the flow separation mechanism on a coarse grid is purely empirical. To remain within the class of high-fidelity methods, our only estimate for the required grid resolution to resolve all scales comes from the Reynolds scaling which indicates that a maximum permitted wall $x+$, $y+$ and $z+$ required to resolve the smallest eddy should be approximately equal 0.3.

In the current simulation set-up the rod diameter is equal to 0.01 m. The inflow velocity is 72 m/s which corresponds to the free-stream Mach number of about 0.2. The flow case is conducted for the standard atmospheric pressure and temperature $\mathrm{T} = 293$ K, and the Reynolds number of the simulation is circa 48,000. The rod shedding frequency that is the characteristic frequency of the problem is expected to be in the region of 1.3 kHz.

The problem is sub-divided into two parts according to the pursued strategy that is firstly, investigating whether the method of choice is capable of predicting the separation point correctly via resolving 'enough' of the fine scales which are ultimately responsible for the separation mechanism. Secondly, the wake zone can be incorporated when a sufficient near-wall resolution is determined. In the first case, a simple O-grid is specifically designed to resolve vortices only within a close proximity of the cylinder, which is within ~1d behind the trailing edge. Consequently, the vortex pair formation and re-circulation is simulated which affects the shear layers and the floating separation. Therefore, for the first part of investigation, the vortex shedding does not need to be fully resolved over a large distance and following this strategy allows saving on the total number of elements which is particularly important as this problem is computationally demanding.

Alongside the numerical investigation into the required grid resolution for capturing the correct separation point a mesh incorporating a wake zone has been developed. Alterations in the near-wall region were introduced step-by-step constantly referring to the first part of the problem. Figure 18 shows the final version of the computational domain in *x*-*y* plane designed for capturing a vortex street. The domain extends from -15d to 25d in the streamwise direction and from -15d to 15d in the crosswise direction. The extent of the computational domain in the spanwise *z*-direction, which is assumed to be the homogeneous direction of the problem, is up to 5d for the biggest simulation tested. The spanwise extension was selected in accordance with recommendations in [59] where experimentally measured pressure coherence function for the peak frequency was found to be correlated for over 5-7 rod diameters. For the simulation which includes the wake, the *x*-*y* computational domain is covered by a multi-block 2D C-grid which is body-fitted around the rod and is roughly Cartesian in the wake region in all three dimensions. The 3D grid is generated by stacking the 2D slices in *z*-direction and the mesh is generated using the standard CFD package (ICEM). However, it has been quickly recognised that for the first mesh cell requiring $y+ < 1$ it is nowhere near affordable to maintain the aspect ratio of 1, which is assumed standard for 'LES-type' grids. For this problem it has been a significant restriction when using a large

cylinder span length required for simulating fine scale three-dimensional structures so it is regarded as a compromise.

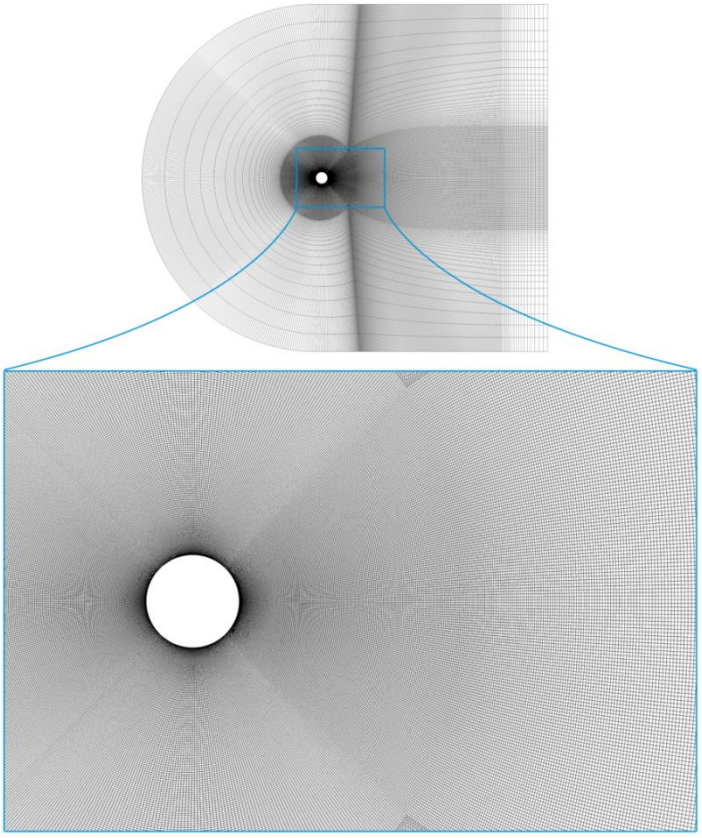

Figure 18 – Computational grid in *x*-*y* plane

Table 3 shows the wake zone grid comparison with meshes used in [83] for a similar flow case. The "check point from central axis" column denotes distances measured from the midpoint of the cylinder in *x*-*y* plane, followed by the actual diameter used and the largest cell width Δ with reference to the diameter independent of the direction. The last column in Table 3 shows the number of mesh points per diameter in *y*-direction which is where the reference profiles are to be measured. [59] The reference points for the LES solution also apply to the mesh used for testing the separation apart from the three '*U-profiles*' where the computational mesh was deliberately coarsened. It could be noted that the grid resolution in the wake region of the LES case is much finer than that of DES, mainly because of the $x+$ requirement which then enforces extra constraint to the wall normal resolution when the cell is maintained roughly Cartesian. For the largest simulation with the wake zone, $y+ \sim 5$ is achieved in the wall-normal coordinates and $\Delta x \cong 3\Delta y$ next to the wall. There were 256 mesh points in the spanwise direction over 5 diameters with $\Delta z \cong 4\Delta x$ to maintain a low aspect ratio cuboid shape in the wake zone. The total grid size was around 52 million cells.

Simulation run	Re	Grid	Check point from central axis (*x*,*y*)	Ref. d (m)	Δ/d	mesh pnts./d
DES LS2*	50,000	Medium	0.75, 0.5	1.0	0.048	
DES LS3*	50,000	Fine	0.75, 0.5	1.0	0.034	
MILES	48,000	Wake**	0.0075, 0.005	0.01	0.017	
			0.025, 0 (*2d behind*)	0.01	0.023	43
			0.013, 0 (*ref. U profile*)	0.01	0.017	82
			0.0745, 0 (*second U profile*)	0.01	0.053	22

* DES simulation cases of Travin *et al.* [83]

** Corresponds to the largest simulation having 5d in *z*-direction.

Table 3 – Computational grid comparison with a well-documented case [83] at the specified check points.

Finally, for the first part of the numerical investigation that is related to modelling the separation a mesh with a target y+ of 0.3 has been put to the test using GPU computing. However, it was still nowhere near as affordable to use the comparable $x+$ as it would almost approach the DNS resolution. In our case the finest $x+ \sim 1$ and a limited span width ($z/d = 0.1$) had to be used due to reaching the limit of computational resources. The computational time step was less than 1/2 of a nano-second.

Figure 19 shows instantaneous contours of velocity in a close proximity of the cylinder where separated shear layers form turbulent eddies after a short transition. Following a laminar separation, instability in the shear layers grows, resulting in a burst of turbulence. Afterwards, the recirculation and shedding of vortices takes place. A sequence of slides is reproduced from the animation for the finest simulation run with a wall $y+$ of 0.3. In Figure 19(*a*) the formation of two counter-rotating large vortices can be observed. The stage depicted in Figure 19(*a*) is associated to an early stage of the simulation. As vortices keep on rotating inwards due to a pressure drop in the separated region their size increases reaching the point when one vortex displaces the other as seen in Figure 19(*b*) and convection effects carry one of the two vortices downstream. From Figure 19(*c*) it can be seen that the bottom vortex has left and the area behind the cylinder becomes solely occupied by the top vortex. Since it is no longer supported by the bottom fluid layers, following further growth, the trailing edge vortex rapidly follows the previously departed vortex, convecting downstream.

a) *b)* *c)*

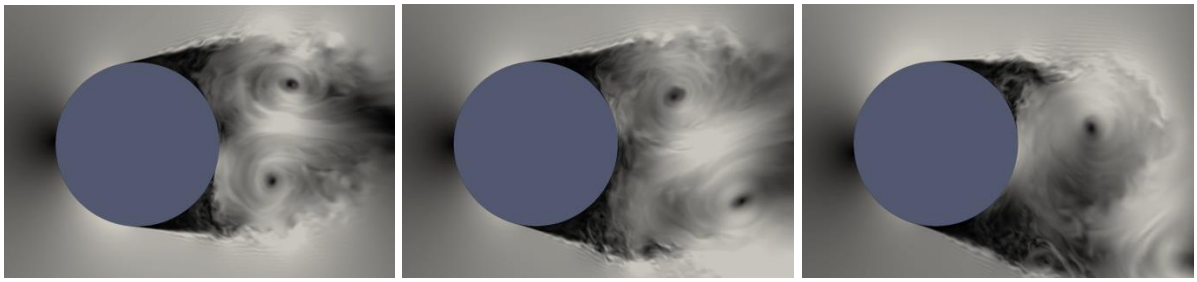

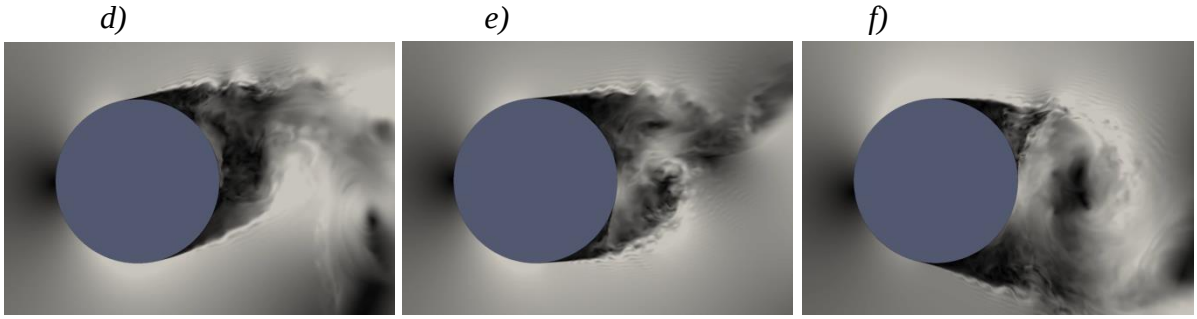

Figure 19 – Instantaneous contours of velocity showing key flow evolution stages within one vortex shedding period past a circular cylinder.

At this moment in time simulated flow instability is observed as depicted in Figure 19(*d*) and the flow swings to one side. The flow around the cylinder acts on the separated layers attempting to line them up in the direction of the mean flow and the new vortex pair formation takes place as seen in Figure 19(*e*) with the trail from the recirculating vortex being still visible on the outmost right side of Figure 19(*e*). The trail can be regarded as the connection between vortex pairs. (For example, see Figure 20) Finally, Figure 19(*f*) shows the vortex swing the other way depicting the sliding separation point throughout the flow evolution stages. This visualisation further confirms that for the considered flow regime the formation of laminar shear layers is influenced by the simulated vortex pair.

Figure 20 shows instantaneous contours of vorticity magnitude obtained on the wake-resolving grid previously shown in Figure 18. It can be seen that for propagating vortices the highest magnitude is found at a vortex midpoint being the part with a quickest rotation. This is physical due to the vortex scale. In the close proximity behind the trailing edge the flow is highly turbulent with the smaller size eddies mixing and forming large scale circulating eddies.

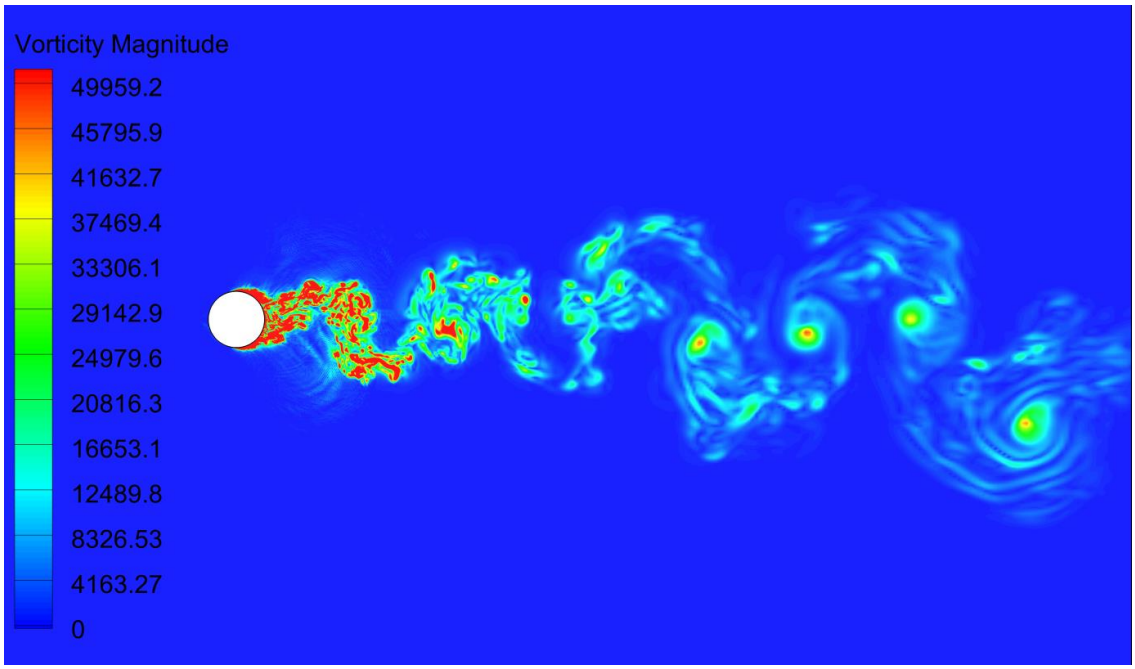

Figure 20 – Instantaneous contours of vorticity magnitude shown on the wake-resolving grid.

The plot in Figure 21 shows the comparison for the time-averaged surface pressure coefficient between numerical simulations and experimental data of Norberg *et al.* [158]. The DES simulation of Travin *et al.* [83] which mesh details are provided in Table 3 (see LS3 case) achieved an excellent agreement to the experiment. An attempt to reproduce similar results using the Spalart-Allmaras DES model available in ANSYS shows that it is no match for the in-house code of Travin *et al.* [83]. Figure 21 clearly shows that c_p is over-predicted for the part where the largest pressure drop is seen. This difference could be due to model calibration specifics.

In the experiment it was reported that the average separation point is situated at ~80° [158] and the range of sliding of the separation point for this flow regime should be within 70°~90° as discussed by Zdravkovich [84]. In the CABARET simulation on the finest grid the average separation point was closer to 90° with approximately the same range for the sliding point centred about the separation, meaning that the separation is slightly delayed in comparison to the experiment.

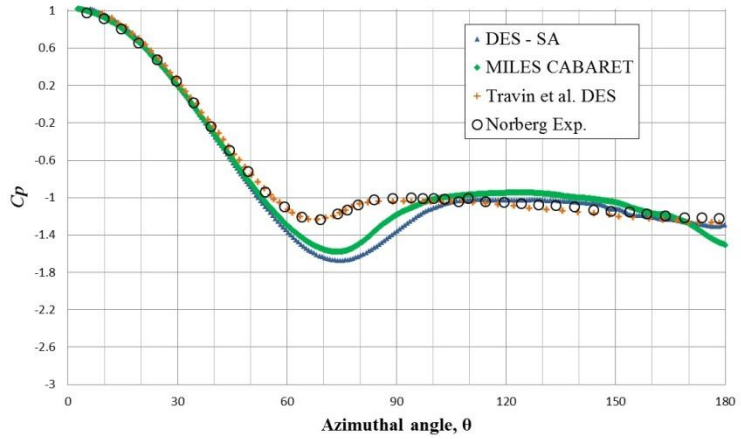

Figure 21 – Plot of the surface pressure coefficient against the azimuthal position shown for top half of the cylinder for MILES CABARET on the finest grid, ANSYS DES SA and DES of Travin *et al.* [83] compared to the experimental data of Norberg *et al.* [158].

The investigation into grid resolutions which ultimately led to the finest affordable grid producing the closest separation point to the experiment just shows how challenging this case is for the MILES CABARET method. The time averaged velocity profiles measured downstream would be sensitive to the azimuthal location of the separation point as the slight shift in the vortex formation (e.g. in Figure 19) due to the behaviour of separated shear layers will affect the resulting profile. Moreover, the vortex shedding frequency increases with increasing azimuthal angle of the separation point. For the finest MILES CABARET simulation run it was only affordable to resolve the turbulent wake in a close proximity of the cylinder where beyond ~1d behind the trailing edge the grid density has been rapidly increased. Hence, it has not been possible to produce reliable mean and rms-velocity profiles at this stage which is left for the future work. Also, with a relatively large $x+$ the aspect ratio of the first cell has been far from ideal affecting the accuracy of the calculation of small scales with the MILES method. The resolution has turned out to be simply insufficient even

on the finest grid. With the development of GPU computing it may be possible to use even finer near-wall mesh resolution and in that case $x+ \sim y+ = 0.3$ should be considered first, at least for the frontal part where the flow is attached, before reducing the wall-normal resolution any further as the wall-normal refinement can be sufficient already. Another possibility is using a larger span length which should benefit the separation and the formation of turbulent flow structures according to correlations data reported in [59]. In the publication of Travin *et al.* [83] for the reference DES simulations it is also acknowledged that span-wise correlations are known to be important, especially for predicting the flow over bluff bodies.

Main strength of the CABARET solver for airframe flow and noise problems is attributed to superior wake preservation due to non-dissipative properties. This could be particularly important when the benchmark case is extended to the rod-aerofoil setup by placing an aerofoil in the wake 10d downstream. For the rod-aerofoil case, maintaining the correct physics while accurately transporting vortices over a large distance could prove crucial for accurate flow and noise calculation. According to experimental measurements, vortex impact on the leading edge generates the most noise for such setup. [59] Experience gained with the cylinder flow modelling will be used in application to a tripped aerofoil benchmark case in the following section. From the modelling viewpoint, a fixed separation point which is prescribed on the leading edge of an aerofoil according to the experiment should eliminate the necessity of predicting the separation location from the first principles which appeared to be the most challenging part of modelling in the cylinder case.

4.2.1 Boundary layer tripping technique for overcoming insufficient near-wall grid resolution

In this work, the advanced tripping method which is based on principles of stochastic white noise has been put to the test where a fine-scale disturbance is thought to provide a flow separation mechanism. A point sink/source stationary stochastic white noise which is correlated in space (along the wall) has been employed trying to overcome the grid resolution limitation in the cylinder benchmark case. (See Eq. (4.3)). The tripping has been applied to the cell boundary face in a form of a Gaussian function over a defined portion of the wall, selected to extend from 70° to 90° which corresponds to the experimental range of the floating separation point for both top and bottom halves of the cylinder.

$$u'_{\omega,t} = \sum_{(N)} \frac{A_\alpha}{\sqrt{N}} \cos(\omega_N t - \kappa x + \psi) \tag{4.3}$$

In Eq. (4.3), N is the number of ω test frequencies, t is the time and $\psi = \psi[0,1]$ is a random phase. Additional quantities, namely the arc length, x, and κ coefficient ($\omega_N / U_{||}$) are introduced, where $U_{||}$ is a wall-parallel flow velocity. A_α is a Gaussian function composed of α azimuthal angles over which tripping is active and of the constant σ and the peak amplitude A_0 is shown below:

$$A_\alpha = A_0 exp\left[-\left(\frac{\alpha-\alpha_0}{\sigma(\alpha_1-\alpha_2)}\right)^2\right] \tag{4.4}$$

where the constant σ helps to prescribe the desired Gaussian shape. The boundary layer tripping initiated by stochastic fluctuations gives greater control over the tripping mechanism and also, reproducing fine scale fluctuations that are otherwise absent due to the grid resolution limitation as discussed in Section 4.2. The application of Eq. (4.3) for initiating earlier separation in the cylinder case has indeed resulted in the mean separation point shift towards 80° which matched the experimental location. However, the behaviour of the separated shear layers was still incorrect as the flow over the cylinder remained overly accelerated judging from experimental velocity profiles. Thus, the fine scale effect that contributes to creating 'drag' can be assumed important over the entire frontal area from the leading edge up to the separation point and cannot be easily reproduced even by such sophisticated tripping approach. Nevertheless, the white noise stochastic tripping proved to be worth considering as a tripping technique. The tripping technique which incorporates the spatial correlation, given by the second term in brackets in Eq. (4.3), has been discovered to have a more pronounced effect in comparison to using the uncorrelated white noise for boundary layer excitation. Hence, relatively low peak amplitude A_0 can be selected which in some cases can prevent causing an adverse effect on acoustics.

4.3 Aerofoil flow simulations

4.3.1 Description of the test case with a sharp trailing edge and RANS flow solution validation

First, the benchmark NACA 0012 aerofoil case with a sharp trailing edge and zero incidence angle of attack from the workshop on Benchmark problems for Airframe Noise Computations (BANC) [68] is considered. The aerofoil chord length is 0.4 m and the free-stream velocity is 56 m/s, which correspond to a Reynolds number of about 1.5×10^6 and a free-stream Mach number of 0.1664. In this section the CFD part of a problem is solved with a 2D RANS simulation using the $k-\omega$ SST turbulence model in the framework of ANSYS CFX.

A C-type mesh with 216 grid points per side of the aerofoil has been generated paying special attention to the wake resolution zone behind the trailing edge. The grid resolution in wall-normal units, y+ is of the order of 1, the far-field domain boundaries are placed 25 chords from the aerofoil leading edge and the total count of grid elements is approximately 70×10^3. The mesh is shown in Figure 22(*a*). In addition, the grid refinement was performed in the stream-wise direction using twice as many points per side of the aerofoil to demonstrate that trailing edge velocity and turbulent kinetic energy profiles are not sensitive to the aspect ratio of the near-wall elements in the RANS solution. As RANS solutions are to be used for acoustic modelling in Chapter 5 it is important to mention that in the framework of FRPM, the source modelling consists of two parts. One part is the RANS solution and the other is the FRPM particle emulation with the use of the corresponding auxiliary stochastic particle grid. The auxiliary grid is made consistent with the RANS solution which defines the corresponding filter length scale and amplitude of the stochastic particle distribution function as discussed in Chapter 3 as well as the particle convection speed. Hence, for consistency of

the source modelling in the FRPM method, it is important to establish a low sensitivity of the statistical parameters to the RANS grid resolution.

Figure 22(*b*) shows the numerical solution for the Mach number distribution around the aerofoil and the location of the "numerical probe" at 1.0038 x/c from the leading edge. The latter location is typical of the trailing edge noise sources and this is where the experimental flow data from the Institute of Aerodynamics & Gas Dynamics (IAG) at University of Stuttgart is also available for comparison with the modelling as provided in [68].

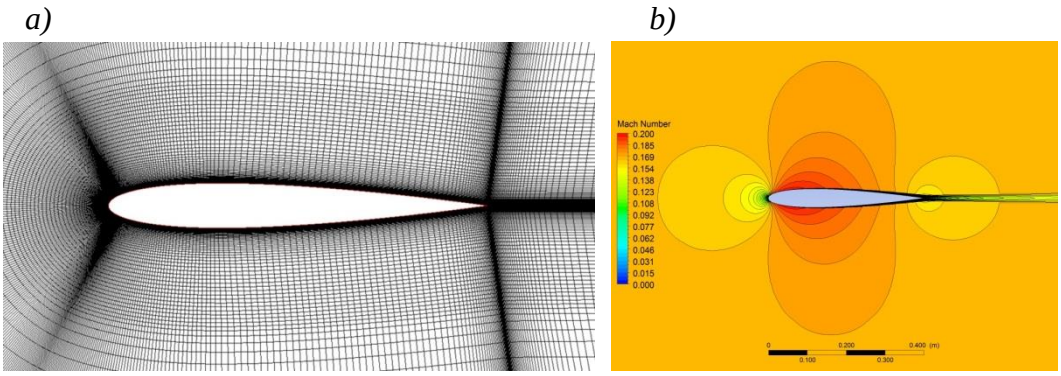

Figure 22 – Computational grid in *x-y* plane (*a*) and the Mach number contours with the numerical probe location (*b*).

Figure 23 compares the computed profiles of the mean flow velocity, turbulent kinetic energy, and the integral turbulence length scale, which characterise the convection speed, the amplitude and the filter length scale of the FRPM model for two RANS grid resolutions, with experiment at the 'numerical probe' location just downstream of the trailing edge. The mean flow profile is in an excellent agreement with experimental data including the inflection point being at *y/c* ~ 0.035-0.04 in the simulation, which is at the same location as reported in the BANC workshop for comparison [68]. The profile of the turbulent kinetic energy shows a good agreement with the experiment too with only minor excursions close to the centreline.

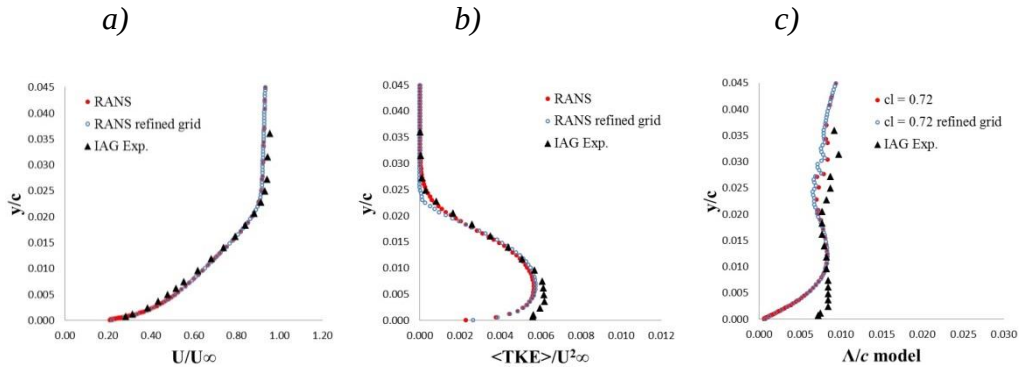

Figure 23 – Comparison of the RANS solutions on the standard grid and the grid that was refined in the stream-wise direction with the experiment downstream of the trailing edge: mean flow velocity (*a*), turbulent kinetic energy (*b*), and integral turbulence scale profile (*c*).

Notably, the definition of the integral turbulence scale length as applied in the experiment would require the determination of velocity auto-correlation function that is not available

from the RANS simulation. Therefore, consistently with the RANS-based acoustic source modelling, the turbulent scale is defined from a combination of variables involving the turbulent kinetic energy and the energy dissipation rate with a calibration coefficient. (See Eq. (3.6)) As a starting point of the present benchmark the calibration length scale parameter, c_l equal to 0.72 is used. This value shows a reasonable match with the experimental profile in Figure 23(c) of the integral turbulence length scale apart from small distances by the centreline. The same characteristic turbulence length scale is then used for the FRPM source model where it corresponds to the characteristic width of the FRPM filter that is applied on the random particles to generate the stochastic velocity field. The filter width amounts to the second-order velocity correlation length scale in case of the Gaussian filter used.

4.3.2 MILES CABARET flow solution

For LES simulations the same flow setup as in the BANC Workshop Case 1 aerofoil with a sharp trailing edge and zero incidence angle of attack has been investigated. In the experiment, a tripping device with a rectangular cross section of 0.36 mm in height and 1.5 mm in width, centred at x/c 0.05 on both the Suction Side (SS) and the Pressure Side (PS) was used. In LES simulations, there are two tripping techniques tested: (1) the rectangular "step" tripping device as in the experiment and (2) a steady suction/blowing numerical tripping technique from [64].

4.3.2.1 Boundary layer tripping techniques

Steady suction/blowing

For the numerical tripping mechanism, one possibility is using a steady suction/blowing in a form of a step function with no net mass injection applied over the portion of the leading edge. Specifically, in this case, steady suction is applied over the region $0.015 < x/c < 0.040$ and steady blowing over the region $0.040 < x/c < 0.065$ acting as outlet/inlet boundary condition. Suction/blowing has been applied over the entire length of the span with the magnitude of the suction/blowing velocity chosen to be 1.5% of the free-stream velocity, whereas 3% was reported in [64]. In the present LES simulations it was noticed that with increasing span length keeping the suction/blowing magnitude at the same level makes tripping more aggressive, which can be judged by comparing velocity profiles behind the trailing edge. In a similar way, the numerical tripping effect is also dependent on the numerical grid resolution. For example, the increased tripping magnitude can be part of the strategy for overcoming the grid resolution limitation. Naturally, by using finer near-wall grids than those commonly reported in the literature in application to LES, the required magnitude of suction/blowing may be less than 3% of the free-stream velocity. Hence, the boundary layer modelling strategy adopted in this study has been based on using a suitable boundary layer tripping with the best numerical grid resolution that is found feasible for simulations presented in this chapter.

Step tripping device which corresponds to the experimental set-up

Another possibility for implementing a boundary layer tripping is using the same methodology that is undertaken in the experiment, which means physically including a tripping device in the simulation. In some experiments tripping is performed by gluing sections of sandpaper which then causes turbulence transition and it makes it difficult in replicating this type of tripping accurately in a simulation. If that is the case, some form of numerical tripping such as suction/blowing can be more appropriate. Fortunately, for this benchmark case the exact dimensions of the rectangular "step" tripping device are known as well as its location on the Suction Side (SS) and the Pressure Side (PS). Thus, by exactly replicating the tripping device it is possible to eliminate an empirical assumption which would be otherwise necessary, for example, when initially estimating the magnitude of suction/blowing. However, since the main interest is at the trailing edge the LES mesh type quality has to be maintained over the entire surface of an aerofoil. Following the transition to turbulence which then develops as vortices roll along the surface, the near-wall mesh resolution requirements can be very demanding. As with the suction/blowing technique, overcoming the grid resolution limitation can be achieved by making the tripping more aggressive with modifications to the tripping device. Figure 24 shows the effect of modification of the tripping device on the boundary layer turbulence. It can be seen that the size of the turbulent wake is clearly affected as a result of changing height of the 'step' tripping device. Hence, it should be possible to fine tune the simulation by selecting an appropriate height of the rectangular 'strip' with a reference to the trailing edge velocity and turbulence intensity profiles obtained from the experiment.

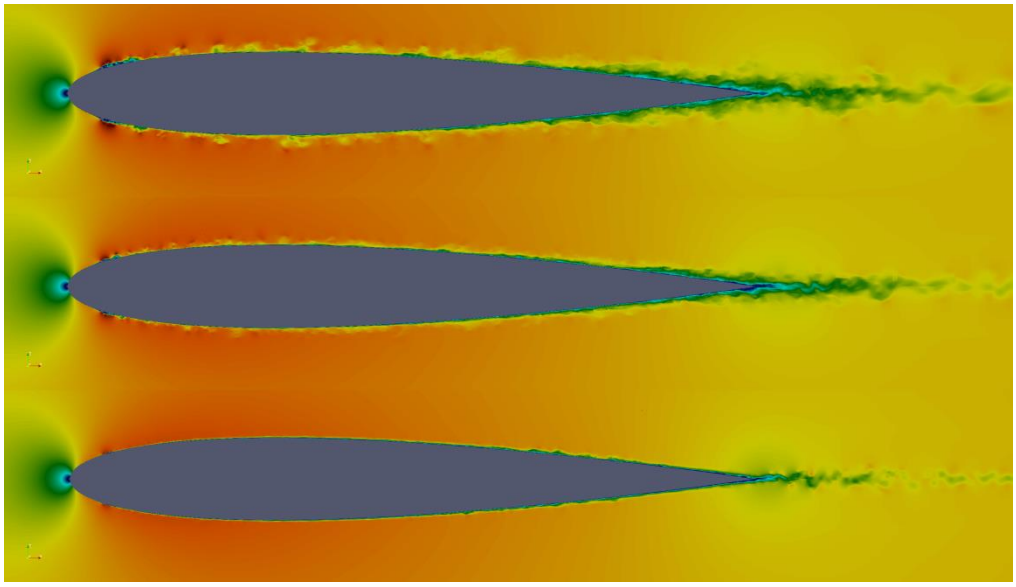

Figure 24 – Contours of instantaneous velocity magnitude for a NACA 0012 aerofoil with a tripped boundary layer showing the effect of modifying height of the tripping device (*increasing height from bottom to top contour*).

4.3.2.2 Computational grid and the flow solution

Various grid refinements and span lengths have been investigated. Following the new methodology proposed in [50], a fine near-wall resolution suitable for LES is achieved by using a snappy hex mesh in all LES aerofoil simulations. The mesh incorporates a fine near-wall layer which is merged with ordered hexahedra where the thickness of the first mesh layer is 1×10^{-5} m which translates to a maximum $\Delta y^+ \sim 2$. The maximum aspect ratio is 1:30 where 30 being in the direction of the chord, rapidly turning into 1:2 for the 8th mesh layer. Figure 25 shows the snappy hex mesh around the aerofoil including the step tripping device for the largest height tested which is by far the trickiest part to mesh with regards to maintaining good mesh quality with this approach. However, the snappy hex technique allows to significantly reduce the computational cost by quickly expanding the grid beyond the boundary layer and in areas of less importance.

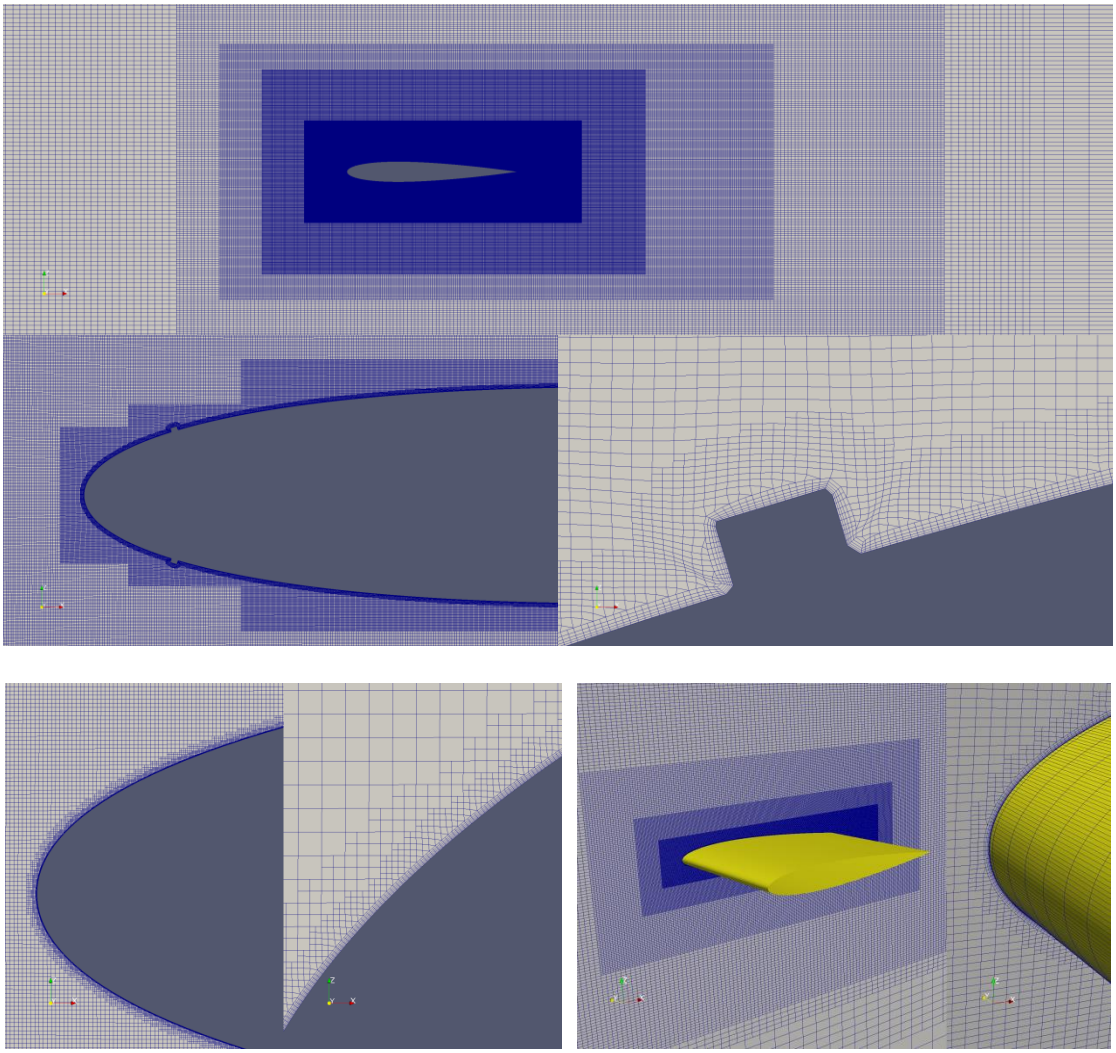

Figure 25 – Snappy hex mesh over the aerofoil.

Various span resolutions have been tested out starting from z/c 0.1 with 32 mesh cells across the span up to simulating a full experimental span, z/c 1.0, with 128 mesh cells for which results are presented in this paper but in general, span resolutions comparable to Δx and Δy

are still not affordable for relatively large spans. For the largest simulated span the aspect ratio of the first mesh layer was 1:30:300, turning into 1:2:20 for the 8th mesh layer. The total number of mesh elements for a biggest simulation run was in the range of 40×10^6. Figure 25 also shows the computational mesh around the aerofoil's leading edge from various angles and zoom levels, where every 10th element is displayed in the span-wise direction. LES simulations were performed on NVidia GeForce GTX1070 (single precision) GPU card with typical speeds of 15 Time Units (TU) per day based on the aerofoil's thickness and the free-stream velocity.

Figure 26(*a*) shows a close up view of instantaneous contours of velocity magnitude for a tripped boundary layer with a step-like rectangular cross section tripping device placed at the same location on the leading edge as in the experiment. As a result of tripping, turbulent wake begins to develop which increases in thickness towards the trailing edge. Figure 26(*b*) shows contours of instantaneous z-vorticity for the suction/bowing tripping method. At the beginning of a mesh refinement process it had been recognised that in absence of very fine near-wall mesh resolution along the entire side of the aerofoil, especially in the x-direction, turbulent vortices become artificially stretched downstream of the leading edge and mostly dissipate towards the trailing edge. Therefore, for a reliable trailing edge acoustic source reproduction from first principles with LES most efforts had gone into keeping the wake resolved, which in this work became possible only with a snappy grid methodology. The image of Q-criterion in Figure 26(*c*) shows that high flow turbulence development starts at around a maximum thickness point which is expected in a tripped boundary layer case contrary to an untripped case where turbulent vortices develop much later towards the trailing edge. The flow is still not of a completely 3D nature and turbulent vortex streaks are not visible along the surface of the aerofoil due to insufficient mesh resolution in the span-wise direction. In this case, with a large span length equivalent to that in the experiment, the limit of affordability of the near-wall mesh quality is quickly reached.

a) *b)* *c)*

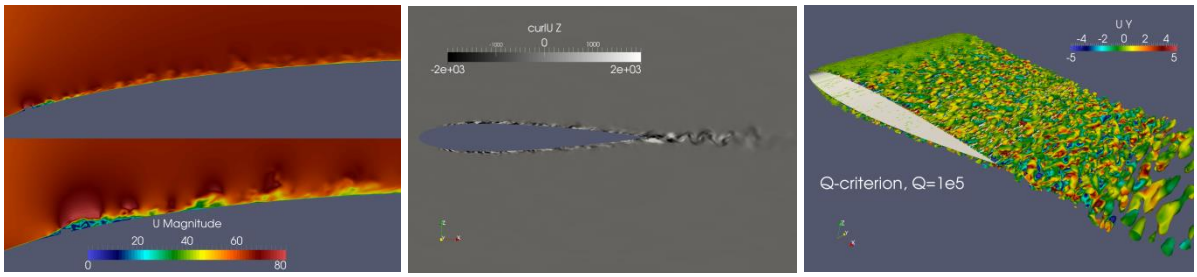

Figure 26 – Contours of instantaneous velocity magnitude for a step-tripped boundary layer (*a*), contours of instantaneous vorticity (*b*), Q-criterion (*c*); (*b*) and (*c*) are produced with the suction/blowing tripping method.

4.3.2.3 Near-field results

The velocity profiles behind the trailing edge serve as an important indicator of the quality of the simulation because with LES in particular, the flow behaviour at the trailing edge region

differs between tripped and untripped cases. For example, when the flow is untripped it remains mostly laminar over the entire surface of an aerofoil with a narrower boundary layer and the flow does not decelerate behind the trailing edge as much as it will be in case of turbulent mixing. In Figure 27 the velocity and turbulent kinetic energy profiles obtained from the numerical simulations are compared to the experiment and to the digitised[6] LES results of George & Lele [64]. It can be seen that a reasonably good agreement is obtained for the velocity profile in both cases, with rectangular step and suction/blowing tripping techniques apart from the centreline location where LES results of George & Lele [64] show a closer match, yet the slope at $y/c \sim 0.2 \ldots 0.3$ deviates from experimental data more than results obtained with MILES CABARET. The peak for the turbulent kinetic energy is over-predicted for both numerical simulations in comparison to the experiment. Distinctly, over-prediction of the peak turbulent kinetic energy close to the centreline is associated with over-predicted stream-wise root-mean-square (rms) velocity component. This is true for both tripping methods tested and the discrepancy of $rms(u')$ close to the centreline is well visible in Figure 28 where 3 velocity components are shown individually for the 'step' tripping method. For the suction/blowing technique the profiles are quite sensitive to the magnitude of the tripping, the area over which tripping is acting and the span length. For consistency with other researchers the same suction/blowing tripping location on the leading edge was used as in [64] but with a lower suction/blowing magnitude of only 1.5% of the free stream velocity. By applying the MILES CABARET method on a fine grid and having a large span length it has been determined that 3% is slightly aggressive, resulting in over predicted boundary layer thickness at the trailing edge. In case of a rectangular step tripping the same location as in the experiment has been used too but with a varying height of the tripping device as shown in section 4.3.2.1.

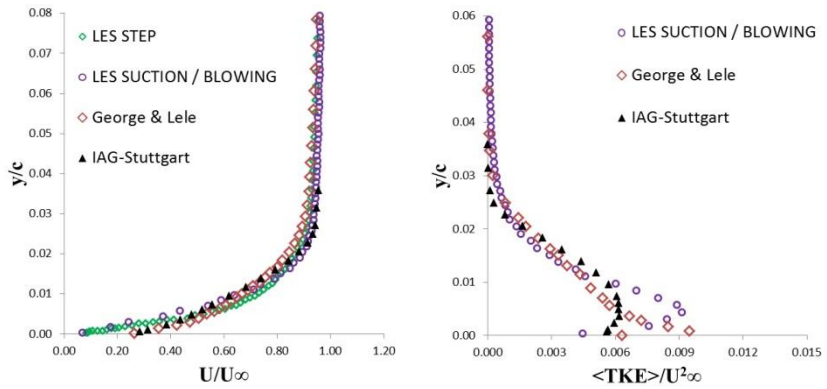

Figure 27 – Comparison with the experiment and LES results from [64] downstream of the trailing edge: mean flow velocity and turbulent kinetic energy profiles.

In LES methodology a type of the near-wall treatment plays an influencing role as well as many other factors such as mesh quality, boundary layer tripping implementation and transition to turbulence modelling which in turn affects the development of the turbulent

[6] Results from the three fluctuating velocity profiles presented in [64] are combined to form the turbulent kinetic energy profile which is a key comparison parameter in the FRPM source derivation.

boundary layer. Also, it appears that a stream-wise component of fluctuations is frequently found to be over-predicted when LES is applied to aerofoil flow modelling.

In the experiment the height of the tripping device with a rectangular cross section was reported to be 0.36 mm, which corresponds to the 'small step' profiles in Figure 28(*a*). It can be seen that all profiles in Figure 28(*a*) are much narrower than in the experiment due to insufficient growth of the boundary layer caused by insufficient grid resolution. The velocity profiles in Figure 28(*a*) look more similar to an untripped case. Therefore, for overcoming the grid resolution limitation the height of the tripping strip was increased. As a result, the medium tripping device where the height of the step was twice the experimental height but keeping the same width of the rectangular strip produced numerical velocity profiles in Figure 28(*b*).

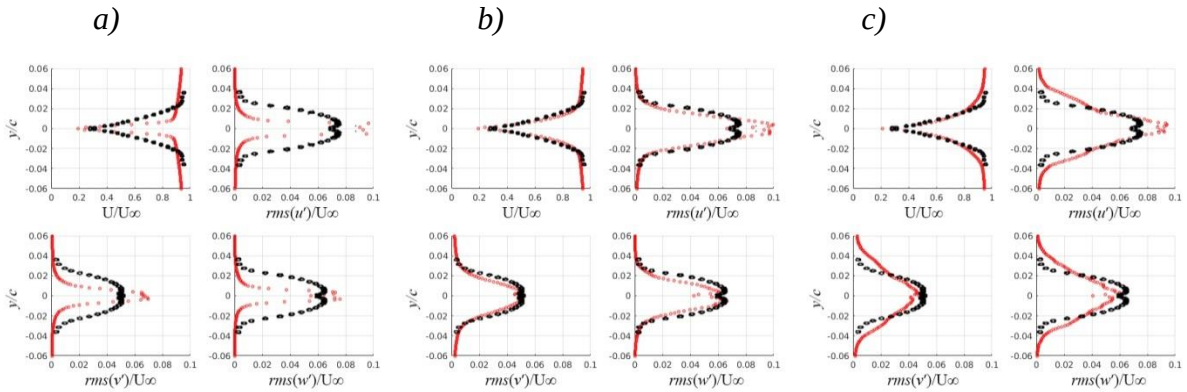

Figure 28 – Comparison of the mean flow velocity and intensity profiles with the experiment for fine-tuned tripping device height: experimental tripping device height, 'small step' (*a*), 2 × experimental height 'medium step' (*b*) and 4 × experimental height 'large step' (*c*).

For the medium step tripping, the mean velocity and turbulent intensity profiles turned out to be in very good agreement to the experiment with an exception of the over-predicted peak for the streamwise $rms(u')$ component. This problem is common between all simulation runs as evident from Figure 28, regardless of the chosen tripping device height. For comparison purposes, trailing edge profiles of a third simulation that employed further twice the height increase of a medium step are shown in Figure 28(*c*). By examining these numerical profiles it can be seen that in the simulation employing the 'large step' velocity profiles appear wider as a result of over-predicted boundary layer thickness. It can be concluded that the tripping is too aggressive for the case with the 'large step'. Therefore, out of three tested heights the 'medium step' tripping produced the closest match to experimental data and this simulation will be further examined for acoustic sources comparison in Chapter 5. Also, instantaneous contours in Figure 24 give a qualitative representation of the boundary layer development which corresponds to tripping step sizes analysed by means of profile comparison in Figure 28. Particularly, it can be seen how the size of the wake grows with the increasing height of the tripping device.

Figure 29 shows the plot of the skin friction coefficient, c_f, comparison between RANS and LES simulations for the medium step tripping. Unlike the pressure coefficient, c_p, which is

not representative for zero incidence angle on a NACA 0012 at this flow regime, the skin friction coefficient comparison at the trailing edge is substantially more important being the prime location of noise sources derived from turbulent velocities in the vortex sound method. From Figure 29 it can be seen that for two simulations with identical flow conditions, the skin friction coefficient beyond $x/c > 0.7$ is in good agreement, meaning that the velocity gradient of a boundary layer at the trailing edge is very similar between RANS and LES. Thus, for the trailing edge source terms comparison in Chapter 5, c_f provides one additional validation. A difference at around the mid-chord between RANS and LES comes from a reaction to boundary layer tripping in the latter case. Unfortunately, there is no experimental validation for c_f reported for this benchmark case. However, as mentioned earlier a similar tripping method to the experiment was used in LES with the same tripping location and therefore, some reaction to tripping which will affect the skin friction coefficient profile can be also expected in the experiment.

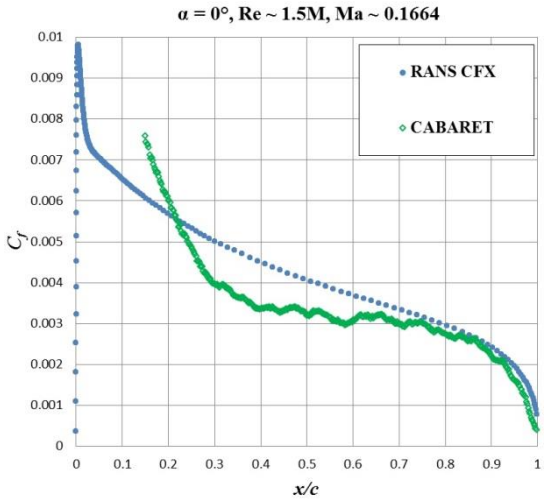

Figure 29 – Skin friction coefficient comparison between RANS and LES with medium step tripping simulations.

4.3.3 Description of the benchmark case with a blunt trailing edge and URANS flow solutions

The second benchmark aerofoil noise problem considered in this work is the experiment of Brooks and Hodgson [92], for an aerofoil with a blunt trailing edge. The chosen case employs the largest trailing edge thickness of 0.0025 m available which exhibits pronounced tonal noise. The aerofoil used in the experiment is a NACA 0012 symmetrical aerofoil section with a chord length of 0.6096 m and a span of 0.46 m at zero incidence to the flow. The free-stream velocity is set to U_∞=69.5 m/s and the corresponding Reynolds number based on the chord length is 2.77×10^6 with a free-stream Mach number equal to 0.2. The blunt trailing edge leads to vortex shedding at 3 kHz which corresponds to a Strouhal number of around 0.1 based on the free-stream velocity and the trailing edge thickness.

Similarly to the sharp trailing edge case, the problem is solved with the 2D $k-\omega$ SST turbulence model but in this case an unsteady RANS model is used to capture the vortex shedding. A second-order accurate scheme in space and time was applied for numerical solution on a C-type grid of approximately the same resolution in comparison with the sharp trailing edge case.

Two unsteady RANS simulations have been performed for the blunt trailing edge problem. The first calculation was conducted for the same geometry as reported in the experiment while assuming a fully turbulent boundary layer condition on the aerofoil boundary. Compared to the experiment, where the transition to turbulence occurred due to the flow tripping on both sides of the aerofoil, the numerically predicted shedding frequency was approximately 2750 Hz which is more than 10% short of the experimental value.

Reproducing the correct transition to turbulence within the URANS model to replicate the boundary condition used in the experiment is very challenging and is likely to involve several calibration parameters of questionable validity since modelling of flow separation within the standard (U)RANS framework could be questionable. Hence, no attempt to model the transition from a laminar to turbulent boundary layer is undertaken here. Instead, a simpler method to capture the correct shedding frequency is chosen for the second URANS simulation, where a slightly elongated aerofoil shape with the trailing edge thickness reduced by 20% is considered. This slight shape modification resulted in capturing the experimental shedding frequency of 3 kHz numerically.

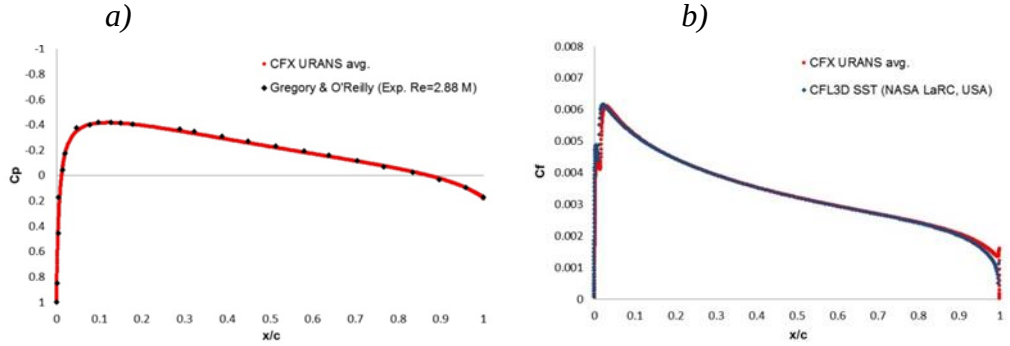

Figure 30 – Comparison of the current RANS solutions with the available flow data for a similar NACA0012 aerofoil case from the literature [159]: pressure (*a*) and skin friction coefficient distributions (*b*).

Figure 30 compares the time-averaged URANS solution having the blunt trailing edge for pressure and skin friction coefficient, c_p and c_f distributions with the experimental data of Gregory and O'Reilly [159] and Langley CFL3D RANS calculation. In comparison to the reference configuration of Brooks and Hodgson, the experiment of Gregory and O'Reilly together with Langley CFL3D solution correspond to the same aerofoil profile except for the sharp trailing edge, the same free-stream Mach number and a similar Reynolds number (2.8×10^6 vs. 2.77×10^6). As can be seen the current URANS simulation is in very close agreement with data reported in the literature, where for this benchmark case the blunt trailing edge is only a small percentage of the aerofoil's thickness and therefore, the overall

geometry could be deemed as almost identical. Notably, in the reference experiment Brooks and Hodgson reported a c_f value of approximately 0.002 at the trailing edge, which is also in a good agreement with the current URANS simulation.

4.3.4 Reconstruction of the unsteady flow field with the FRPM method for trailing edge noise simulations

Following the RANS/URANS simulations for benchmark cases this section discusses the implementation of an acoustic source model presented in Chapter 3, to be used later for broadband and tonal noise simulations. As sound sources are deducted by ameliorating the RANS/URANS flow data it is important to verify that a re-created unsteady flow field matches experimental measurements and is consistent with time-averaged input data. For example, it is important to verify that a time-averaged TKE field which scales the Gaussian kernel and the recovered TKE field obtained from FRPM velocities are equivalent. Also, an integral length scale plays an important part in the model so its implementation with the c_l constant scaling has to be taken into consideration for accurately re-creating the unsteady flow field.

In order to minimise errors related to the filter scaling operation, the size of the Cartesian FRPM grid cell is kept much smaller than the smallest considered characteristic scale of the acoustic source. The latter scale is of the order of the turbulence length scale in the region of significant source amplitudes. In the current 2D simulations a cell size of 4 times as small as compared to the minimal value obtained by Eq. (3.8) in Chapter 3 for the source field is used. Where zero values of turbulence scales are present in the source domain, for example next to the wall, a sufficiently small value thought to be of importance is picked as a reference scale due to resolution limitations. For the aerofoil trailing edge noise simulation with a blunt trailing edge considered in this work this smallest scale within the source region is estimated to be in a range of 6×10^{-4} with reference to the chord C, resulting in a cell size of $1.5 \times 10^{-4}\,\Delta/C$, where Δ is a Cartesian cell width. In addition, 10 stochastic particles per each Cartesian grid cell are specified. It was demonstrated that a sufficient number of particles are required within the FRPM domain [55] such that their area-weight contribution would achieve the target root-means-square *rms* values and therefore, yield a close approximation to Eq. (3.1). This ensures that parameters of the distribution of random particles vary slowly as compared to the convection scale of individual particles so that the particle contributions to the source are statistically converged. Importantly, in [55] converged statistics were obtained with an increase in the total number of particles beyond approximately 5 particles per cell for a sufficiently large domain.

Furthermore, in order to smoothly insert and eliminate particles without spurious noise amplification effects, a numerical decay function is built into the inlet and outlet zones of the FRPM domain which gradually attenuates the amplitude of the filter function after computing noise sources.

When a tone is present in addition to broadband fluctuations, it becomes an additional source of flow solution unsteadiness and consequently contributes to the overall noise. For source modelling, an unsteady flow solution obtained from the URANS is mapped on to the same FRPM Cartesian grid where synthetic turbulence is generated. Figure 31(a) shows a time averaged velocity magnitude field on to the FRPM grid which is required when evaluating u_L' at every CFD time step. (u_L' is shown separately in Figure 31(b)). Vortex shedding obtained in URANS is deterministic in nature where a sequence of CFD time steps may describe one complete period of shedding. Then, after the period is identified it may be looped over to represent continuous vortex shedding. The parameters of interest which include turbulent kinetic energy, turbulent eddy frequency, mean and instantaneous URANS velocities along with the mesh information and a CFD time step are recorded into a separate input file that are later used as an input for the acoustic solver.

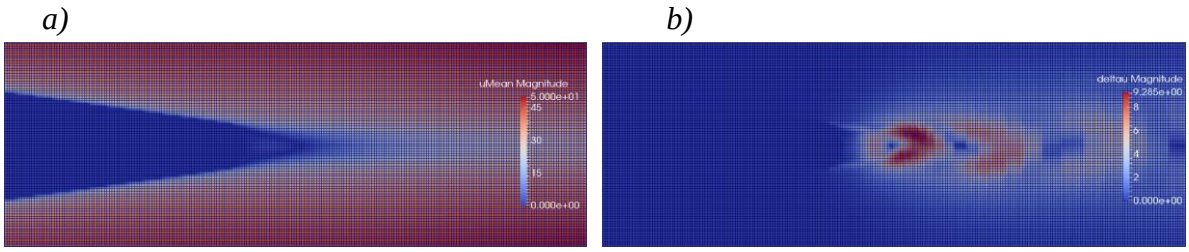

Figure 31 – URANS solution provides an additional fluctuating velocity source for the blunt trailing-edge problem: mean velocity magnitude (a) and its fluctuation field mapped onto the FRPM Cartesian grid (b).

Figure 32 shows the time history of cross-stream velocities in the wake zone normalised with a local mean kinetic energy at the numerical probe placed downstream of the trailing edge.

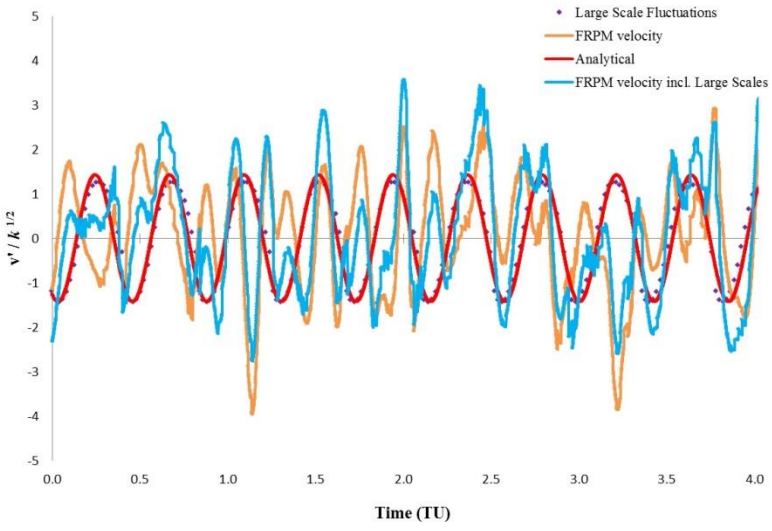

Figure 32 – Time-domain behaviour of various velocity components behind the blunt trailing edge. The analytical function corresponding to the pure tonal velocity signal is included for comparison. $\sqrt{k}$ is a characteristic turbulent kinetic energy obtained from a 2D RANS solution. Time Units (TUs) are based on the free-stream velocity and the chord length, $\mathrm{TU} = tc/U_\infty$.

Figure 32 encompasses the reference v' FRPM velocity signal obtained from purely broadband stochastic sources as well as the modified $v' + v'_L$ velocity that incorporates the tonal noise harmonic. On the same plot, v'_L alone that is at the core of the tonal noise mechanism, shown with markers, represents large scale fluctuations which are a result of Eq. (3.49). Besides, the analytical harmonic function of 2750 Hz with an arbitrarily calibrated amplitude and phase is plotted to approximately fit the shedding frequency of the wake corresponding to the URANS solution. It is interesting to observe how the stochastic part of the solution gets superimposed on the deterministic wave solution corresponding to the vortex shedding and results in the total signal which looks very much like a velocity fluctuation measured in a real experiment where tidal currents were recorded. [160]

In the current method based on the URANS solution there are two possibilities for realisation of turbulent kinetic energy and turbulent length scales on the FRPM grid. The choice is between using mean or instantaneous quantities for scaling the filter kernel in Eq. (3.8-3.9). Investigations with the current aerofoil benchmark vortex shedding case show that acoustic predictions remain similar and consistent for both options. For the results discussed in Chapter 5 instantaneous fields for k and l are used which are directly obtained from parameters of the URANS simulation.

After turbulent velocities are obtained they could be validated, first, for the benchmark case with a sharp trailing edge where near-field velocity data are available from the experiment as well as from the tripped LES simulation. The comparison starts with the TKE field, judging whether it is consistent with the RANS input data as outlined in the beginning of this section. In Figure 33 the time resolved turbulent kinetic energy of the FRPM simulation is compared to the target CFD input statistics. A close examination reveals that the TKE field which was calculated from stochastic velocities has a greater magnitude, particularly in the wall region and down the centreline, with values at the trailing edge peaking ~30 $\mathrm{m}^2/\mathrm{s}^2$ in FRPM. The range of the displayed contour is re-scaled in comparison to ~20 $\mathrm{m}^2/\mathrm{s}^2$ due to the highest reference value seen in the RANS simulation. Ideally, the recovered turbulent kinetic energy should match the one obtained from RANS and the difference in Figure 33 comes from the Gaussian filter kernel scaling used in the FRPM method. The contours in Figure 33 clearly demonstrate the over-predicted time-averaged TKE recovered from FRPM velocities.

a) *b)*

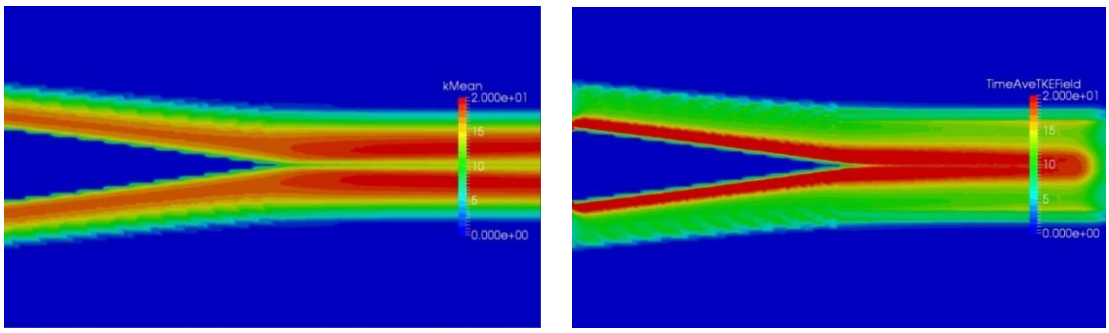

Figure 33 – Contours of mean turbulent kinetic energy from RANS (*a*), time averaged turbulent kinetic energy from FRPM velocities, $c_l = 0.72$ (*b*).

In the FRPM simulation a length scale parameter has a major influence on the acoustic sources calculation and for the reference, in Figure 34 we recall the profile of the integral length scale which was obtained when scaling the Gaussian kernel by the constant calibration parameter $c_l = 0.72$, which value arguably produced the closest match to the experiment.

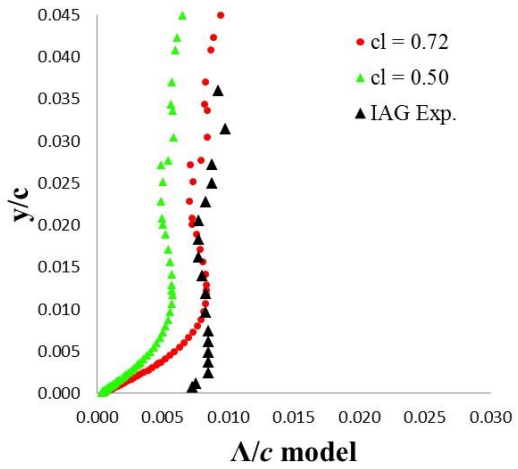

Figure 34 – Integral turbulent length scale agreement between c_l 0.5, 0.72 and the experiment.

Figure 35 shows the profile comparison between the experiment, LES and FRPM for different c_l values where using a lower c_l value of 0.5 resulted in the closest match to the mean TKE obtained from RANS. Peak values of the recovered TKE within the FRPM domain had a maximum magnitude of approximately 22 m^2/s^2 for $c_l = 0.5$, which are within 10% to the target input of the RANS simulation. For TKE profiles reported in [161] over-prediction was approximately 15% for a c_l value of 0.54 which appears to be in line with current findings.

a) *b)*

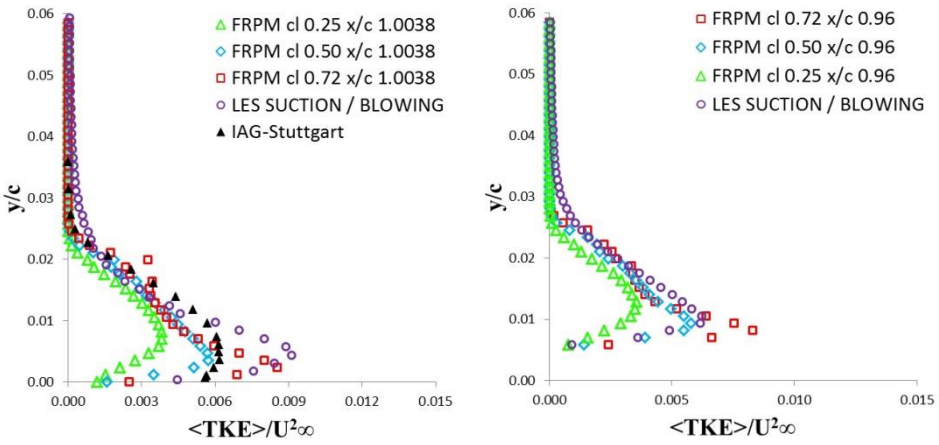

Figure 35 – Turbulent kinetic energy profiles for different c_l values comparison to the experiment and LES at $x/c = 1.0038$ (*a*), between LES and FRPM for $x/c = 0.96$ (*b*).

Figure 36 shows the integral correlation length scales derived from the two point correlations obtained for the FRPM solutions with constant c_l values of 0.5 and 0.72 compared to the available 'Rnoise' numerical data [162] [163] in the stream-wise direction and to the experimental flow data from the Institute of Aerodynamics & Gas Dynamics (IAG) at University of Stuttgart. [68] The integral length scales are derived as following:

$$\Lambda_{ii,n}(n) = \int_0^{\xi c} \frac{\langle u_i(\boldsymbol{x},t) \cdot u_i(\boldsymbol{x}+\boldsymbol{\xi},t) \rangle}{\langle u_i^2(\boldsymbol{x},t) \rangle} d\boldsymbol{\xi} \tag{4.5}$$

In Eq. (4.5) above, the index 'ii,n' denotes the length scale component of fluctuation velocities 'ii' for probe separation in 'n' direction and ξc is the cut-off length scale chosen as 0.1 for FRPM profiles.

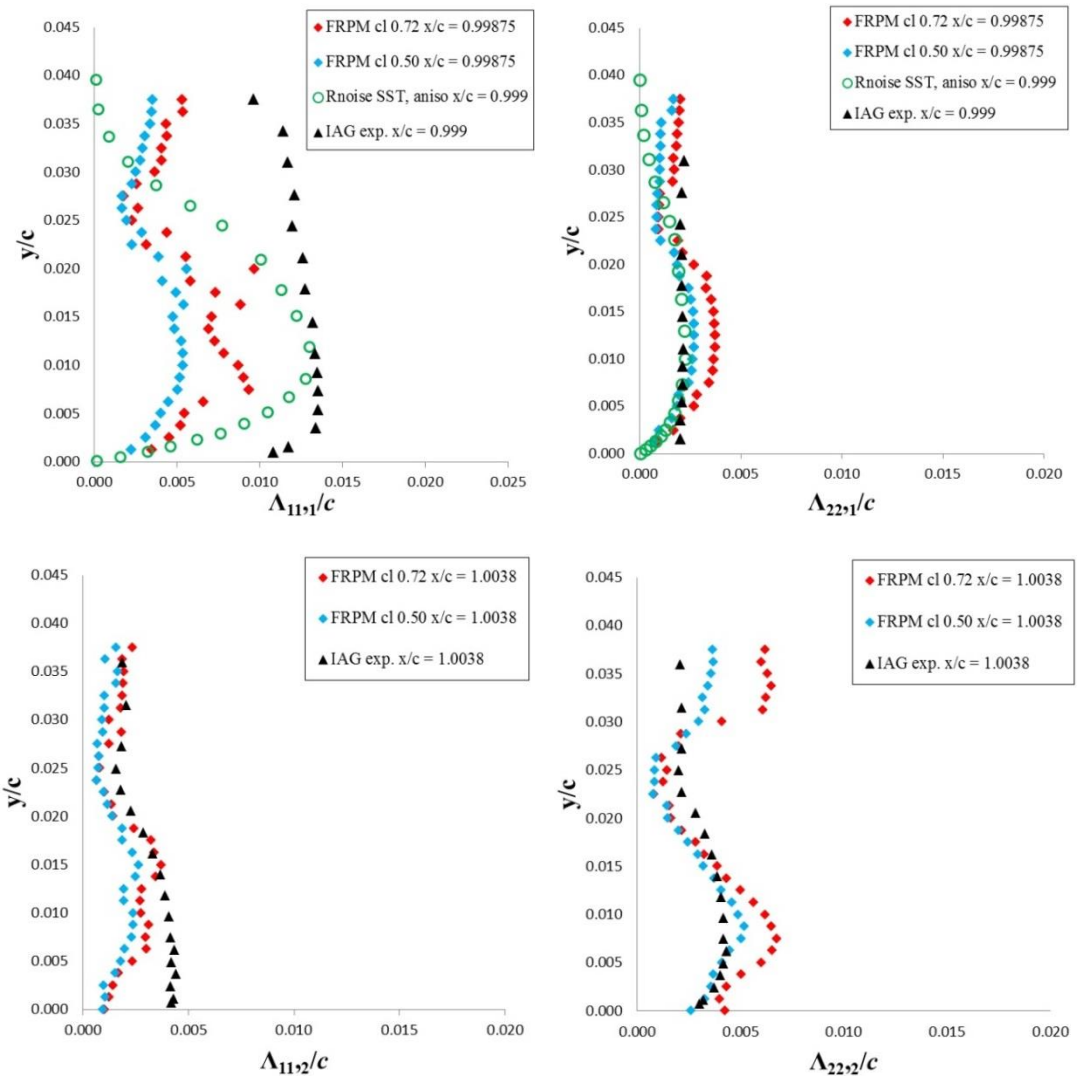

Figure 36 – Integral correlation length scales derived from two point correlation velocity profiles.

It is worth noting that 'Rnoise' results are obtained with the aid of anisotropic scaling integrated into the numerical model while with the FRPM method no anisotropy has been used and the c_l parameter simply scales the entire field. Generally, a good match to

experimental data is found for integral length scales apart from $\Lambda_{11,1}$ which is a stream-wise velocity component in *x*-direction. For $\Lambda_{11,1}$ the FRPM integral length scales, especially obtained for c_l of 0.5, tend to follow the shape of the experimental integral length scales closer than 'Rnoise' simulations that used anisotropic scaling. However, in the FRPM case $\Lambda_{11,1}$ component is under-predicted as the Gaussian scaling was derived from a RANS field. The x/c FRPM reference location for $\Lambda_{11,1}$ and $\Lambda_{22,1}$ corresponds to the closest Cartesian grid point available in comparison to $x/c = 0.999$ in the experiment. Moreover, in the FRPM simulation $\Lambda_{11,1}$ and $\Lambda_{22,1}$ profiles were also checked using the next available grid point ($x/c \sim 1.0038$) as a reference, which resulted in a marginal difference only to profiles seen in Figure 36.

4.4 Discussion on the main outcomes of the numerical flow simulations when applied to benchmark cases of interest

In section 4.1 the results for the ideal flow past a circular cylinder have been presented using the CABARET numerical scheme and compared to some popular schemes used in the commercial software ANSYS Fluent. Encouraging results were obtained for the CABARET scheme where not only the flow remained fully attached which is entirely in agreement with the Euler flow theory for a circular cylinder but also, the scheme produced very small amount of dissipation in comparison to the Roe-FDS scheme which has been a preferred scheme in Fluent. Figure 16 illustrates this fine difference. Ultimately, this result provided the motivation for implementing the MILES method based on the high-fidelity CABARET scheme for solving challenging aero-acoustics benchmark cases.

In section 4.2 the solution of the flow past a circular cylinder at Re 50,000 has been attempted using the MILES CABARET method. By far the most challenging part of the problem at this flow regime is modelling the separation point accurately. The near-wall grid resolution was established to be insufficient for accurately resolving the fine scales for the benchmark case at sufficiently high Re number with the rapid turbulent transition in separated shear layers, which is thought to be the most challenging flow regime for numerical modelling. In the CABARET simulation the flow separation was slightly delayed which also resulted in over-prediction of the shedding frequency. Therefore, applying the stochastic white noise tripping to initiate earlier separation has been regarded as a possible solution. Despite predicting the separation at ~80° which corresponds to theory an overly accelerated flow still affected the formation of separated shear layers. The time-averaged wall pressure coefficient produced a good indication on the near-wall flow behaviour. Even though using a stochastic tripping with the MILES method has not allowed to correctly resolve the flow over the circular cylinder, room for improvement in modelling the separation point with the MILES method exists by applying the new snappy hex meshing technique as demonstrated for the aerofoil case. Possible solution to the problem is eliminating the elongated near-wall cells by only refining the first few layers of the computational grid in the streamwise direction. The current best MILES CABARET simulation was performed within a week on a

single GPU card. Therefore, with the application of the modern computational method, simulation time remains realistic for such a challenging problem. On the other hand, application of the MILES CABARET for resolving the wake can be regarded as one of the strengths of the method. For example, extending the cylinder benchmark to the rod-aerofoil case should not present a problem as long as the physically accurate flow behaviour could be obtained around the cylinder itself. On the other hand, due to the sufficiently large Reynolds number this problem still remains a challenge for other methods including a hybrid RANS-LES. For example, the DES simulation performed in ANSYS Fluent was not close to producing similar results obtained in [83] which closely resembled the theory and experimental measurements. One possible reason for such deviation could be that DES model requires a specific calibration.

In Section 4.3 a comparison of near-field flow solutions has been presented for the two benchmark aerofoil cases with sharp and blunt trailing edges. Numerical flow solutions have been first evaluated by the RANS/URANS methods and supplied to the FRPM for obtaining turbulent flow quantities, which were then compared to LES solutions and to the experiment. By assuming a fully turbulent boundary layer in the RANS simulation, the near-field mean quantities showed encouraging agreement when compared to experimental flow data available. For the blunt trailing edge case the trailing edge has been modified which resulted in the correct shedding frequency as recorded in the experiment. Moreover, surface pressure and the skin friction coefficient showed an excellent agreement at the trailing edge with independently obtained numerical data. For the blunt trailing edge, Brooks & Hodgson [92] reported the c_f value that was also found at the same location in simulations.

LES simulations have been performed with two boundary layer tripping techniques, one that copied the experimental step tripping and the other was a suction/blowing numerical technique, which has been extensively tested in this work and also in [64]. The skin friction coefficient at the trailing edge shown in Figure 29 was found to be in good agreement between LES and RANS methods. Also, the velocity profiles recorded in the vicinity of the trailing edge showed a reasonable agreement with experimental data for both tripping techniques used with LES. For turbulent intensity profiles the best agreement has been obtained for the ‘medium’ step tripping. (See Figure 28) The results of this simulation have been used for derivation of the effective sources of trailing edge noise as will be discussed in Chapter 5 which are then compared to sources obtained in FRPM. Additionally, for the FRPM solution, the re-constructed TKE profiles are shown at the two x/c trailing edge locations for chosen values of the c_l calibration parameter and the value that gives the best agreement to LES data has been determined. Finally, the comparison for the integral correlation length scales between the FRPM solution, ‘Rnoise’ results found in the literature and the experiment has been presented.

Chapter 5

Acoustic modelling

This chapter presents the comparison of acoustic sources between LES and FRPM simulations obtained by reconstructing the noise sources in the vicinity of the trailing edge in accordance to the vortex sound formulation discussed in Chapter 2. After presenting the near-field flow validation and discussing LES and FRPM methodologies in the previous chapter, the acoustic sources obtained via both methods will be compared at the source level. Effective sources comparison is performed by taking a root-mean-square of instantaneously evaluated acoustic sources in the vicinity of a trailing edge over a sufficient period of time so that converged statistics is obtained. Subsequently, a calibration of the FRPM model based on LES is discussed. As far as the far-field acoustic predictions are concerned, in Section 5.2 the APE propagator is tested on a monopole benchmark problem and compared with the analytical solution. Then, in Section 5.3 noise predictions for the sharp trailing edge are obtained and discussed following with application of the scale decomposition approach proposed in Chapter 3 for obtaining acoustic predictions for the blunt trailing edge case.

5.1 Reconstruction of the effective noise sources from FRPM and LES methods in accordance to the vortex sound formulation

This work includes the analysis of individual source terms outlined in Eq. (2.99) in Chapter 2 that are obtained from FRPM and LES simulations. Notably, the FRPM sources involve the calibration length scale parameter, c_l, which value has been discussed in the previous chapter with the reference to the near-field trailing edge flow quantities. Moreover, bearing in mind that the recommended value for the c_l constant in airframe noise is somewhere in the range of $0.5 \ldots 0.75$ as reported in Chapter 3, the two selected values based on the near-field flow results (0.5 and 0.72) turned out to roughly represent both ends of the range. For that reason it has been decided to compare the FRPM vortex sound sources for both values.

For FRPM simulations the source calculations are performed in two dimensions where, for example, in Eq. (2.99) $\boldsymbol{\omega}' \times \boldsymbol{u}_0$ term II matrix consists of two velocity components and a *z*-vorticity which is the vorticity in *x*-*y* plane. For the acoustic source terms comparison like for like 2D terms are obtained from the LES simulation. It should be noted that from LES one can obtain a full non-linear acoustic source matrix as prescribed by Eq. (2.99), including all three types of source terms in 3D.

$$q_x = \{v'\overline{\omega_z} + \bar{v}\omega_z' + v'\omega_z' - w'\overline{\omega_y} - \bar{w}\omega_y' - w'\omega_y'\} \quad (5.1)$$

$$q_y = \{w'\overline{\omega_x} + \bar{w}\omega_x' + w'\omega_x' - u'\overline{\omega_z} - \bar{u}\omega_z' - u'\omega_z'\} \quad (5.2)$$

$$q_z = \{u'\overline{\omega_y} + \bar{u}\omega_y' + u'\omega_y' - v'\overline{\omega_x} - \bar{v}\omega_x' - v'\omega_x'\} \quad (5.3)$$

The terms in Eq. (5.1-5.3) include mean and fluctuating components where depending on assumptions different parts could be used to describe a simplified acoustic source as would be discussed in the following sections where a trailing edge comparison is drawn. Thus, Eq. (5.1-5.3) serve as a reference for a complete vortex source model used in trailing edge noise computations.

5.1.1 Source term II comparison

The acoustic source term II in Eq. (2.99), which can be represented by the $\boldsymbol{\omega}' \times \boldsymbol{u}_0$ matrix is regarded as the dominant source term contributing to the far-field pressure in trailing edge noise simulations. Figure 37 and Figure 38 shows the RMS of q_x and q_y components obtained for a 2D source model, where $q_x = \{\bar{v}\omega_z'\}$ and $q_y = \{-\bar{u}\omega_z'\}$. The *x*-*y* dimensions of the comparison area are equal between FRPM and LES that is also the size of the FRPM auxiliary grid patch which extends from x/c 0.9 to 1.1 and y/c from -0.06 to 0.06.

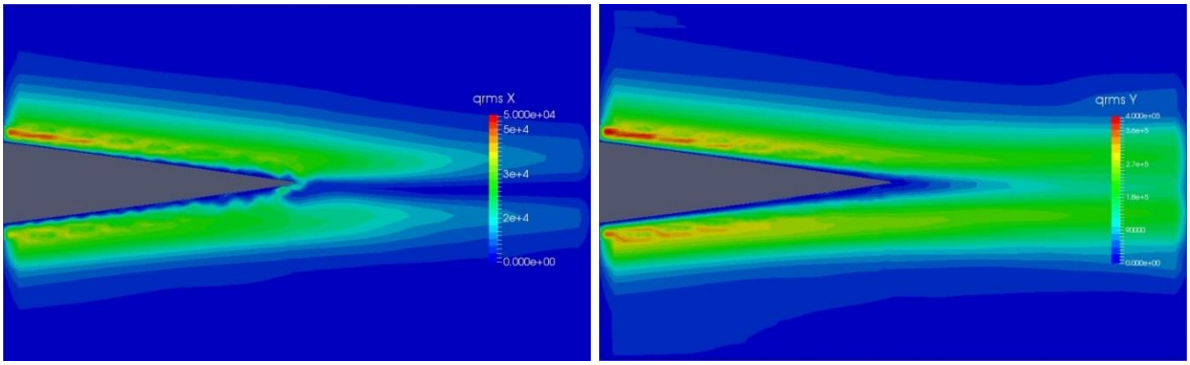

Figure 37 – MILES CABARET RMS contours of the acoustic sources $\boldsymbol{q_x}$ and $\boldsymbol{q_y}$ for term II in Eq. (2.99).

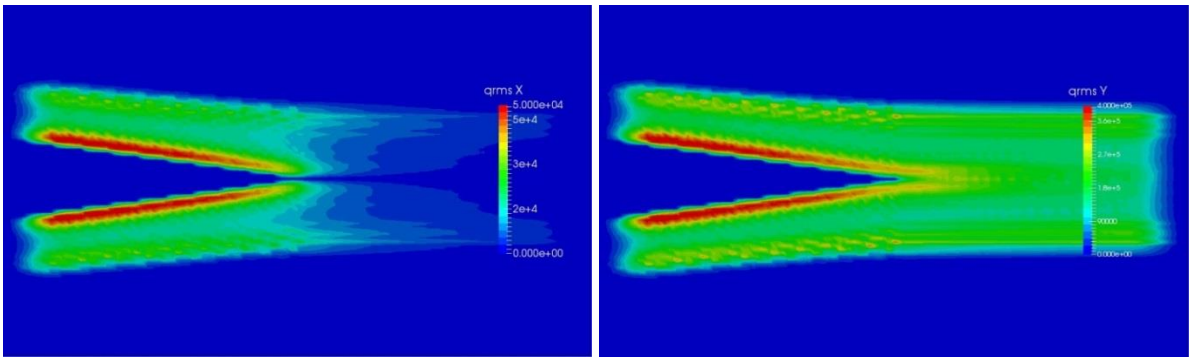

Figure 38 – Altus FRPM RMS contours of the acoustic sources $\boldsymbol{q_x}$ and $\boldsymbol{q_y}$ for term II in Eq. (2.99)

In the FRPM model, a Cartesian cell width is chosen $\Delta/c = 1.25 \times 10^{-3}$ that is 4 times smaller than a minimal reference integral length scale of importance ~0.002 from Figure 23(c). A total of 151050 particles were used to discretise Eq. (3.1), so that the recommended particle density [55] was achieved with 10 particles per cell. A rectangular decay function that ranges from zero to 1 is applied to acoustic sources at the sides of the FRPM domain as can be seen from Figure 38 to avoid possible spurious sources generation in an acoustic simulation, whereas contours in Figure 37 are calculated directly on the LES grid. The last percentage of the area over which a decay function acts in the FRPM domain affects the overall source volume. Hence, it should be taken into account when comparing acoustic predictions between different runs. In FRPM the wall boundary condition is automatically prescribed by the mean flow from RANS. In this case no special treatment is applied when evaluating near-wall gradients on a Cartesian grid and nodes which fall inside the boundary, by definition, have zero velocity. It can be seen that at the trailing edge q_y RMS is much stronger than q_x RMS which holds true for both LES and FRPM simulations. In the LES simulation, Figure 37, strongest sources are found in a close proximity to the wall upstream of the trailing edge. Vortex sound sources become weaker moving downstream towards the tip of the trailing edge where flow merges. From theory, it is expected to find the strongest acoustic sources in a close proximity of a trailing edge tip. High upstream magnitudes in Figure 37 may have resulted due to boundary layer tripping artifacts or hydrodynamic contribution to the vortex source term. In the FRPM simulation, strongest sources are also found in a close proximity to the wall with a decreasing magnitude towards the trailing edge but despite having comparable maximum RMS values to those calculated from LES, in FRPM sources are spread along the entire surface of the aerofoil's trailing edge, apart from the upstream portion where a decay function gradually kills all of the source.

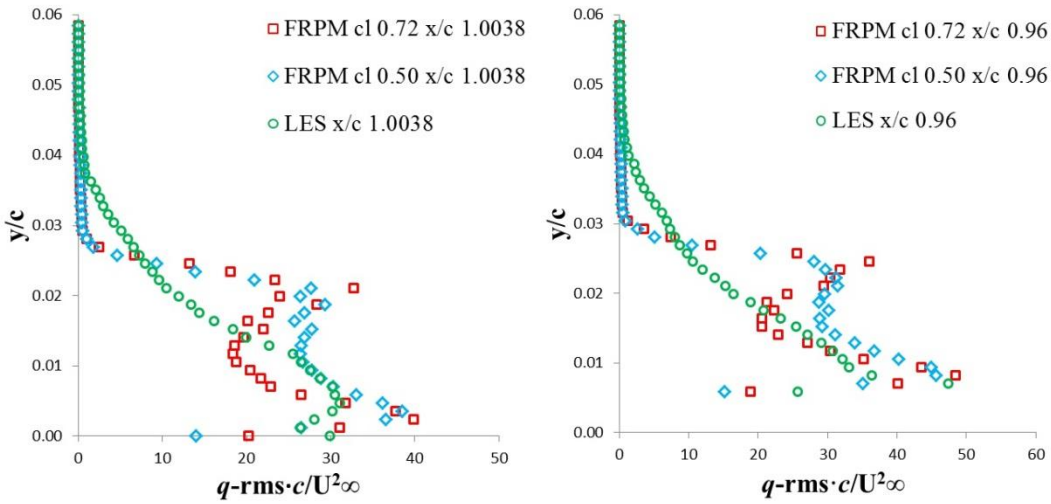

Figure 39 – Comparison of the trailing edge profiles between LES and FRPM (with different c_l coefficients) at $x/c = 0.96$ and $x/c = 1.0038$ locations, showing the magnitude of source *q-rms* for term II normalised by the chord and the square of free-stream velocity.

The chord-normal contour pattern is different between the two simulations – in LES there is a consistent decrease in the acoustic source strength in a wall normal direction, whereas in the FRPM method a second amplification is observed within the zone of high acoustic sources

concentration. Figure 40 illustrates the non-physical kink at $y/c \sim 0.2$ present in the vorticity component of the FRPM simulation which is further amplified for the source term. This non-physical effect is caused by the rapid variation of the integral length scale around the trailing edge, whereas the implemented FRPM source model relies on smoothly varying length scale gradients. The c_l value has some control over the length scale field which in turn influences the FRPM source contour pattern seen in Figure 38 for $c_l = 0.72$ at the stage when turbulent perturbations are derived.

Figure 39 shows the trailing edge profiles of the source RMS derived from LES and FRPM simulations at two comparison locations. All source profiles shown for LES results in this section are derived from the simulation which employed the medium step tripping which showed the closest agreement to the near-field experimental data in Chapter 4. In Figure 39 the distinctive difference between FRPM simulations for different c_l values tested mainly is in profiles' shape, where for the highest c_l value of 0.72 the second peak at $y/c \sim 0.2 \ldots 0.25$ is well pronounced that is smoothed out with a decreasing c_l coefficient to a lower value. The source averaging has been taken over the entire acoustic simulation. RMS source convergence into symmetric looking contours as well as convergence in terms of magnitude was achieved approximately at 1/5 of time into the simulation run. In terms of the source magnitude, the best agreement between LES and FRPM was found for the c_l value of 0.5 for which the turbulent kinetic energy profiles in Figure 35 also showed the closest match.

The mean velocity profiles were validated against the experiment at the trailing edge location $x/c = 1.0038$; in the previous chapter. Hence, for the term II matrix $\boldsymbol{\omega}' \times \boldsymbol{u}_0$ the instantaneous vorticity is the only remaining component derived from the simulation which validation should close the source derivation in Figure 39 and also, for better arguing the effect of an integral length scale. Figure 40 shows the comparison for the vorticity term which concludes the validation for the entire source term II in 2D.

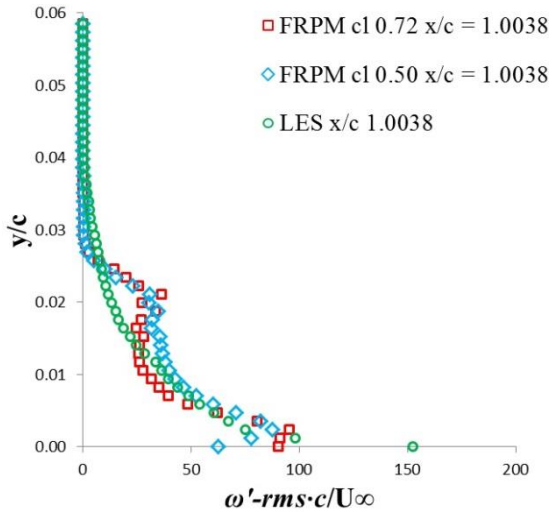

Figure 40 – Comparison of the trailing edge profiles between LES and FRPM (with different c_l coefficients) showing the RMS of *z*-vorticity normalised by the chord and the free-stream velocity.

5.1.2 Source term I comparison

The source term I in Eq. (2.99) reads: $\boldsymbol{\omega}_0 \times \boldsymbol{u}'$, meaning this time velocity perturbations are combined with the mean vorticity. By using Eq. (5.1-5.3) with a 2D assumption results in the sources $q_x = \{v'\overline{\omega_z}\}$ and $q_y = \{-u'\overline{\omega_z}\}$, where in the FRPM simulation $\overline{\omega_z}$ may be supplied directly from RANS and instantaneous velocities are evaluated by the FRPM method in a usual way. Figure 41 shows the mean z-vorticity profiles comparison between LES and RANS at the two trailing edge locations. There is a slight discrepancy between peak amplitudes which is seen right next to the wall/centreline for both x/c locations. Although, the mean vorticity is roughly in the same range up to y/c ~ 0.2 between the two simulations but the rate at which it reduces when moving away from the wall/centreline is different, where the RANS simulation profiles clearly show the inflection. Most vortical structures are extinct beyond approximately y/c of 0.3 which is true for both simulations.

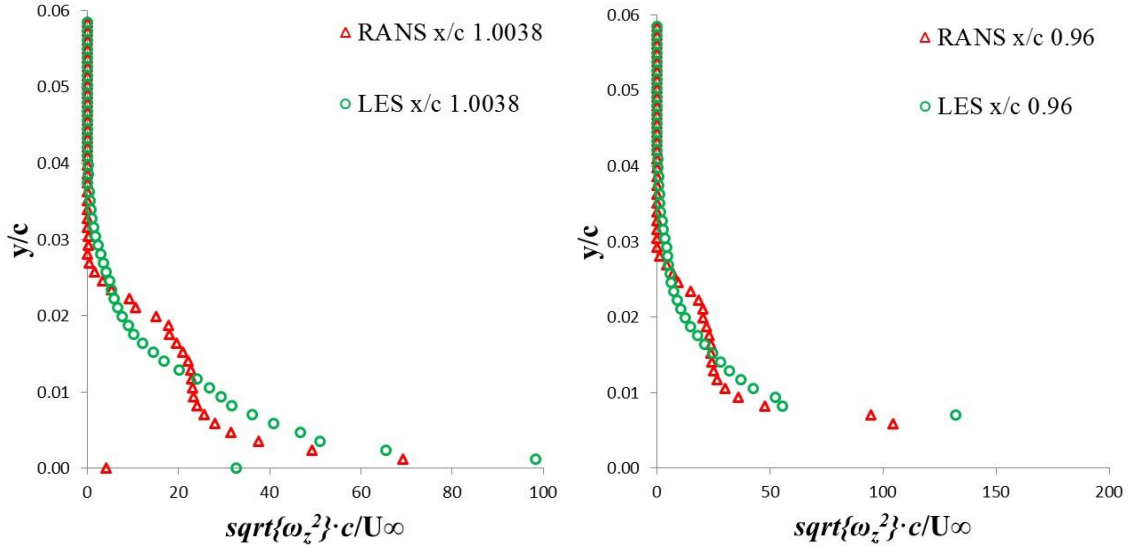

Figure 41 – Comparison of the trailing edge profiles between LES and RANS at $x/c = 0.96$ and $x/c = 1.0038$ locations, showing the mean vorticity normalised by the chord and the free-stream velocity.

The profiles presented in Figure 42 show the magnitude of the RMS source term I for two FRPM simulations when compared to the result from LES. Also, for $x/c = 1.0038$ where the experimental data is available, the additional source term is derived using the combination of the mean vorticity from the LES shown in Figure 41 and experimental rms velocities at the nearest probe location. In Figure 42 for $x/c = 1.0038$ location it can be seen that by using the experimental stream-wise velocity component values to compile the source term instead of RMS(u') velocities from the LES, which were slightly over-predicted close to the centreline, the resulting peak magnitude of the source term I is very close to magnitudes seen in the FRPM method. By comparing results in Figure 42 with the term II sources in Figure 39 it becomes evident that the peak amplitudes for the RMS source term I are several times lower than those for the RMS source term II. This finding supports the hypothesis discussed in [57], where the vortex source term II is stronger than term I for trailing edge noise simulations. Nevertheless, it cannot be assumed negligible, especially at the near-wall region

where the source interaction, possibly, may have an influence on the far-field acoustic predictions.

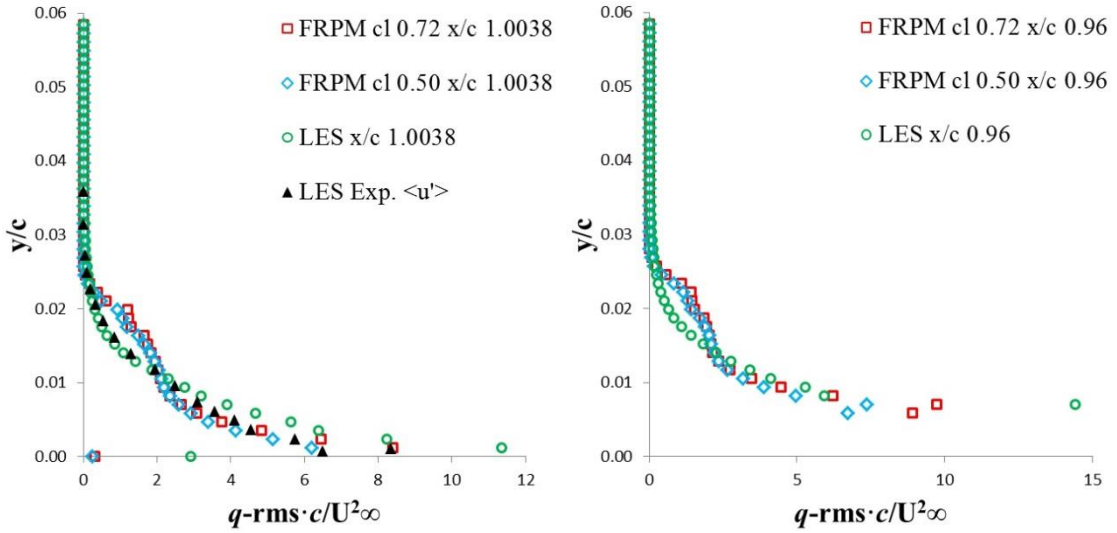

Figure 42 – Comparison of the trailing edge profiles between LES, combination of LES/Exp. and RANS at $x/c = 0.96$ and $x/c = 1.0038$ locations, showing the magnitude of source q-RMS for term I normalised by the chord and the square of free-stream velocity.

5.1.3 Source term III comparison

The source term III in Eq. (2.99) is a non-linear source which is comprised of $\boldsymbol{\omega}' \times \boldsymbol{u}'$ matrix where for the 2D source model $q_x = \{v'\omega_z'\}$ and $q_y = -\{u'\omega_z'\}$ reads according to Eq. (5.1-5.2). The comparison between term III obtained from LES and RANS is presented in Figure 43.

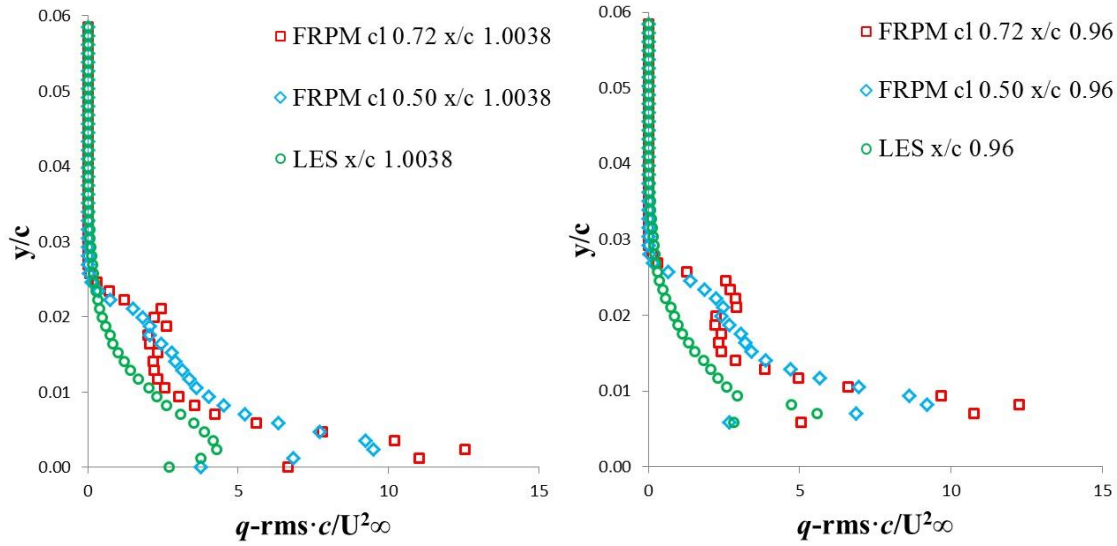

Figure 43 – Comparison of the trailing edge profiles between LES and RANS at $x/c = 0.96$ and $x/c = 1.0038$ locations, showing the magnitude of source q-RMS for term III normalised by the chord and the square of free-stream velocity.

The peak RMS amplitude of the quadrupole source term is found to be greater in the FRPM simulations which are considerably more difficult to validate since the source term III involves multiplication of instantaneous quantities first and only then the average effect is evaluated. The peak values have a comparable magnitude to the source term I. However, one must note that the sound power of the quadrupole term at the far-field scales with $\sim u^8$ while the sound power of the dipole scales as $\sim u^6$. Hence, the non-linear source term III is typically ignored for low Mach number flows. In Figure 43 the comparison is presented to completely analyse the vortex source term given by Eq. (2.99).

After comparing all three terms which are part of the vortex source model Eq. (2.99) at the two trailing edge locations it is possible to conclude that noise sources are similar enough between LES and FRPM simulations. First of all, the mean flow velocity obtained in the RANS simulation showed an excellent agreement to experimental measurements. (See Figure 23) The remaining part of the source term II is a vorticity fluctuation which comparison has been presented in Figure 40. The apparent similarity in magnitude and shape of the RMS plots obtained via different numerical techniques inspire confidence in the FRPM method. Secondly, velocity fluctuations which are part of term I are also available from the experiment and were analysed for the numerical simulations in Chapter 4. Overall, source term I is found to be in very good agreement between FRPM and LES simulations. A slight inflection seen in the FRPM results for term I can be traced back to the z-component of the mean vorticity (see Figure 41) which is ultimately the artifact of the RANS simulation. The agreement for the non-linear term is less convincing than for the two linear terms. Fortunately, term III is considered to be insignificant for the far-field acoustic predictions in the trailing edge noise case. The wave propagator which is a core part of the Altus solver is considered next where a representative case may help to assess the validity of noise predictions at an observer location.

5.2 Testing the APE propagator on the monopole benchmark problem

After presenting the source terms comparison with LES data for the sharp trailing edge in the previous section, wave propagation techniques into the far-field are to be considered. So far it has been established that the FRPM model gives similar enough results to LES for linear sources (term I & II) in the context of the vortex source model. Also, having established a low sensitivity of the FRPM source model on the CFD numerical grid resolution in Chapter 4, the remaining step is to verify the performance of the numerical propagation model. Hence, the test problem which permits an analytical solution is considered first.

For a monopole propagation test, zero mean flow conditions are used for comparison with the analytical problem. However, where APEs are employed for obtaining an acoustic solution of more complicated cases, such as aerofoil's trailing edge noise, presented in the following section, the RANS mean flow is mapped to the acoustic grid for the purpose of providing local density and velocity information. The flux reconstruction at the faces of control

elements is achieved using the Roe flux-splitting scheme. The governing equations are integrated in time using the 4th order explicit ADER method [82] of Titarev and Toro. All of these features are available in the framework of Altus solver which is used together with the FRPM method as discussed in Chapter 3.

For solving the acoustic propagation problem the computational domain is covered by a triangular prism grid with the numerical "microphone" inserted at the far-field. The prismatic layer has one element in the span-wise direction that is the homogeneous direction of the problem. A symmetry plane condition is used in the span-wise direction and far-field characteristic boundary conditions are imposed at all other open-domain boundaries. The acoustic grid is generated with the goal to resolve frequencies up to 10 kHz, which is designed with an aerofoil problem in mind, with at least 2 elements of order 6 per acoustic wavelength in the coarse grid region. In the current implementation a P6 element has 56 degrees of freedom for a prism wedge, where in general the number of degrees of freedom per element follows the equation $(po+1)\times(po+2)$ where po stands for the polynomial order. A monopole source is located in the rectangular source region of the same type as used for trailing edge noise simulations which is covered by the first order elements, which are of the smallest size comparing to higher order elements in the rest of the domain.

A cylindrical wave propagates from a point harmonic force at frequency Ω, which corresponds to the fluctuating force, $\boldsymbol{f}$ in the momentum equations so that $\boldsymbol{f}=-\delta(\boldsymbol{x}-\boldsymbol{y})\boldsymbol{q}(\tau)$, where $\boldsymbol{q}(\tau)=\boldsymbol{A}\exp(i\Omega\tau)$, $\boldsymbol{x}$ and $\boldsymbol{y}$ are the observer and the source coordinates, respectively, and τ is the time in the source reference frame. The resulting acoustic propagation problem is governed by the familiar non-homogeneous linear wave equation:

$$\left(\frac{1}{c_0^2}\frac{\partial^2}{\partial t^2}-\nabla^2\right)p=\boldsymbol{Q} \tag{5.4}$$

where $\boldsymbol{Q}=\nabla\cdot\boldsymbol{f}=-\boldsymbol{q}(\tau)\nabla\delta(\boldsymbol{x}-\boldsymbol{y})$ is the effective source as expressed through the fluctuating force. Eq. (5.4) can be solved in cylindrical coordinates (r,Θ) centred at the source with the appropriate radiation condition at the far field ($r\to+\infty$). The resulting solution for the Fourier wave amplitude of the acoustic pressure wave derived in [164] [165] is given by:

$$p=-\frac{i}{4}\kappa\mathcal{H}_1^{(2)}(\kappa r)\frac{\boldsymbol{x}-\boldsymbol{y}}{r}\cdot\boldsymbol{A}\exp(i\Omega\tau) \tag{5.5}$$

where $\kappa=\Omega/c_0$ and $\mathcal{H}_1^{(2)}(\kappa r)$ is the Hankel function of the 2nd kind. At large distances from the source, $r\gg 1/k$ the asymptotic solution is valid.

$$p(r,t)=\frac{1}{\sqrt{8\pi}}\kappa^{\frac{1}{2}}e^{-i(\kappa r-\pi/4)}\frac{\boldsymbol{x}-\boldsymbol{y}}{r^{3/2}}\cdot\boldsymbol{A}\exp(i\,\Omega\tau) \tag{5.6}$$

which at a 90^0 observer angle leads to a scaling of the pressure amplitude with frequency so that $|p|\sim\kappa^{\frac{1}{2}}\sim\Omega^{\frac{1}{2}}$.

For zero flow conditions, the acoustic propagation equations are solved with a localised source in the momentum equations which approximate the fluctuating point source $\delta(\boldsymbol{x}-\boldsymbol{y})$ by a Gaussian profile, $\delta^{(Numerical)}(\boldsymbol{x}-\boldsymbol{y})$:

$$\delta^{(Numerical)}(\boldsymbol{x}-\boldsymbol{y}) = e^{-ln2\frac{|x-y|^2}{\sigma^2}} \tag{5.7}$$

where the characteristic size of the numerical source distribution, σ, was taken to be around 4-5 grid elements. The latter choice was a compromise between the grid resolution required to capture the source function numerically and making sure that the source remains compact, e.g. $\sigma \ll 1/\kappa$.

Figure 44 shows the result of comparison between the calculations and the theory in terms of the far-field sound pressure amplitude when increasing the sound frequency, Ω while keeping all other test parameters the same. The observer location corresponds to a typical position of the far-field microphone in the trailing edge noise experiments at a 90^0 observer angle to the chord. The amplitude of the numerical solution is Fourier transformed from the corresponding pressure signal. The amplitude of the analytical solution is calibrated so that it exactly matches the numerical solution at the lowest sound frequency corresponding to 2 kHz and then scaled in accordance with theory so that $|p|\sim\Omega^{\frac{1}{2}}$. The numerical solution is within 5% from the analytical solution up to frequencies around 12 kHz, which demarcates the limit of the numerical resolution. Eventually, propagation errors become larger as one would expect beyond the frequency resolution limit of the grid where for 16 kHz the average peak amplitude drops significantly in comparison to the expected value. However, even at the highest frequency considered, 16 kHz, the numerical solution deviates within 10% of the analytical solution meaning that in terms of the acoustic power on the Decibel scale, this is still within 1 dB.

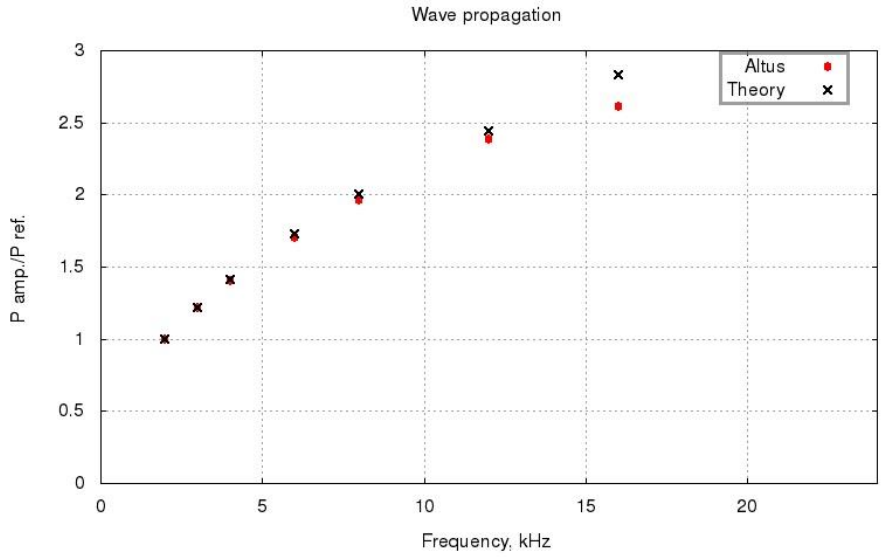

Figure 44 – Comparison with the analytical solution for the acoustic wave propagation problem.

5.3 Acoustic predictions for the sharp trailing edge case

In this section we shall begin with discussing some details for obtaining an acoustic solution via solving APEs which are coupled to the FRPM method in Altus. First of all, in the existing implementation there are two different numerical grids employed for the acoustic simulation. The trailing edge noise sources discussed previously are evaluated on the FRPM grid nodes, which are part of an auxiliary Cartesian grid (see Chapter 3). Then, the sources are mapped to an acoustic grid where the wave propagation takes place, using an unstructured prism grid as described in Section 5.2 for solving the monopole benchmark problem. Therefore, due to the difference in mesh types where source interpolation from a Cartesian FRPM to an unstructured 2D prism acoustic grid takes place, the resolution of the latter in the source region should be roughly the same as that of the FRPM grid for an improved accuracy of interpolation and accurate spatial representation of source terms. Secondly, mean flow quantities extracted from a CFD solution are mapped to the acoustic grid so that the mean flow effects can be taken into account by the APE propagator.

Figure 45(*a*) shows an example of an acoustic grid in *x*-*y* plane which is comprised of prism elements and this grid is used for acoustic propagation of the trailing-edge noise sources to a far-field. It can be seen that the centre of the grid in Figure 45(*a*) is slightly offset downstream from the aerofoil's trailing edge location. This offset is calculated based on the mean flow velocity which is used to improve the numerical efficiency of the far-field boundary conditions, as in this configuration, the far-field boundary is normal to the direction of the acoustic wave propagation. Hence, possible numerical reflections are minimised. At the aerofoil boundary, a no-slip wall ghost point boundary condition is applied.

a) *b)*

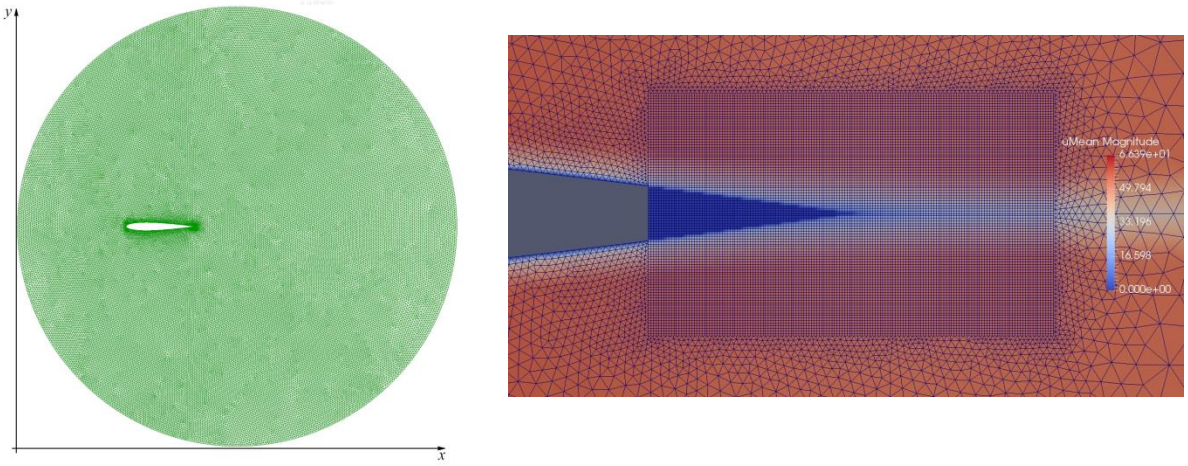

Figure 45 – An example of the computational acoustic grid used for solving sound propagation problem (*a*), mean flow velocity at the trailing edge mapped on both FRPM and CAA grids (*b*)

Figure 45(*b*) shows the mean velocity magnitude in the vicinity of the sharp trailing edge, mapped to both the Cartesian domain shown as a patch over the trailing edge and the

surrounding acoustic grid which is body-fitted around the aerofoil having the refined region inside the Cartesian source grid, i.e. the two grids overlap in the source zone. The acoustic grid rapidly expands away from the source region and the aerofoil wall, reaching the order 6 elements in the far-field with the goal to resolve frequencies up to 10 kHz same as for the monopole benchmark.

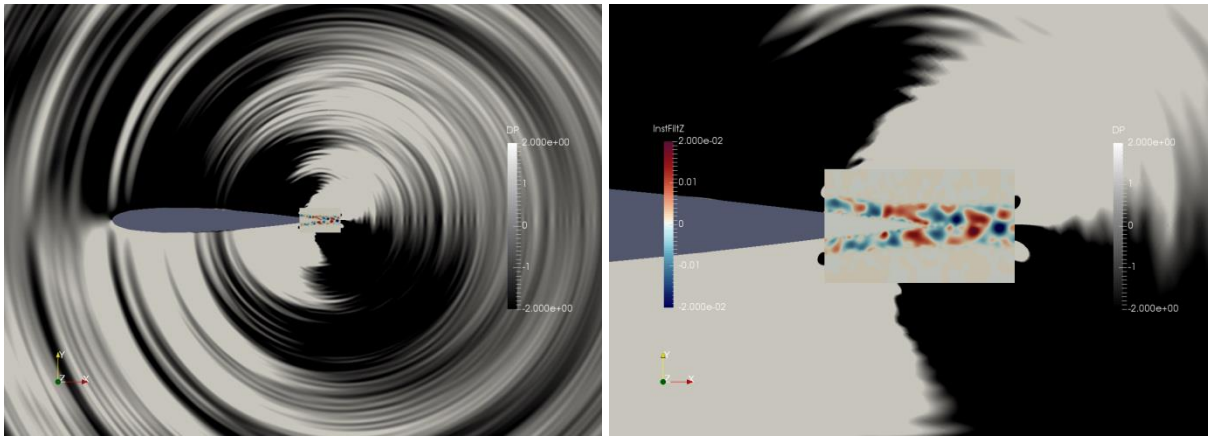

Figure 46 – Contours of an instantaneous acoustic pressure field shown together with the instantaneous acoustic sources at the trailing edge obtained via FRPM method.

The acoustic data available for the sharp trailing edge experiment from the BANC workshop [68] provided by DLR corresponds to a microphone location at 1 m distance or 2.5 chord units from the aerofoil trailing edge and a 90° observer angle. Figure 46 shows the snapshot of the Lamb vector $\{\boldsymbol{u}_0 \times \boldsymbol{\omega}'\}$ as a patch over the sharp trailing edge representing noise sources which are displayed over the instantaneous acoustic pressure field on the grid shown in Figure 45(*a*).

Figure 47 compares the DLR data for the Sound Pressure Level ($\mathrm{SPL} = 20\log_{10} p_{avg}/p_{ref}$) 1/3 octave band noise spectra with the current FRPM numerical predictions. The reference pressure level is taken as 20 μPa. Results for two implementations of the FRPM source model are shown: one is the complete source model including the non-linear source in Eq. (2.99) and the other includes just the first two linear terms. Notably, for the current benchmark problem, the full source model including the nonlinear terms and the linear source model produce virtually the same noise spectra. This agreement is consistent with findings reported in [57] which discussed FRPM model results for broadband aerofoil noise predictions with the assumption that the nonlinear source terms are not important.

For comparison with the experiment which corresponds to a finite span size, the amplitude correction has been applied to noise predictions of the current 2D numerical model to account for 3D effects. Overall, the 2D source model implemented is thought to give a very close approximation to the sound sources found in the vicinity of the thin trailing edge where fluctuating quantities become quickly uncorrelated along the aerofoil's span. However, at low frequencies, the spanwise correlations which are not reproduced by the RANS or the 2D source model may have an impact on the far-field acoustics. Due to two-dimensionality of the current FRPM-based predictions the current model is not applicable for low frequencies,

estimated below ~850 Hz, where the span length of the aerofoil section becomes comparable to the acoustic wavelength. On the other hand, the noise behaviour at low frequencies requires further investigation since the experimental data in the low frequency range is not available and accuracy of the empirical Brooks-Pope-Marcolini (BPM) model for the blunt trailing edge in Section 5.4 for these frequencies is questionable too. Following the 2D FRPM model framework by Ewert *et al.* [62], the absolute levels of the numerical power spectra are adjusted by the same value to match the peak frequency of the experimental data.

The sound pressure levels were scaled with $10n\log(M)$ for 2D to 3D correction originally proposed for the FRPM method, where M is the free-stream Mach number and n is a calibration parameter to match the required amplitude. In the present work the empirical calibration offset corresponds to $n \sim 1.5$. This amplitude correction has been performed only once for the full source model corresponding to the sharp trailing edge experiment. The same amplitude calibration is then applied for all other models including the blunt trailing edge noise predictions considered in the following section. In essence, it can be argued that this amplitude correction can be agglomerated in the definition of the filter amplitude scaling based on the RANS flow solution as described in Eq. (3.10). Such agglomeration then leads to the RANS-based aerofoil noise prediction scheme to be dependent only on two calibration parameters. Overall, the shape of the noise spectra is captured well including the roll-off at high frequencies which are within 3-4 dB from the experiment. Note that the empirical amplitude correction applied appears to be case sensitive and needs to be re-evaluated. For cases with complicated geometries another wave propagation strategy shall be used, primarily to account for 3D effects.

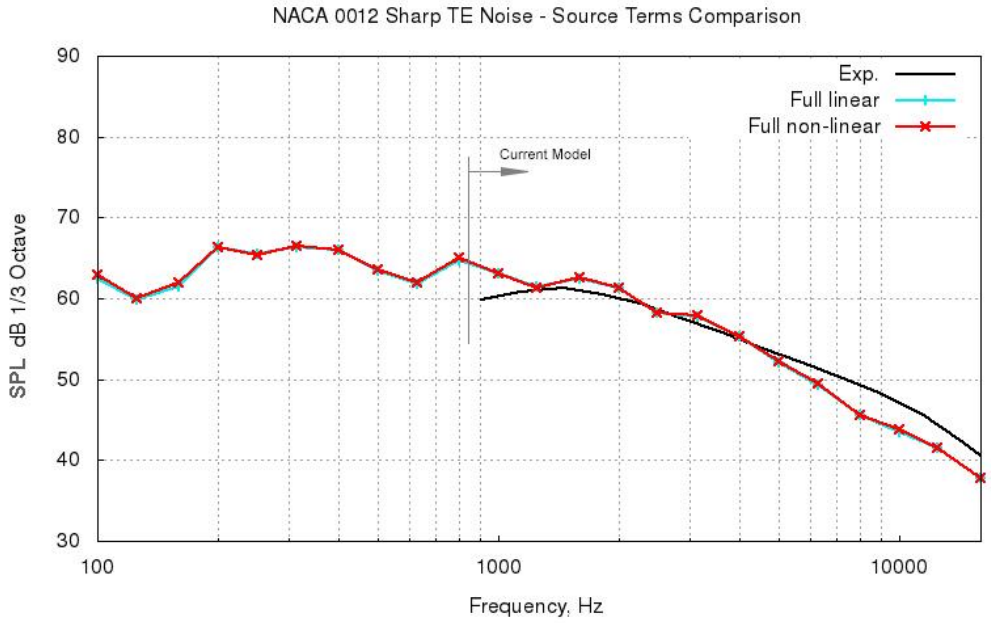

Figure 47 – Comparison with the DLR experiment for the sharp trailing edge case: Sound Pressure Level (SPL) 1/3 octave band noise spectra predictions with and without including the non-linear sound source term.

Figure 48 compares contributions of different noise sources to the far-field noise spectra. Except for the low frequencies at which the current quasi-2D acoustic modelling is less valid, the source term II, $\boldsymbol{\omega}' \times \boldsymbol{u_0}$, remains dominant compared to all other terms for the sharp trailing edge noise case. Again, this finding is consistent with [57].

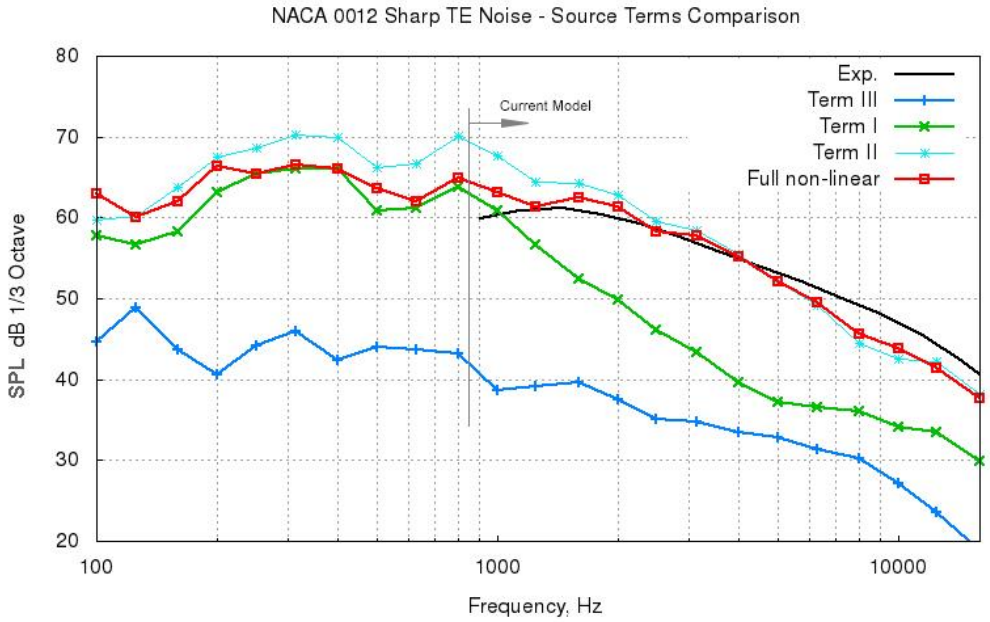

Figure 48 – Sound spectra predicted by simulations employing individual noise source terms, Term I, II and III of Eq. (2.99) respectively and the full source model consisting of all source terms in comparison with the DLR spectra for the sharp trailing edge case.

After analysing the contribution of individual source terms for a reference case with the c_l parameter equal to 0.72 it is necessary to compare a 1/3 octave band spectra calculated for a c_l value of 0.5 which had a better agreement to LES near-field results. Figure 49 compares noise predictions obtained using source term II for different c_l values previously analysed. For the calibration constant $c_l = 0.5$ the peak noise is lower at low frequencies than for the c_l value of 0.72 and for the former results are closer to the experimental curve consistently using the same amplitude scaling. Also, findings in Section 5.1 indicate that higher turbulent velocities have been recorded in the latter case, with the c_l value of 0.72, which can be the cause of slightly amplified noise levels. For high frequencies the difference between the two simulations is marginal with a similar roll-off slope. It should be pointed out that in our simulations the length scale limiters have not been applied meaning that the calibration constant c_l scales the entire turbulent length scale field originally derived from RANS data, contrary to the FRPM trailing edge noise modelling shown in [57] and [62]. It is thought that without lower or upper limit adjustments a finer assessment is presented when comparing the trailing edge sources with those from LES. In this case the lower cut-off scale is prescribed entirely by the FRPM grid, which dimensions were discussed in Section 5.1.1.

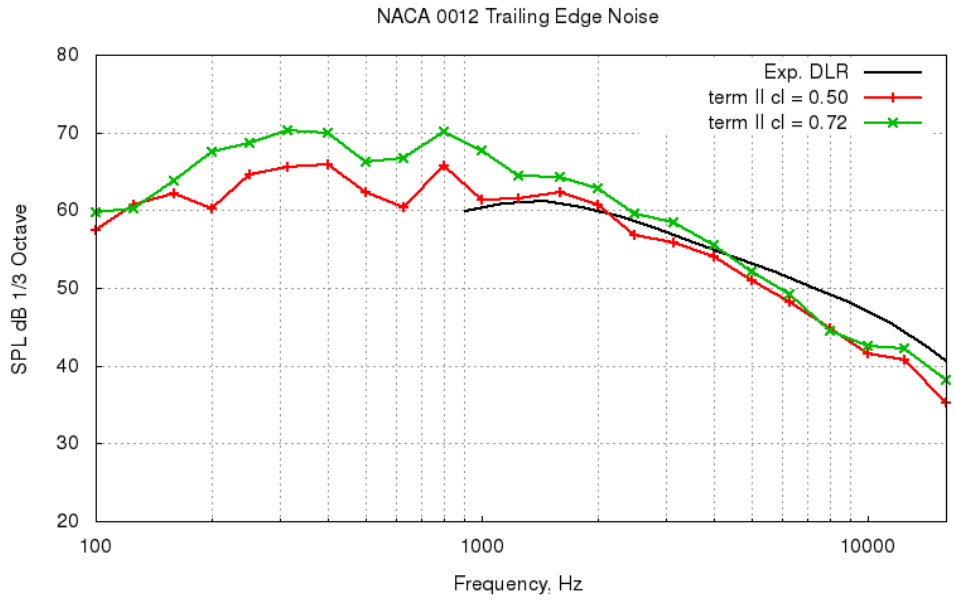

Figure 49 – Comparison with the DLR experiment: SPL 1/3 octave band noise spectra prediction for source term II using two different c_l calibration constants.

Having established the sensitivity of the FRPM noise predictions to the length scale calibration parameter with all other identical inputs an investigation into parameters that can affect the amplitude has been carried on. As there is no strict reference for the FRPM domain size several simulations were performed with alterations to the overall FRPM source volume. After such investigation it is proposed that the amplitude calibration should also take the FRPM source region into account. It has been discovered that the far-field acoustics is sensitive to the source volume in the vicinity of the trailing edge over which the FRPM simulation is performed. For example, by expanding the source calculation zone, and thus, capturing the newly exposed area of high velocity gradients in the near-wall region, which inevitably results in the stochastically generated noise contributing to the overall acoustic source volume, produces amplification of noise at the far-field. A decay function built into the FRPM source region has a similar effect of changing the overall source volume. Arguably, the strongest dipole source should be found behind the trailing edge tip and by expanding the source volume, i.e. including the upstream portion of sources, should not greatly affect the noise levels at the observer location. For this matter, Figure 50 shows the sensitivity of the FRPM method to the increased source zone by narrowing the effective area of the decay function from the last 30 down to the last 10 per cent of the FRPM source region which dimensions were provided in Section 5.1.1. The noise spectrum shown in Figure 50 is also obtained for the source term II with a c_l calibration parameter of 0.72 and all other inputs identical to the ones used for acoustic predictions in Figure 49. It can be seen that the roll-off slope and high-frequency noise are clearly affected. Moreover, such augmentation of the FRPM source zone led to empirical calibration amplitude offset being adjusted to $n \sim 2.8$ to counteract the noise amplification due to increase of the effective source zone. Hence, as the best practice, when comparing between different FRPM simulations the calibration constant and the source region should remain unchanged.

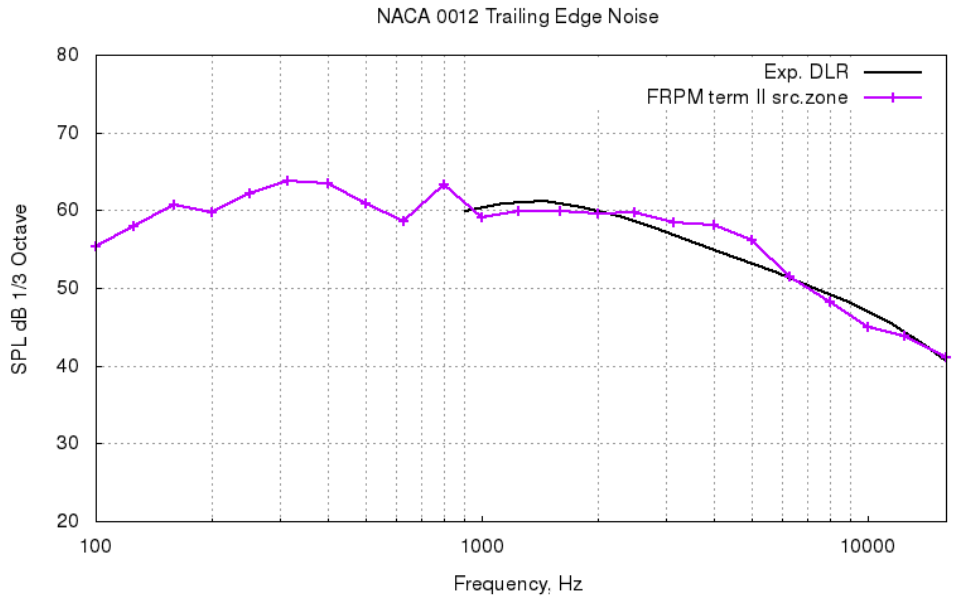

Figure 50 – Comparison with the DLR experiment: SPL 1/3 octave band noise spectra prediction for source term II showing the sensitivity to the FRPM source calculation zone.

For LES simulations an integral method for obtaining far-field acoustics has been used instead of solving APEs. There are a few aspects that need attention regarding the implementation of the FW-H integral method when coupled to a high-fidelity solver for low Mach number flows. In general, resolving boundary layer flow features with LES requires a fine near-wall grid which in turn is a limiting factor for a computational time step as it was discussed in Chapter 4. Usually, in airframe noise problems the strongest acoustic sources are found in the close proximity to a solid body which is also true for the trailing edge noise problem considered in this section. Therefore, in LES simulations an impermeable control surface S is placed in the highest source concentration region that is next to a wall. As a consequence, for the size of problems typically found in engineering, data storage of variables recorded over time often becomes an issue. It is possible to overcome this constraint by processing acoustic data 'on the fly' during the simulation run. [50] In either case, for a rapidly changing turbulent field, for example, in the zone of intensive turbulent mixing, selecting relatively large time integration intervals presents a risk associated with obtaining incorrect time derivatives of the turbulent quantities. Moreover, for a low Mach, near-wall perturbation density and pressure signals may appear excessively noisy, inevitably leading to non-physical pressure amplification, which in the worst case results in errors dominating over genuine fluctuations. Figure 51 shows a raw data for density, three components of velocity and energy being collected over a time period at the trailing edge location, which shows that the noisiest signal is found for the density and energy being the second noisiest. This problem is particularly evident for high frequencies on a sound pressure spectrum which has a direct impact on acoustic predictions shown in Figure 52.

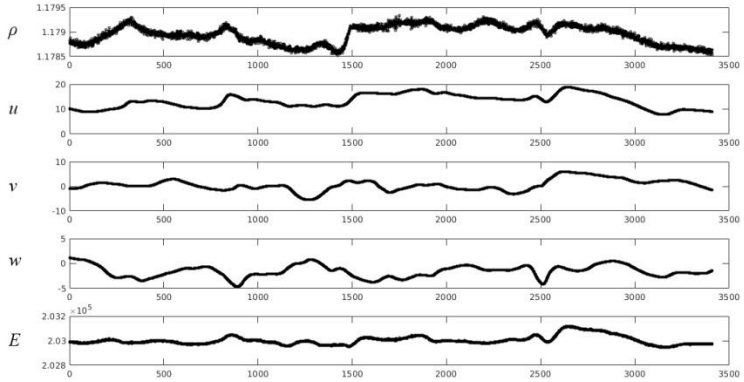

Figure 51 – Raw data showing fluctuations of turbulent quantities recorded over a time period at the trailing edge of a NACA 0012 aerofoil in MILES CABARET simulation.

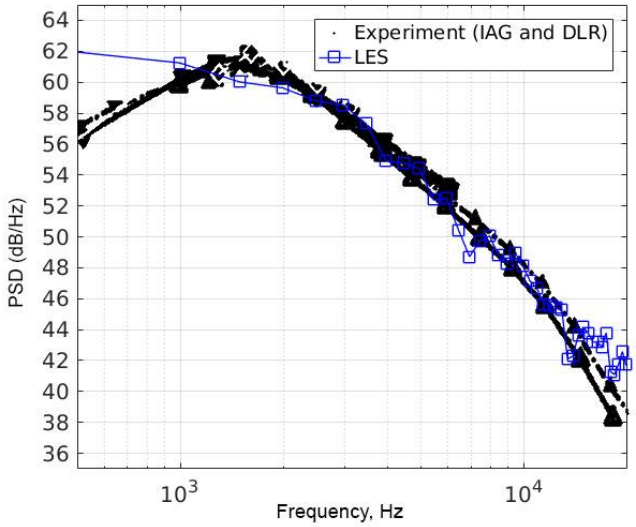

Figure 52 – Comparison with the IAG and DLR experiments: PSD (dB/Hz) noise spectra prediction for MILES CABARET using the FW-H integral method.

The far-field narrowband PSD results seen in Figure 52 are normalised to the 1 m span following the procedure undertaken in [64] and to 1 Hz. In general, the LES acoustic results are in very good agreement with the experiment for most parts of the spectrum, where only beyond 10 kHz a slight amplification is observed. The spectrum shows that the deviation of the peak amplitude is only 1∼2 dB at the experimental peak location and the roll-off slope is accurately captured. Overall, such close agreement with experimental measurements for the far-field sound pressure level inspires confidence in the FRPM source scaling at the source level which was adjusted according to the source information of the LES simulation.

5.4 Acoustic predictions for the blunt trailing edge case

Following the scale decomposition approach proposed in Section 3.3 of Chapter 3 the acoustic results are obtained for the blunt trailing edge benchmark problem in the framework of the FRPM method. Large scale fluctuations are derived from the URANS solution presented in Section 4.3.4. For noise predictions the 2D aerofoil profile is considered following the same methodology as for the sharp trailing edge. The domain is meshed using a variable order of the finite elements, starting from the first-order elements in the finest grid region close to the aerofoil boundary and in the source region around the blunt edge while using the 6^{th} order elements in the far-field region. Figure 53(*a*) shows an acoustic grid in the vicinity of the blunt trailing edge.

a) *b)*

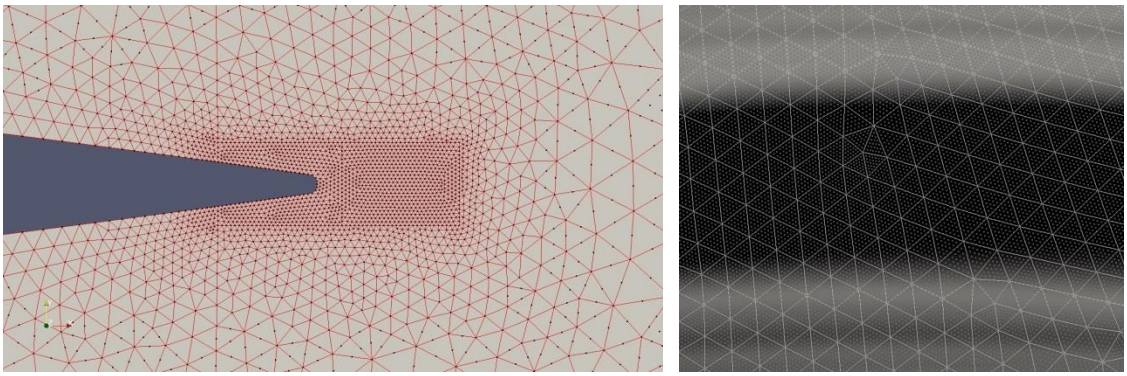

Figure 53 – Computational acoustic grid in *x-y* plane. Grid elements in the vicinity of a trailing edge *(a)* and the far-field showing high order elements over an instantaneous acoustic pressure wave *(b)*.

For the blunt trailing edge experiment of Brooks & Hodgson [92], the observer location is again at 90° to the free stream and the distance to the far-field microphone corresponds to $L = 1.222$ m which is approximately 2 chords lengths. Figure 53(*b*) shows the high order elements over instantaneous acoustic pressure waves in the far-field zone roughly at the observer's location where dots represent degrees of freedom.

Figure 54 shows the comparison of noise spectra predictions from various computations based on the first URANS simulation, which slightly under-predicts the vortex shedding frequency of the experiment as discussed in Section 4.3.4. Results of the empirical Brooks-Pope-Marcolini (BPM) solution from [66] are shown on the same plot for comparison. There are two solutions for noise spectra shown. The first solution is based on the standard FRPM formulation where the velocity source fluctuation includes only the stochastic turbulence component defined through the time-local URANS scale. The other solution is based on using the full velocity fluctuation including the tone as discussed in Section 3.3. For comparison, the acoustic prediction corresponding to the isolated tonal part of the source (without the broadband part) which exhibits a secondary weak tone at ~5 kHz, is shown in the same figure. The secondary peak is not visible for the combined URANS solution due to

overwhelming impact of broadband noise at 5 kHz. It can be noticed that unlike either the pure broadband FRPM solution or the pure tonal noise solution, the prediction of the new unified approach includes both elements and is within 3dB agreement from the experiment apart from some offset of the tone. As expected, the numerical tone prediction is shifted towards a lower frequency within 2-3 kHz range in accordance with under prediction of the shedding frequency by the first URANS simulation. 3dB is approximately the same error bar as demonstrated by the FRPM method implementation in the previous sharp trailing edge noise test.

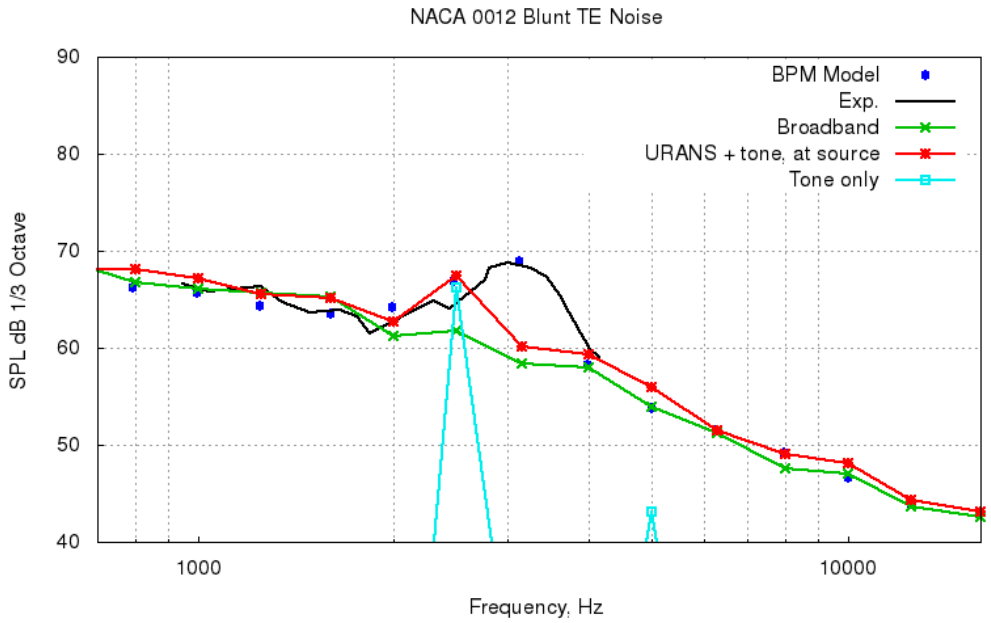

Figure 54 – Comparison with experiment and the reference empirical model [66] for the blunt trailing edge case: Sound Pressure Level (SPL) 1/3 octave band noise spectra predictions based on the first URANS model with and without including the tonal noise source component and also for the pure tonal noise component.

To address the question of correlation between the broadband signal and the tonal noise at the far field, Figure 55 compares the spectra prediction of the model that accounts for both noise components, broadband and tonal, at the source level and the synthetic spectra obtained by simply adding squares of the acoustic pressure amplitudes of the pure broadband and the pure tonal noise signals in the far-field at the post-processing stage. The difference between the two spectra for the relevant frequency range is within 2dB which is within the accuracy of the current FRPM model and the two far-field signals are found to be uncorrelated in this particular case.

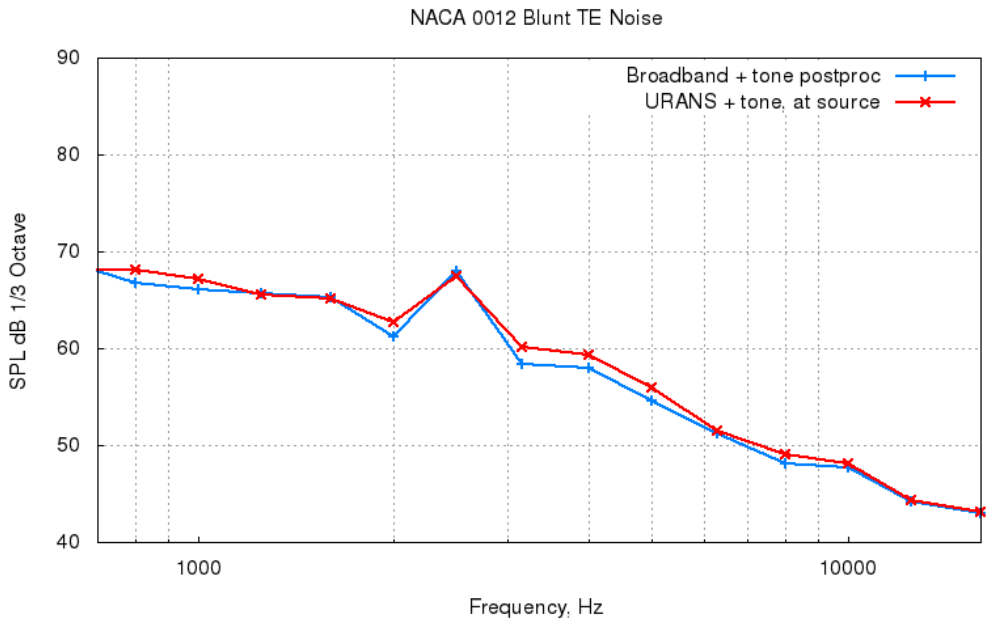

Figure 55 – Sound Pressure Level (SPL) 1/3 octave band noise spectra comparison between the full term including the broadband and the tone at the source and the synthetic spectra obtained by simply adding squares of the acoustic pressure amplitudes of the pure broadband and the pure tonal noise signals in the far-field.

Figure 56 shows the spectra predicted using the current URANS model with the tone included which are broken down into individual linear and non-linear source contributions in accordance with Eq. (2.99) : $\boldsymbol{\omega}_0 \times \boldsymbol{u}'$ (term I), $\boldsymbol{\omega}' \times \boldsymbol{u}_0$ (term II), and $\boldsymbol{\omega}' \times \boldsymbol{u}'$ (term III) as well as the total spectra.

It can be observed that while term II remains dominant for the broadband part of the spectra as compared to the other terms, term I is equally important in the region of the tonal peak. The importance of term I for the blunt trailing edge case is a clear distinction as compared to the sharp trailing edge flow, where the noise mechanism was purely broadband.

Interestingly, for the tonal peak, the noise contribution from source terms I and II are of a similar magnitude to the total signal. This means that the sound pressure powers produced by the two sources do not simply add up to produce the total since acoustic source interference of the two source terms is not negligible in contrast to the broadband and tonal noise components in Figure 54. Instead, the phase difference between the corresponding pressure signals produced by the two sources is close to $\pi/2$. The latter is consistent with relating the tonal noise mechanism to a linear shear wave transport where velocity and vorticity fluctuations are offset in phase by $\pi/2$. For the blunt trailing edge aerofoil case, the contribution of the non-linear term III remains insignificant in comparison with the linear sources as observed for the sharp trailing edge aerofoil problem. This further reconfirms that in this case the interference of the tonal and broadband noise sources is not important.

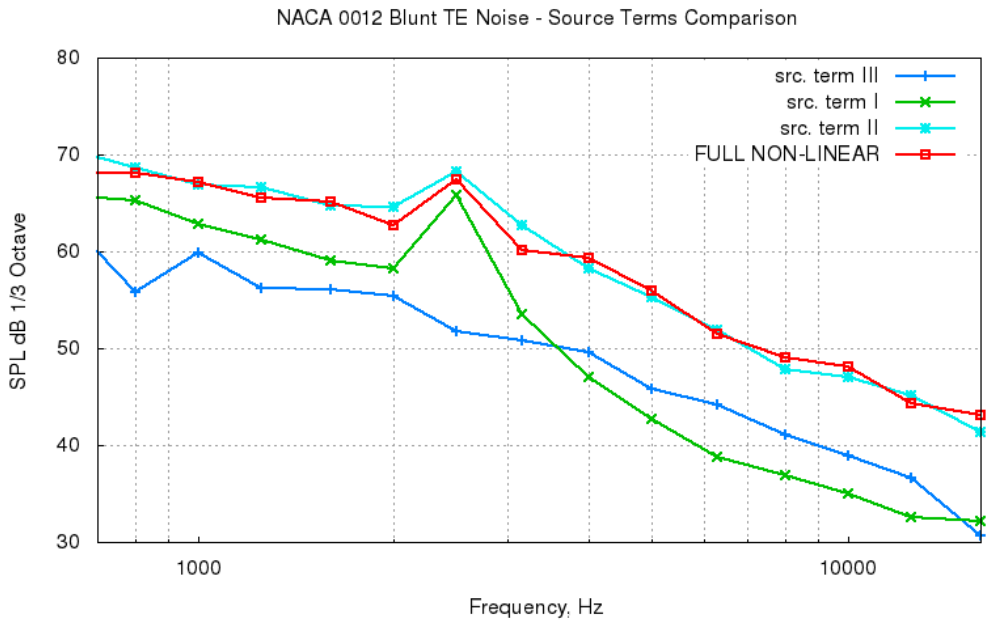

Figure 56 – Sound level predicted by simulations employing individual noise source terms, Term I, II and III of Eq. (2.99) respectively and the full source model for the blunt trailing edge case.

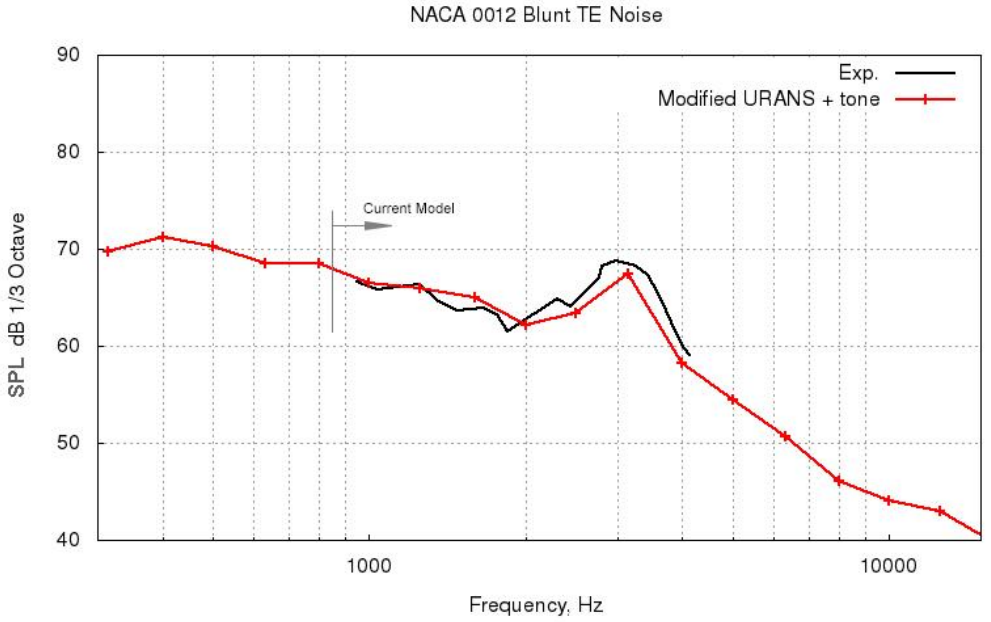

Figure 57 – Comparison with experiment [92] for the blunt trailing edge case: Sound Pressure Level (SPL) 1/3 octave band noise spectra predictions based on the modified URANS flow solution.

Figure 57 shows the total noise spectra predictions obtained with the second URANS solution, which was fine-tuned in accordance with the description in Section 4.3.4 to reproduce the correct shedding frequency of the experiment where the blunt trailing edge was slightly elongated, thus, reducing its thickness. As a result of such alteration the wake shedding frequency increased compensating for inaccuracy of the URANS model. The

acoustic predictions based on this second URANS solution are in excellent agreement with the experiment including both the broadband and the tonal part of the spectra. Overall, the current predictions are in agreement within 2-3 dB to the measurements. Importantly, except for the modified URANS solution, there was no other calibration used for obtaining the improved acoustic predictions with the FRPM model.

Chapter 6

Conclusions and future work

For the aerofoil trailing-edge noise applications a Fast Random Particle Mesh (FRPM) method combined with solving the time-domain Acoustic Perturbation Equations (APE) are used in the framework of the BAE Altus solver. The simulations were performed for a 2D model setting which made them amenable to a 48 hour run time per case on 64 computational cores running double precision.

Comparison of the aerofoil trailing-edge RMS noise sources between the FRPM method and Large Eddy Simulations (LES) has been presented for the sharp trailing edge case considered in the Benchmark problems for Airframe Noise Computations (BANC) workshop. LES simulations were performed with two boundary layer tripping techniques, one that imitated the experimental tripping device and the other was implemented by introducing boundary conditions in the form of a suction/blowing numerical approach. For the Reynolds-Averaged Navier-Stokes (RANS) method a fully turbulent boundary layer assumption was used. Numerical flow results for all cases were then compared against experimental data and a good agreement for mean quantities was reported.

The calibration length scale parameter c_l used in the FRPM method was adjusted with the help of LES data. The difference between the two ends of the recommended range, which in general for airframe noise is 0.5 … 0.75 as suggested in the literature, is found to be within several dB on the noise spectra for the sharp trailing edge. (See Figure 49) However, for obtaining accurate acoustic sources using the FRPM method a RANS simulation has to be closely examined first. As discussed in Chapter 3 the turbulent integral length scale derived from the two-equation RANS model consists of a turbulent kinetic energy (TKE) and a turbulence dissipation rate. For the aerofoil benchmark case, the RANS model produced an excellent agreement of the TKE with the experiment. On the other hand, there was a large deviation of the integral length scale close to the centreline when comparing to the BANC workshop data as a result of incorrectly predicted turbulence dissipation rate. This side of the problem deserves attention where for *y/c* up to ~ 0.01 the length scale has a direct influence on noise sources and it also happens to fall within a highest source concentration zone. It is worth emphasizing that despite an excellent agreement found for the velocity and TKE quantities, the two-equation RANS model failed to give a credible ‘epsilon’ prediction up to *y/c* ~ 0.01.

To further improve the accuracy of noise sources prediction with the FRPM method which is based on a stochastic stream function one option can be to fine tune the RANS model for improved dissipation rate prediction. However, this would not automatically solve the problem of missing anisotropic turbulence length scales which are not obtainable from

RANS. In general, it is possible to assign different dimensional scaling of turbulence. However, such mechanism will be based on the additional empirical scaling which is complicated to perform correctly for cases containing rich physics. Since the FRPM method is efficient with regard to obtaining acoustic sources on a Cartesian grid and it takes only a fraction of the computational expense, the problem could be naturally extended to model 3D sources. However, the information on flow correlations cannot be simply obtained from the RANS/URANS methods. Possibly, one has to look into methods that are much cheaper than LES but at the same time can provide the correlation information. For addressing this issue, the stochastic realisation of turbulent sources could be performed using a Forced Linear Advection-Diffusion-Dissipation (FLADD) equation [166] which concept is regarded as promising, leading to further development of the FRPM method.

In the FRPM simulation the TKE field can be recovered from stochastic velocities and because an excellent agreement was found for the mean data with the experiment in the case of flow past a NACA 0012 aerofoil, this parameter is also used for comparison with LES data. If the FRPM method is to be used under a 'blind test' condition, as an initial check, it should be ensured that the recovered TKE matches the target input from a RANS simulation. For the sharp trailing edge simulation it was determined that a statistical convergence is reached by averaging the near-field data over time equivalent to approximately 1/5 of the total acoustic simulation run time. Hence, performing the calibration of the c_l parameter only takes a fraction of the total simulation time.

As far as the wave propagation is concerned, solving APEs in the time domain has been a preferred technique used in conjunction with the FRPM method. Initially, for an analytical problem of a fluctuating point force provided to the right-hand side of the governing acoustic equations and using a zero mean flow conditions, the accuracy of the current numerical wave propagation method for a grid resolution typical of the trailing edge noise problems of interest has been verified in comparison with the theory. For the trailing edge noise predictions, simulations showed an encouraging agreement (2-3 dB) with the experiment for both broadband and tonal noise. All model predictions are essentially based on RANS simulations with just two calibration parameters: one for the correlation length scale and the other for the amplitude correction. However, the wave propagation method based entirely on APEs is found to be the bottleneck in the current methodology as not only a two-dimensional propagation restriction applies but importantly, the amplitude correction which involves the second empirical scaling coefficient is found to be of a questionable validity. There is a possibility that such correction accounts for more than just 2D to 3D effects. In addition, the acoustic spectra are found to be sensitive to the FRPM source region as shown in Figure 50. Therefore, in the context of the current model only the relative difference in noise levels can be judged, providing the two FRPM far-field acoustic predictions are obtained using the same amplitude scaling and for the equivalent source volume. For the future work, employing an integral method such as Ffowcs-Williams and Hawkings (FW-H) also coupled to APEs or the Linearised Navier-Stokes (LNS) equations in the near-field may be considered, which should allow efficiently extending the source model and wave propagation to 3D.

Generally, a good agreement is found for the trailing edge vortex sources obtained via the FRPM method when comparing to those in LES at the source level. The ability of the FRPM method to reproduce similar looking source terms to LES with only one c_l calibration parameter which has quite a narrow range is the significant finding.

For the flow over a bluff body, flow quantities are normally correlated over a large distance as for example, seen in the case of the flow past a circular cylinder where the pressure coherence is recorded over 5 cylinder diameters in the span-wise direction in the benchmark experiment. [59] These fluctuations are the underlying mechanism for broadband and tonal noise and for that reason the current FRPM model cannot give reliable source predictions for a cylinder benchmark. For overcoming one of the disadvantages of the method, the original FRPM technique has been extended to include tonal noise sources based on the idea of scale separation by combining the large-scale flow solution available from URANS with the fine-scale FRPM solution. This modification allows for a unified treatment of the broadband and tonal noise sources at the source level, consistently accounting for source interference and possible nonlinear source interaction effects.

For the new model validation the benchmark aerofoil case has been selected featuring a NACA 0012 aerofoil with a blunt trailing edge since similar modelling experience is gained having a sharp trailing edge. The benchmark problem investigated corresponded to the blunt trailing edge experiment conducted in 1980s by Brooks & Hodgson [92] for which the far-field acoustic data is available. A zero incidence flow angle at a high Reynolds number of the order 2×10^6 has been used assuming fully turbulent boundary layer conditions as for the first benchmark case. For the blunt trailing edge benchmark, two CFD simulations were performed. First, the simulation was performed using the reference trailing edge geometry and then with a 20% reduced trailing edge thickness, thus, accounting for the URANS modelling inaccuracy to reproduce the vortex shedding frequency of the experiment. Main accent was on the development of the stochastic source model which reflected this change in frequency showing that the model is sensitive to the CFD input. No modelling of the laminar/turbulent boundary layer transition occurring in the experiment was attempted.

The importance of including a separate tonal noise source in the original broadband FRPM model as well as having an appropriate flow model that captures the relevant tonal scale is investigated. By comparing the predictions of the new unified model with the synthetic spectra obtained by simply adding squares of the acoustic pressure amplitudes of the pure broadband and the pure tonal noise signals in the far-field, it is shown that the broadband and the tonal sources are virtually uncorrelated for the test case considered. However, not to mention its generality, the new unified approach is approximately two times computationally more efficient since otherwise, the calculation of the synthetic spectra from the individual broadband and tonal signals requires 2 solutions of the far-field sound propagation problem.

Using the current modified FRPM model it is shown that while the linear source term II associated with the vorticity fluctuation is dominant for the broadband noise both linear terms I and II which involve the fluctuating vorticity and the fluctuating velocity can be significant for tonal noise. In the latter case the total far-field spectra resulted from the acoustic

interference of sources I and II which cannot be simply added up because of the phase difference. It is also confirmed that for the current benchmark cases the effect of the nonlinear source is negligible as compared to the linear sources.

For LES simulations the MILES CABARET method has been extensively tested on benchmark problems leading into investigation and implementation of various tripping techniques employed for overcoming the grid resolution limitation. In the aerofoil benchmark case with a Re number of 1.5M based on the chord a reasonably good agreement of the near-field data has been reported. Moreover, it was possible to achieve a good match of the trailing edge flow quantities with experimental data using both the numerical suction/blowing boundary layer tripping and technique which involved simulating the actual step tripping device. The calibration of the boundary layer tripping was also discussed and once the time-averaged flow results have been validated against the experiment, it led to the LES simulation providing a valuable insight into trailing edge noise sources.

On the topic of MILES, for the flow over a circular cylinder considering the laminar separation (LS) case it has been anticipated that the biggest challenge is capturing 'enough' of the small scales responsible for the flow separation. A stochastic white noise boundary layer tripping technique has been applied to initiate a slightly earlier separation and although the tripping has been successfully implemented which produced the average separation point at a target 80° azimuthally, the flow over a cylinder remained overly accelerated. By operating without any SGS some influence on the boundary layer was likely required over the entire frontal area of the cylinder where the flow is attached to the wall and further implementation of the complicated enough tripping was discontinued. Further suggestions were outlined at the end of Section 4.2. In an attempt to accurately simulate the boundary layer for the finest simulation discussed in Chapter 4 the time step was only a fraction of a nanosecond. Nevertheless, the simulation was performed on a single GPU card and approximately 50 TUs based on the cylinder diameter that are required for obtaining the near-field comparison were achieved within a week. It is predicted that by using a new technique which is applied in this work for simulating the flow over a NACA 0012 aerofoil which employs a snappy-hex grid and asynchronous time stepping [50] may significantly boost the performance in comparison to the finest cylinder simulation run presented in this work. Hence, it may be possible to determine the threshold for a maximum cell size that yields the accurate flow solution for a cylinder benchmark at Re 50,000 in the near future.

Appendix A

Monopole source

When the sound pressure is expressed in the form:

$$p(x,t) = P(x)e^{-i(\omega t+\phi_p)} \tag{A.1}$$

where $P(x)$ is the magnitude of pressure and ϕ_p is the phase in space and $i = \sqrt{-1}$. Note, $\phi_p = f(x)$. From Euler's equation:

$$\frac{\partial \boldsymbol{u}(x,t)}{\partial t} = -\frac{1}{\rho_0}\frac{\partial p}{\partial x} \tag{A.2}$$

Hint: a quick way to evaluate the pressure gradient and velocity:

$$\frac{\partial p}{\partial x} = \left\{\frac{dP}{dx} - j\left(\frac{d\phi_p}{dx}\right)P\right\}e^{-i(\omega t+\phi_p)} \tag{A.3}$$

$$u(x,t) = -\frac{1}{\omega\rho_0}\left\{P\left(\frac{d\phi_p}{dx}\right) + i\left(\frac{dP}{dx}\right)\right\}e^{-i(\omega t+\phi_p)} \tag{A.4}$$

where $P = P(x)$ from Eq. (A.1) and when ϕ_p is expressed through κr, re-calling that $\kappa = \omega/c$ will result in $1/\rho_0 c$ constant in Eq. (A.4). Also, while the first term in brackets Eq. (A.4) is in phase with the pressure Eq. (A.1) the second term is 90° out of phase.

Dipole source

$$p(r,\theta,\varphi) = \lim_{\Delta\to 0} A\left(\frac{e^{i(\kappa r_1)}}{r_1} - \frac{e^{i(\kappa r_2)}}{r_2}\right) \tag{A.5}$$

Let two sources be located on the z axis and the midpoint between the two (x,y,z). Then, defining r_1 and r_2:

$$r_1^2 = x^2 + y^2 + (z - \Delta/2)^2 \tag{A.6}$$

$$r_2^2 = x^2 + y^2 + (z + \Delta/2)^2 \tag{A.7}$$

Eq. (A.5) could be expanded using Taylor series with high order terms neglected, which yields the following expression:

$$p(r,\theta,\varphi) = \lim_{\Delta\to 0} A\left\{\left(\frac{e^{i(\kappa r_1)}}{r_1} - \frac{e^{i(\kappa r_2)}}{r_2}\right)\Big|_{\Delta=0} + \frac{d}{d\Delta}\left(\frac{e^{i(\kappa r_1)}}{r_1} - \frac{e^{i(\kappa r_2)}}{r_2}\right)\Big|_{\Delta=0}\Delta\right\} \tag{A.8}$$

It follows that the first term in Eq. (A.8) can be neglected and the second term remains:

$$p(r,\theta,\varphi) = \lim_{\Delta\to 0} A\,\Delta\left\{\frac{d}{dr_1}\left(\frac{e^{i(\kappa r_1)}}{r_1}\right)\frac{dr_1}{d\Delta}\Big|_{\Delta=0} - \frac{d}{dr_2}\left(\frac{e^{i(\kappa r_2)}}{r_2}\right)\frac{dr_2}{d\Delta}\Big|_{\Delta=0}\right\} \tag{A.9}$$

When $\Delta \to 0$, r_1 and r_2 become r. Hence,

$$\frac{d}{dr}\left(\frac{e^{i(\kappa r)}}{r}\right) = \frac{j\kappa r e^{i(\kappa r)} - e^{i(\kappa r)}}{r^2} \tag{A.10}$$

And two remaining derivatives are simplified using the assumption in Eq. (A.6-A.7), such as:

$$\left.\frac{dr_1}{d\Delta}\right|_{\Delta=0} = -\frac{1}{2}\frac{z}{r} = -\frac{1}{2}\cos\theta \tag{A.11}$$

$$\left.\frac{dr_2}{d\Delta}\right|_{\Delta=0} = \frac{1}{2}\frac{z}{r} = \frac{1}{2}\cos\theta \tag{A.12}$$

Let D represent the dipole-moment amplitude vector, so $A\Delta = D$. Then, using Eq. (A.10-A.12) and rearranging terms, the equation for the dipole sound pressure follows:

$$p(r,\theta,\varphi) = D\frac{z}{r}\left\{-\frac{i\kappa r e^{i(\kappa r)}}{r^2} + \frac{e^{i(\kappa r)}}{r^2}\right\} = -j\kappa D\frac{e^{i(\kappa r)}}{r}\frac{z}{r}\left(1 + \frac{i}{\kappa r}\right) \tag{A.13}$$

$$p(r,\theta,\varphi) = -j\kappa D\frac{e^{i(\kappa r)}}{r}\cos\theta\left(1 + \frac{i}{\kappa r}\right) \tag{A.14}$$

In a spherical coordinate system, with angles θ and φ where the convention is:

$$z = r\cos\theta$$

$$y = r\sin\theta\sin\varphi$$

$$x = r\sin\theta\cos\varphi$$

Using Euler's equation for obtaining velocity by taking the time integral of the pressure gradient which is determined from Eq. (A.14) yields:

$$u_r(r,\theta,\varphi) = -i\frac{\kappa D}{\rho_0 c}\frac{e^{i(\kappa r)}}{r}\cos\theta\left(1 + 2i\left(\frac{1}{\kappa r}\right) - 2\left(\frac{1}{\kappa r}\right)^2\right) \tag{A.15}$$

Then, as a final step dividing Eq. (A.14) by Eq. (A.15) gives the impedance in the r direction:

$$z_r(r,\theta,\varphi) = \rho_0 c\frac{1 + i\left(\frac{1}{\kappa r}\right)}{1 + 2i\left(\frac{1}{\kappa r}\right) - 2\left(\frac{1}{\kappa r}\right)^2} \tag{A.16}$$

Quadrupole source

$$p(r,\theta,\varphi) = \lim_{\Delta\to 0}(-i\kappa D)\left[\frac{e^{i(\kappa r_1)}}{r_1}\cos\varphi_1\left\{1 + i\left(\frac{1}{\kappa r_1}\right)\right\} - \frac{e^{i(\kappa r_2)}}{r_2}\cos\varphi_2\left\{1 + i\left(\frac{1}{\kappa r_2}\right)\right\}\right] \tag{A.17}$$

$$r_1^2 = (x - \Delta/2)^2 + y^2 + z^2 \tag{A.18}$$

$$r_2^2 = (x + \Delta/2)^2 + y^2 + z^2 \tag{A.19}$$

If $\cos\varphi_1 = z/r_1$ and $\cos\varphi_2 = z/r_2$ relations are substituted in Eq. (A.17) we get:

$$p(r,\theta,\varphi) = \lim_{\Delta\to 0}(-i\kappa D)\left[\left\{\frac{e^{i(\kappa r_1)}}{r_1^2} - \frac{ie^{i(\kappa r_1)}}{\kappa r_1^3}\right\}z - \left\{\frac{e^{i(\kappa r_2)}}{r_2^2} - \frac{ie^{i(\kappa r_2)}}{\kappa r_2^3}\right\}z\right]$$

Rearranging terms in a neat way:

$$p(r,\theta,\varphi) = \lim_{\Delta\to 0} Dz\left[\frac{1}{r_1^3}(1-i\kappa r_1)e^{i(\kappa r_1)} - \frac{1}{r_2^3}(1-i\kappa r_2)e^{i(\kappa r_2)}\right] \tag{A.20}$$

As a next step, expanding the above expression using Taylor series as previously done for a dipole source, yields:

$$p(r,\theta,\varphi) = \lim_{\Delta\to 0} Dz\Delta\left\{\frac{d}{dr_1}\left[\frac{1}{r_1^3}(1-i\kappa r_1)e^{i(\kappa r_1)}\right]\frac{dr_1}{d\Delta}\bigg|_{\Delta=0} - \frac{d}{dr_2}\left[\frac{1}{r_2^3}(1-i\kappa r_2)e^{i(\kappa r_2)}\right]\frac{dr_2}{d\Delta}\bigg|_{\Delta=0}\right\} \tag{A.21}$$

where

$$\frac{d}{dr}\left[\frac{1}{r^3}(1-i\kappa r)e^{i(\kappa r)}\right]\bigg|_{\Delta=0} = e^{i(\kappa r)}\left(-3\frac{1}{r^4} + 3i\frac{\kappa}{r^3} + \frac{\kappa^2}{r^2}\right) \tag{A.22}$$

Appendix B

Altus solver algorithm

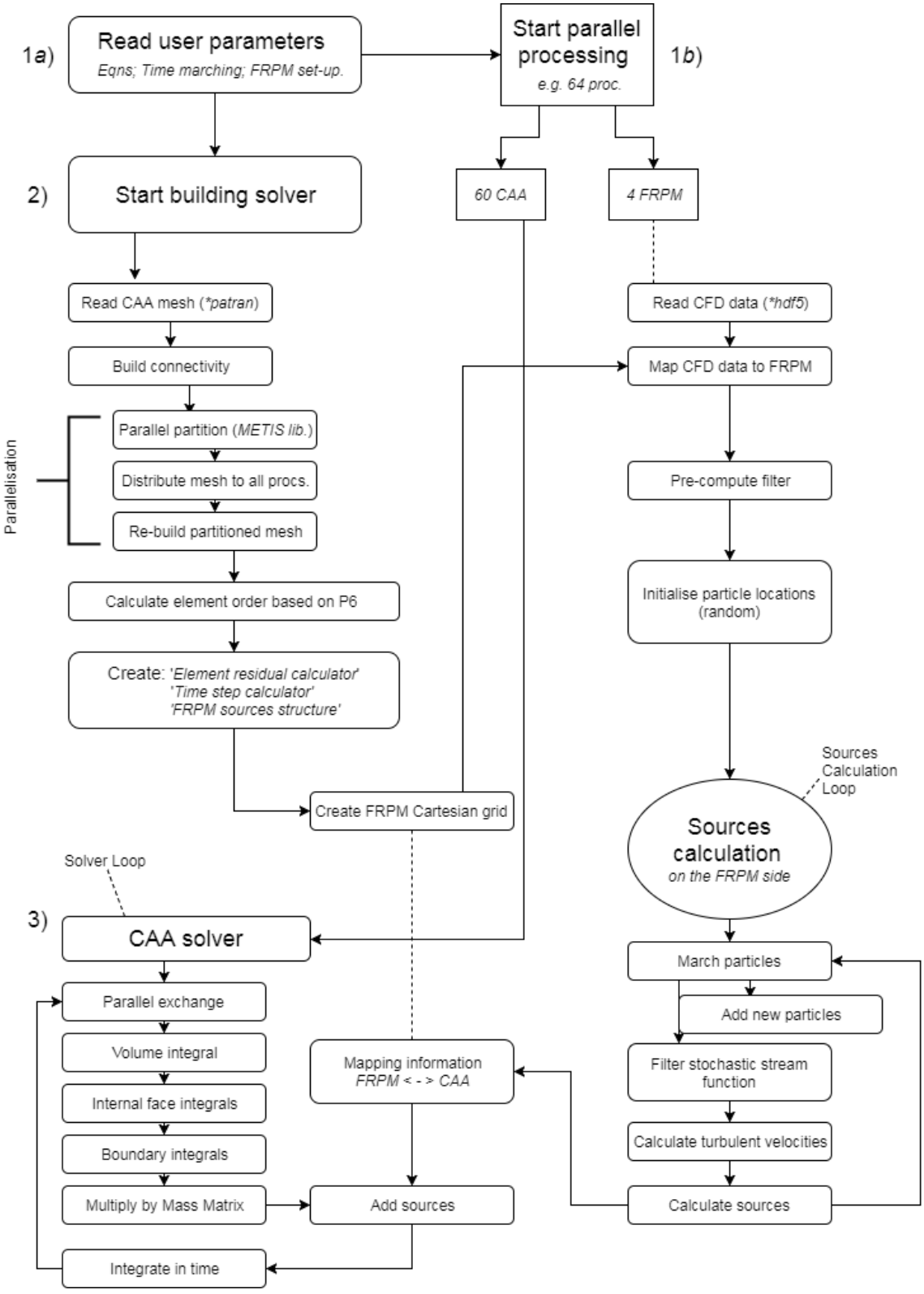

Appendix C

In [131], Spalart-Allmaras (SA) one equation RANS model is claimed to perform well for the attached boundary layer flows as well as being able to deal with adverse pressure gradients. One additional benefit of the SA model is the enhanced wall treatment, meaning that the model can be insensitive to y+ resolution[7], as long as the boundary layer is resolved with adequate number of cells. Figure 58(a) shows the lift coefficient against the angle of attack (AoA) and Figure 58(b) shows the lift versus drag comparison for a NACA 0012 aerofoil simulated using the SA turbulence model. The flow Reynolds number is 5.97×10^6 and Mach number is 0.17, typical to the take-off condition for a full size aeroplane wing. Simulations were performed using the open source CFD package OpenFOAM v.2.2.2 and the commercial ANSYS Fluent solver v.14.5 which were then compared with a free-transition and mild tripped experimental data of Ladson [167] (NASA). For mildly tripped experiments the flow tripping has been initiated by abrasive "80" grit strip where the number refers to a sandpaper labelling system, which is proportional to the mean particle size. Although, none of the RANS models can predict the flow separation, the SA model has performed reasonably well in comparison with the experiment for low angles of attack where the flow remains mostly attached. Arguably, the comparison with a free-transition flow data may not be the best for evaluating the accuracy of a RANS model since the RANS uses a fully turbulent boundary layer assumption which usually means that predictions tend to be similar to tripped experimental cases where earlier separation as well as higher induced drag is observed.

a) *b)*

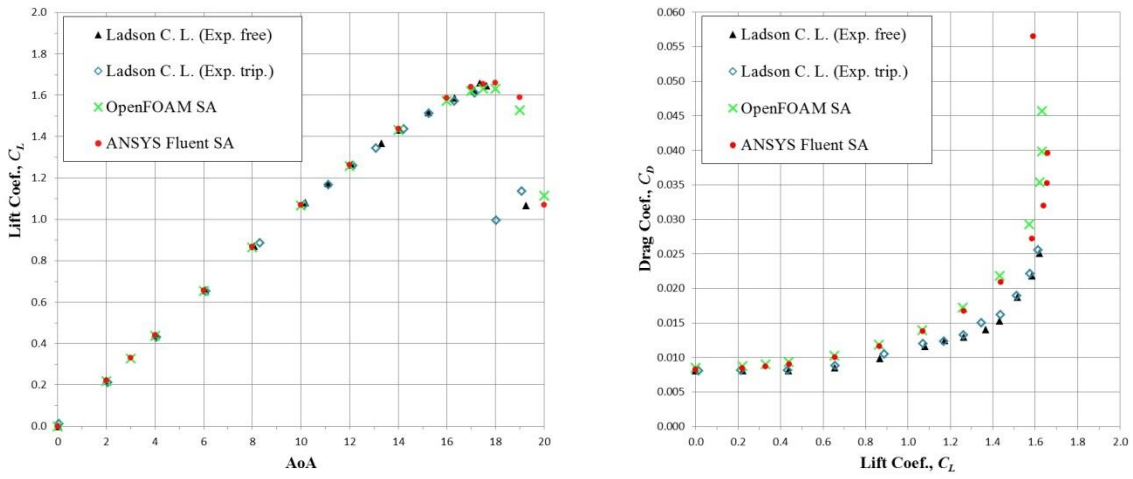

Figure 58 – NACA 0012 SA model simulations of lift coefficient, c_L against AoA (a) and c_L vs. c_D (b) comparison with experimental data.

The appropriate mesh resolution at the wall (y+ spacing) has to be estimated when applying most CFD methods, including the $k-\omega$ *SST* model. Some RANS models offer a wall function option where large spacing of the first mesh element, falling within the log-law

[7] y+ is the target spacing for the first mesh cell next to a wall. Eq. (C.4) shows how y+ is related to physical spacing of the first cell, Δy.

region, is permitted. This is done for several reasons, primarily, to save on computational resources and sometimes to aid convergence. For example, the classic $k-\varepsilon$ model needs coupling with a low-Re model for fine meshes as it may not converge otherwise. However, if the scheme allows, it is be best to include the linear sub-layer (y+ < 5) for an improved accuracy since most RANS calculations are relatively inexpensive. In order to estimate the maximal size of the first element at the trailing edge where the boundary layer is the thickest for a symmetric NACA 0012 wing section, a suitable approximation can be obtained using a flat plate analogy. The same flow conditions as in Figure 58 are used where the Re number is calculated as following:

$$Re = \frac{\rho U_\infty L}{\mu} = \frac{U_\infty L}{\nu} = \frac{59\ m/s \times 1.52\ m}{15.02\times10^{-6}\ m^2/s} \cong 5.97 \times 10^6 \tag{C.1}$$

Assuming the analogy with a flat plate, the skin friction coefficient can be determined empirically:

$$c_f = \frac{2\tau_w}{\rho U^2} \approx 0.074 Re_L^{-0.2} \approx 3.266 \times 10^{-3} \tag{C.2}$$

The wall shear stress, τ_w and the corresponding friction velocity, u^* can be evaluated using the estimated value for c_f:

$$\tau_w = \frac{c_f \rho U_\infty^2}{2} \approx 6.96381; \qquad u^* = \sqrt{\frac{\tau_w}{\rho}} \approx 2.3843 \tag{C.3}$$

The spacing of the first element, Δy with the y+ target value of 5 is then:

$$\Delta y = \frac{y^+ \nu}{u^*} = \frac{5\times(15.02\times10^{-6})}{2.3843} \approx 3.1 \times 10^{-5}\ m \tag{C.4}$$

Fortunately, with RANS methods, Δx to Δy ratio of near-wall cells can be fairly large [168], apart from areas with a strong change. Particularly, when calculating the time-averaged flow over a wing section the refinement normal to the symmetry plane (in the span-wise direction) is not required because in this case the flow is inherently two dimensional. However, as briefly mentioned previously, the number of mesh points required to resolve the boundary layer has to be estimated as well as determining whether or not the element stretching ratio is acceptable. For simplicity, Δy is set to equal $6 \times 10^{-6}\ m$, estimated within $\Delta y \sim 1$ zone, the allowed stretching could be roughly estimated as:

$$\delta = 0.376 L (Re_x)^{-1/5} = 0.376 \times 1.52 \times (5.97 \times 10^6)^{-1/5} \cong 0.02523$$

$$\frac{\delta}{y^+} = \frac{0.02523}{6\times10^{-6}} \cong 4205 \leq \left(\frac{1-f^N}{1-f}\right) \tag{C.5}$$

There would be at least 63 elements in the boundary layer with 10% stretching ratio, f. Usually, experienced modellers have a good judgement for the mesh requirements which are tailored for a specific flow case, also, taking into account the numerical method and scheme to be used. Figure 59 shows the plot of surface pressure coefficient, c_p for 0° and 6° AoA obtained using one and two-equation RANS models previously discussed. As can be seen the

results are in perfect agreement with experimental data. [159] It should be noted that for a NACA 0012 wing profile c_p is quite insensitive to the computational mesh refinement and as discussed in [64] this characteristic may not be used as an indication of the simulation quality. On the other hand, for the accurate prediction of skin friction coefficient the computational grid has to be designed in accordance to best practice, paying respect to parameters such as mesh smoothness, skewness, stretching and the aspect ratio to name the few. Figure 60 shows the plot of c_f for the upper surface compared to the available Langley CFL3D RANS validation data. The independently obtained numerical results presented in Figure 60 are in very good agreement for both flow incidence angles considered.

a) *b)*

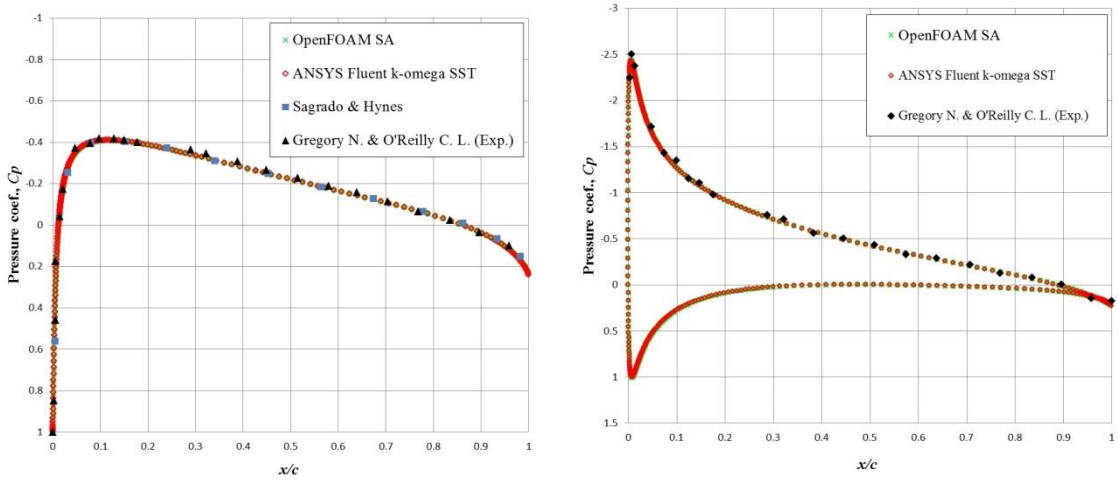

Figure 59 – Pressure coefficient at 0° AoA (*a*) and 6° AoA (*b*) using various RANS models compared with experimental data.

From Figure 61 it could be seen that even for a relatively high AoA of 10° the wall y+ obtained in the simulation is ~1 or below for most part including the trailing edge, conforming to a target design value.

a) *b)*

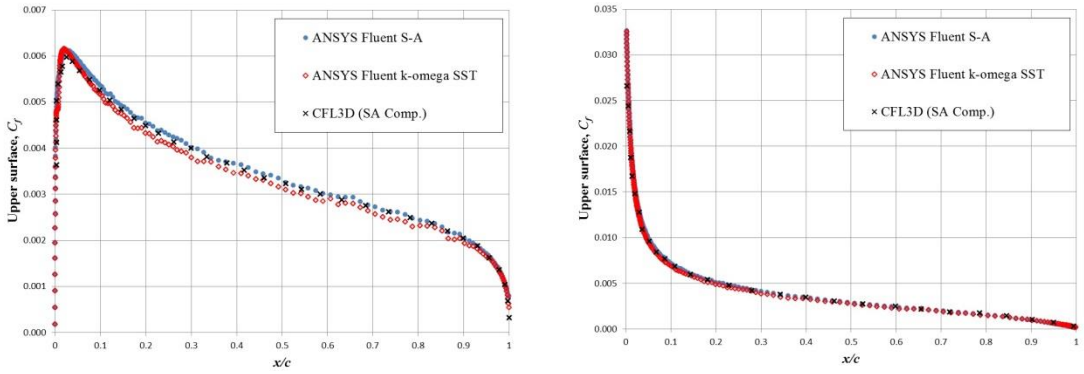

Figure 60 – Skin friction coefficient at 0° AoA (*a*) and 10° AoA (*b*) for SA and $k-\omega$ *SST* models, compared with Langley CFL3D RANS solution.

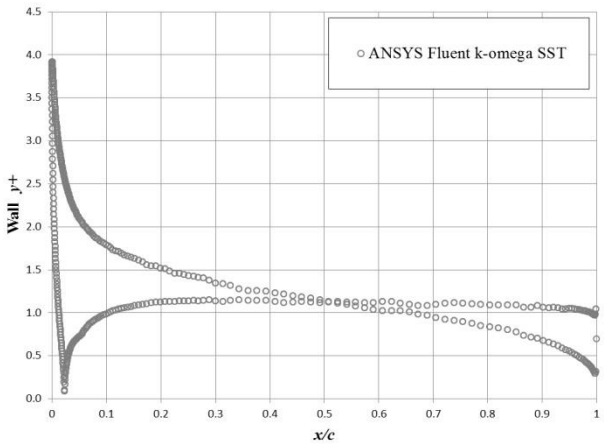

Figure 61 – wall y+ for 10° AoA from a simulation using $k-\omega$ *SST* model.

Turbulent models described so far rely on eddy viscosity hypothesis which is not ideal for complex flows. With the development of RANS, the Reynolds Stress Model (RSM) emerged in late 1980s [169] [170], allowing for anisotropic behaviour of turbulence. In RSM, the transport equations are derived for individual Reynolds stresses $\langle u_i u_j u_k \rangle$ from Navier-Stokes equations and the dissipation, e.g. ε or ω that provides a length scale of turbulence. The RSM equations can be summarised as following:

$$\frac{D\langle u_i u_j \rangle}{Dt} + \frac{\partial}{\partial x_k}\langle u_i u_j u_k \rangle = \nu \nabla^2 \langle u_i u_j \rangle + \mathcal{P}_{ij} + \Pi_{ij} - \varepsilon_{ij} \tag{C.6}$$

In order, the terms in Eq. (C.6) are referred to as mean convection, turbulent convection, viscous diffusion, production, pressure and dissipation.

Π_{ij} is the velocity-pressure-gradient tensor:

$$\Pi_{ij} = -\frac{1}{\rho}\langle u_i \frac{\partial p\prime}{\partial x_j} + u_j \frac{\partial p\prime}{\partial x_i} \rangle \tag{C.7}$$

$\mathcal{P}_{ij}$ is the production tensor:

$$\mathcal{P}_{ij} = -\langle u_i u_k \rangle \frac{\partial \langle \bar{u}_j \rangle}{\partial x_k} - \langle u_j u_k \rangle \frac{\partial \langle \bar{u}_i \rangle}{\partial x_k} \tag{C.8}$$

ε_{ij} is the dissipation tensor:

$$\varepsilon_{ij} = 2\nu \langle \frac{\partial u_i}{\partial x_k} \frac{\partial u_j}{\partial x_k} \rangle \tag{C.9}$$

Considering the normal stress balances, $\partial\langle \bar{u} \rangle / \partial y$ is usually the only significant velocity gradient inside the boundary layer, contributing to the source $\mathcal{P}_{11}$. Furthermore, bearing in mind the similarities with the turbulent kinetic energy balance, where p' appears is in the transport term $\frac{1}{2}\Pi_{ii} = -\nabla \cdot \langle \boldsymbol{u} p'/\rho \rangle$, playing its main role in energy redistribution through extraction of energy from $\langle u^2 \rangle$ and transferring it to $\langle v^2 \rangle$ and $\langle w^2 \rangle$, Π_{ii} would be relatively small in comparison to Π_{ij}. This redistributive effect is evident from the following decomposition:

$$\Pi_{ij} = \mathcal{R}_{ij} - \frac{\partial}{\partial x_k} T_{kij}^{(p)} \tag{C.10}$$

In Eq. (C.10), $\mathcal{R}_{ij}$ is the pressure rate of strain tensor, defined as:

$$\mathcal{R}_{ij} \equiv \langle \frac{p'}{\rho} \left(\frac{\partial u_i}{\partial x_j} + \frac{\partial u_j}{\partial x_i} \right) \rangle \tag{C.11}$$

The pressure rate of strain tensor happily vanishes from the turbulent kinetic energy equation due to the continuity equation, $\nabla \cdot \boldsymbol{u} = 0$ but it is of great importance for energy redistribution and is most challenging to model accurately in RSM. In most textbooks [95] the RSM model is expressed using the Reynolds stress flux and the pressure rate of strain tensor as in Eq. (C.10) to obtain:

$$\frac{D\langle u_i u_j \rangle}{Dt} + \frac{\partial}{\partial x_k} T_{kij}^{(p)} = \mathcal{P}_{ij} + \mathcal{R}_{ij} - \varepsilon_{ij} \tag{C.12}$$

The mean flow convection $\frac{D\langle u_i u_j \rangle}{Dt}$ and production tensor $\mathcal{P}_{ij}$ are in closed form while the rest of the terms of Eq. (C.12) require modelling, involving a large number of empirical constants. In some cases, due to its complexity the RSM model is numerically not well conditioned and in most cases, experiences poor convergence. The RSM is not used in this work primarily because the results may be difficult to reproduce. Nevertheless, it is briefly outlined in Eqs. (C.6-C.12) for a reference as RSM is physically the most complete RANS model that has built in triple correlations $\langle u_i u_j u_k \rangle$, potentially offering a better solution for complex flows.

Appendix D

I.) Two-point correlation in wavenumber space

From theory, the Fourier transform of the correlation $C(r)$ can be defined as:

$$C(r) = \frac{1}{(2\pi)^n} \int_{\mathbb{R}^n} \hat{C}(\boldsymbol{\kappa}) e^{-i\boldsymbol{\kappa}\cdot\boldsymbol{r}} d\boldsymbol{\kappa} \tag{D.1}$$

where $\boldsymbol{\kappa}$ stands for the three-dimensional wavenumber vector for $n = 3$, and $\hat{C}$ denotes the Fourier transform of C.

In spherical coordinates, $\boldsymbol{r}$ and $\boldsymbol{\kappa}$ read:

$\boldsymbol{r} \equiv (r_x, r_y, r_z) = (r\cos\varphi\cos\theta\,, r\cos\varphi\sin\theta\,, r\sin\varphi)$

$\boldsymbol{\kappa} \equiv (\kappa_x, \kappa_y, \kappa_z) = (\kappa\cos\alpha\sin\beta\,, \kappa\cos\alpha\sin\beta\,, \kappa\sin\alpha)$

By assumption, $r = |\boldsymbol{r}|$, $\kappa = |\boldsymbol{\kappa}|$, $\varphi, \alpha \in \left[-\frac{\pi}{2}; \frac{\pi}{2}\right]$ and $\theta, \beta \in [0; 2\pi]$, we get:

$$\boldsymbol{\kappa}\cdot\boldsymbol{r} = \kappa r[\cos\varphi\cos\alpha\cos(\beta-\theta) + \sin\varphi\sin\alpha] \tag{D.2}$$

Furthermore, for isotropic turbulence, where the directional information is only dependent on the distance, one may assume φ and θ to be zero. Hence, due to trigonometric properties,

$$\boldsymbol{\kappa}\cdot\boldsymbol{r} = \kappa r\cos\alpha\cos\beta \tag{D.3}$$

Then, inserting Eq. (D.3) into Eq. (D.1) with limits set prior to Eq. (D.2) in 3D yields:

$$C(r) = \frac{1}{8\pi^3}\int_0^\infty \hat{C}(\boldsymbol{\kappa}) \int_{-\frac{\pi}{2}}^{\frac{\pi}{2}} \kappa\cos\alpha \int_0^{2\pi} \exp(i\kappa r\cos\alpha\cos\beta) d\beta d\alpha d\kappa \tag{D.4}$$

By using the definition of the Bessel function of order 0:

$$J_0(x) = \frac{1}{2\pi}\int_0^{2\pi} \exp(ix\cos\theta)\, d\theta \tag{D.5}$$

and inserting Eq. (D.5) into Eq. (D.4) gives:

$$C(r) = \frac{1}{4\pi^2}\int_0^\infty \hat{C}(\boldsymbol{\kappa}) \int_{-\frac{\pi}{2}}^{\frac{\pi}{2}} \kappa\cos\alpha\, J_0(\kappa r\cos\alpha) d\alpha d\kappa \tag{D.6}$$

where the integral with respect to α in the above equation is:

$$\int_{-\frac{\pi}{2}}^{\frac{\pi}{2}} \kappa\cos\alpha\, J_0(\kappa r\cos\alpha) d\alpha = 2\frac{\sin(\kappa r)}{\kappa r} \tag{D.7}$$

Then, Eq. (D.6) can be simplified as following:

$$C(r) = \frac{1}{2\pi^2}\int_0^\infty \hat{C}(\boldsymbol{\kappa})\, J_0(\kappa r) d\kappa \tag{D.8}$$

On the other hand, starting from a 2D definition of Eq. (D.1) where

$$C(r) = \frac{1}{4\pi^2}\int_{\mathbb{R}^2} \hat{C}(\boldsymbol{\kappa}) e^{-i\boldsymbol{\kappa}\cdot\boldsymbol{r}} d\boldsymbol{\kappa} \tag{D.9}$$

with corresponding $\boldsymbol{r}$ and $\boldsymbol{\kappa}$ definitions:

$\boldsymbol{r} \equiv (r_x, r_y) = (r\cos\alpha\,, r\sin\alpha)$

$\boldsymbol{\kappa} \equiv (\kappa_x, \kappa_y) = (\kappa\cos\theta\,, \kappa\sin\theta)$

where, $r = |\boldsymbol{r}|$, $\kappa = |\boldsymbol{\kappa}|$, and $\theta, \alpha \in [0; 2\pi]$, Eq. (D.9) becomes:

$$C(r) = \frac{1}{4\pi^2}\int_0^\infty \kappa\hat{C}(\boldsymbol{\kappa}) \left[\int_0^{2\pi} \exp(i\kappa r\cos(\theta-\alpha)) d\theta\right] d\kappa \tag{D.10}$$

Inserting Eq. (D.5) yields:

$$C(r) = \frac{1}{2\pi}\int_0^\infty \kappa\hat{C}(\boldsymbol{\kappa})\, J_0(\kappa r) d\kappa \tag{D.11}$$

II.) Lateral and longitudinal autocorrelation functions

The aim is to show the relationship given by Eq. (D.12)

$$g(r) = f(r) + \frac{r}{2}\frac{df(r)}{dr} \tag{D.12}$$

A stationary two-point correlation of the stream function ψ, given in Eq. (D.8) in the wavenumber space, could be expressed in terms of a Gaussian filter using the convolution properties of the FRPM method, $C(r) = \{G * G\}(r)$ such as:

$$C(r) = \frac{1}{2\pi^2}\int_0^\infty \hat{G}(\kappa)^2 J_0(\kappa r) d\kappa \tag{D.13}$$

As shown in [52], a stationary two-point correlation of the velocity field, $\mathcal{R}_{ij}(r,\tau) = \langle u_i'(\boldsymbol{x},t)\, u_j'(\boldsymbol{x}+\boldsymbol{r}, t+\tau)\rangle$, where an incompressibility condition is assumed, i.e. $\nabla u(\boldsymbol{x},t) = 0$, could be written in terms of the lateral and longitudinal autocorrelation functions, $f(r)$ and $g(r)$ respectively.

$$\mathcal{R}_{ij}(r,0) = [f(r) - g(r)]n_i n_j + g(r)\delta_{ij} \tag{D.14}$$

where n_i is the unit vector in the direction of the relative separation between points and δ_{ij} is the Kronecker symbol. Moreover, due to the incompressibility condition and the restriction

$\sum_j \{\partial \mathcal{R}_{ij}(r,\tau)/\partial r_j\} = 0$; applies and functions $f(r)$ and $g(r)$ and its derivation follows below.

$$g(r) = f(r) + \frac{r}{2}\frac{df}{dr}(r) \tag{D.15}$$

By expressing u' in $\mathcal{R}_{ij}(r)$ in terms of the stream function gives:

$$\mathcal{R}_{ij}(r) = \langle \varepsilon_{imn}\frac{\partial}{\partial x_m}\psi_n(\boldsymbol{x})\ \varepsilon_{jpq}\frac{\partial}{\partial x_p}\psi_q(\boldsymbol{x}+\boldsymbol{r})\rangle \tag{D.16}$$

In the above equation, ε stands for the Levi-Civita symbol defined by:

$$\varepsilon_{ijk} = \begin{cases} 1, & \text{if } (i,j,k) \text{ are in the cyclic order;} \\ -1, & \text{if } (i,j,k) \text{are in the reverse cyclic order;} \\ 0, & \text{otherwise.} \end{cases} \tag{D.17}$$

The properties of the correlation function allow taking the Levi-Civita symbols out of the ensemble average and, also, using the properties of partial derivatives, $\partial/\partial x_p\ \psi_q(\boldsymbol{x}+\boldsymbol{r}) = \partial/\partial r_p\ \psi_q(\boldsymbol{x}+\boldsymbol{r})$ a slightly re-arranged Eq. (D.16) reads:

$$\mathcal{R}_{ij}(r) = \varepsilon_{imn}\varepsilon_{jpq}\frac{\partial}{\partial r_p}\langle\frac{\partial}{\partial x_m}\psi_n(\boldsymbol{x})\ \psi_q(\boldsymbol{x}+\boldsymbol{r})\rangle \tag{D.18}$$

For isotropic flows, $\partial/\partial x_m\ \langle\psi_n(\boldsymbol{x})\ \psi_q(\boldsymbol{x}+\boldsymbol{r})\rangle = 0$;

$$\mathcal{R}_{ij}(r) = -\varepsilon_{imn}\varepsilon_{jpq}\frac{\partial}{\partial r_p}\langle\psi_n(\boldsymbol{x})\frac{\partial}{\partial x_m}\psi_q(\boldsymbol{x}+\boldsymbol{r})\rangle \tag{D.19}$$

Again, using the properties of partial derivatives leads to:

$$\mathcal{R}_{ij}(r) = -\varepsilon_{imn}\varepsilon_{jpq}\frac{\partial^2}{\partial r_m \partial r_p}\langle\psi_n(\boldsymbol{x})\ \psi_q(\boldsymbol{x}+\boldsymbol{r})\rangle = -\varepsilon_{imn}\varepsilon_{jpq}\frac{\partial^2}{\partial r_m \partial r_p}C(\boldsymbol{r})\delta_{nq} \tag{D.20}$$

In Eq. (D.20), $C(r) = \langle\psi_n(\boldsymbol{x})\ \psi_q(\boldsymbol{x}+\boldsymbol{r})\rangle$ is the correlation tensor, $C(r) = \{G * G\}|\boldsymbol{r}|\delta_{ij}$. Hence, performing the second order partial derivative of $C(r)$ with respect to r_m and r_p,

$$\frac{\partial^2}{\partial r_m \partial r_p}C(\boldsymbol{r}) = \delta_{pm}\frac{1}{r}\frac{d}{dr}C(r) - \frac{r_m r_p}{r^3}\frac{d}{dr}C(r) + \frac{r_m r_p}{r^2}\frac{d^2}{dr^2}C(r) \tag{D.21}$$

Then, Eq. (D.20) becomes:

$$\mathcal{R}_{ij}(r) = -\varepsilon_{imn}\varepsilon_{jpq}\delta_{pm}\delta_{nq}\frac{1}{r}\frac{d}{dr}C(r) - \varepsilon_{imn}\varepsilon_{jpq}\delta_{nq}\left[\frac{d^2}{dr^2}C(r) - \frac{1}{r}\frac{d}{dr}C(r)\right]\frac{r_m r_p}{r^2} \tag{D.22}$$

In Eq. (D.22), $\varepsilon_{imn}\varepsilon_{jpq}\delta_{pm}\delta_{nq} = 2\delta_{ij}$ and $\varepsilon_{imn}\varepsilon_{jpq}\delta_{nq} = \delta_{mp}\delta_{ij} - \delta_{ip}\delta_{jm}$. Hence,

$$\mathcal{R}_{ij}(r) = -2\frac{1}{r}\frac{d}{dr}C(r)\delta_{ij} - \left[\frac{d^2}{dr^2}C(r) - \frac{1}{r}\frac{d}{dr}C(r)\right]\frac{r_m r_p}{r^2}\delta_{mp}\delta_{ij} + \left[\frac{d^2}{dr^2}C(r) - \frac{1}{r}\frac{d}{dr}C(r)\right]\frac{r_m r_p}{r^2}\delta_{ip}\delta_{jm} \tag{D.23}$$

Re-arranging terms in Eq. (D.22) gives:

$$\mathcal{R}_{ij}(r) = \left(\frac{d^2}{dr^2}C(r) - \frac{1}{r}\frac{d}{dr}C(r)\right)\frac{r_i r_j}{r^2} + \left(-\frac{d^2}{dr^2}C(r) - \frac{1}{r}\frac{d}{dr}C(r)\right)\delta_{ij} \tag{D.24}$$

Finally, comparing Eq. (D.23) to Eq. (D.14) the individual lateral and longitudinal correlation functions can be deducted:

$$g(r) = -\frac{d^2}{dr^2}C(r) - \frac{1}{r}\frac{d}{dr}C(r) \tag{D.25}$$

$$f(r) - g(r) = \frac{d^2}{dr^2}C(r) - \frac{1}{r}\frac{d}{dr}C(r)$$

$$f(r) = -\frac{2}{r}\frac{d}{dr}C(r) \tag{D.26}$$

Therefore, it can be shown that the relation between autocorrelation functions is,

$$g(r) = f(r) + \frac{r}{2}\frac{df(r)}{dr} \tag{D.27}$$

Bibliography

[1] M. J. Lighthill, “On sound generated aerodynamically. I. General theory,” *Proceedings of the Royal Society (London),* vol. A. 211, no. 1107, pp. 564-587, 1952.

[2] O. K. Mawardi and I. Dyer, “On noise of aerodynamic origin,” *The Journal of the Acoustical Society of America,* vol. 25, no. 3, 1952.

[3] M. J. Lighthill, “Sound generated aerodynamically,” *Proceedings of the Royal Society (London),* vol. A. 267, 1961.

[4] G. M. Lilley, “On the noise from air jets,” *Aeronaut. Res. Council Rep. Mem.,* vol. 20, no. 376, 1958.

[5] J. E. Ffowcs-Williams, “The noise from turbulence convected at high speed,” *Phil. Trans. Royal Society (London),* vol. 255, pp. 469-503, 1963.

[6] H. S. Ribner, “The generation of sound by turbulent jets,” *In Advances in Applied Mechanics,* vol. 8, pp. 108-182, 1964.

[7] R. Mani, “The influence of jet flow on jet noise,” *Journal of Fluid Mechanics,* vol. 73, pp. 753-793, 1976.

[8] A. P. Dowling, J. E. Ffowcs-Williams and M. E. Goldstein, “Sound production in a moving stream,” *Phil. Trans. Royal Society (London),* vol. A. 288, no. 1353, 1978.

[9] M. E. Goldstein, “A generalized acoustic analogy,” *Journal of Fluid Mechanics,* vol. 488, pp. 315-333, 2003.

[10] W. Y. Liu, “A review on wind turbine noise mechanism and de-noising techniques,” *Renewable Energy,* vol. 108, pp. 311-320, 2017.

[11] M. Allan and O. Darbyshire, “Comparison of LES and Stochastic Source Generation Methods for Aero- and Hydro-Acoustic Design Guidance,” in *20th AIAA/CEAS Aeroacoustics Conference*, Atlanta, GA, 16-20 June 2014, 2014.

[12] Y. S. Wang, L. N. Sui, Z. Y. Yin, X. L. Wang, N. N. Liu and H. Guo, “A hybrid prediction for wind buffeting noises of vehicle rear window based on LES-LAA method,” *Applied Mathematical Modelling,* vol. 47, pp. 160-173, 2017.

[13] A. Jäger, F. Decker, M. Hartmann, M. Islam, T. Lemke, J. Ocker, V. Schwarz, F. Ullrich, B. Crouse and G. Balasubramanian, “Numerical and Experimental Investigations of the Noise Generated by a Flap in a Simplified HVAC duct,” in *14th AIAA/CEAS Aeroacoustics Conference*, Vancouver, British Columbia, Canada, 5-7 May 2008.

[14] J. Kennedy, O. Adetifa, M. Carley, N. Holt and I. Walker, “Aeroacoustic sources of motorcycle helmet noise,” *Journal of Acoustical Society of America,* vol. 130, no. 3, pp. 1164-1172, 2011.

[15] C. Jordan, O. Hetherington, A. Woodside and H. Harvey, “Noise Induced Hearing Loss in Occupational Motorcyclists,” *Journal of Environmental Health Research,* vol. 3, no. 2, pp. 66-77, 2004.

[16] Y. H. Kim and J. W. Choi, Sound visualization and manipulation, John Wiley & Sons Singapore Pte. Ltd., 2013.

[17] S. W. Rienstra and A. Hirschberg, An introduction to acoustics, extended and revised edition of IWDE 92-06, Eindhoven University of Technology, 2004.

[18] C. Wagner, T. Hüttle and P. Sagaut, Large-Eddy Simulation for Aeroacoustics, Cambridge: Cambridge University Press, 2006.

[19] J. Ffowcs-Williams and D. Hawkings, “Sound generation by turbulence and surfaces in arbitrary motion,” *Philosophical Transactions of the Royal Society of London. Series A, Mathematical and Physical Sciences,* vol. 1151, no. 264, pp. 321-342, 1969.

[20] C. Bailly and D. Juvé , “A Stochastic Approach To Compute Subsonic Noise Using Linearized Euler's Equations,” *AIAA,* vol. 99, pp. 496-506, 1999.

[21] F. Bassi and S. Rebay, “High-Order Accurate Discontinuous Finite Element Solution of the 2D Euler Equations,” *Journal of Computational Physics,* vol. 138, pp. 251-285, 1997.

[22] R. Ewert and W. Schröder, “Acoustic perturbation equations based on flow decomposition via source filtering,” *Journal of Computational Physics,* no. 188, pp. 365-398, 2003.

[23] H. L. Atkins and C.-W. Shu, “Quadrature-Free impementation of Discontinuous Galerkin method for hyperbolic equations,” NASA Langley Research Center Contract 201594, Hampton, Virginia, USA, 1996.

[24] C. Hirsch, Numerical Computation of Internal and External Flows. Volume 1 Fundamentals of Computational Fluid Dynamics. 2nd Edition., John Willey & Sons Ltd., 2007.

[25] A. A. Samarskii, The theory of difference schemes, Marcel Dekker Inc., 2001.

[26] J. von Neumann and R. D. Richtmyer, “A method for numerical calculation of hydrodynamic shocks,” *Journal of Applied Physics,* vol. 21, pp. 232-237, 1950.

[27] D. L. Book, “The conception, gestation, birth, and infancy of FCT, in: D. Kuzmin, R. Löhner, S. Turek (Eds.),” in *Flux-Corrected Transport: Principles, Algorithms and Applications*, Berlin, Springer, 2005, pp. 5-28.

[28] J. P. Boris and D. L. Book, “Flux-corrected transport. I. SHASTA, a fluid transport algorithm that

works," *Journal of Computational Physics,* vol. 11, no. 1, pp. 38-69, 1973.

[29] A. Harten, "On High Resolution Schemes for Hyperbolic Conservation Laws," *Journal of Computational Physics,* vol. 49, no. 3, pp. 357-393, 1983.

[30] A. Harten and P. D. Lax, "On a Class of High Resolution Total-Variation-Stable Finite-Difference Schemes," *SIAM Journal on Numerical Analysis,* vol. 21, pp. 1-23, 1984.

[31] H. O. Yee, R. F. Warming and A. Harten, "Implicit Total Variation Diminishing (TVD) Schemes for Steady-State Calculations," *Journal of Computational Physics,* vol. 57, no. 3, pp. 327-360, 1985.

[32] C. K. W. Tam and J. C. Webb, "Dispersion-relation-preserving finite difference schemes for computational acoustics," *Journal of Computational Physics,* vol. 107, pp. 262-281, 1993.

[33] A. Harten, B. Engqist, S. Osher and S. Chakravarthy, "Uniformly High Order Accurate Essentially Non-Oscillatory Schemes III," *Journal of Computational Physics,* vol. 71, pp. 231-303, 1987.

[34] X. D. Liu, S. Osher and T. Chan, "Weighted essentially non-oscillatory schemes," *Journal of Computational Physics,* vol. 115, pp. 200-212, 1994.

[35] S. A. Karabasov and V. M. Goloviznin, "Compact Accurately Boundary-Adjusting high-Resolution Technique for Fluid Dynamics," *Journal of Computational Physics, No. 228,* pp. 7426-7451, 2009.

[36] A. Iserles, "Generalized Leapfrog Methods," *IMA Journal of Numerical Analysis,* vol. 6, no. 3, pp. 381-392, 1986.

[37] R. L. Roe, "Linear Bicharacteristic schemes without dissipation," *SISC,* no. 19, pp. 1405-1427, 1998.

[38] A. A. Samarskii and V. M. Goloviznin, "Difference approximation of convective transport with spatial splitting of time derivative," *Math. Model.,* no. 10, pp. 86-100, 1998.

[39] V. M. Goloviznin, "Balanced characteristic method for systems of hyperbolic conservation laws," *Doklady Math.,* no. 72, pp. 619-623, 2005.

[40] F. F. Grinstein and C. Fureby, "From Canonical to Complex Flows: Recent Progression Monotonically Integrated LES," *Computing in Science & Engineering,* vol. 6, no. 2, 2004.

[41] E. Garnier, M. Mossi, P. Sagaut, P. Comte and M. Deville, "On the use of shock-capturing schemes for large-eddy simulation," *J. Comp. Physics,* vol. 153, pp. 273-311, 1999.

[42] V. M. Goloviznin, V. N. Semenov, I. A. Korortkin and S. A. Karabasov, "A novel computational method for modelling stochastic advection in heterogeneous media," *Transport in Porous Media,* vol. 66, no. 3, pp. 439-356, 2007.

[43] V. Semiletov, S. Karabasov, G. Faranosov and M. Zaitsev, “Airfoil Flow and Noise Computation Using Monotonically Integrated LES and Acoustic Analogy,” *AIAA-2012-2108,* 2012.

[44] S. A. Karabasov and V. M. Goloviznin, “A New Efficient High-Resolution Method for Non-Liner problems in Aeroacoustics,” *AIAA Journal,* vol. 45, no. 12, pp. 2861-2871, 2007.

[45] A. V. Obabko, P. F. Fischer, T. J. Tautges, S. A. Karabasov, V. M. Goloviznin, M. A. Zaytsev, V. V. Chudanov, V. A. Pervichko and A. E. Aksenova, “CFD Validation in OECD/NEA T-Junction Benchmark,” *ANL/NE,* vol. 11, no. 25, 2011.

[46] G. A. Faranosov, V. M. Goloviznin, S. A. Karabasov, V. G. Kondakov, V. F. Kopiev and M. A. Zaitsev, “CABARET method on unstructured hexahedral grids for jet noise computation,” *Computers and Fluids,* vol. 88, pp. 165-179, 2013.

[47] V. A. Semiletov and S. A. Karabasov, “CABARET scheme for computational aero acoustics: extension to asynchronous time stepping and 3D flow modelling,” *International Journal of Aeroacoustics,* vol. 13, no. 3-4, pp. 321-336, 2014.

[48] A. P. Markesteijn, V. A. Semiletov and S. A. Karabasov, “CABARET GPU Solver for Fast-Turn-Around Flow and Noise Calculations,” *AIAA,* 2015.

[49] A. P. Markesteijn, V. A. Semiletov and S. A. Karabasov, “GPU CABARET solutions for the SILOET jet noise experiment: Flow and noise modelling,” *AIAA,* 2016.

[50] A. P. Markesteijn, V. A. Semiletov and S. A. Karabasov, “GPU CABARET Solver Extension to Handle Complex Geometries utilizing snappyHexMesh with Asynchronous Time Stepping,” *AIAA,* 2017.

[51] M. W. Evans and F. H. Harlow, “The particle-in-cell method for hydrodynamic calculations,” Los Alamos Scientific Laboratory, USA, 1957.

[52] A. Careta, F. Sagues and J. Sancho, “Stochastic Generation of Homogeneous Isotropic Turbulence with Well-Defined Spectra,” *Physical Review E,* vol. 48, no. 3, pp. 2279-2287, 1993.

[53] R. Ewert and M. Bauer, “Towards the prediction of broadband trailing edge noise via stochastic surface sources,” in *10th AIAA/CEAS Aeroacoustcs Conference*, Manchester, United Kingdom, 2004.

[54] R. Ewert and R. Edmunds, “CAA Slat Noise Studies Applying Stochastic Sound Sources Based on Solenoidal Digital Filters,” *AIAA 2005-2862,* 2005.

[55] R. Ewert, “RPM - the fast Random Particle-Mesh method to realize unsteady turbulent sound sources and velocity fields for CAA applications,” in *13th AIAA/CEAS Aeroacoustics Conference (28th AIAA Aeroacoustics Conference)*, Rome, Italy, 21-23 May 2007, 2007.

[56] R. Ewert, “Broadband slat noise prediction based on CAA and stochastic sound sources from a

fast random particle-mesh (RPM) method," *Computers & Fluids,* vol. 37, pp. 369-387, 2008.

[57] R. Ewert, J. Dierke, J. Siebert, A. Neifeld, C. Appel, M. Siefert and O. Kornow, "CAA broadband noise prediction for aeroacoustic design," *Journal of Sound and Vibration,* vol. 330, pp. 4139-4160, 2011.

[58] M. Herr and M. Kamruzzaman, "Benchmarking of trailing-edge noise computatons: outcome of the BANC II Workshop," in *19th AIAA/CEAS Aeroacoustics Conference*, Berlin, Germany, 27 May 2013.

[59] M. C. Jacob, J. Boudet, D. Casalino and M. Michard, "A rod-airfoil experiment as benchmark for broadband noise modeling," *Theoretical and Computational Fluid Dynamics,* no. 19, pp. 171-196, 2005.

[60] J. E. Ffowcs-Williams and L. H. Hall, "Aerodynamic sound generation by turbulent flow in the vicinity of a scattering half plane," *Journal of Flud Mechanics,* vol. 40, no. 4, pp. 657-670, 1970.

[61] D. G. Crighton and F. G. Leppington, "On the scattering of aerodynamic noise," *Journal of Fluid Mechanics,* vol. 46, pp. 721-736, 1971.

[62] R. Ewert, C. Appel, J. Dierke and M. Herr, "RANS/CAA based prediction of NACA 0012 broadband trailing edge noise and experimental valdation," *American Institute of Aeronautics and Astronautics,* 2009.

[63] W. R. Wolf and S. K. Lele, "Trailing Edge Noise Predictions Using Compressible LES and Acoustic Analogy," in *17th AIAA/CEAS Aeroacoustic Conference*, 05 - 08 June, Portland, Oregon, 2011.

[64] K. J. George and S. K. Lele, "Large Eddy Simulation of Airfoil Self-Noise at high Reynolds Number," in *22nd AIAA/CEAS Aeroacoustic Conference*, 30 May - 1 June, Lyon, France, 2016.

[65] M. Herr, C. Appel, J. Dierke and R. Ewert, "Trailing-Edge Noise Data Quality Assessment for CAA Validation," in *16th AIAA/CEAS Aeroacoustics Conference*, Stockholm, Sweden, 7-9 June, 2010.

[66] T. F. Brooks, D. S. Pope and M. A. Marcolini, "Airfoil Self-Noise and Prediction," NASA Reference Publication 1218, NASA, 1989.

[67] W. Devenport, R. A. Burdisso, H. Camargo, E. Crede, M. Remillieux, M. Rasnick and P. Van Seeters, "Aeroacoustic Testing of Wind Turbine Airfoils," National Renewable Energy Laboratory (NREL), Blacksburg, Virginia, 2010.

[68] M. Herr, C. Bahr and M. Kamruzzaman, "Third Workshop on Benchmark Problems for Airframe Noise Computations (BANC III)," in *20th AIAA/CEAS Aeroacoustics Conference*, Atlanta, Georgia, USA, 14-15 June, 2014.

[69] E. Manoha, B. Troff and P. Sagaut, "Trailing edge noise prediction using large-eddy simulation

and acoustic analogy," *AIAA J. ,* vol. 4, no. 38, pp. 575-583, 2000.

[70] M. Wang and P. Moin, "Computaton of Trailing-Edge Flow and Noise Using Large-Eddy Simulation," *AIAA J.,* vol. 38, no. 12, pp. 2201-2209, 2000.

[71] M. Wang and P. Moin, "Dynamic wall modelling for large-eddy simulation of complex turbulent flows," *Phys. Fluids,* vol. 14, no. 7, pp. 2043-2051, 2002.

[72] A. L. Marsden, M. Wang, J. E. Dennis and P. Moin, "Trailing-edge noise reduction using derivative-free optimisation and large-eddy simulation," *J. Fluid Mech.,* vol. 572, pp. 13-36, 2007.

[73] R. D. Sandberg and N. D. Sandham, "Direct numerical simulation of turbulent flow past a trailing edge and the associated noise generation," *J. Fluid Mech.,* vol. 596, pp. 353-385, 2008.

[74] L. E. Jones, R. D. Sandberg and N. D. Sandham, "Stability and receptivity characteristics of a laminar separation bubble on an aerofoil," *J. Fluid Mech.,* vol. 648, pp. 257-296, 2010.

[75] R. K. Amiet, "Noise due to turbulent flow past a trailing edge," *J. Sound and Vibration,* vol. 47, no. 3, pp. 387-393, 1976.

[76] T. Le Garrec, X. Gloerfelt and C. Christophe, "Direct noise computation of trailing edge noise at high Reynolds numbers," in *14th AIAA/CEAS Aeroacoustics Conference* , Vancouver, British Columbia, Canada, 5-7 May, 2008.

[77] T. Le Garrec and X. Gloerfelt, "Trailing edge noise from an isolated airfoil at a high Reynolds number," in *15th AIAA/CEAS Aeroacoustics Conference*, Miami, Florida, USA, 11-13 May, 2009.

[78] A. Garbaruk, M. Shur, M. Strelets and P. Spalart, "Jet Noise Computation Based on Enhanced DES Formulation Accelerating RANS-to-LES Transition in Free Shear Layers," in *CEAA*, Svetlogorsk, Russia, 22-26 Sept., 2014.

[79] B. A. Singer, K. S. Brentner, D. P. Lockard and G. M. Lilley, "Simulation of Acoustic Scattering from a Trailing Edge," *J. Sound and Vibration,* vol. 230, no. 3, pp. 541-560, 2000.

[80] S. M. Grace, D. L. Sondak, W. Eversman and M. J. Cannamela, "Hybrid Prediction of Fan Tonal Noise," *AIAA,* no. 2992, 2008.

[81] A. Serrano and G. Torres, "ESTIMATION OF TURBINE NOISE BENEFITS DUE TO ACOUSTICALLY TREATED OUTLET GUIDE VANES," in *11th European Conference on Turbomachinery Fluid Dynamics & Thermodynamics*, Madrid, Spain, 2015, March 23-27.

[82] V. A. Titarev and E. F. Toro, "ADER: Arbitrary high order Godunov approach," *Journal of Scientific Computing,* no. 17, pp. 609-618, 2002.

[83] A. Travin, M. Shur, M. Strelets and P. Spalart, "Detached-Eddy Simulations Past a Circular

Cylinder," *Flow, Turbulence and Combustion,* vol. 63, pp. 293-313, 1999.

[84] M. M. Zdravkovich, Flow Around Circular Cylinders, Oxford: Oxford University Press, 1997.

[85] D. Casalino, M. C. Jacob and M. Roger , "Prediction of rod-airfoil interaction noise using the Ffowcs-Williams and Hawkings analogy," *American Institute of Aeronautics and Astronautics,* vol. 241, no. 2, pp. 182-191, 2003.

[86] B. Greschner, S. Peth, Y. J. Moon, J. H. Seo, M. C. Jacob and F. Thiele, "Three-dimensional predictions of the rod wake-airfoil interaction noise by hybrid methods," in *Proceedings of the 14th International Congress on Sound and Vibration*, Cairns, Australia, July 9-12, 2007.

[87] B. Greschner, F. Thiele, D. Casalino and M. C. Jacob, "Prediction of sound generated by a rod-airfoil configuration using EASM DES and the generalised Lighthill/FW-H analogy," *Comput. & Fluids,* vol. 37, no. 4, pp. 402-413, 2008.

[88] S. Galdéano, S. Barré and N. Réau, "Noise radiated by a rod-airfoil configuration using DES and the Ffowcs-Williams & Hawkings' analogy," in *16th AIAA/CEAS Aeroacoustics Conference*, Stockholm, Sweeden, June 8-9, 2010.

[89] J. Boudet, N. Grosjean and M. C. Jacob, "Wake-airfoil interaction as broadband noise source: a large-eddy simulation study," *Int. Journal Aeroacoustics,* vol. 4, no. 1, pp. 93-116, 2005.

[90] J.-C. Giret, A. Sengissen, S. Moreau, M. Sanjosé and J.-C. Jouhaud, "Prediction of the sound generated by a rod-airfoil configuration using a compressible unstructured LES solver and a FW-H analogy," in *18th AIAA/CEAS Aeroacoustics Conference (33rd AIAA Aeroacoustics Conference)*, Colorado Springs, CO, USA, June 4-6, 2012.

[91] A. Powell, "Theory of vortex sound.," *Journal of the Acoustical Society of America,* vol. 36, no. 1, pp. 177-195, 1964.

[92] T. F. Brooks and T. H. Hodgson, "TRAILING EDGE NOISE PREDICTION FROM MEASURED SURFACE PRESSURES," *Journal of Sound and Vibration,* no. 78, pp. 69-117, 1981.

[93] S. Proskurov, O. R. Darbyshire and S. A. Karabasov, "Aerofoil broadband and tonal noise modelling using stochastic sound sources and incorporated large scale fluctuations," *Journal of Sound and Vibration,* vol. 411, pp. 60-74, 2017.

[94] S. Proskurov, A. P. Markesteijn and S. A. Karabasov, "Investigation into the sources of trailing edge noise using the Acoustic Perturbation Equations, LES and RANS-based FRPM technique," in *AIAA/CEAS Aeroacoustics Conference*, Denver, Colorado, USA, 5-9 June 2017.

[95] S. Pope, Turbulent Flows, Cambridge University Press, 2000.

[96] W. Möhring, Modelling low mach number noise. Mechanics of Sound Generaton in Flows., Berlin: Springer, 1979.

[97] W. Möhring, “A well posed acoustic analogy based on a moving acoustic medium.,” in *SWING workshop*, Dresden, 1999.

[98] Y. H. Kim, Sound propagation: an impedance based approach, Singapore: John Wiley & Sons (Asia) Pte Ltd., 2010.

[99] K. S. Brentner and F. Farassat, “Analytical comparison of the acoustic analogy and Kirchhoff formulation for moving surfaces.,” *AIAA Journal,* vol. 36, pp. 1379-1386, 1998.

[100] G. Ghorbaniasl, L. Siozos-Rousoulis and C. Lacor, “A time-domain Kirchhoff formula for the convective acoustic wave equation,” *Proc Math Phys Eng Sci, Royal Society,* vol. 472, no. 2187, 2016.

[101] A. S. Lyrintzis, “ Review: the use of Kirchhoff’s method in computational aeroacoustics,” *Journal of Fluids Engineering,* vol. 116, no. 665, 1994.

[102] F. Farassat and M. K. Myers, “Multidimensional generalized functions in aeroacoustics and fluid mechanics - part 1: basic concepts and operations.,” *International Journal of Aeroacoustics ,* vol. 10, pp. 161-200, 2011.

[103] P. di Francescantonio, “A new boundary integral formulation for the prediction of sound radiation,” *Journal of Sound and Vibration,* vol. 202, no. 4, pp. 491-509, 1997.

[104] A. S. Morgans, S. A. Karabasov, A. P. Dowling and T. P. Hynes, “Transonic Helicopter Noise,” *AIAA Journal,* vol. 43, no. 7, pp. 1512-1524, 2005.

[105] W. Möhring, “On vortex sound at low Mach number,” *Journal of Fluid Mechanics,* vol. 85, pp. 685-691, 1978.

[106] C. Schram and A. Hirschberg, “Application of vortex sound theory to vortex-pairing noise: Sensitivity to errors in flow data.,” *Journal of Sound and Vibration,* vol. 266, pp. 1079-1098, 2003.

[107] M. S. Howe, Theory of Vortex Sound, Cambridge: Cambridge University Press, 2002.

[108] B. Cockburn and C. W. Shu, “TVB Runge-Kutta local projection Discontinuous Galerkin finite element method for conservation laws II: general framework.,” *Mathematics of Computation,* vol. 52, pp. 411-435, 1989.

[109] B. Cockburn and C. W. Shu, “The Runge-Kutta local projection P1-Discontinuous-Galerkin finite element method for scalar conservation laws,” *Mathematical Modelling and Numerical Analysis,* vol. 25, pp. 337-361, 1991.

[110] B. Cockburn, G. Karniadakis and C. W. Shu, “The development of Discontinuous Galerkin methods,” in *Discontinuous Galerkin Methods: Theory, Computation and Applications, Lecture Notes in Computational Science and Engineering*, Springer, Part I: Overview, 2000, pp. 3-50.

[111] R. J. LeVeque, Finite Volume Methods for Hyperbolic Problems: Cambridge Texts in Applied Mathematics, Cambridge University Press, 2004.

[112] G. Dal Maso, P. LeFloch and F. Murat, “Definition and weak stability of non-conservative products,” *Journal de Mathématiques Pures et Appliquées,* vol. 74, pp. 483-548, 1995.

[113] C. W. Shu, “Discontinuous Galerkin methods: general approach and stability,” RI 02912, USA, Division of Applied Mathematics, Brown University Providence, RI02912, USA, 2009, pp. 1-44.

[114] P. L. Roe, “Characteristic-based schemes for the Euler equations,” *Annual review of fluid mechanics,* vol. 18, no. 1, pp. 337-365, 1986.

[115] S. K. Godunov, “Finite Difference Method for Numerical Computation of Discontinuous Solutions of the Equations of Fluid Dynamics,” *Math. Sb.,* vol. 47, no. 89, pp. 271-306, 1959.

[116] O. Zanotti, F. Fambri and M. Dumbser, “Solving the relativistic magnetohydrodynamics equations with ADER discontinuous Galerkin methods, a posteriori subcell limiting and adaptive mesh refinement,” *Monthly Notices of the Royal Astronomical Society,* vol. 452, pp. 3010-3029, 2015.

[117] J. Hesthaven and T. Warburton, Nodal Discontinuous Galerkin Methods: Algorithms, Analysis and Applications, Texts in Applied Mathematics. Springer. , 2007.

[118] P. Solin, Partial Differential Equations and the Finite Element Method, Pure and Applied Mathematics, Wiley-Interscience, 2006.

[119] D. S. Balsara, C. Altmann, C. Munz and M. Dumbser, “A sub-cell based indicator for troubled zones in RKDG schemes and novel class of hybrid RKDG+HWENO schemes,” *Journal of Computational Physics,* vol. 226, pp. 586-620, 2007.

[120] J. C. Butcher, Numerical Methods for Ordinary Differential Equations, 2nd Ed., John Wiley & Sons, Ltd., 2008.

[121] E. F. Toro, R. C. Millington and L. A. M. Nejad, “Towards very high-order godunov schemes,” in *Godunov Methods: Theory and Applications. Conference in Honour of S. K. Godunov*, New York, Boston and London, Kluwer Academic / Plenum Publishers, 2001, pp. 897-902.

[122] M. Dumbser and O. Zanotti, “Very High Order PNPM schemes on unstructured meshes for the resistive relativistic MHD equations,” *Journal of Computational Physics,* vol. 228, pp. 6991-7006, 2009.

[123] D. Balsara, C. Meyer, M. Dumbser, H. Du and Z. Xu, “Efficient implementation of ADER schemes for Euler and magnetohydrodynamical flows on structured meshes - Speed comparisons with Runge-Kutta methods.,” *Journal of Computational Physics,* vol. 235, pp. 934-969, 2013.

[124] M. Dumbser, M. Käser, V. A. Titarev and E. F. Toro, “Quadrature-free non-oscillatory finite volume schemes on unstructured meshes for nonlinear hyperbolic systems,” *Journal of Computational Physics,* vol. 226, pp. 204-243, 2007.

[125] O. Zanotti and M. Dumbser, “Efficient conservative ADER schemes based on WENO reconstruction and space-time predictor in primitive variables,” *Computational Astrophysics and Cosmology,* vol. 3:1, 2016.

[126] V. M. Goloviznin and A. A. Samarskii, “Some characteristics of finite difference scheme CABARET,” *Math. Model. ,* vol. 10, no. 1, pp. 101-116, 1998.

[127] J. P. Boris, D. L. Book and K. Hain, “Flux-corrected transport: generalization of the method,” *Journal of Computational Physics,* vol. 31, pp. 335-350, 1975.

[128] T. Colonius and S. K. Lele, “Computational aeroacoustics: progress on nonlinear problems of sound generation,” *Journal of Scientific Computing,* vol. 40, pp. 345-416, 2004.

[129] S. A. Karabasov, P. S. Berloff and V. M. Goloviznin, “CABARET in ocean gyres,” *Ocean Modelling,* vol. 30, pp. 155-168, 2009.

[130] V. M. Goloviznin, “"The balance-characteristic method for the numerical solution to one-dimensional gas dynamic equations in Euler coordinates". In Russian: Балансно-характеристический метод численного решения одномерных уравнений газовой динамики в Эйлеровых переменных,” *Math. Modelling,* vol. 18, no. 11, pp. 14-30, 2006.

[131] P. R. Spalart and S. R. Allmaras, “A one-equation turbulence model for aerodynamic flows,” in *AIAA 30th Aerospace Sciences Meeting and Exhibit.*, 6-9 January, Reno, NV, USA, 1992.

[132] B. S. Baldwin and T. Barth, “A One-Equation Turbulence Transport Model for High Reynolds Number Wall-Bounded Flows,” NASA TM-102847, 1990.

[133] F. R. Menter, “Two-Equation Eddy-Viscosity Turbulence Models or Engineering Applications,” *AIAA J.,* vol. 32, no. 8, pp. 1598-1605, 1994.

[134] B. E. Launder and D. B. Spalding, “The numerical computation of turbulent flows,” *Computer Methods in Applied Mechanics and Engineering,* vol. 3, no. 2, pp. 269-289, 1974.

[135] D. C. Wilcox, Turbulence modeling for CFD, 1st edition, La Canada, CA: DCW Industries, Inc., 1993.

[136] T. J. Barth and D. C. Jespersen, “The Design and Application of Upwind Schemes on Unstructured Meshes,” in *AIAA, 27th Aerospace Sciences Meeting*, Reno, NV, USA, 9-12 Jan, 1989.

[137] M. L. Shur, P. R. Spalart, M. K. Strelets and A. K. Travin, “An enhanced version of DES with rapid transition from RANS to LES in separated flows,” *Flow, turbulence and combustion,* vol. 95, no.

4, pp. 709-737, 2015.

[138] A. Leonard, “Energy cascade in large-eddy simulations of turbulent fluid flows,” *Advances in Geophysics A,* vol. 18, pp. 237-248, 1974.

[139] J. P. Boris, F. F. Grinstein, E. S. Oran and R. L. Kolbe, “New insights into large-eddy simulation,” *Fluid Dynamics Research,* vol. 10, pp. 199-228, 1992.

[140] R. H. Kraichnan, “Diffusion by a Random Velocity Field,” *Physics of Fluids,* vol. 13, no. 1, pp. 22-31, 1970.

[141] C. Bailly, P. Lafon and S. Candel, “A stochastic approach to compute noise generation and radiation of free turbulent flows,” *AIAA ,* pp. 669-674, 1995.

[142] W. Béchara, C. Bailly, P. Lafon and S. M. Candel, “Stochastic Approach to Noise Modelling for Free Turbulent Flows,” *AIAA Journal,* vol. 32, no. 3, pp. 455-463, 1994.

[143] C. Bailly, P. Lafon and S. Candel, “Computation of Noise Generation and Propagation for Free and Confined Turbulent Flows,” in *2nd AIAA/CEAS Aeroacoustcs Conference*, State College, PA, USA, May 6-8, 1996.

[144] M. Billson, L. E. Eriksson and L. Davidson, “Jet Noise Prediction Using Stochastic Turbulence Modelling,” in *9th AIAA/CEAS Aeroacoustics Conference*, Hilton Head, SC, USA, 12-14 May, 2003.

[145] A. Smirnov, S. Shi and I. Celik, “Random Flow Generation Technique for Large Eddy Simulations and Particle-Dynamics Modeling,” *Journal of Fluids Engineering,* vol. 123, no. 2, pp. 359-371, 2001.

[146] M. Billson, L. E. Eriksson, L. Davidson and P. Jordan, “Modeling of Synthetic Anisotropic Turbulence and its Sound Emission,” in *10th AIAA/CEAS Aeroacoustics Conference*, Manchester, Great Britain, 10-12 May, 2004.

[147] M. Karweit, P. Blanc-Benon, D. Juvé and G. Comte-Bellot, “Simulation of the Propagation of an Acoustic Wave through a Turbulent Velocity Field: A Study of Phase Variance,” *Journal of the Acoustical Society of America,* vol. 89, no. 1, pp. 52-62, 1991.

[148] S. H. Huang, Q. S. Li and J. R. Wu, “A General Inflow Turbulence Generator for Large Eddy Simulation,” *Journal of Wind Engineering and Industrial Aerodynamics ,* vol. 98, no. 10-11, pp. 600-617, 2010.

[149] H. G. Castro and R. R. Paz, “A Time and Space Correlated Turbulence Synthesis Method for Large Eddy Simulations,” *Journal of Computational Physics,* vol. 235, pp. 742-763, 2013.

[150] A. M. Wohlbrandt, F. Guerin and R. Ewert, “Extension of the Random Particle Mesh method to periodic turbulent flows for fan broadband noise prediction,” in *21st AIAA/CEAS Aeroacoustics*

Conference, Dallas, TX, USA, 2015.

[151] S. Heo, C. Cheong and T. Kim, "Unsteady Fast Random Particle Mesh method for efficient prediction of tonal and broadband noises of a centrifugal fan unit," *AIP Advances,* vol. 5, no. 9, 2015.

[152] M. Van Dyke, Perturbation Methods in Fluid Mechanics, The Parabolic Press, 1975.

[153] M. Siefert and R. Ewert, "Sweeping Sound Generation in Jets Realized with a Random Particle-Mesh Method," in *15th AIAA/CEAS Aeroacoustics Conference*, Miami, FL, USA, 11-13 May, 2009.

[154] N. G. van Kampen, Stochastic processes in physics and chemistry. 4th Ed., Amsterdam, The Netherlands: Elsevier Science B. V., 2003.

[155] M. Dieste, "Random-Vortex-Particle Methods Applied to Broadband Fan Interaction Noise," PhD thesis, Faculty of Engineering and the Environment, Institute of Sound and Vibration Research , University of Southampton, June 2011.

[156] M. Dieste and G. Gabard, "Predicting broadband fan interaction noise using a random-vortex-particle method," in *20th International Congress on Acoustics (ICA)*, Sydney, Australia, 23-27 August, 2010.

[157] A. Cahuzac, "Ph.D. Thesis: Aspects cinetiques et acoustiques en simulation numerique des grandes echelles, et application a l'etude du controle de l'ecoulement de jeu en turbomachines.," L'Ecole Centrale de Lyon, 2013.

[158] C. Norberg, "Pressure forces on a circular cylinder," *Bluff-Body Wakes, Dynamics and Instabilities,* pp. 275-278, 1993.

[159] N. Gregory and C. L. O'Reilly, "Low-Speed Aerodynamic Characteristics of NACA0012 Aerofoil Section, including the Effects of Upper-Surface Roughness Simulating Hoar Frost," R. & M. No. 3726, London, 1970.

[160] I. A. Milne, R. N. Sharma, R. G. J. Flay and S. Bickerton, "Characteristics of the turbulence in the flow at a tidal stream power site," *Phil Trans R Soc,* 14 January 2013.

[161] C. Rautmann, J. Dierke, R. Ewert, N. Hu and J. W. Delfs, "Generic Airfoil Trailing-Edge Noise Prediction using Stochastic Sound Sources from Synthetic Turbulence," in *20th AIAA/CEAS Aeroacoustic Conference*, Atlanta, GA, USA, 16-20 June 2014.

[162] M. Kamruzzaman, T. Lutz, W. Würz and E. Krämer, "On the Length Scales of Turbulence for Aeroacoustic Applications," in *17th AIAA/CEAS Aeroacoustics Conference*, Portland, Oregon, USA, 5-8 June 2011.

[163] M. Kamruzzaman, T. Lutz, A. Herrig and E. Krämer, "Semi-Empirical Modeling of Turbulent

Anisotropy for Airfoil Self-Noise Predictions," *AIAA Journal,* vol. 50, no. 1, pp. 46-60, 2012.

[164] D. G. Crighton, A. P. Dowling, J. E. Ffowcs Williams, M. Heckl and F. G. Leppington, Modern Methods in Analytical Acoustics, London: Springer-Verlag, 1996.

[165] H. M. Atassi, "Teaching Notes: Introduction to Acoustics - AME 60633," University of Notre Dame, 2016. [Online]. Available: https://www3.nd.edu/~atassi/teaching.html. [Accessed 17 08 2016].

[166] R. Ewert, "Canonical Stochastic Realization of Turbulent Sound Sources via Forced Linear Advection-Diffusion-Dissipation Equation," in *22nd AIAA/CEAS Aeroacoustics Conference* , Lyon, France, 2016.

[167] C. L. Ladson, "Effects of Independent Variation of Mach and Reynolds Numbers on the Low-Speed Aerodynamic Characteristics of the NACA 0012 Airfoil Section," NASA Technical Memorandum 4074, Langley Reseach Center , Hampton, Virginia, 1988.

[168] P. R. Spalart, S. Deck, M. L. Shur, K. D. Squires, M. K. Strelets and A. K. Travin, "A new version of detached-eddy simulation, resistant to ambiguous grid densities," *Theoretical and computational fluid dynamics,* vol. 20, no. 3, pp. 181-195, 2006.

[169] S. Hogg and M. A. Leschziner, "Computation of Highly Swirling Confined Flow with a Reynolds Stress Turbulence Model," *AIAA J.,* vol. 27, no. 1, pp. 57-63, 1989.

[170] P. Batten, T. J. Craft and M. A. Leschziner, "Reynolds-stress-transport modelling for compressible aerodynamic flows," *AIAA J.,* vol. 37, pp. 785-796, 1999.

[171] J. Smagorinsky, "General circulation experiments with the primitive equations. I: The basic experiment," *Monthly Weather Review,* vol. 91, no. 3, pp. 99-165, 1963.